1989

Exclusive neutral strange particle production from Double Pomeron Exchange produced by proton-proton interactions at [square root of s] = 62 GeV

John Donovan Skeens
Iowa State University

Recommended Citation

Skeens, John Donovan, "Exclusive neutral strange particle production from Double Pomeron Exchange produced by proton-proton interactions at [square root of s] = 62 GeV " (1989). *Retrospective Theses and Dissertations*. 9179.
https://lib.dr.iastate.edu/rtd/9179

INFORMATION TO USERS

The most advanced technology has been used to photograph and reproduce this manuscript from the microfilm master. UMI films the text directly from the original or copy submitted. Thus, some thesis and dissertation copies are in typewriter face, while others may be from any type of computer printer.

The quality of this reproduction is dependent upon the quality of the copy submitted. Broken or indistinct print, colored or poor quality illustrations and photographs, print bleedthrough, substandard margins, and improper alignment can adversely affect reproduction.

In the unlikely event that the author did not send UMI a complete manuscript and there are missing pages, these will be noted. Also, if unauthorized copyright material had to be removed, a note will indicate the deletion.

Oversize materials (e.g., maps, drawings, charts) are reproduced by sectioning the original, beginning at the upper left-hand corner and continuing from left to right in equal sections with small overlaps. Each original is also photographed in one exposure and is included in reduced form at the back of the book. These are also available as one exposure on a standard 35mm slide or as a 17″ x 23″ black and white photographic print for an additional charge.

Photographs included in the original manuscript have been reproduced xerographically in this copy. Higher quality 6″ x 9″ black and white photographic prints are available for any photographs or illustrations appearing in this copy for an additional charge. Contact UMI directly to order.

U·M·I

University Microfilms International
A Bell & Howell Information Company
300 North Zeeb Road, Ann Arbor, MI 48106-1346 USA
313/761-4700 800/521-0600

Order Number 9014954

Exclusive neutral strange particle production from double Pomeron exchange produced by proton-proton interactions at $\sqrt{s} = 62$ GeV

Skeens, John Donovan, Ph.D.

Iowa State University, 1989

U·M·I
300 N. Zeeb Rd.
Ann Arbor, MI 48106

Exclusive neutral strange particle production from Double Pomeron Exchange produced by proton-proton interactions at $\sqrt{s} = 62$ GeV

by

John Donovan Skeens

A Dissertation Submitted to the
Graduate Faculty in Partial Fulfillment of the
Requirements for the Degree of
DOCTOR OF PHILOSOPHY

Department: Physics
Major: High Energy Physics

Approved:

Signature was redacted for privacy.

In Charge of Major Work

Signature was redacted for privacy.

For the Major Department

Signature was redacted for privacy.

For the Graduate College

Iowa State University
Ames, Iowa
1989

CONTENTS

1 INTRODUCTION

1.1 Experimental Interest

Considerable attention has been given to the study of single and multiple Pomeron exchange [Kaidalow and Ter-Martirosyan 1974, Roy and Roberts 1974]. The Pomeron is helpful in the calculation of cross sections, and explains many features of strong interactions. As a result of this study, bare Pomeron models [Low 1975, Nussinov 1975], and a subtractive quark model which incorporates the Pomeron [Pumplin and Lehman 1981], have been constructed to explain the nature of the Pomeron. The study of Double Pomeron Exchange (DPE) is of particular importance, as it may be a way of searching for gluonic bound states which are of considerable interest in verification of Quantum Chromodynamics (QCD) theory [Robson 1977]. QCD theory is a means of explaining the fundamental strong nuclear forces in nature [Quigg 1983, Huang 1982]. The mediators of this force are called gluons. Gluons are thought to hold matter together on the nucleon level (i.e., to hold the quarks in protons together).

Experiments at the European Laboratory for Particle Physics (CERN) using the Intersecting Storage Rings (ISR) have shown that study of DPE is feasible [Drijard et al. 1978, Breakstone et al. 1986]. By careful selection of the reaction $pp \rightarrow ppX$, where X consists of a central system of particles, using certain trigger requirements, it is a relatively straightforward process to obtain a sample of these types of events. This chapter will briefly describe the DPE mechanism and possible existing states which may be produced.

1.2 Pomeron Exchange Model

Figure 1.1 shows some of the gluon couplings possible in single and multiple Pomeron exchange [Nussinov 1975]. In the diagrams, gluons are represented by wavy lines, and fermions by smooth lines. Diagram (a) shows the simplest case of two gluons forming the Pomeron. Diagrams (b-d) show some of the various stages of generating intermediate states from (a). Diagram (e) shows the simplest case for forming the DPE particle vertex and (f) shows a possible multi-gluon ladder vertex into which the particle produced in (e) could be incorporated. It has been suggested that (e) and higher order diagrams may produce gluonic bound states [Robson 1977].

The model of the Pomeron is a mechanism which accounts for approximately constant total hadronic cross sections (at high energy 3-300 GeV), zero real parts of scattering amplitudes, and limiting fragmentation of particles (i.e., low particle multiplicity) in hadron hadron collisions [Low 1975]. This model is useful, in that experiment has shown these qualities to exist in hadron collisions and it explains these phenomena very well.

1.2.1 Regge theory and its relationship to Pomerons

The Pomeron was named for I. Ia. Pomeranchuk, who first proved a theorem which states that at high energies, the elastic cross sections for particles and anti-particles should become equal and be isospin independent [Perkins 1982, Pomeranchuk 1956, 1958, and Okun and Pomeranchuck 1956].

Regge theory treats the angular momentum as a continuous complex variable and physical states may take integral or half integral values along the real axis called "Regge poles". This variable is denoted by $\alpha(E)$, where α is a function of

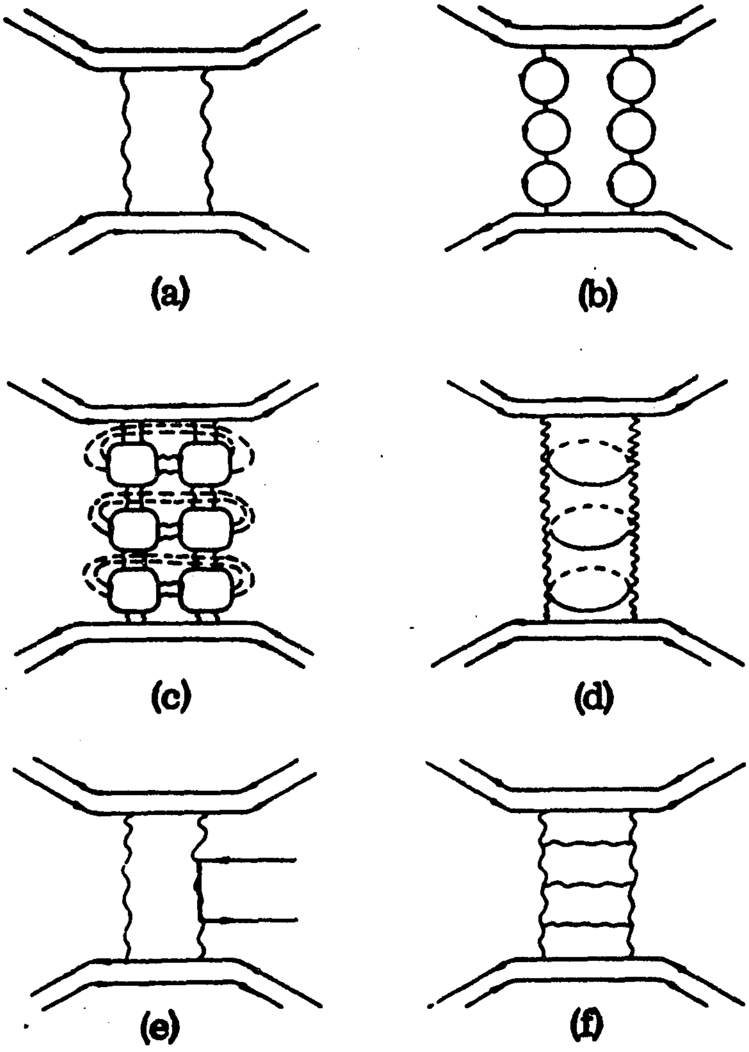

Figure 1.1 Some gluon couplings possible in single and multiple Pomeron exchange; gluons are represented by wavy lines, fermions are represented by smooth lines, and the dashed lines indicate any number of possible intermediate states [Nussinov 1975]

the energy of the particle. The path in the complex energy plane followed by α as the energy, E, increases is called a "Regge trajectory". When the real part of $\alpha(E)$ is equal to the angular momentum, L, (an integer or half-integer) a resonant state can occur. Each resonance on a given trajectory must have the same quantum numbers except for the angular momentum [Chew et al. 1962, Perkins 1982]. In order to obtain conservation of parity, this requires that each successive resonance on a Regge trajectory be separated by two units of angular momentum (the parity sign is given by $P = -1^L$ for natural states, and $P = -1^{L+1}$ for unnatural states). For a nearly constant total cross section at high energies, $\alpha(0) = 1$ is needed [Perkins 1982]. In order to explain all elastic scattering phenomena, this trajectory must also have vacuum quantum numbers (i.e., strangeness, charm, isospin, baryon no., etc.). Since the vacuum pole exchange dominates the elastic scattering, then the elastic cross sections for particles and antiparticles must be equal. This vacuum trajectory has been termed the "Pomeranchuk trajectory" and the exchanged particle is called the "Pomeron". In addition, the Pomeron exchange process may account for the characteristics of interactions where one of the two incident particles is excited slightly, and the other particle is left unchanged except for a small amount of momentum transfer. These types of interactions are called quasi-elastic or diffractive scattering processes. Extensive work has been done using the Regge model to describe correctly several aspects of these types of interactions [Amaldi et al. 1976], including multiple Pomeron exchange.

1.3 Double Pomeron Exchange (DPE) Process

Double Pomeron Exchange (DPE) is the process in which two Pomerons are exchanged. In the center of mass frame of a system, this creates two fast forward outgoing systems which can be made up of quasi-elastically scattered protons, and a slower central system, X, consisting of whatever is formed by the interaction of the two Pomerons. The resulting Feynman x_f value (i.e., the ratio of a particle's longitudinal momentum or the momentum along the incoming beam axes to its maximum kinematically allowed momentum, see Equation 2.5) of each proton remains close to unity. All the centrally produced particles in the system, X, must have small Feynman x_f near zero. The cross sections in the DPE process are of the order of ten to thirty microbarns (μb, $1\mu b = 10^{-30}$ cm^2). This is only about 1/2000 of the total proton proton (pp) cross sections at the energies used in this experiment. Thus, the process is rare, and requires careful setup of the experiment in order to isolate the event sample [Drijard et al. 1978, Breakstone et al. 1986].

Figure 1.2 illustrates the normal diffractive processes (a) and (b), which show Reggeon-Pomeron exchange for the case $pp \rightarrow pp\pi^+\pi^-$. In this case the Reggeon remains close to one of the proton vertices, i.e., the rapidity (see Equation 2.4) of the central system is not well separated from the rapidity of one of the protons. This means that the central system travels in the direction of one of the forward protons and does not have low enough Feynman x_f. Figure 1.2(c) shows the Pomeron-Pomeron exchange process with a large gap in rapidity between the two central system pions and the forward protons. This is an important property of a DPE event which can be used to distinguish it from other interactions [Drijard et al. 1978].

The double inclusive distribution for the quasi-elastically scattered protons is

$$\frac{x_1 x_2 d^2\sigma}{dx_1 dx_2 dp_{t_1}^2 dp_{t_2}^2} = \frac{1}{8\pi^2}\gamma_1^2(t_1)\gamma_2^2(t_2)|\eta(t_1)||\eta(t_2)|\frac{\sigma_{pp}(M^2, t_1, t_2)}{(1-x_1)^{(2\alpha(t_1)-1)}(1-x_2)^{(2\alpha(t_2)-1)}} \tag{1.1}$$

where the function γ gives the proton couplings, η is the signature factor of the

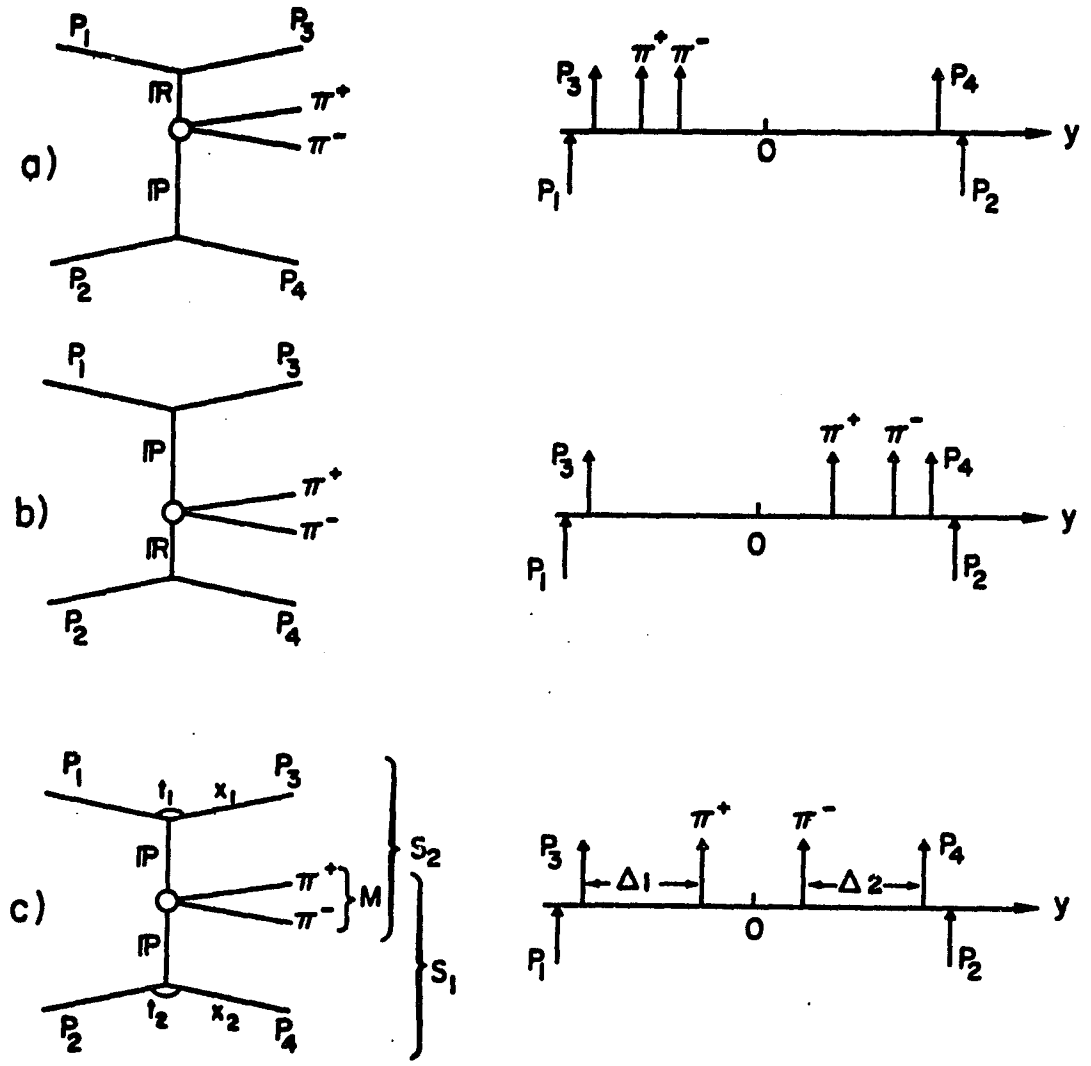

Figure 1.2 Normal diffractive processes which show (a-b) Reggeon-Pomeron exchange for the case $pp \to pp\pi^+\pi^-$, and (c) Pomeron-Pomeron exchange process for the same reaction, showing the large rapidity gap between the two central system pions and the forward protons [Drijard et al. 1978]

Reggeons, α is the Regge intercept (which is 1.0 for Pomerons and only 0.5 for Reggions), p_{t_i} is the transverse momentum of the protons, M^2 is the central system mass squared, t_i is the momentum transfer of each proton, x_i is the Feynman x_f value of each proton, and σ_{pp} is the total Pomeron-Pomeron cross section [Amaldi et al. 1976].

In DPE, $\alpha_i = 1$ for $i = 1, 2$ so that Equation 1.1 gives the relation

$$\frac{d\sigma}{dx_1 dx_2} \sim \frac{1}{(1-x_1)(1-x_2)} \tag{1.2}$$

This shows the double pole term near $x_1, x_2 = 1$. It should be noted that one needs to be careful to look at the x_1 and x_2 values to ensure double pole behavior for this experiment, i.e., $x_1, x_2 \approx 1$. If the dominant reaction were single diffraction then there would be a loss of events in this double pole region. The cross section in the case of single diffraction,

$$\frac{d\sigma}{dx_1 dx_2} \sim \frac{1}{1-x_1} + \frac{1}{1-x_2} \tag{1.3}$$

contains only single pole terms [Amaldi et al. 1976].

Another requirement of DPE is that the two fast outgoing protons' momenta must be uncorrelated. This is evident from the absence of cross terms in the proton couplings and signature factors in Equation 1.1. Thus, the azimuthal angles of the outgoing protons about the beam axis are uncorrelated. Also, the two momentum transfers t_1 and t_2 are not correlated in DPE. In elastic scattering, the behavior is well described by the function e^{at}. For DPE this behavior is expected also with the constant, a, equal to one-half of the value for an elastic scattering process with the same energy [Drijard et al. 1978].

The remaining characteristic of DPE processes is given by the possible quantum numbers of the central system resulting from the two Pomerons. As mentioned previously, a Pomeron carries the quantum numbers of the vacuum, $J^{PC} = 0^{++}$. Since two Pomerons are identical bosons, the DPE system must be symmetric in the spatial part of its wave function. Therefore, the total orbital angular momentum must be even, i.e., $L = \{0, 2, 4, ...\}$. Since the Pomerons have zero spin, $J = L$. The parity, P, must be even and the charge conjugation, C, must be even (since $C = -1^{L+S}$, and the total strangeness, $S = 0$). Thus, in DPE only the states $J^{PC} = \{0^{++}, 2^{++}, 4^{++}, ...\}$ are possible in the central system.

1.4 Possible States (Resonances)

Using the fact that the reactions in DPE must have the quantum numbers $\{0^{++}, 2^{++}, 4^{++}, ...\}$, and the isospin ($I$) and G parity, must be $I^G = 0^+$, the possible resonant states that may be produced can be tabulated from the "Review of Particle Properties" [Particle Data Group 1988]. In what follows, only the lowest lying states are considered, i.e., 0^{++} and 2^{++} states. Some of the possible DPE states based on the quantum numbers are summarized in Table 1.1. The $f_2(1270)$ meson has been seen in this experiment via the reaction $pp \rightarrow pp(\pi^+\pi^-)$ [Breakstone et al. 1986]. There is some evidence that the $f_0(975)$ may have been produced also [Breakstone et al. 1989] in this experiment. In addition, the reaction $pp \rightarrow pp(p\bar{p})$ shows an enhancement near 2000 MeV in the $p\bar{p}$ mass distribution which may be identified with the $f_2(2010)$ particle resonance, although so far it has only been seen to decay to $\phi\phi$ pairs [Breakstone et al. 1989]. The non-established resonant states which are consistent with allowed DPE states are listed in Table 1.2. These states have been seen by only one or two groups, or have discrepancies in the measured widths and masses [Particle Data Group 1988].

Table 1.1 Some established resonant states which may be formed in DPE

Particle (Mass MeV)	J^{PC}	Width (MeV)	Decay Modes
$f_0(975)$	0^{++}	34	$(\pi\pi)$, $(K\bar{K})$
$f_2(1270)$	2^{++}	180	$(\pi\pi)$, $(K\bar{K})$, $(2\pi 2\pi)$
$f_0(1400)$	0^{++}	150-400	$(\pi\pi)$, $(K\bar{K})$, $(\eta\eta)$
$f_2(1525)$	2^{++}	76	$(K\bar{K})$, $(\pi\pi)$, $(\eta\eta)$
$f_0(1590)$	0^{++}	175	$(\eta\eta)$, (4π)
$f_2(1720)$	2^{++}	138	$(K\bar{K})$, $(\eta\eta)$, $(\pi\pi)$
$f_2(2010, 2300, 2340)$	2^{++}	150-300	$(\phi\phi)$

Table 1.2 Some non-established resonant states which may be formed in DPE

Particle (Mass MeV)	J^{PC}	Width (MeV)	Decay Modes
$f_0(1240)$	0^{++}	140	$(K\bar{K})$
$f_2(1430)$	2^{++}	14-150	$(\pi\pi)$, $(K\bar{K})$
$f_0(1525)$	0^{++}	90	$(K\bar{K})$
$f_0(1750)$	0^{++}	50-200	$(K\bar{K})$, $(\eta\eta)$
$f_2(1810)$	2^{++}	180-390	$(\pi\pi)$, $(K\bar{K})$, $(\eta\eta)$
$f_2(2150)$	2^{++}	250	$(\pi\pi)$

1.5 Glueball Candidates Consistent With DPE

Quantum Chromodynamics Theory (QCD) predicts the existence of gluonic bound states or "glueballs" and a firm calculation of their masses would shed light on their identity. Early attempts at calculation of the glueball mass range were made in the early times of lattice gauge theories [Ishikawa et al. 1982, Berg et al. 1982]. These early calculations were unreliable in their control of systematic and statistical errors and thus, their results were uncertain.

A qualitative study of glueballs has been performed for the lightest possible glueball states using low-dimension, gauge invariant, colorless operators [Jaffe et al. 1986]. The results indicate that the possible quantum numbers of the lightest glueballs are $J^{PC} = \{0^{++}, 0^{-+}, 2^{++}, 2^{-+} ...\}$ and the lowest excited state glueballs have quantum numbers of $J^{PC} = \{1^{++}, 3^{++}, ...\}$. Thus, the lightest three glueball states are expected to have $J^{PC} = \{0^{\pm+}, 1^{++}, 2^{\pm+} ...\}$ for possible quantum numbers. For a two gluon system only the 0^{++} and 2^{++} states are expected for the lightest states.

Theoretical predictions of the 0^{++} and 2^{++} glueball masses have been made using lattice gauge theory. These calculations were carried out using high speed supercomputers and large statistics Monte-Carlo simulation techniques. The results of these studies have been somewhat successful at computing the masses of these two states. The mass ratio of the two states is found to be $m(2^{++})/m(0^{++}) \approx 1.5$ [Kamenzki and Berg 1986, Berg et al. 1986, and Schierholz 1987, 1988a, 1988b]. The computations of the 0^{++} mass have yielded values in the range 1.2-1.5 GeV [Schierholz 1988b, Degrand 1987]. While the 2^{++} mass has been computed to have a range of 1.7-2.2 GeV [Schierholz 1988a, 1988b, Forcrand et al. 1986]. It should be noted that the above computations were performed without taking into account the possible mixing effects with $q\bar{q}$ states. Since glueballs are thought to have widths on the order of a few hundred MeV, mixing effects are possible.

Regarding glueball candidates, it should be noted that no known particle state has been unambiguously identified as a glueball. Some of the known states have been considered as glueballs, but their identity as possible $q\bar{q}$ states or exotic states (e.g., $qq\bar{q}\bar{q}$) is not ruled out either. In the 0^{++} (at 1-2 GeV mass) mesonic area, there are only three well established resonances consistent with DPE quantum numbers, the $f_0(975)$, $f_0(1400)$, and $f_0(1590)$ (see Table 1.1). In order to account for possible glueball states, one must consider also the non-established f_0 resonances, i.e., the $f_0(1240)$, $f_0(1525)$, and $f_0(1750)$. Although it is likely that the well established 0^{++} states are $q\bar{q}$ states, the possibility of one of these being a result of glueball and $q\bar{q}$ mixing cannot be ruled out [Particle Data Group 1988]. For the possible 2^{++} states, there are four to six established mesonic states to consider, i.e., the $f_2(1270)$, $f_2(1525)$, $f_2(1720)$, and $f_2(2010-2340)$. The $f_2(1270)$ and $f_2(1525)$ are thought to be predominantly $q\bar{q}$ states although the $f_2(1270)$ has been seen in DPE [Breakstone et al. 1986] and in the radiative J/Ψ decays [Augustin et al. 1987] which is a gluon rich decay channel. The $f_2(1720)$ (formerly called the $\theta(1690)$ resonance) is one of the leading glueball candidates [Ward 1986]. In addition, the three $f_2(2010-2340)$ resonances are all glueball candidates. Other 2^{++} objects that are not well established are the $f_2(1430)$, $f_2(1810)$, and $f_2(2150)$ states any of which may be glueballs or gluonium and $q\bar{q}$ mixtures.

2 EXPERIMENT DESCRIPTION

This experiment was conducted using facilities at the European Laboratory for Particle Physics (CERN) in Geneva, Switzerland. The CERN Laboratory, as its name indicates, is a collaboration of European countries for research in particle physics. It supports accelerator programs in different areas of particle physics research and is an excellent example of international collaboration in basic science research. The accelerator facility used for this experiment was the Intersecting Storage Rings (ISR), and the detector utilized was the Split Field Magnet.

2.1 Energy and Luminosity of the Intersecting Storage Rings (ISR)

A schematic view of the Intersecting Storage Rings (ISR) is shown in Figure 2.1. The beam starts in a duoplasmatron ion source which supplies positive hydrogen ions to a Cockcroft-Walton accelerator. The source gives several pulses in sequence and the protons are accelerated to 750 keV [Michaelis 1981]. The beam pulses are then injected into a linear accelerator (Linac) and accelerated to 50 MeV. Next, the beam is injected into a booster synchrotron and its energy increased to 800 MeV. The pulses are stored and collected until bunches containing roughly 10^{13} protons are obtained. These bunches are injected into the Proton Synchrotron (PS) which in turn injects the beam into the ISR. The beam lines of the ISR are filled with a few hundred injections from the PS.

The ISR consisted of two interleaved rings, approximately 300 meters in diameter, which intersect at eight points [Keil 1972]. Each ring or beam line, is an evacuated pipe in which protons circulate. The two rings are filled with counter-rotating beams of protons, which collide at the eight intersection points. The

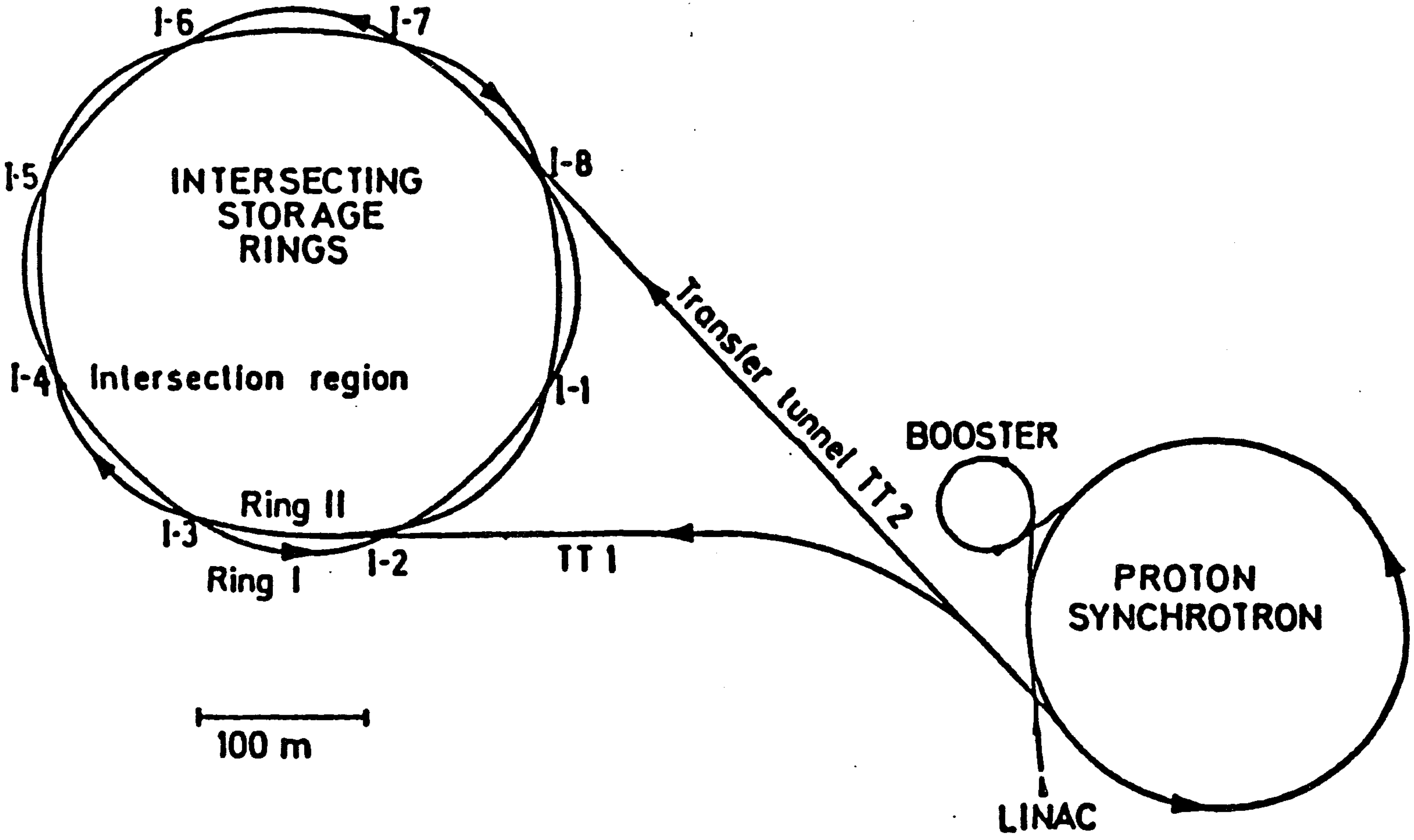

Figure 2.1 Layout of the ISR showing the relative location of the LINAC, Booster, and Proton Synchrotron

horizontal beam crossing angle at each intersection is approximately 14.8 degrees and the pressure in the pipes is 10^{-13} torr. The beam profile in its final state is in the form of a thin slab 1 cm high and 6 cm wide. The current for each beam in the experiment was 30 amps. This is the normal current used at the highest available ISR energy. The energy at which the PS injected proton bunches to the ISR was 26.5 GeV for the experiment under study. The final momentum of the protons in each of the beams was 31.46 GeV and the final acceleration from 26.5 GeV to 31.46 GeV was performed in the ISR itself [Henrichsen et al. 1974, Fischer et al. 1979]. The total center of mass energy available in the ISR for this experiment was therefore $\sqrt{s} = 62$ GeV.

The luminosity of the machine is a parameter of importance for the experiment. The luminosity, "L", is defined as the counting rate for an interaction per unit cross section for that particular interaction. It is expressed by the equation

$$L = \frac{1}{\sigma}\frac{dN}{dt} \tag{2.1}$$

where σ is the cross section for an interaction and dN/dt is the counting rate. An expression for the counting rate is given by

$$\frac{dN}{dt} = \frac{\sigma}{ce^2}\frac{I_1 I_2}{h\ tan(\frac{\alpha}{2})} \tag{2.2}$$

where I_1 and I_2 are the currents of the beams, h is the beam height, α is the beam crossing angle, c is the speed of light, and e is the charge of an electron [Hubner 1977]. Using this equation, one finds a luminosity of $L = 9.0 \times 10^{32} \mathrm{s}^{-1}\mathrm{cm}^{-2}$ for the two intersecting proton beams in the ISR. The luminosity in this experiment is actually slightly different due to the effect of the Split Field Magnet on the crossing angle as will be discussed in the next section.

2.2 Split Field Magnet Detector (SFM)

The experiment was performed at the intersection region I4 of the ISR. The Split Field Magnet detector (SFM) was used to analyze the proton proton interactions. A schematic diagram of the SFM is shown in Figure 2.2. The magnet has a length of 10.3 meters, a width of 2.0 to 3.5 meters and a height of 7.2 meters. The distance between pole pieces is 1.1 meters and there is an effective magnetic volume of 28 cubic meters. The magnet has a total weight of about 880 tons and a maximum field strength of 1.14 tesla [Heiden 1982]. In using storage beams for an experiment, one has to ensure that the net deflection of the beams is zero, i.e., $\oint B \cdot dl = 0$. The SFM has a vertical field and is arranged so that the field points up on one side of the detector and down on the other side. This arrangement gives a net integral of the flux seen by the proton beams of $\oint B \cdot dl \approx 0$. In order to yield a total net beam deflection of exactly zero within experimental errors, there are two large compensator magnets located at the two outgoing beam pipes. These magnets compensate for small net deflections of the beams caused by the SFM detector.

With the magnetic field of the SFM one can measure the momenta of charged particles from the curvature of their trajectories in the field. The magnetic field was set to 1.0 tesla for this experiment. Together with beam momenta of 31.46 GeV for each proton beam, this resulted in a total beam crossing angle of $\alpha = 17.477$ degrees [Bryant 1973]. The center of mass motion in the laboratory frame then becomes $\beta_{cm} = sin\frac{\alpha}{2}\ \beta_{beam} = 0.15\ \beta_{beam}$ towards the center of the ISR. The adjusted luminosity using this value for α is $L = 7.6 \times 10^{32} \mathrm{s}^{-1}\mathrm{cm}^{-2}$.

The volume between the pole pieces of the SFM is filled with Multi-Wire Proportional Chambers (MWPCs). These are more commonly called SFM chambers

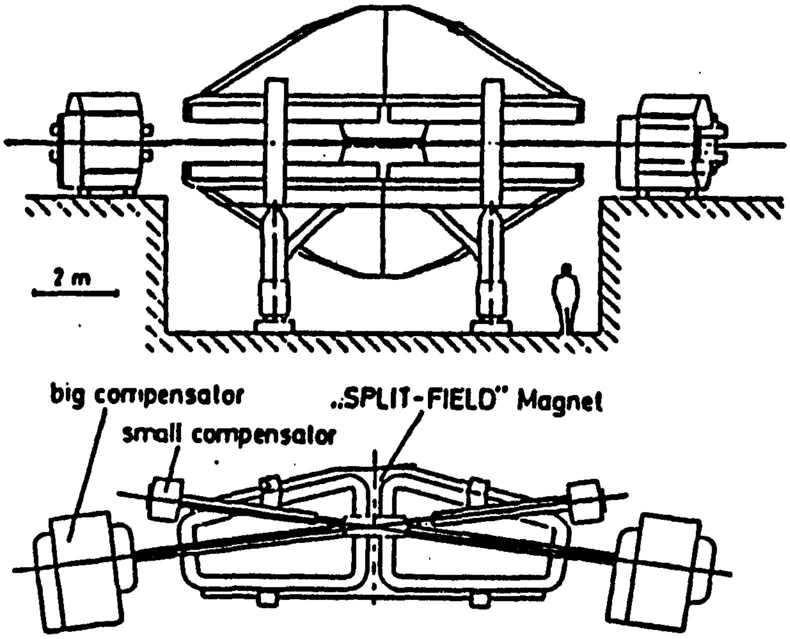

Figure 2.2 Diagram of the SFM showing the side and the top views

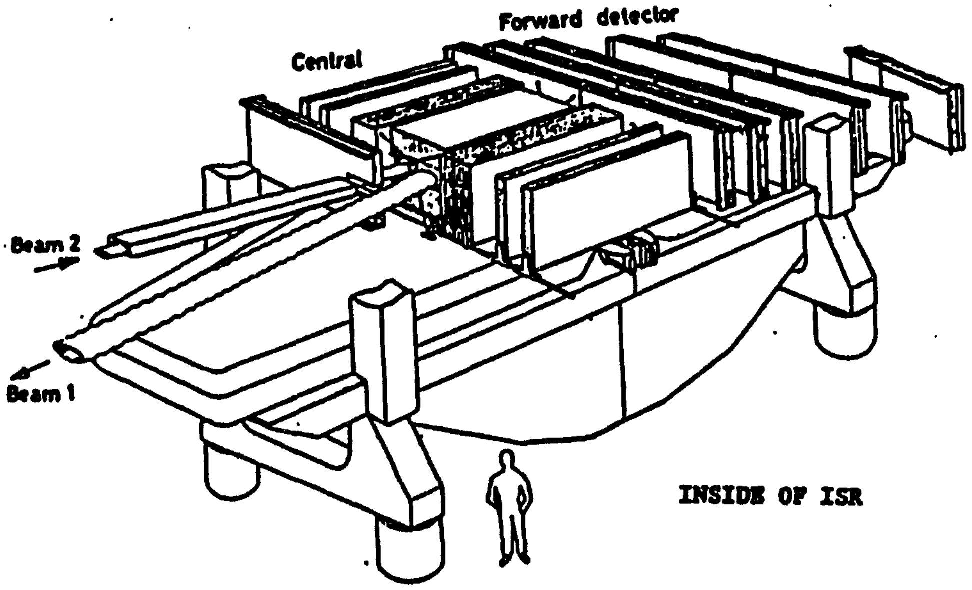

Figure 2.3 Cutaway view of the SFM detector

in the experiment. Their purpose is to measure the trajectories of the charged particles emerging from the interaction. The set-up of the chambers is shown in the diagrams of Figures 2.3 and 2.4. The chambers have been described in various papers [Bouclier et al. 1974, 1975, Brand et al. 1975, Bell et al. 1975, 1978]. The SFM chambers have a self supporting design for the wire planes with sandwiched polyurethane foam sheets layered with silver to provide cathodes for the wires. The design increases the amount of solid angle coverage of the detector, but also increases the amount of material the detected particles had to pass through. This extra material causes energy losses for the particles passing through the chambers, and these losses must be corrected for in the analysis of the data. From the figures, one can see that the SFM separates into three groups of MWPCs. Each describes a particular region of the detector. One group of MWPCs defines the central region and measures the tracks of particles produced at large angles with respect to the incident proton beam directions. The other two groups define two forward regions, one on each side of the detector in the $\pm y$ directions respectively. Table 2.1 shows the number of planes and wire spacings for each of the SFM chambers in the experiment. V, H, and I stand for vertical, horizontal, and inclined planes. The first number in each of the planes indicates which group the chamber is in. The chambers numbered in the range 100 and 200 define the central region, the chambers numbered in the range 300 define the forward telescope in the negative y direction and the chambers in the 400 range define the forward telescope in the positive y direction.

The remaining part of the detector of importance for this experiment is the Time of Flight (TOF) system. It is an array of scintillation detectors set around the SFM (see Figure 2.4) and is used for particle identification. There are 67 counters

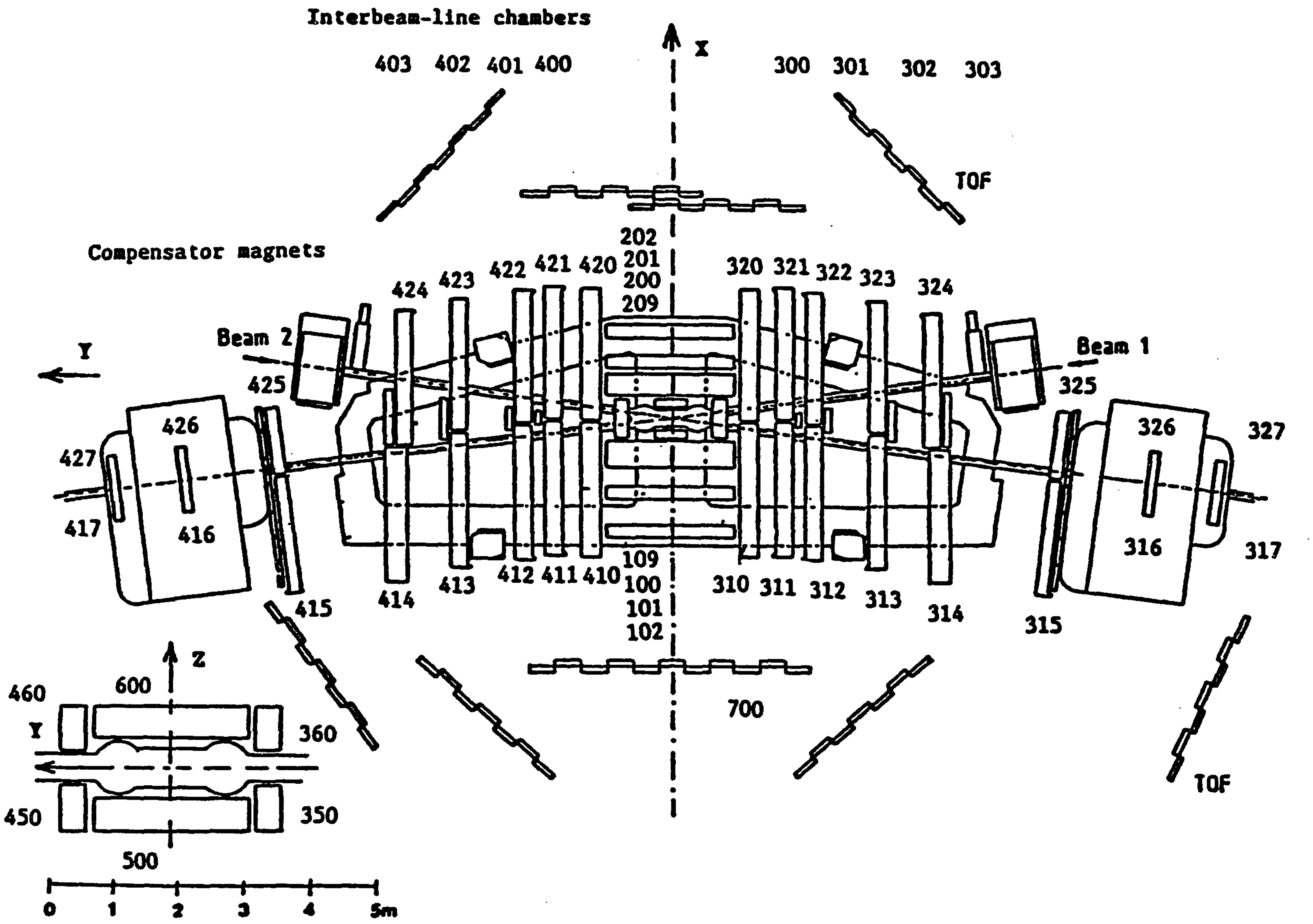

Figure 2.4 Top view of the SFM chamber layout

Table 2.1 Parameters of the MWPCs in the SFM detector

Chamber index	Number of Planes V H I	Wire spacing (cm)
100, 200	4 4 2	0.4
101, 102, 201, 202	1 1 1	0.4
109, 209	3 1 0	0.4
350, 360, 450, 460	2 2 1	0.4
500, 600	5 4 2	0.4
310, 314, 320, 410, 414, 420	3 3 2	0.4
311-313, 321-324, 411-413, 421-424	1 1 0	0.4
315-317, 325-327, 415-417, 425-427	1 1 0	0.2
300-303, 400-403	2 2 2	0.4

arranged in modules of seven counters each and one with 11 counters for a total of nine modules. The size of a single scintillator is 225 cm high by 40 cm wide by 2 cm thick. The arrangement of the counters yields a coverage of about 10 percent of the solid angle. Each scintillator is viewed by photomultiplier tubes situated at its two ends [Heiden 1982]. A TOF counter measures the time of flight for a particle's trajectory from the vertex to the counter. One can thus estimate the velocity of the particle and use the momentum measured by the SFM chambers to identify the mass of the particle from the equation

$$m^2 = p^2 \left(\frac{t^2}{l^2} - \frac{1}{c^2}\right) \tag{2.3}$$

where t is the measured time of flight, l is the length of the trajectory, p is the particle momentum, m is the particle mass and c is the speed of light.

2.3 Trigger Descriptions

Of particular importance to this experiment are the central chambers shown in Figure 2.4. The chambers 100-102, 200-202, 109, and 209 are the central MWPCs which play an important role in defining central system particles in the trigger. Chambers 301, 302, 312, 313, 322, 323, 401, 402, 412, 413, 422, and 423 were used in veto for the trigger to screen out events not containing central tracks. The TOF counters help to provide time of flight information giving mass information on some of the central particles to aid in particle identification. Finally, there are two TOF stands and forward telescopes in the outgoing beam directions to define the two fast outgoing protons in the trigger.

The data taken in the experiment have three distinct sets defined by three different trigger setups. The three triggers are termed OR, AND, and TOF. All triggers required two fast protons, one in each outgoing beam pipe, which was accomplished via the TOF stands near the large compensator magnets. In addition all three sets of data required at least one central particle. The triggers were not completely efficient in selecting the fast forward protons. Therefore, prior to full event reconstruction, the raw data were first run through a filter program in order to select only those events which had one fast proton in each forward direction. This program only reconstructed forward tracks in the SFM. The events with only one positively charged particle in each forward telescope, and momentum greater than 18 GeV were passed on for full reconstruction.

The OR trigger required the detection of one central particle in the positive-x side of the detector or one particle in the negative-x side. The data rate was the greatest for OR data at 52 Hz with a total event count of 1.6 million. Of these 1.6 million events, 500,000 passed the filter stage. 490,000 of these events were successfully reconstructed and written out to a Data Summary Tape (DST). These data were taken in December of 1981 during one ISR run period.

The AND trigger required two central particle tracks to be produced in the detector; one in the positive-x side and one in the negative-x side. It was thus more restrictive than the OR trigger and had a much slower data rate of only 17 Hz with a total event count of 1.4 million events. 420,000 of these events passed the filter stage. A total of 406,000 of these filtered events were successfully reconstructed and written out to a DST. These data were taken during December of 1981 and May of 1982 during two ISR run periods.

The TOF trigger required at least one detected particle in the central region and had the additional constraint of hitting a 700 TOF stand with a delay of at least 32 ns. The TOF trigger was the most restrictive with a data rate of 1 Hz and a total of 2.3 million events recorded. Of the 2.3 million events, 400,000 passed the filter stage. Of these filtered events, 390,000 were successfully reconstructed and written to a DST. These data were taken during a period from March through May of 1983 in 13 ISR runs. The TOF trigger was unique in that it enhanced the average number of kaons and protons produced in an interaction. The total number of kaons and protons for the TOF trigger was roughly equal to the number of pions, i.e., $n_\pi \sim n_K \sim n_p$ in the central region.

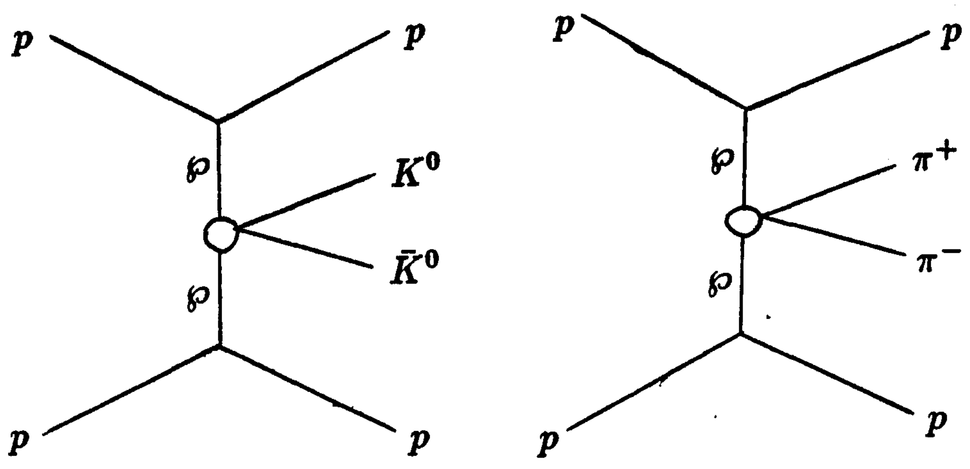

Figure 2.5 Two possible DPE interactions (a) $pp \rightarrow pp(K^0 K^0)$, and (b) $pp \rightarrow pp(\pi^+\pi^-)$

2.4 Evidence for Double Pomeron Exchange (DPE)

Each of these data sets favors Double Pomeron Exchange (DPE). Figure 2.5 shows possible scenarios where two pomerons form a bound state which then decays into two neutral kaons in the interaction $pp \rightarrow pp$ $(K^0\bar{K}^0)$ or two charged pions in the interaction $pp \rightarrow pp$ $(\pi^+\pi^-)$.

Figure 2.6 shows the rapidity distribution of charged particles produced in the interaction $pp \rightarrow pp$ $(\pi^+\pi^-)$ [Breakstone et al. 1986]. The rapidity of a particle is defined by:

$$y = \frac{1}{2}\, ln \frac{(E + p_L)}{(E - p_L)} \tag{2.4}$$

where E and p_L are the energy and longitudinal momentum component of a given particle. The larger the momentum in the beam or longitudinal direction of the particle, the larger the rapidity. The two peaks at $y = \pm 4$ rapidity are the two outgoing fast protons, and the peak between $y = -2$ and $y = +2$ are the two pions which make up the central system. Thus, one sees a good separation of central particles from the fast protons. As mentioned in Chapter 1, this separation is needed in order to isolate a sample of DPE events. The rapidity plot for the interaction $pp \rightarrow pp\ (\pi^{\pm}\pi^{\mp}\pi^{\pm}\pi^{\mp})$ is similar. Figure 2.7 shows a correlation plot [Isenhower 1986] of the Feynman x_f variable of each of the fast outgoing protons where

$$x_f = \frac{p_L}{p_{Lmax}} \approx \frac{p_L}{E} \tag{2.5}$$

It is seen that most of the momentum is in the longitudinal beam direction. Thus, it is apparent that these events are good candidates for DPE events.

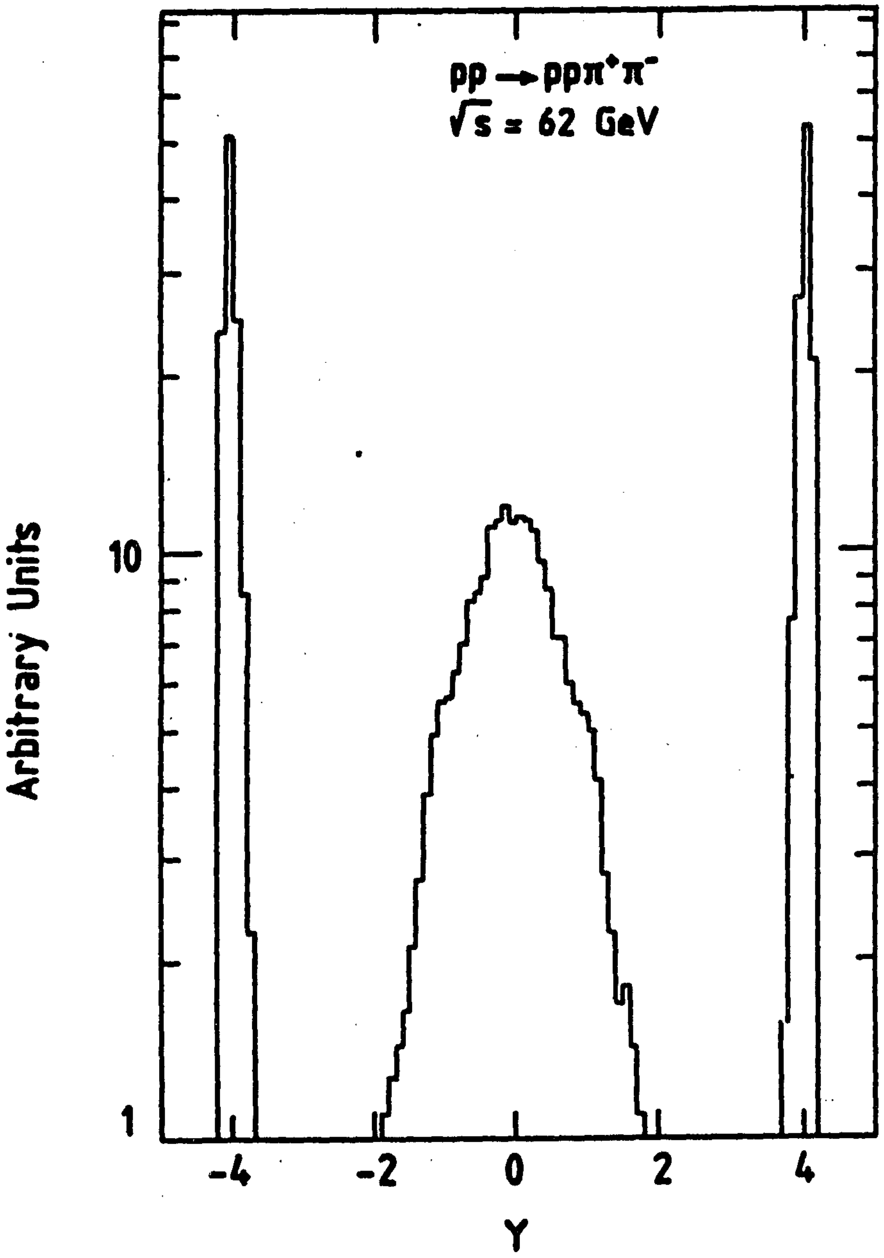

Figure 2.6 Rapidity distributions of charged particles produced in the reaction $pp \to pp(\pi^+\pi^-)$ [Breakstone et al. 1986]

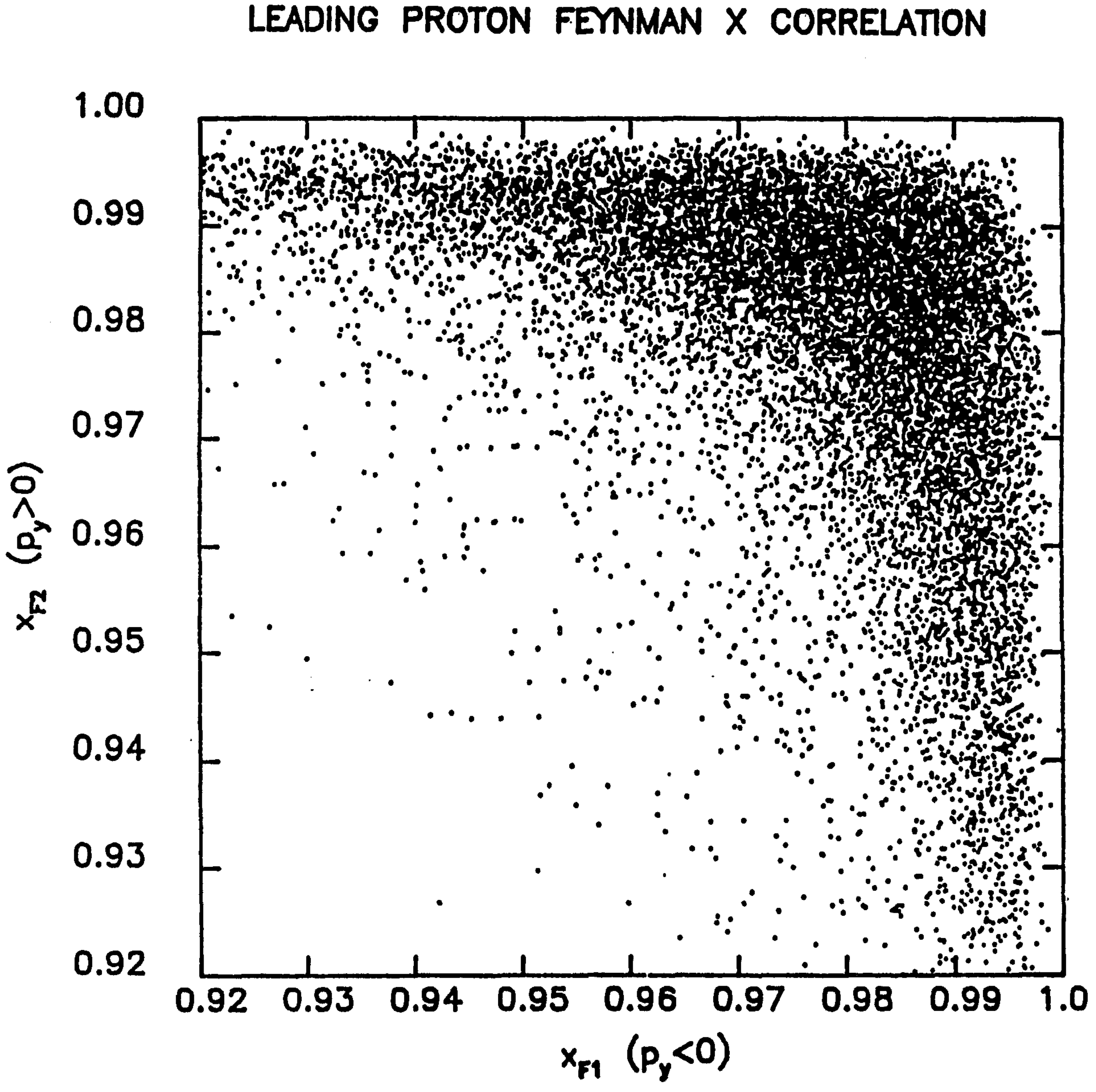

Figure 2.7 Correlation plot of the Feynman x_f variable of each of the fast outgoing protons in the reaction $pp \rightarrow pp(\pi^+\pi^-)$; p_y corresponds to the y momentum direction [Isenhower 1986]

3 DATA REDUCTION

3.1 Track Reconstruction

The track reconstruction in the SFM is based on algorithms produced by H. Wind [Wind 1974, 1978, Aubert and Broll 1974]. The track candidates are found by routines called "WTRAs". The WTRAs determine what combinations of chamber hits may form a valid track. In effect, it defines a road through the SFM detector which a charged particle might take. Each region of the SFM is covered by one or more of these WTRAs. After a valid track candidate is found, it is passed through a routine called SPLINE. The SPLINE routine performs a quintic spline fit to the measured points of the particle track [Drijard 1976]. It effectively refines the measurements of position, momentum, and the directions of each valid track candidate. After the spline fit, the tracks are extrapolated back to the interaction region in order to fit them to a common vertex, called the primary vertex. This primary vertex fitting procedure is accomplished by a Runge-Kutta integration method.

Once an approximate position of the primary vertex is found, it is used as an additional space point to search for other track candidates. Thus, a second track finding step is performed in order to find short tracks and also tracks crossing chambers in different regions (i.e., central and forward regions) which were poorly defined without the vertex. The primary vertex fit is then repeated using all the tracks in order to refine the vertex position measurement. If the chi-square value of this fit is too large, the tracks with largest contributions to the chi-square are dropped, and the fit is retried. The process continues until an acceptable vertex is found.

After the vertex fitting is complete, all individual tracks are checked for compatability with the vertex. Those tracks found to be too far away from the primary vertex (i.e., three times the error on the distance of closest approach from the track to the vertex) and also those tracks with an uncertainty in momentum of $\Delta p/p > 30\%$, are candidates for tracks not associated with the primary vertex. These non-vertex-associated tracks are called secondary tracks. When the entire process is complete, the primary vertex position, a list of vertex and non-vertex associated tracks, the momenta, charges, and all other detector information, such as TOF and energy loss information are stored on a Data Summary Tape (DST) to be used for further analysis. In addition, in order to deal with non-vertex associated tracks, a V^0 fitting program was developed.

3.2 V^0 Track Reconstruction

The SFM is capable of detecting and measuring 90% of all charged tracks produced in high energy proton proton interactions [Minten 1972, Bell et al. 1975]. Thus, it is often called an electronic bubble chamber. However, as far as reconstruction of neutral charged particle decays is concerned, there is a major difference between an electronic detector such as the SFM and a bubble chamber. In a bubble chamber a V^0 decay may be easily identified by the direct observation of a secondary vertex which is well separated from the primary vertex or interaction point. Both the primary and the secondary vertex are usually reconstructed with acceptable accuracy. In addition, the momentum vectors of both V^0 decay particles may be measured directly at the decay vertex. Thus, a three constrained fit (3-C fit) hypothesis of a neutral particle decaying into two charged particles can be performed using momentum conservation at the decay vertex.

As seen in Section 3.1, it is not possible to observe directly the vertices of an interaction in the SFM. Instead one has to reconstruct tracks with computer code from the MWPC information and the magnetic field. A special fit procedure has been designed to determine the geometrical and kinematical variables of a V^0 decay in the SFM [Raschnabel 1981]. In order to find neutral particle decays, two oppositely charged particle trajectories which have similar vertices (i.e., starting points) and which do not point back to the primary vertex are searched for (see Figure 3.1).

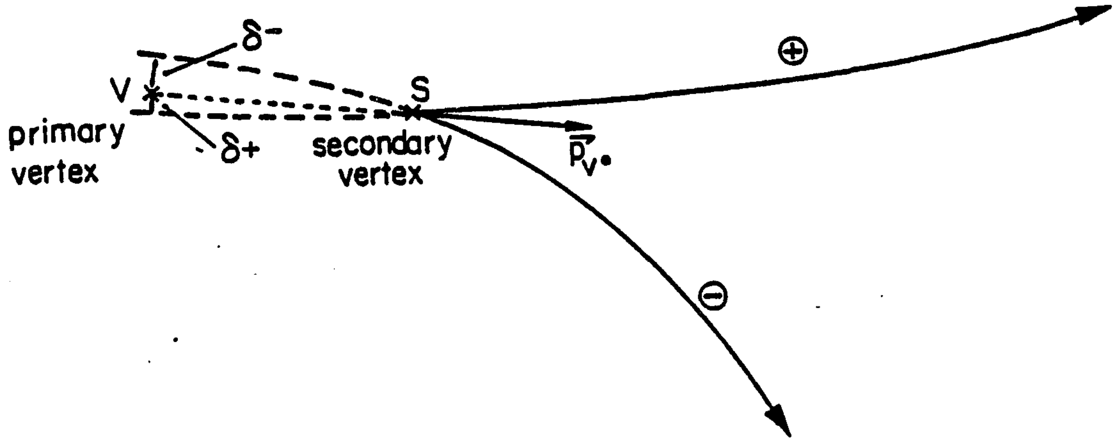

Figure 3.1 Diagram of a V^0 particle showing both the primary (V) and secondary (S) vertices, the distance of closest approach $\delta^{\pm}$, and the V^0 momentum vector

The process of looking for secondary vertices is used to locate three neutral strange particles in the SFM. They are K_s^0, Λ^0, and $\bar{\Lambda}^0$ which decay via the following detectable modes:

$$K_s^0 \rightarrow \pi^+\pi^- \tag{3.1}$$

$$\Lambda^0 \rightarrow \pi^- p \tag{3.2}$$

$$\bar{\Lambda}^0 \rightarrow \pi^+ \bar{p} \tag{3.3}$$

Other neutral particles cannot be searched for by using this method because they either decay too quickly (e.g., π^0, η, ρ, etc.) or they do not decay quickly enough (e.g., K^0_l, n) to be seen with a secondary vertex in the SFM detector.

The search for secondary vertices begins with the secondary tracks' original parameter information found prior to the primary vertex fit and proceeds from there. This is because the secondary tracks often had a primary vertex fit performed which yielded a low probability of fit value (i.e., a high chi-square value) and therefore the original track parameters are a more accurate place to start. For all pairs of oppositely charged secondary tracks, the invariant mass is calculated for the three mass assignments: $\pi^+\pi^-$, π^-p, and $\pi^+\bar{p}$. If any of the combinations gives a mass value close to the K^0_s mass (497 ± 100 MeV) or to the $\Lambda^0/\bar{\Lambda}^0$ mass (1115 ± 125 MeV), a secondary vertex fit is tried. The mass limits are increased by a factor of 1.5 for tracks missing the vertex completely, i.e., for those tracks which did not have a primary vertex fit tried at all. This is done to take into account the poorer determination of track direction for these tracks. As in the primary vertex fitting procedure, a Runge-Kutta integration technique is used for fitting to a secondary vertex which consists of two tracks. In the secondary vertex fit, the point of closest approach (point "S" in Figure 3.1) of two particle trajectories is calculated. Once the secondary decay vertex is found, the kinematical quantities of the two tracks are allowed to vary, i.e., the momenta of the tracks are varied according to their error matrices. The following constraints are imposed on the fit:

1. Both tracks must originate from the secondary decay vertex.
2. The sum of the momentum vectors of the charged particles constituting the V^0 must point back to the primary vertex.

3. For a given mass hypothesis the momenta and angles of the two V^0 tracks are no longer independent variables, but are coupled by decay kinematics; specifically, the invariant mass of the pair is required to be consistent with the mass hypothesis for the V^0.

The fitting process is continued iteratively until an acceptable V^0 candidate is found. If there are no acceptable secondary vertices found for a particular event, the V^0 fitting procedure is abandoned for that event. The details of the V^0 fitting are described by Rauschnabel [Rauschnabel 1981].

3.3 6-prongs

The type of interaction studied consists of two incoming colliding protons and some number n of outgoing charged particles. Two of the n particles are fast outgoing beam protons, n_f, as mentioned in Section 2.3. The rest of the outgoing particles, n_c, are in the central region of the detector. Therefore, the total number of charged particles detected in an event is given by

$$n = n_f + n_c \tag{3.4}$$

The events are called n-prongs signifying the n charged particle tracks detected by the SFM detector. This work is restricted to a subset of the n-prong events, i.e., those events having exactly six charged particles. In addition, the four central particles in any particular 6-prong event are required to be of zero net charge.

Earlier work studying DPE in the SFM have shown that the majority of the charged particles produced in the central region are relatively long-lived charged mesons. This includes pions and kaons with pions comprising the largest number of particles (about 83%) and kaons the second largest (about 12%) [Breakstone et al. 1989]. In addition, protons and anti-protons are occasionally produced in the central region (about 5% of the time).

3.4 Interactions To Be Studied

Results of the V^0 fitting procedure are used as a starting point to look for the following interactions;

$$pp \rightarrow pp(K_s^0 K_s^0) \tag{3.5}$$

$$pp \rightarrow pp(K_s^0 K^{\pm} \pi^{\mp}) \tag{3.6}$$

$$pp \rightarrow pp(\Lambda^0 \bar{\Lambda}^0) \tag{3.7}$$

$$pp \rightarrow pp(\Lambda^0 \bar{\Lambda}^{0*}) \tag{3.8a}$$

$$pp \rightarrow pp(\Lambda^{0*} \bar{\Lambda}^0) \tag{3.8b}$$

Each candidate event is required to have at least one identified V^0 particle. In the case where an event had TOF information for a charged particle, the mass assignments are checked for consistency with the mass predicted by its time of flight trajectory using Equation 2.3. This helps screen out a fraction of about five to ten percent of the events that are not properly identified. In the case of reaction 3.5, the two central region charged particles not associated with the V^0 are assigned pion masses. In reaction 3.6, the two central region charged particles not associated with the V^0 are assigned first K^+ and π^- masses, and then π^+ and K^- masses for each event. This introduces a rather large combinatorial background which is partially reduced with TOF information when available. In the case of reaction 3.7, the other two central particles are assigned pion and proton masses appropriate to their charge and the type of V^0 fit, i.e., either Λ^0 or $\bar{\Lambda}^0$. In the case of reaction 3.8, a Λ^{0*} or $\bar{\Lambda}^{0*}$ resonance is searched for by assigning the appropriate proton and kaon masses to the two charged central particles not associated with the V^0 particle. In Sections 3.4.1 and 3.4.2 the results of the V^0 routines will be considered for each of the interactions with no additional constraints applied to the 6-prong data.

3.4.1 Interactions involving at least one K_s^0

The decay length distributions of K_s^0 tracks for 6-prong events having at least one K_s^0 track found are shown in Figure 3.2. The decay length shown is the distance in the laboratory frame from the primary vertex to the secondary vertex. The figure at the top shows the distribution in the decay length for the OR trigger data. The decay length distribution peaks at approximately two centimeters with a large tail. The average calculated error in the decay length from the V^0 fit routine is 20-30% of the decay length. The AND trigger data (center) and TOF trigger data (bottom) are very similar. The sharp cut-off in the decay length at 1.0 cm is due to the constraint placed on the allowed decay length by the V^0 fitting program.

The decay plane orientation angle ϕ of the K_s^0 is shown in Figure 3.3 for each of the three triggers. The decay plane orientation angle is calculated from the V^0 direction, $\widehat{w}$, and the direction of the positive track, $\widehat{u}$, in a frame of reference defined by $\widehat{w}$ and the beam direction, $\widehat{y}$. The three axes are given by $\widehat{w}$, $\widehat{e}_1$, and $\widehat{e}_2$. The axes $\widehat{e}_1$ and $\widehat{e}_2$ are computed by the cross products

$$\widehat{e}_1 = \frac{\widehat{y} \times \widehat{w}}{|\widehat{y} \times \widehat{w}|}, \quad \widehat{e}_2 = \widehat{w} \times \widehat{e}_1 \tag{3.9}$$

and the angle ϕ is found from the unit vectors, $\widehat{u}$, $\widehat{w}$, $\widehat{e}_1$, and $\widehat{e}_2$,

$$\widehat{u} \cdot \widehat{w} = cos(\theta_+) \tag{3.10a}$$

$$\widehat{u} \cdot \widehat{e}_1 = sin(\theta_+)cos(\phi) \tag{3.10b}$$

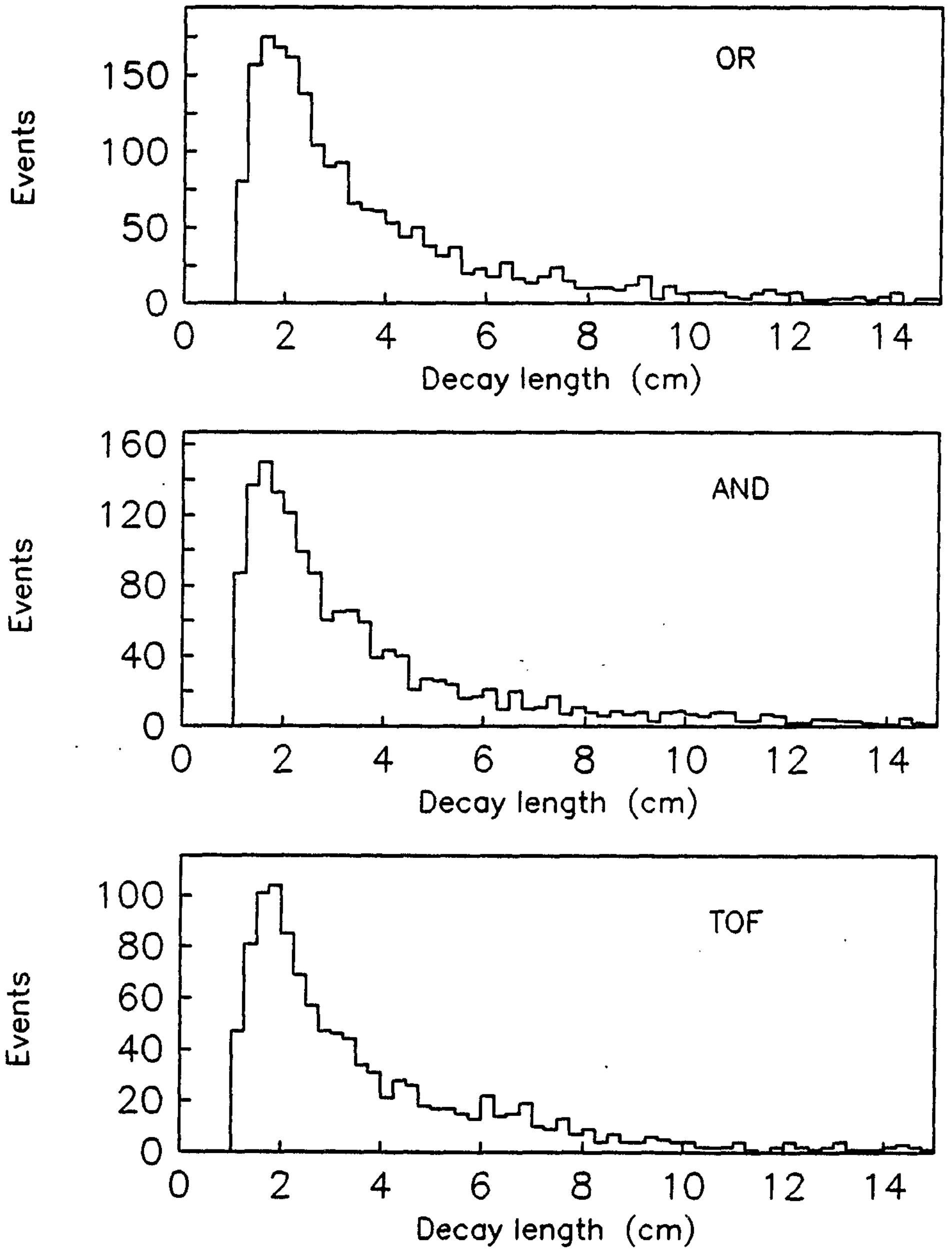

Figure 3.2 Decay length of the K_s^0 particle for the OR (top), AND (center), and TOF (bottom) triggers

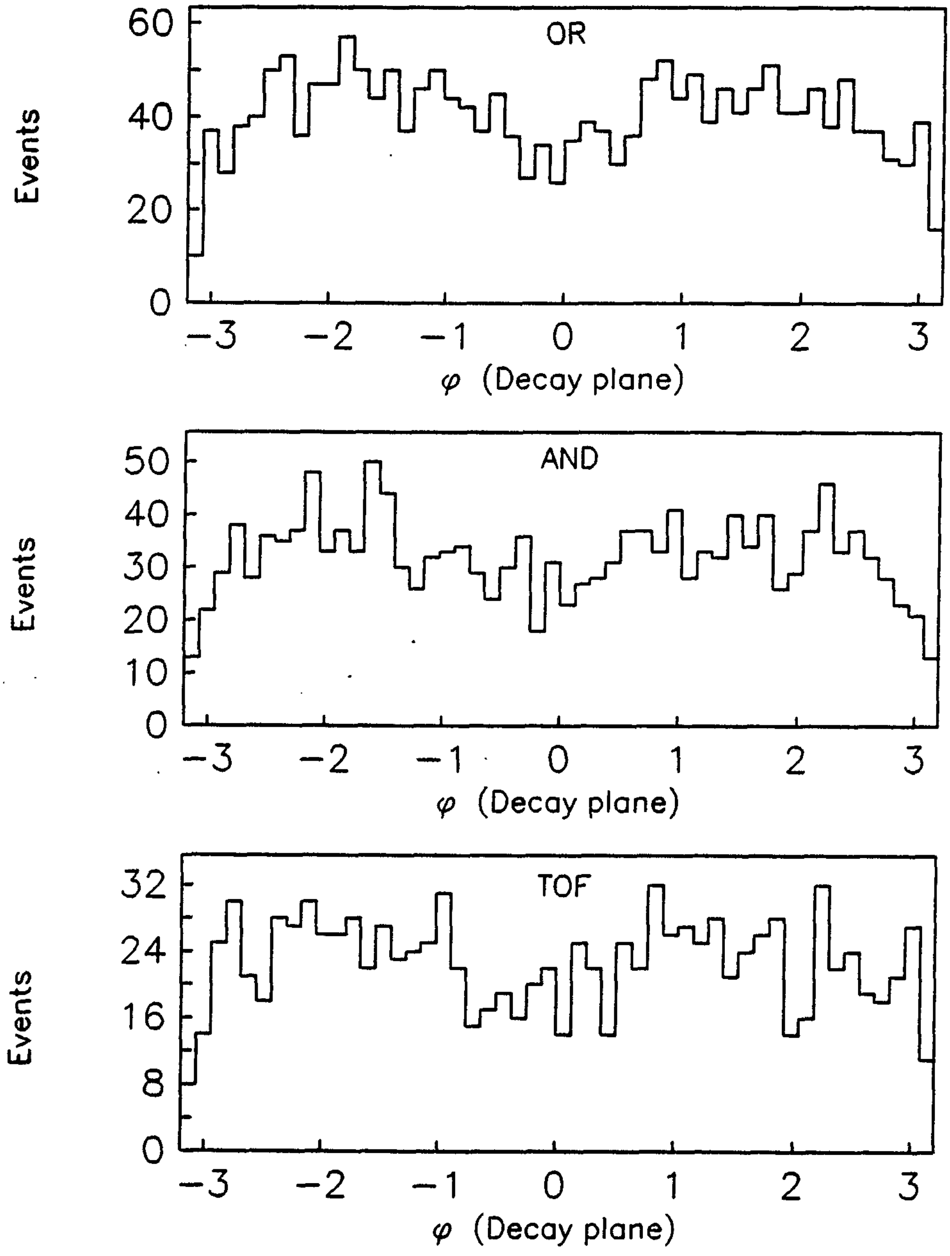

Figure 3.3 Decay plane orientation angle (in radians) of the K_s^0 particle for the OR (top), AND (center), and TOF (bottom) triggers

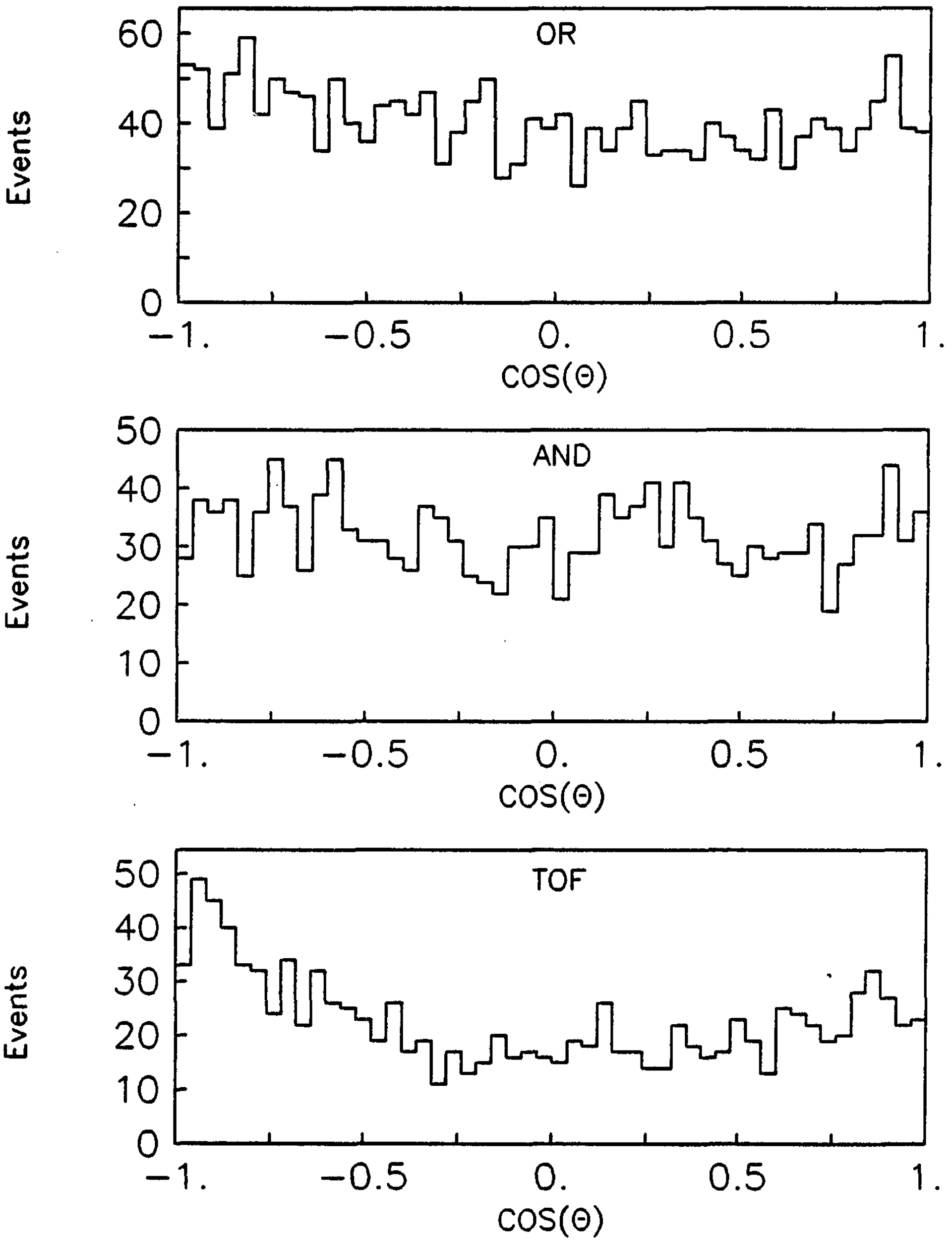

Figure 3.4 Cosine of the angle in the K_s^0 rest frame between the K_s^0 and its π^+ decay particle for the OR (top), AND (center), and TOF (bottom) triggers

$$\hat{u}\cdot\hat{e}_2 = sin(\theta_+)sin(\phi) \tag{3.10c}$$

where θ_+ is the angle between the positive decay product and the V^0 particle in the laboratory frame. The phi decay angle appears to be fairly uniformly distributed except for a loss of acceptance in the regions of 0 and $\pm\pi$ radians. These cases correspond to the K_s^0 particles emerging in the beam direction where there is a forward veto for the central particles. Therefore, the losses are likely due to trigger acceptance.

The distribution in cosine of theta for the K_s^0, where theta is the angle between the K_s^0 and its positive decay particle in the K_s^0 rest frame, are shown for each of the three data triggers in Figure 3.4. The OR and AND triggers show fairly uniform distributions, while the TOF trigger is somewhat biased toward $cos(\theta) = \pm 1$. This shows the loss of acceptance in the TOF trigger due to the requirement of at least one particle passing through a TOF stand which covers only part of the full solid angle in this experiment.

The K_s^0 mass distribution for each event containing at least one K_s^0 particle is shown in Figure 3.5 for each of the three triggers. All distributions feature a peak at the true K^0 particle mass with a rather large width of about 100 MeV. The TOF trigger also has a small peak in the region of the Λ^0 mass. These events had an ambiguity in the V^0 fits that resulted in both a K_s^0 fit and a Λ^0 fit being successful. Since the TOF trigger favors heavy charged particles such as protons, more events will have a Λ^0 particle produced. Since the fit is not perfect, some of the Λ^0 particles get through the K_s^0 fits as well.

The invariant mass distributions of the $\pi^+\pi^-$ pair not associated with the K_s^0 vertex for reaction 3.5 are shown for each of the three triggers in Figure 3.6. All three triggers feature enhancements near 500 MeV close to the K_s^0 mass. But,

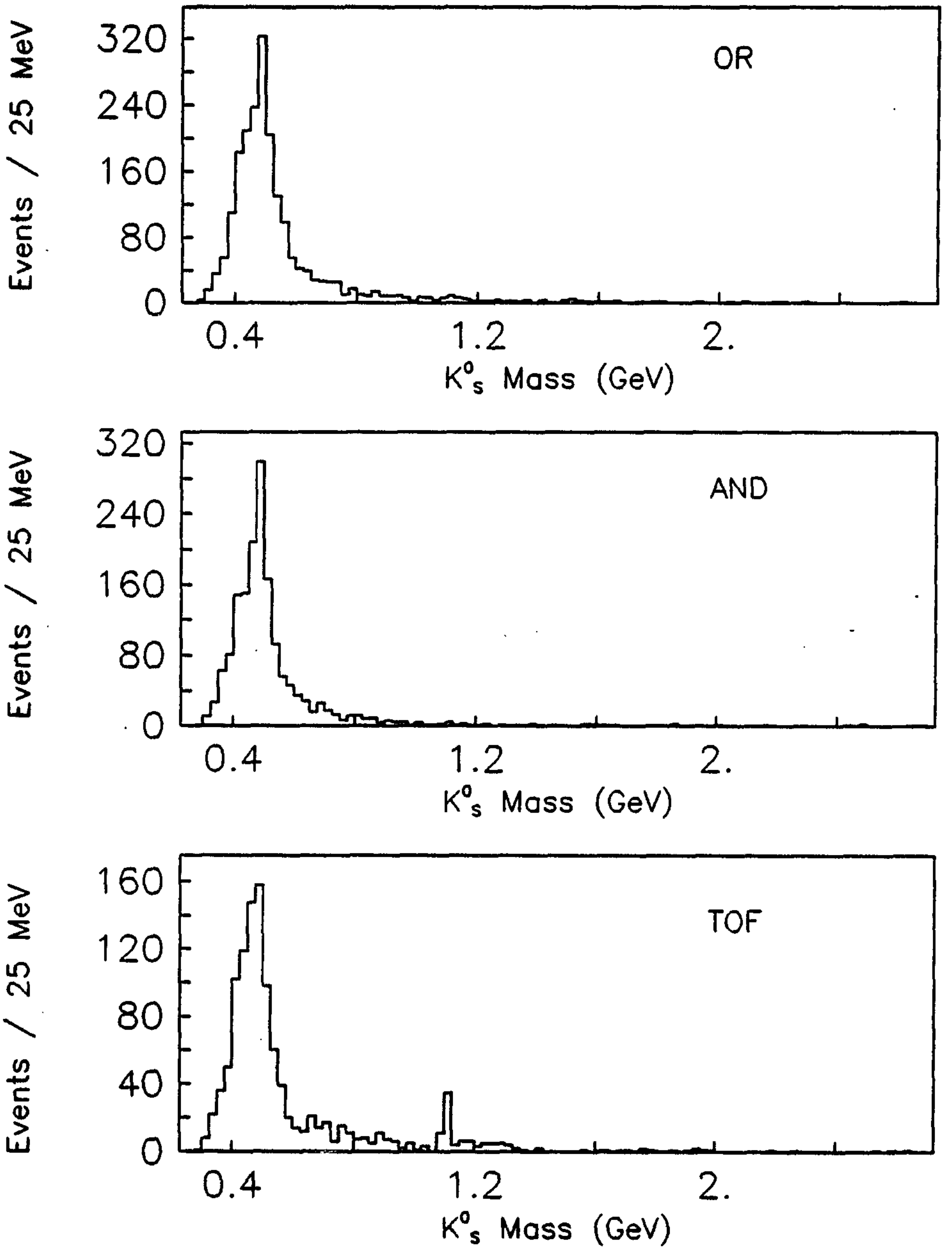

Figure 3.5 Mass of the K^0_s from the V^0 fit for the OR (top), AND (center), and TOF (bottom) triggers

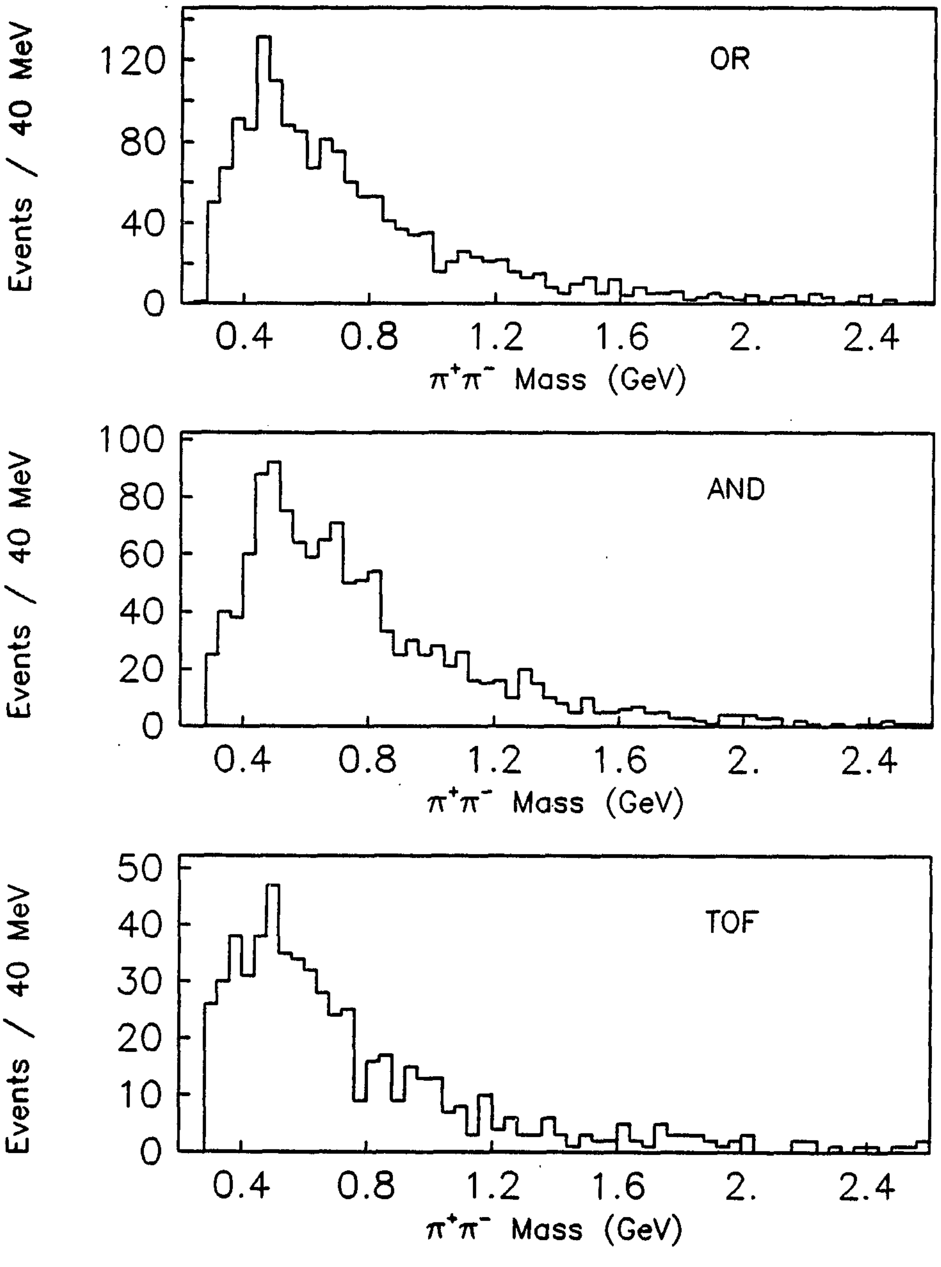

Figure 3.6 Mass of the $\pi^+\pi^-$ pair not associated with the K_s^0 particle for the OR (top), AND (center), and TOF (bottom) triggers

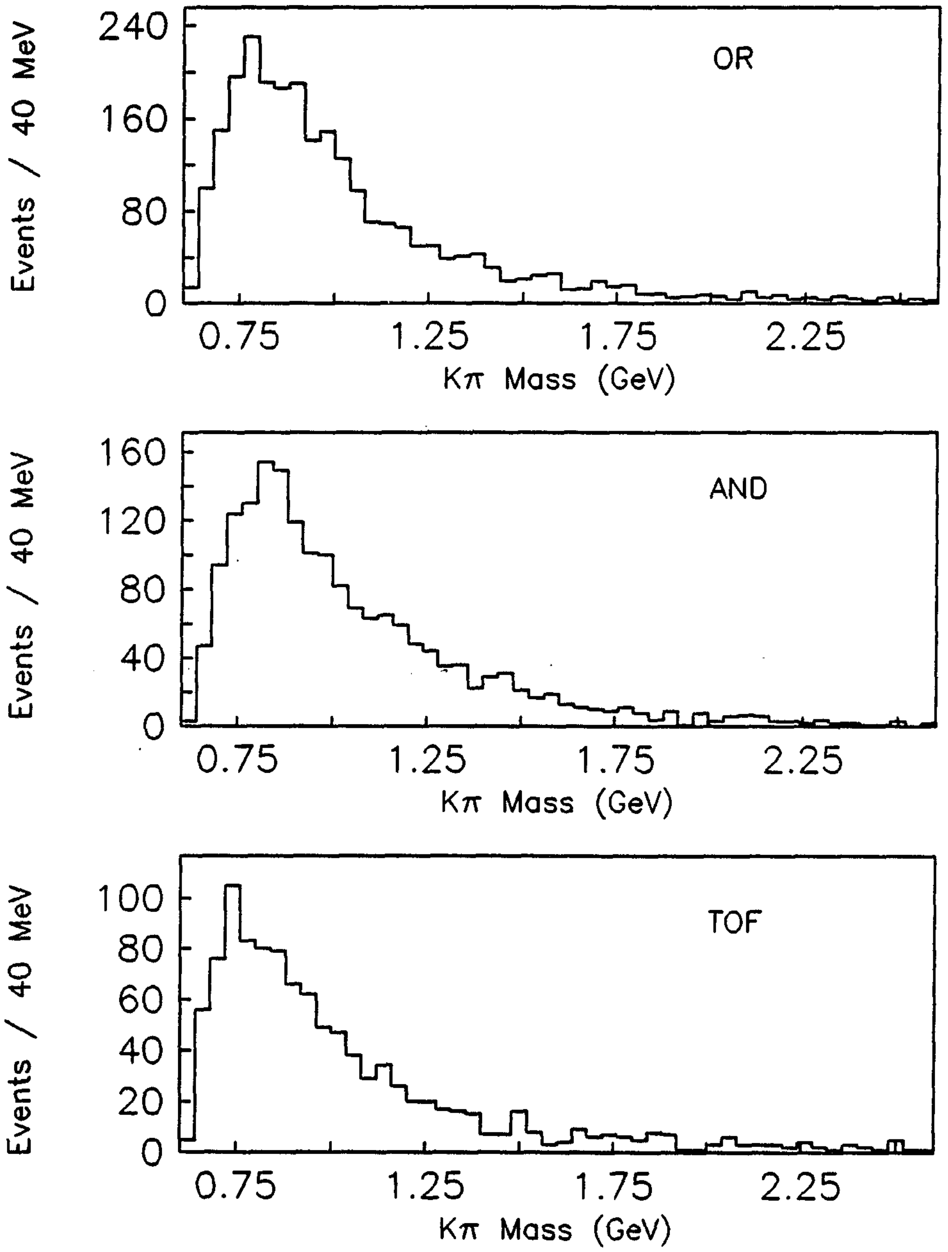

Figure 3.7 Mass of the $K^{\pm}\pi^{\mp}$ pair for the OR (top), AND (center), and TOF (bottom) triggers

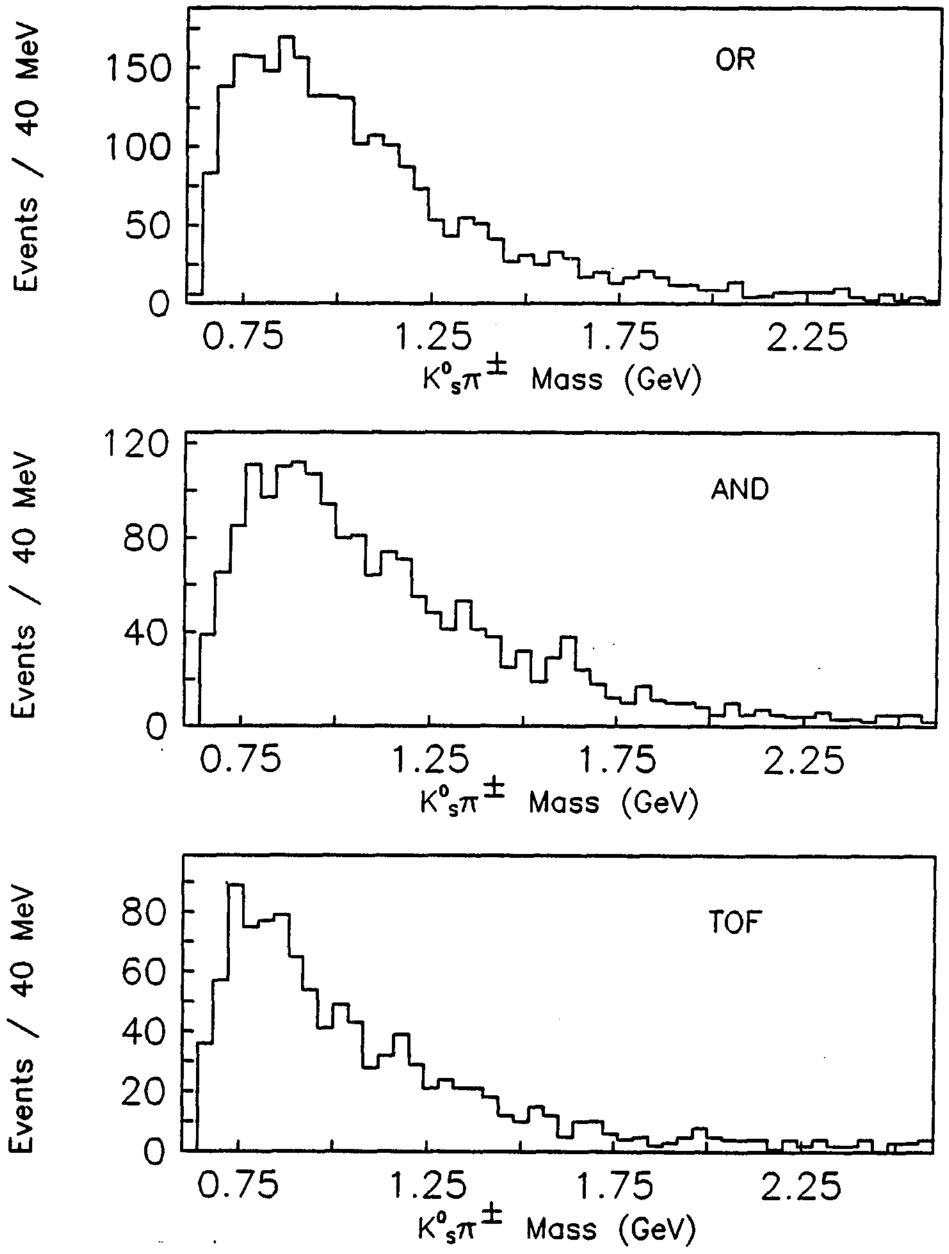

Figure 3.8 Mass of the $K^0_s\pi^\pm$ pair for the OR (top), AND (center), and TOF (bottom) triggers

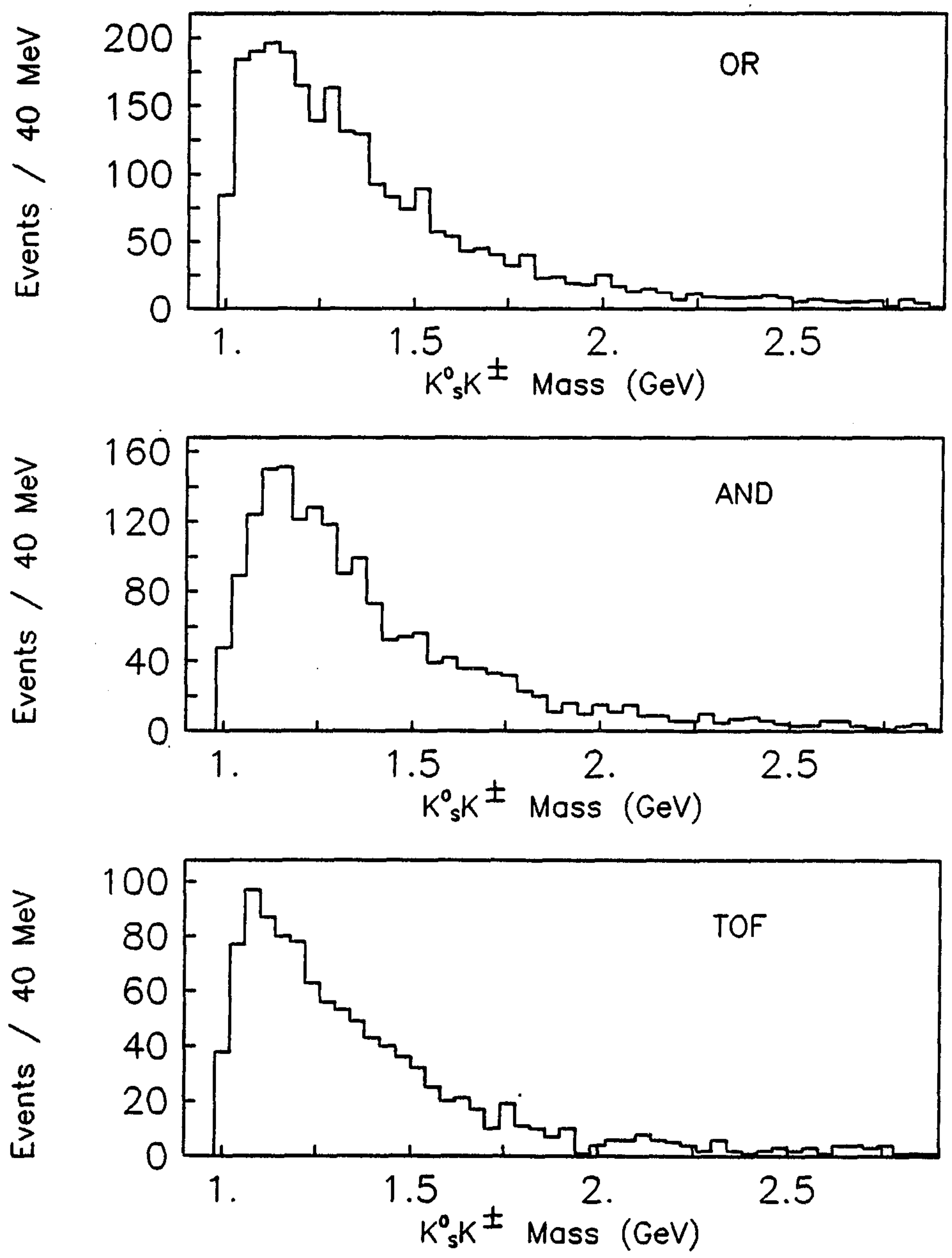

Figure 3.9 Mass of the $K^0_sK^\pm$ pair for the OR (top), AND (center), and TOF (bottom) triggers

it is not easy to distinguish the signals from the backgrounds. For this reason, the study of the $K_s^0\bar{K}_s^0$ central system using this method is pursued no further. The invariant mass distributions for the $K^{\pm}\pi^{\mp}$ pairs in reaction 3.6 are shown in Figure 3.7. There is a slight peak near the $K^*(890)$ mass for the AND trigger data, but the OR and TOF data do not exhibit the enhancement. The invariant mass distributions for the $K_s^0\pi^{\pm}$ pairs in reaction 3.6 are shown in Figure 3.8. Again there is a slight enhancement near the $K^*(890)$ mass and in this case it is exhibited for all three triggers, however, it is not easy to distinguish the signal from the background. The invariant mass distributions of the $K_s^0K^{\pm}$ pairs are shown in Figure 3.9, and no enhancements are observed. Since no clear enhancements are observed from reaction 3.6, the study of the $K_s^0K^{\pm}\pi^{\mp}$ system using this method is pursued no further.

3.4.2 Interactions involving at least one $\Lambda^0/\bar{\Lambda}^0$

The decay length distributions of Λ^0 and $\bar{\Lambda}^0$ tracks for 6-prong events having at least one Λ^0 or $\bar{\Lambda}^0$ track found are shown in Figure 3.10. The figure at the top shows the distribution in the decay length for the OR trigger data. The decay length distribution peaks at approximately 2.5 cm with a large tail. The average calculated error in the decay length from the V^0 fit routine is typically of the order of 20-30% of the decay length for each event. The AND trigger data (center) and TOF trigger data (bottom) are similar. The cut-off in the decay length at 1.0 cm is due to the constraint placed on the allowed decay length by the V^0 fitting program.

The decay plane orientation angle ϕ of the $\Lambda^0/\bar{\Lambda}^0$ is shown in Figure 3.11 for each of the three triggers. The decay angle appears to be uniformly distributed except for a loss of acceptance in the regions of 0 and $\pm\pi$ radians. As mentioned previously in the K_s^0 case, this is due to trigger acceptance.

The distribution in cosine of theta for the $\Lambda^0/\bar{\Lambda}^0$, where theta is the angle between the $\Lambda^0/\bar{\Lambda}^0$ and its positive decay particle, are shown for each of the three data triggers in Figure 3.12. All three triggers exhibit sharp spikes near $cos(\theta) = \pm 1$. These events most likely correspond to γ conversions into e^+e^- pairs leaking through the V^0 fit routines [Rauschnabel 1981].

The $\Lambda^0/\bar{\Lambda}^0$ mass distribution for each event containing at least one $\Lambda^0/\bar{\Lambda}^0$ particle is shown in Figure 3.13 for each of the three triggers. All distributions feature a peak at the true $\Lambda^0/\bar{\Lambda}^0$ mass with a width of about 50 MeV.

The invariant mass distributions of the $p^\pm\pi^\mp$ pair not associated with the Lambda vertex for reaction 3.7 are shown for each of the three triggers in Figure 3.14. No obvious enhancements are observed. For this reason, study of reaction 3.7 using this method is pursued no further. The invariant mass distributions of the $p^\pm K^\mp$ pair not associated with the Lambda vertex for reaction 3.8 are shown for each of the three triggers in Figure 3.15. No obvious enhancements are observed. For this reason, study of reaction 3.8 using this method is pursued no further.

3.4.3 Conclusions of short study

It is clear from the widths of the mass distributions of these reactions that more work is needed on the events to improve the mass determination of the V^0 events and also to screen out those events in which energy and momentum are apparently not conserved by the detected particles. For this reason, a four constrained fit (4-C fit) will be used on the events to improve the momentum determination of each of the charged particles not associated with the V^0 and also the momentum determination of the V^0 particle.

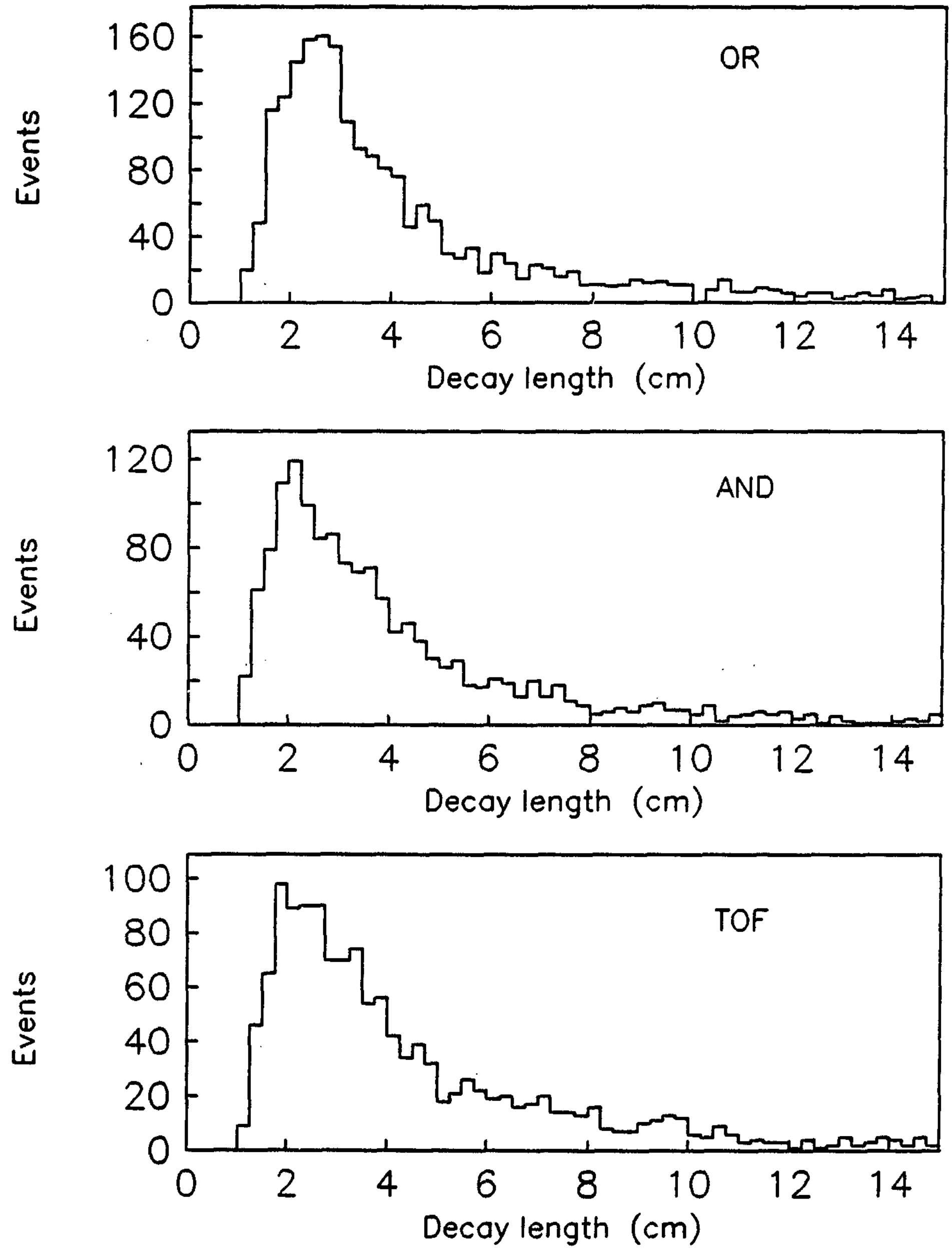

Figure 3.10 Decay length of the Λ^0 particle in the laboratory frame for the OR (top), AND (center), and TOF (bottom) triggers

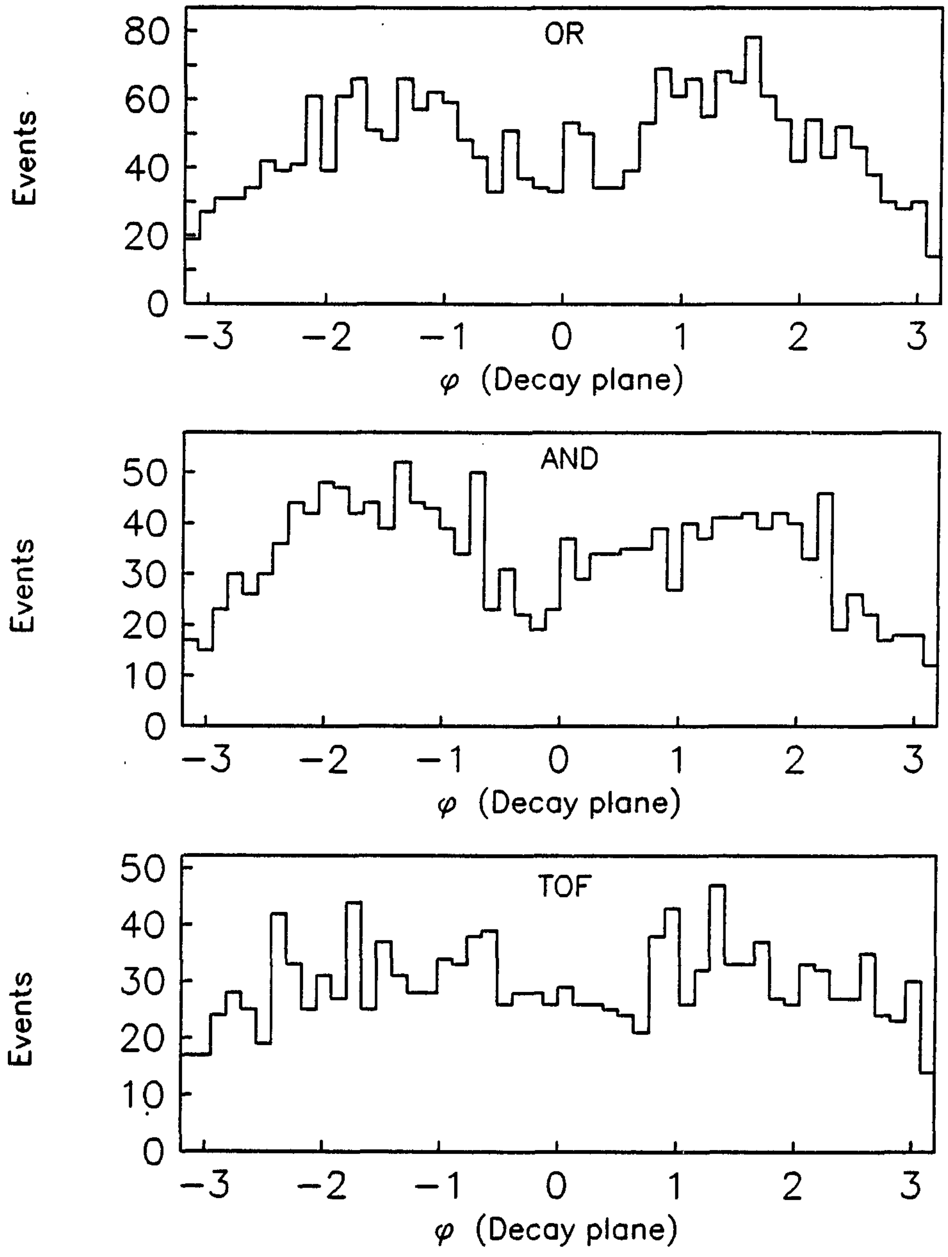

Figure 3.11 Decay plane orientation angle (in radians) of the Λ^0 particle for the OR (top), AND (center), and TOF (bottom) triggers

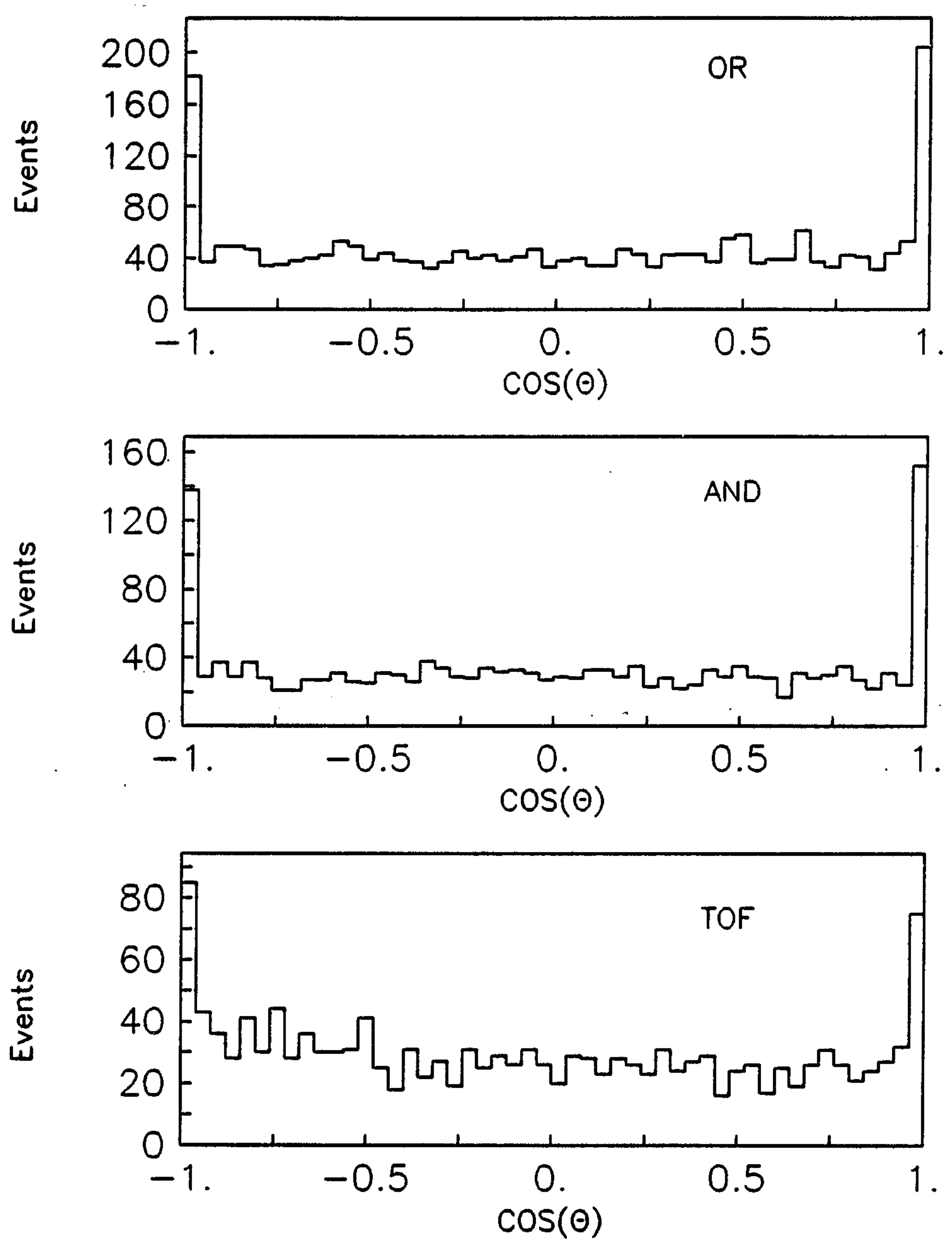

Figure 3.12 Cosine of the angle in the Λ^0 rest frame between the Λ^0 and its positive decay particle for the OR (top), AND (center), and TOF (bottom) triggers

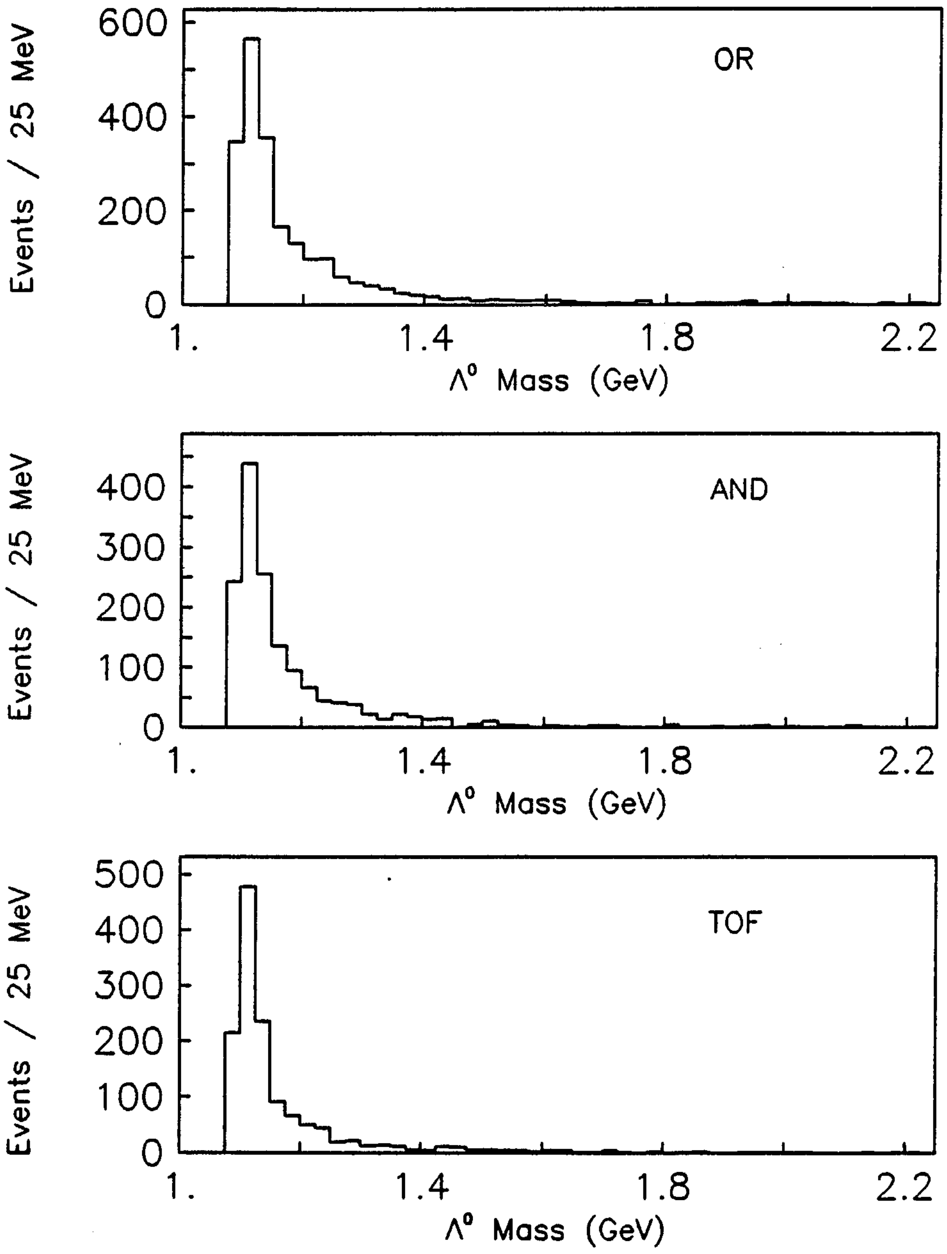

Figure 3.13 Mass of the Λ^0 from the V^0 fit for the OR (top), AND (center), and TOF (bottom) triggers

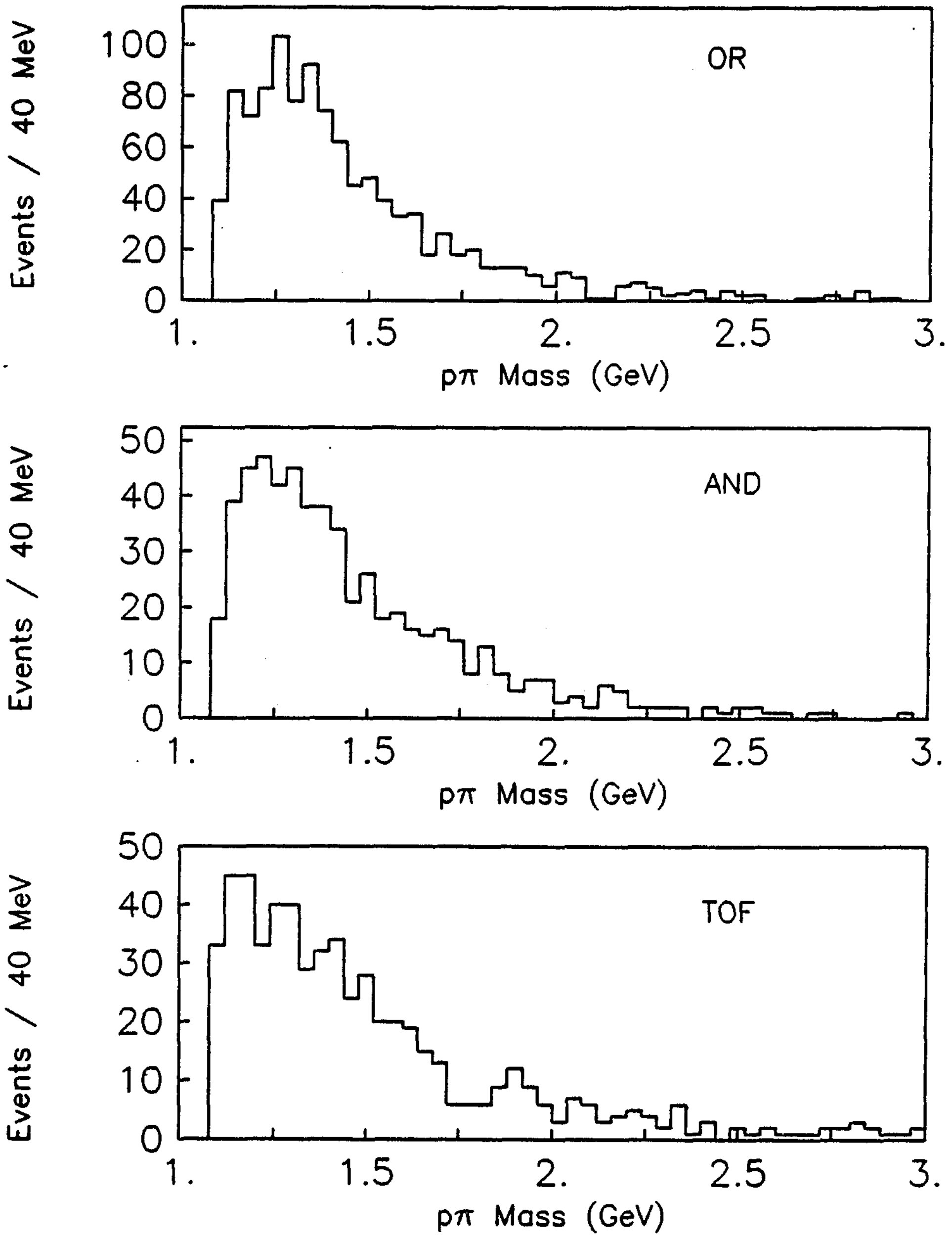

Figure 3.14 Mass of the $p^{\pm}\pi^{\mp}$ pair not associated with the Λ^0 particle for the OR (top), AND (center), and TOF (bottom) triggers

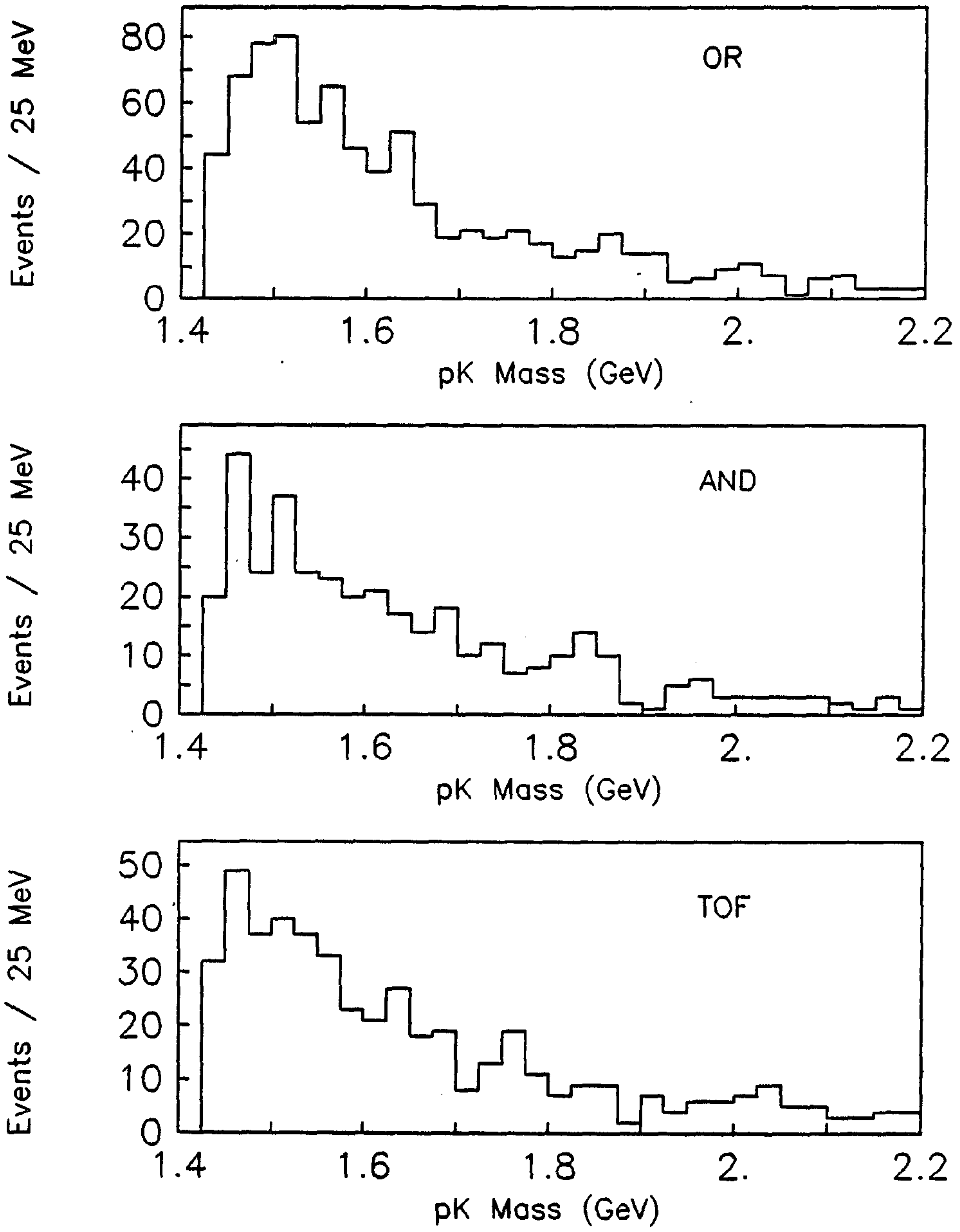

Figure 3.15 Mass of the $K^{\pm}p^{\mp}$ pair for the OR (top), AND (center), and TOF (bottom) triggers

3.5 Four Constrained Fit of Particle Track Momenta

The 4-C fit adjusts the measured parameters of all the detected tracks in an event, according to their measured errors with the aim of satisfying conservation of energy and momentum in the interaction. The result of the fit is a set of new improved parameters and a chi-square (χ^2) value which shows how well the fit functioned for each event. Kinematical fitting of measured track parameters is a straight forward procedure and has already been developed and used successfully for this experiment [Isenhower 1986].

The fit is based on techniques described by Frodesen, Skeggestad, and Tofte [Frodesen, Skeggestad, and Tofte 1979]. The 4-C fit uses a χ^2 minimization technique with Lagrange multipliers. The constraint equations are written as a C-row column matrix $F(X)$ with Lagrange multipliers λ. The resulting equation to be minimized is

$$\chi^2 = (X - X^m)^T V^{-1} (X - X^m) + 2\lambda^T F(X) \tag{3.11}$$

where χ^2 is the chi-square, X is a C-component column matrix containing the adjusted track parameters, X^m is a C-component column matrix of the measured values of the track parameters, and V is the $C \times C$ covariance matrix (related to an error matrix) of the measured track parameters.

The equations to be solved are obtained by setting the partial derivatives of χ^2 with respect to the track parameters, X, and Lagrange multipliers, λ, equal to zero, i.e.,

$$\frac{\partial \chi^2}{\partial X} = 2V^{-1}(X - X^m) + 2\frac{\partial F(X)}{\partial X}\lambda = 0 \tag{3.12}$$

$$\frac{\partial \chi^2}{\partial \lambda} = 2F(X) = 0 \tag{3.13}$$

The χ^2 minimum is found by an iterative procedure. At the end of each iteration a

χ^2 value is calculated and compared to the previous value. The process is continued until the following convergence criteria are met,

$$\left| \frac{\chi_\nu^2 - \chi_{\nu+1}^2}{\chi_{\nu+1}^2} \right| < .0005\, n \tag{3.14}$$

where the subscript refers to the iteration order and n is the number of outgoing tracks in Equation 3.4. If the convergence criteria are not satisfied within a given number of iterations, the fit is abandoned.

Each iteration in the fit required several matrix multiplication operations including calculation of the inverse of the covariance matrix. Therefore, high precision calculations were required on a computer. The various matrix operations required for the fitting were performed on a VAX-11/785 computer using 15-digit extended precision variables.

The variables used to parametrize the kinematical fitting measurements for this experiment were $1/p$, θ, and ϕ of each charged particle. The magnitude of the measured momentum is given by p, θ is the angle out of the horizontal x-y plane of the SFM, and ϕ is the angle from the x-axis of the SFM detector (see Figure 2.4). The momentum and angle errors for each particle track are stored on the DST as momentum and direction cosines. The errors are transformed according to the appropriate fit variables. Complete details of the 4-C fit are given by Isenhower [Isenhower 1986]. The output from the fit contains new track parameters consistent with energy and momentum conservation, the errors on the new parameters, the χ^2 value, and the pull quantities for each track, i.e., the difference between the original measured parameter and the final fitted parameter necessary to obtain convergence divided by the calculated error in the fitted quantity.

3.6 Corrections to Track and Beam Parameters

The errors in the track parameters are available on the DST for all measured charged particle tracks for each event. In addition, the V^0 fitting routines give error estimates for the V^0 track momenta. Therefore, these errors can be passed to the 4-C fit routine following any needed corrections. The only additional corrections required to all the outgoing particles' momenta and angles from an interaction were those due to energy losses and scattering. These have been described in detail by Isenhower [Isenhower 1986] and are briefly summarized below.

The corrections to the fast outgoing protons involved correcting the errors on the θ angle. This was needed due to multiple scattering in the beam pipe. The errors on the two parameters p and ϕ were adjusted using the pull quantities from the 4-C fit. This was done with great caution. All pull quantities were required to be adjusted consistently and only after a successful fit with low χ^2 was already completed. The corrections made for the outgoing central particles were simply due to energy losses in traversing the SFM chambers. These corrections apply only for low momentum tracks and account for the average loss in energy of a particle of a particular mass in traversing the central region of the detector.

The beam parameters were used as input to the kinematic fit routine as the beam momenta are not measured directly in this experiment on an event by event basis. Only the average momenta of the two incoming proton beams is available on the DST. The ISR beams actually had a momentum spread of ±3%. However, it was discovered that one can use the known correlation between the beam momenta and horizontal position of the beam particles to determine the beam momenta to an accuracy of 0.2% on an event by event basis. These small errors allow excellent determination of longitudinal momentum conservation.

4 EXCLUSIVE INTERACTIONS INVOLVING AT LEAST ONE $\mathbf{K_s^0}$ PARTICLE

4.1 $\mathbf{K_s^0K_s^0}$ Central System

All of the 6-prong events containing at least one identified K_s^0 particle given from the V^0 program were further processed using the 4-C fit routine discussed in Section 3.5. The masses of the particles for the reaction 3.5 were assigned as discussed in Section 3.4 and are listed in Table 4.1. These masses were required to be consistent with any available time of flight information on the DST. The momenta and angles as described in Section 3.5 for each of the particles were input to the 4-C fit routine.

Table 4.1 Summary of particles whose four momenta are input to the 4-C fit in the $K_s^0K_s^0$ central system hypothesis

Particle(s)	Mass (MeV)	Description
p, p	938.2796	Two ingoing beam protons
π^+, π^-	139.5685	Two oppositely charged central pions
K_s^0	497.72	One V^0 Central particle
p, p	938.2796	Two fast outgoing protons

4.1.1 OR trigger data

The chi-square (χ^2) distribution from the 4-C fit is shown in Figure 4.1 for the OR trigger. This χ^2 value is shown transformed into a probability for a successful fit for each event in Figure 4.2. This probability is a measure of the goodness of fit for each event based on the χ^2 value and the four degrees of freedom in the fit. The probability of fit distribution is then used to make a final cut on the data to exclude events that do not satisfy energy and momentum conservation. The procedure is to search for a point in the distribution where it becomes approximately flat. Therefore, the cut decided on from this distribution was set at 0.02. A total of 1565 events were fitted and of these, 245 passed the criterion for the probability of fit. The distribution of cosine theta between the K_s^0 and its positive decay particle, and the phi angle decay plane orientation of the K_s^0 are shown for the K_s^0 for the fitted events that passed the probability cut in Figure 4.3. Aside from the lower statistics, these distributions are similar to those in Figures 3.3 and 3.4 for the OR trigger.

The invariant mass of the $\pi^+ \pi^-$ pair not associated with the K_s^0 is shown in Figure 4.4 for both the fitted and unfitted variables. Both reveal an enhancement in the region of the K_s^0 mass, but the distribution using the fitted variables shows a much enhanced peak. This is a strong indication that a second K_s^0 is produced which can be isolated from the background in this event sample. Therefore, a cut on the fitted invariant mass of the $\pi^+ \pi^-$ pair is made on the range 0.44 GeV $< m <$ 0.56 GeV, where m is the mass of this pair, in order to further analyze these events. The $\pi^+ \pi^-$ pair mass distribution is shown in Figure 4.5 after the mass cut with a gaussian fit for both unfitted and fitted momentum variables. The gaussian fit yields a central value of 474 ± 9.6 MeV and a width of 62 ± 7.0 MeV for the unfitted momentum variables. The gaussian fit gives a central value of 498 ± 4 MeV and a width of 31 ± 3.6 MeV for the fitted variables. Thus, the mass resolution is improved considerably by the 4-C fit and the fitted distribution correctly reproduces the known K_s^0 mass.

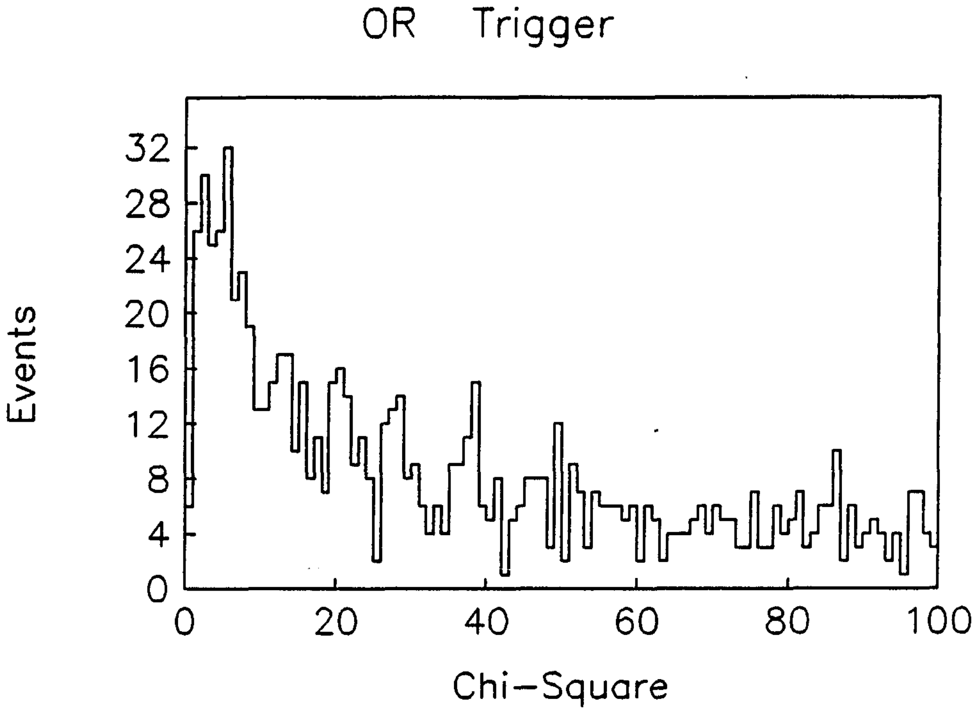

Figure 4.1 χ^2 distribution from the 4-C fit routine for the OR data

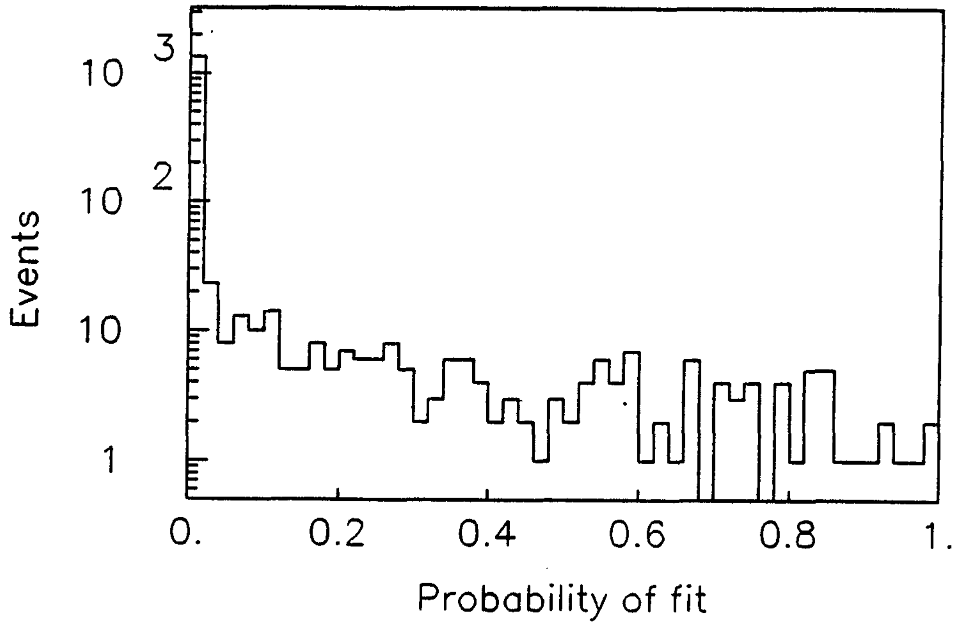

Figure 4.2 Probability of fit distribution for the OR trigger data

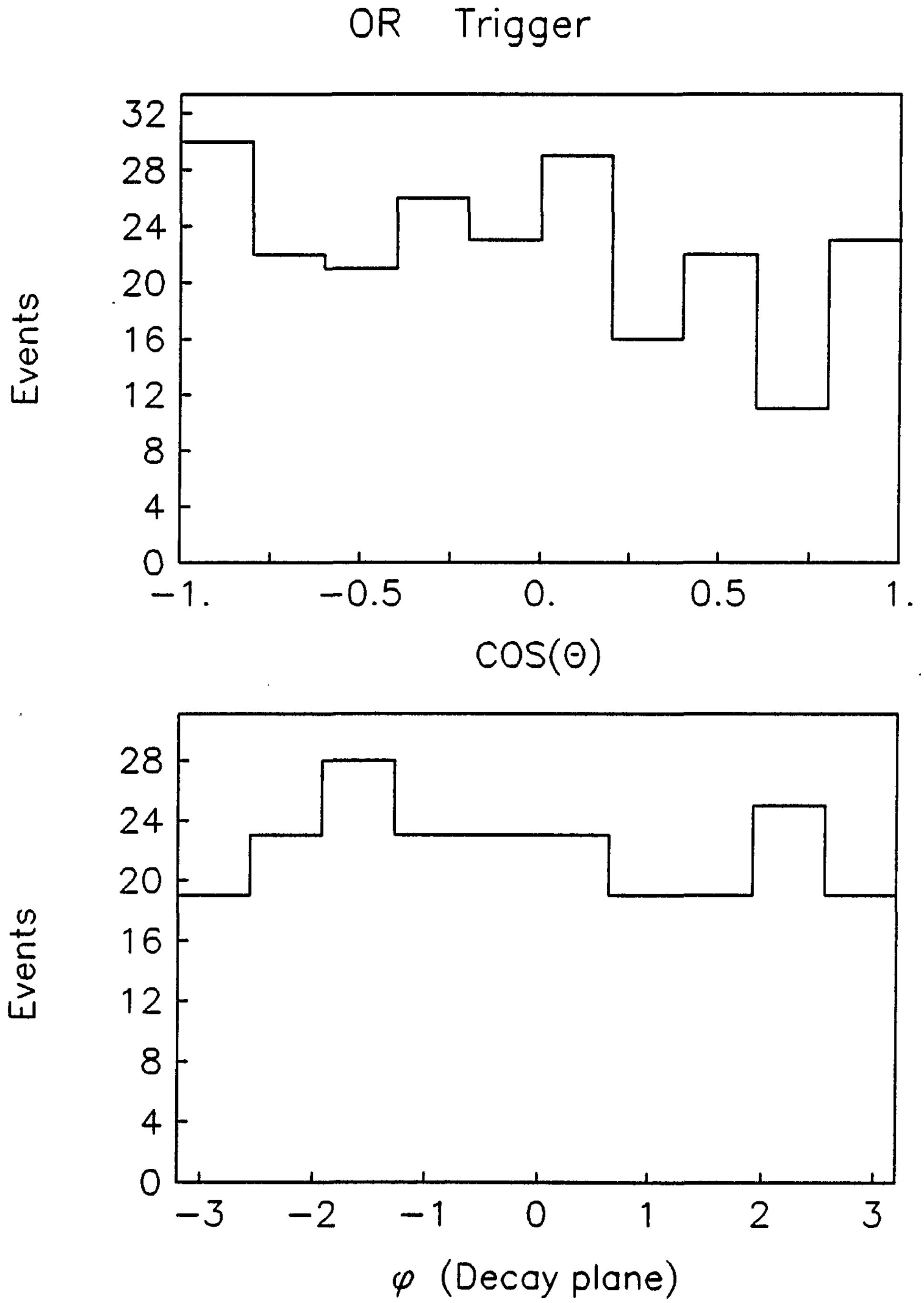

Figure 4.3 K_s^0 distribution of $cos(\theta)$ (top), and of the decay plane orientation angle, for the OR trigger data

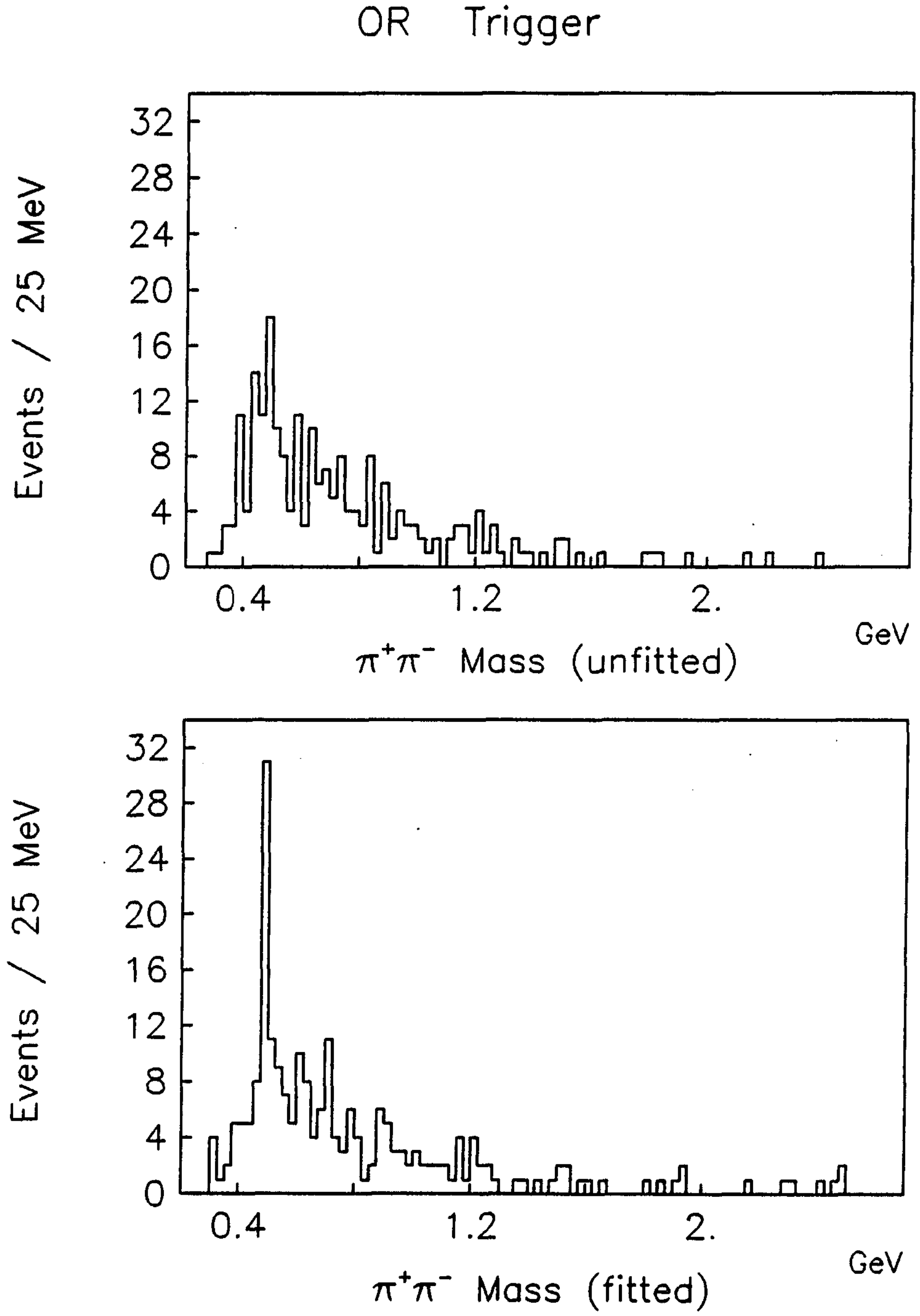

Figure 4.4 Invariant mass of the $\pi^+\pi^-$ pair not associated with the K^0_s particle for the OR trigger data. Both the unfitted (top) and fitted (bottom) variables are shown

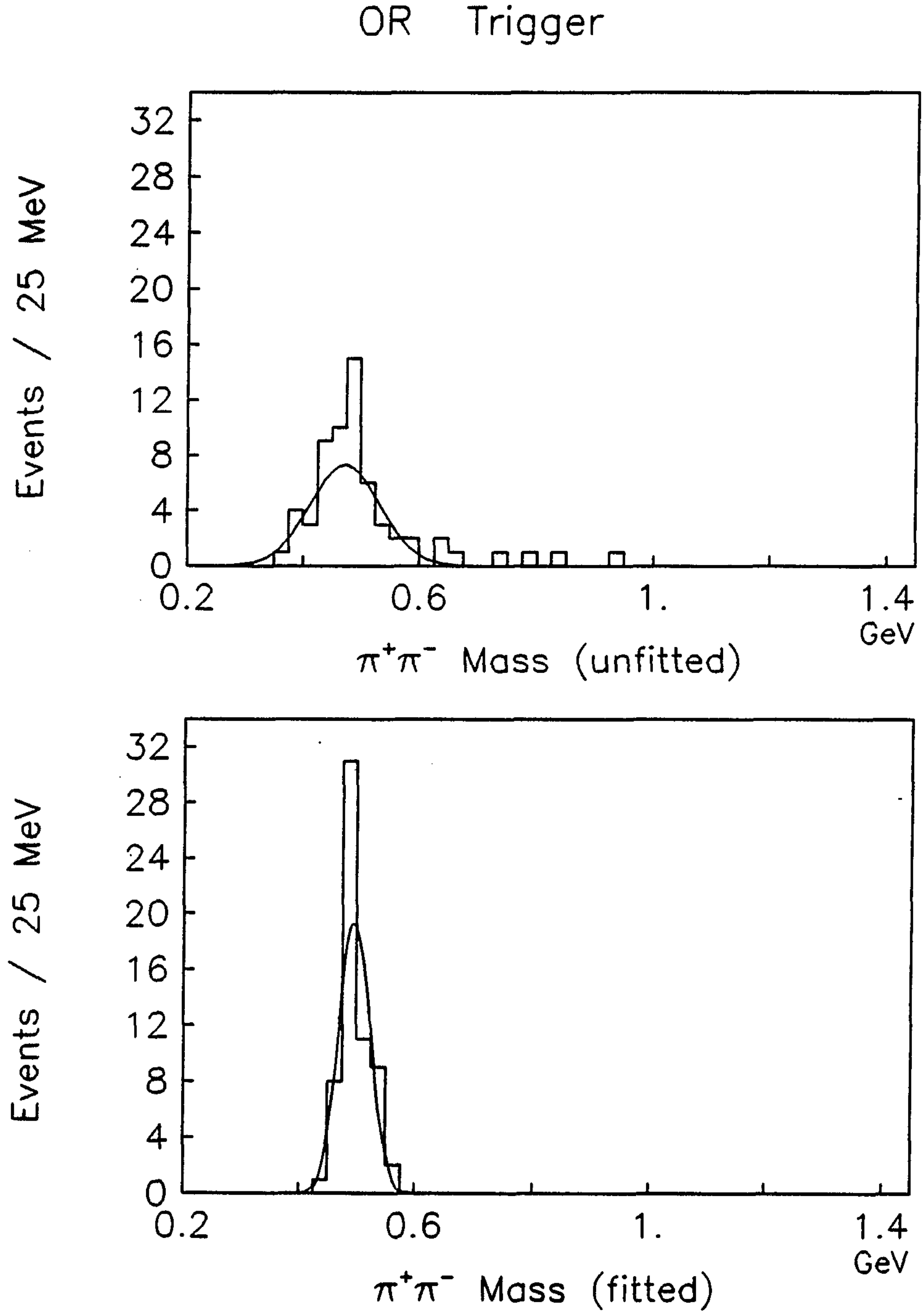

Figure 4.5 The $\pi^+\pi^-$ pair mass distribution of the OR trigger data after the mass cut on the fitted variables for unfitted (top) and fitted (bottom) variables; a gaussian fit is shown superimposed for each

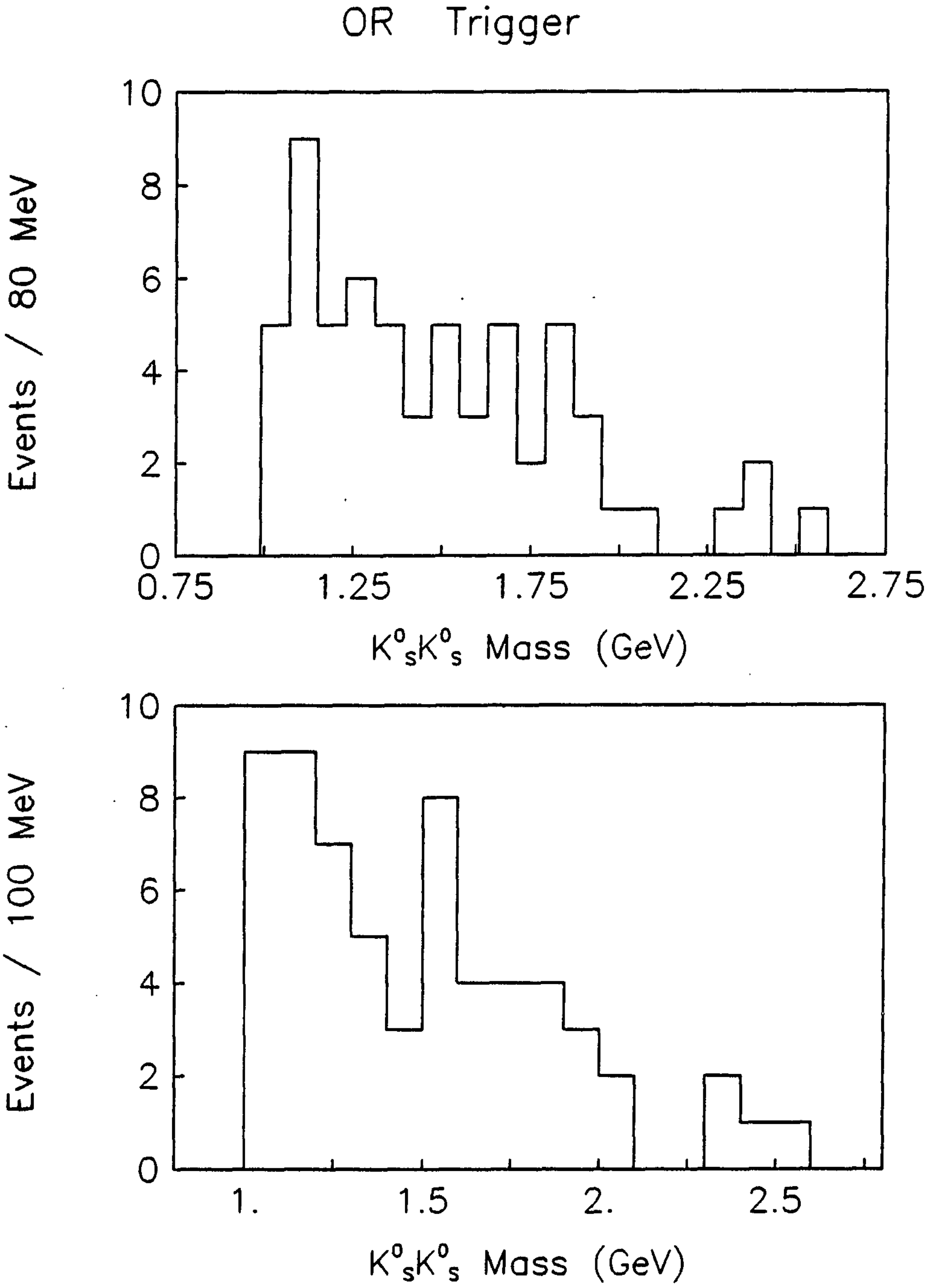

Figure 4.6 $K_s^0 K_s^0$ central system mass distributions with 80 MeV bins (top) and 100 MeV bins (bottom) for the OR trigger data

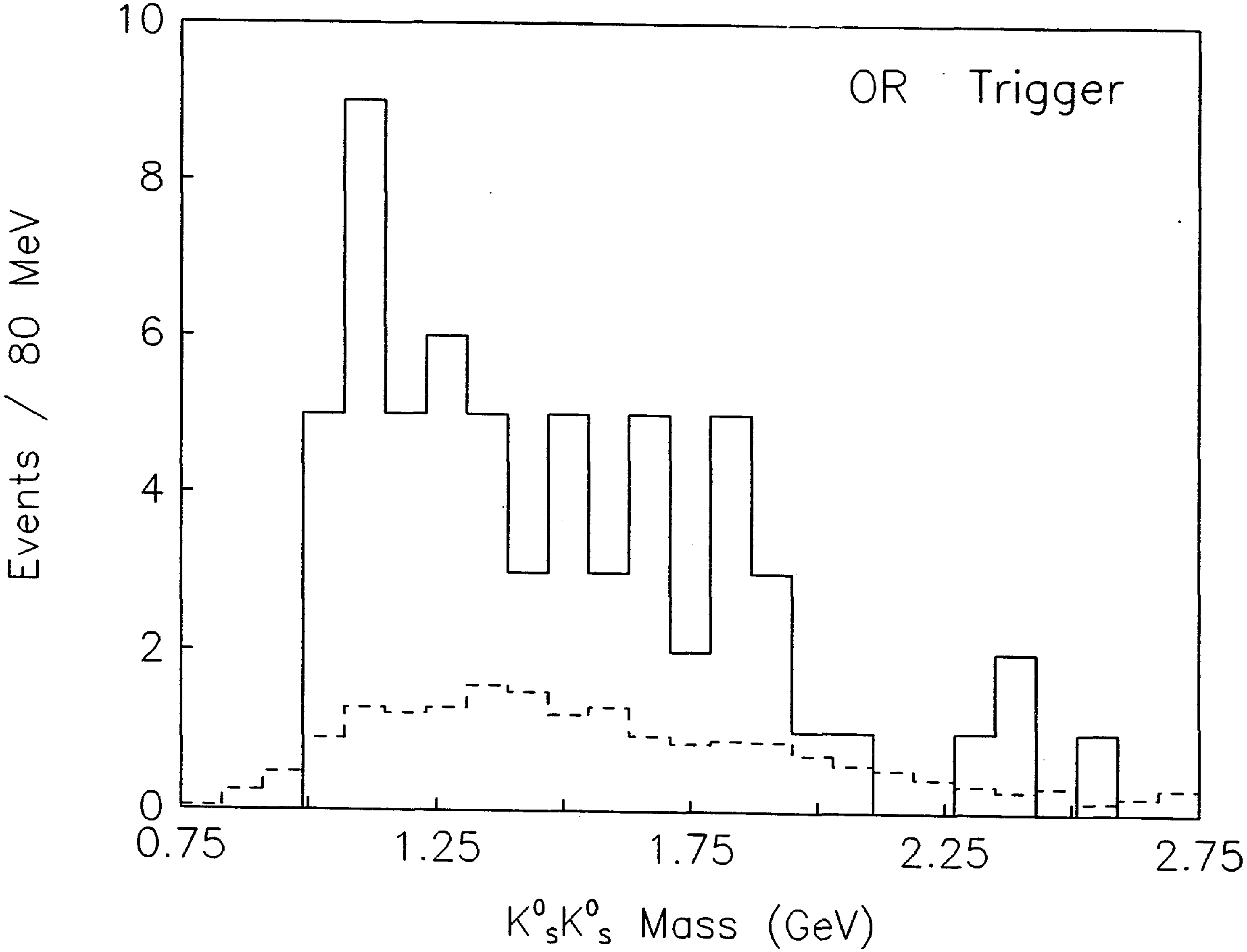

Figure 4.7 **$K^0_s K^0_s$ central system mass (solid line) with the background superimposed (dashed line)**

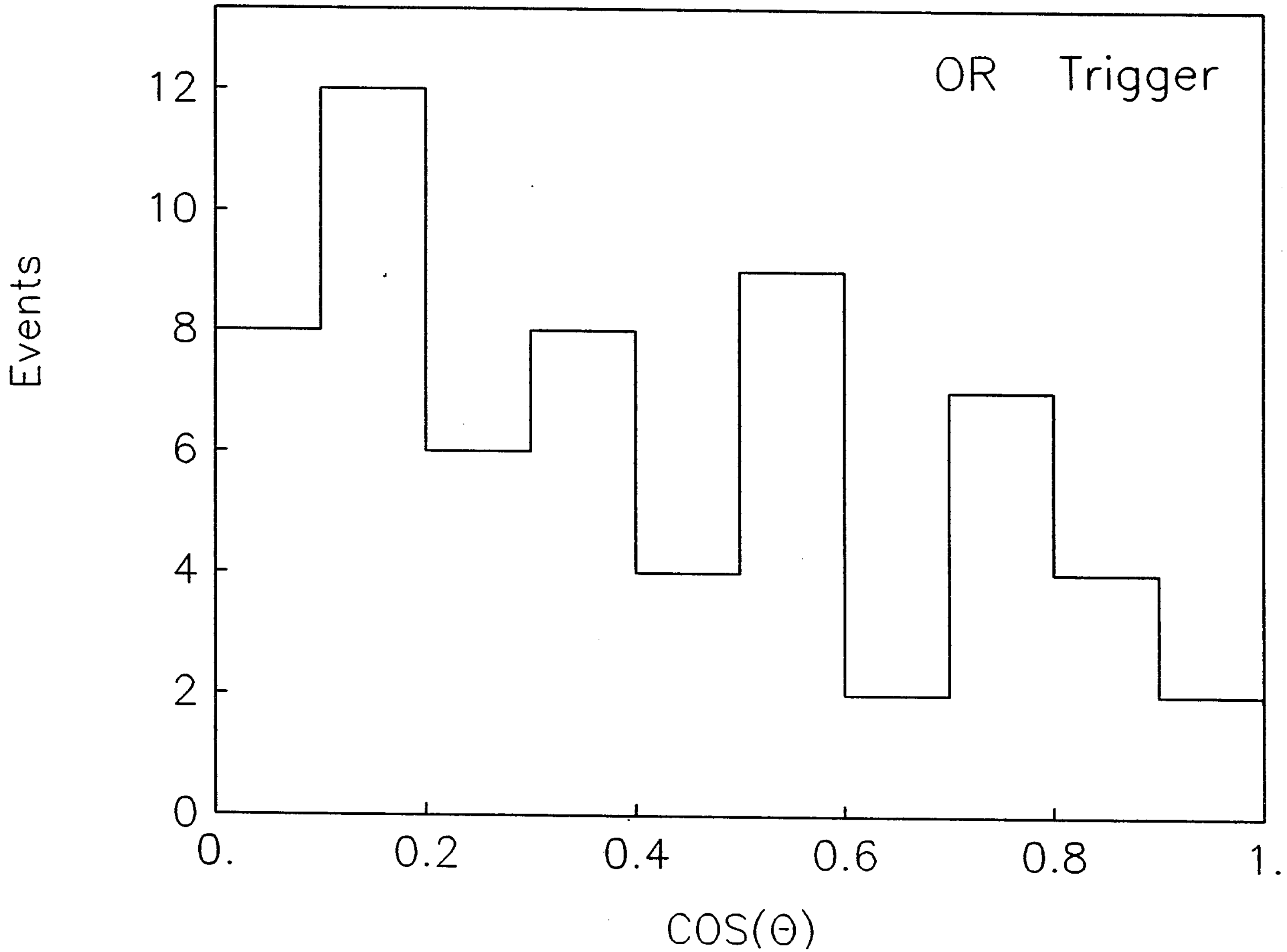

Figure 4.8 $cos(\theta)$ distribution of the angle between the K_s^0 particle and one of the Pomerons in the Pomeron-Pomeron rest frame

The number of events remaining in the $K_s^0 K_s^0$ sample after this final mass cut is 62 events. The distribution of the invariant mass of the $K_s^0 K_s^0$ central system particles, is shown in Figure 4.6 for 80 and 100 MeV bin sizes. The first histogram with 80 MeV bins indicates a concentration of events around 1200 MeV which is more clear in the second histogram with 100 MeV bins. There is also a concentration of events around 1500-1800 MeV. The lower peak is centered at about 1200 MeV while the upper is at about 1600 MeV. The peak at 1600 is fairly broad and could be evidence of the f^0 meson (mass = 1590 MeV, width = 180 MeV) with $J^{PC} = 0^{++}$ [Particle Data Group 1988]. The peak at 1200 is not near any established meson mass resonances with quantum numbers consistent with a decay into $K_s^0 K_s^0$, (i.e., even spin and positive parity) so it may be some new resonant state, a threshold effect due to the $f_0(975)$ particle, or a combination of both. There is a $f_0(1240)$ resonance (see Table 1.2) seen by one group to decay to $K\bar{K}$ [Etkin et al. 1982].

The background for this interaction can be estimated from the $\pi^+\pi^-$ mass distribution. From Figure 4.4 the background is estimated to be 30%. The shape of the background in the $K_s^0 K_s^0$ mass distribution may be estimated with the events from Section 3.4 using the unfitted $K_s^0\pi^+\pi^-$ mass distribution. This distribution is shown superimposed on the data (dashed line) in Figure 4.7, normalized to the observed number of events in the region $M > 1.5$ GeV, with each bin multiplied by 0.30, and the 62 fitted events subtracted out of the sample. From the distributions it is evident that the enhancements are not due to background in the data sample.

The distribution in cosine theta, where theta is the angle in the Pomeron-Pomeron rest frame between the K_s^0 particle and one of the Pomerons, is shown in Figure 4.8 for the $K_s^0 K_s^0$ events. From the relatively flat shape of the distribution it appears that the central system is probably in a spin 0 state, i.e., the decay of the $K_s^0 K_s^0$ system is mostly s-wave. However, in order to verify this conclusion, it is necessary to correct the data for geometric and trigger acceptances of the SFM detector. This will be discussed in Chapter 6.

4.1.2 AND trigger data

The treatment of the data was carried out using the same method as in the OR data. The equivalent Figures to 4.2-4.8 are shown for the AND trigger data in Figures 4.9-4.15. A probability cut of 0.02 was decided upon for this trigger also. The distributions in the decay angle cosine theta and the phi angle are similar to those in Figures 3.3 and 3.4 for the AND trigger.

From Figures 4.11 and 4.12 it is clear that the AND data also feature a second K_s^0 in the event sample. The gaussian fits yield a central value of 480 ± 10 MeV with a width of 48 ± 7.0 MeV for the unfitted momentum variables and a central value of 496 ± 6 MeV with a width of 37 ± 6.0 MeV for the fitted variables. Thus, the mass resolution is improved considerably by the 4-C fit.

The number of events in the $K_s^0 K_s^0$ sample is 46 events. The distribution of the invariant mass of the $K_s^0 K_s^0$ central system particles is shown in Figure 4.13 for 80 MeV and 100 MeV bin sizes. Unlike the OR trigger data, neither of these distributions shows any enhancements in the region of 1200 Mev, but there is a slight enhancement at 1500 MeV. However, the statistics are poor. From Figure 4.11 the background is estimated to be 30%. With the shape of the background in the $K_s^0 K_s^0$ mass distribution of Figure 4.14, it is evident that the enhancement is not due to background in the data sample. In Figure 4.15 it appears that the system is probably in a spin 0 state and is dominated by s-wave decay.

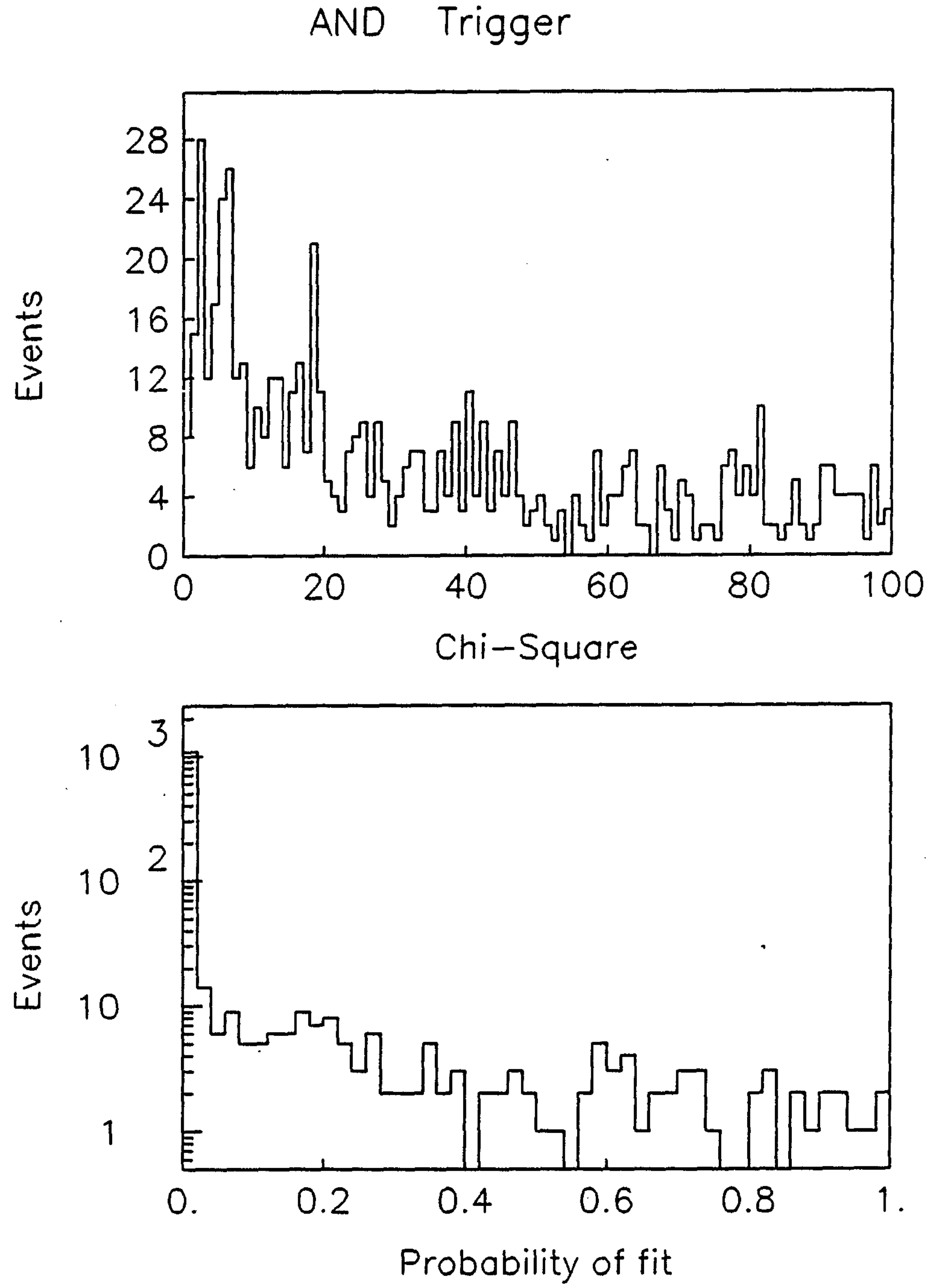

Figure 4.9 χ^2 (top) and probability of fit (bottom) distributions for the AND data

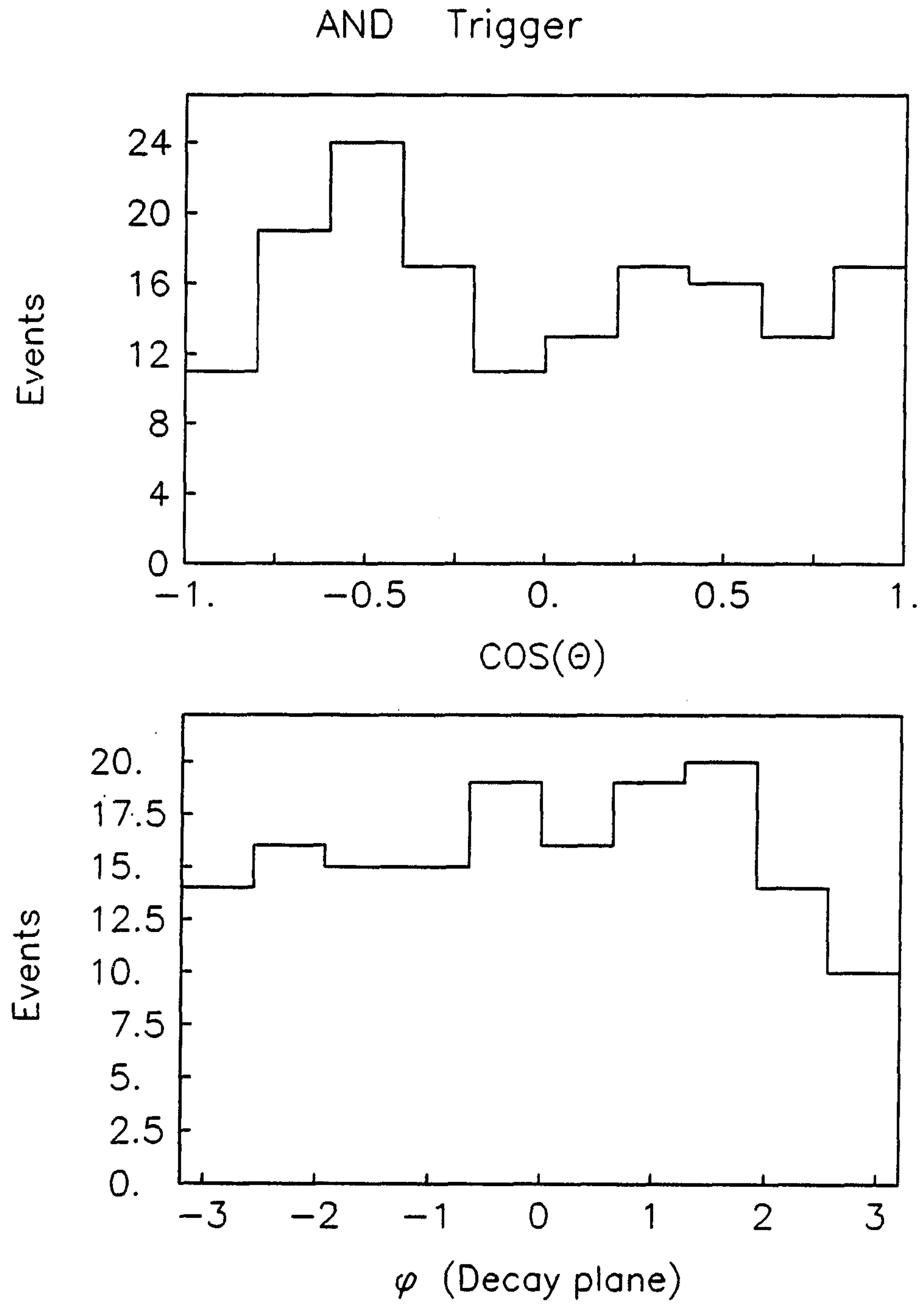

Figure 4.10 K^0_s distribution of $cos(\theta)$ (top), and of the decay plane orientation angle, for the AND trigger data

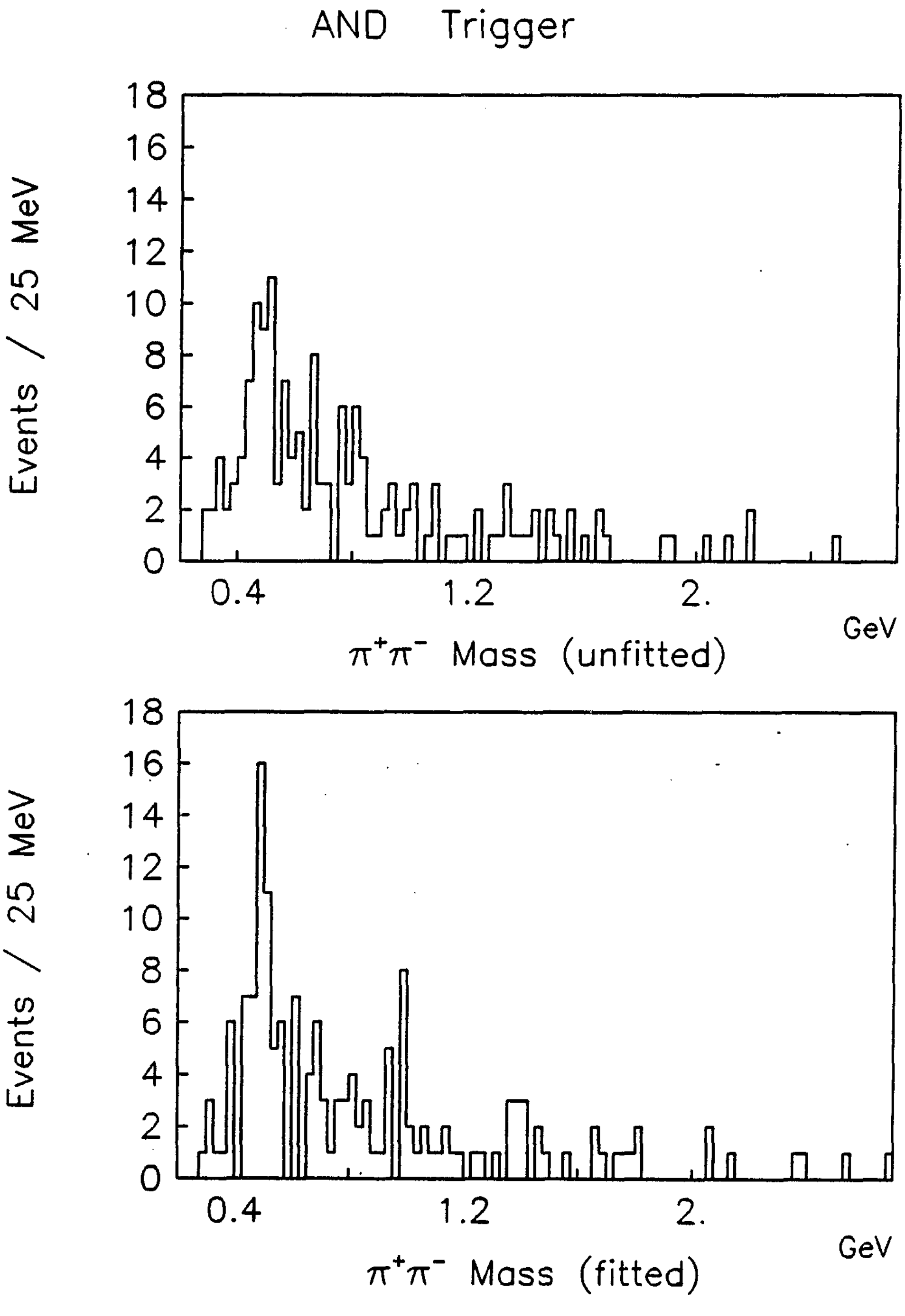

Figure 4.11 Invariant mass of the $\pi^+\pi^-$ pair not associated with the K^0_s particle for the AND trigger data; both the unfitted (top) and fitted (bottom) variables are shown

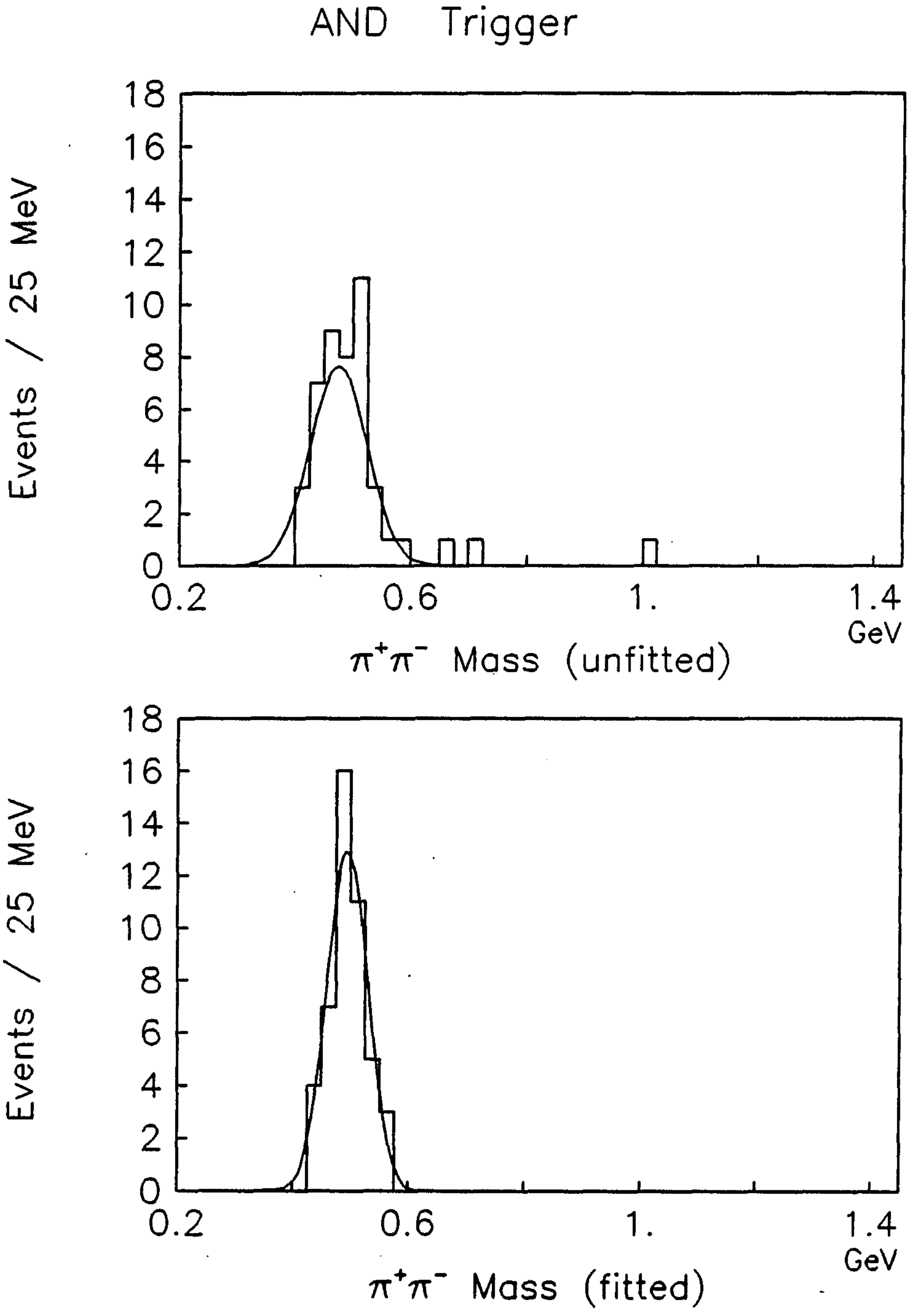

Figure 4.12 The $\pi^+\pi^-$ pair mass distribution of the AND trigger data after the mass cut on the fitted variables for unfitted (top) and fitted (bottom) variables; a gaussian fit is shown superimposed for each

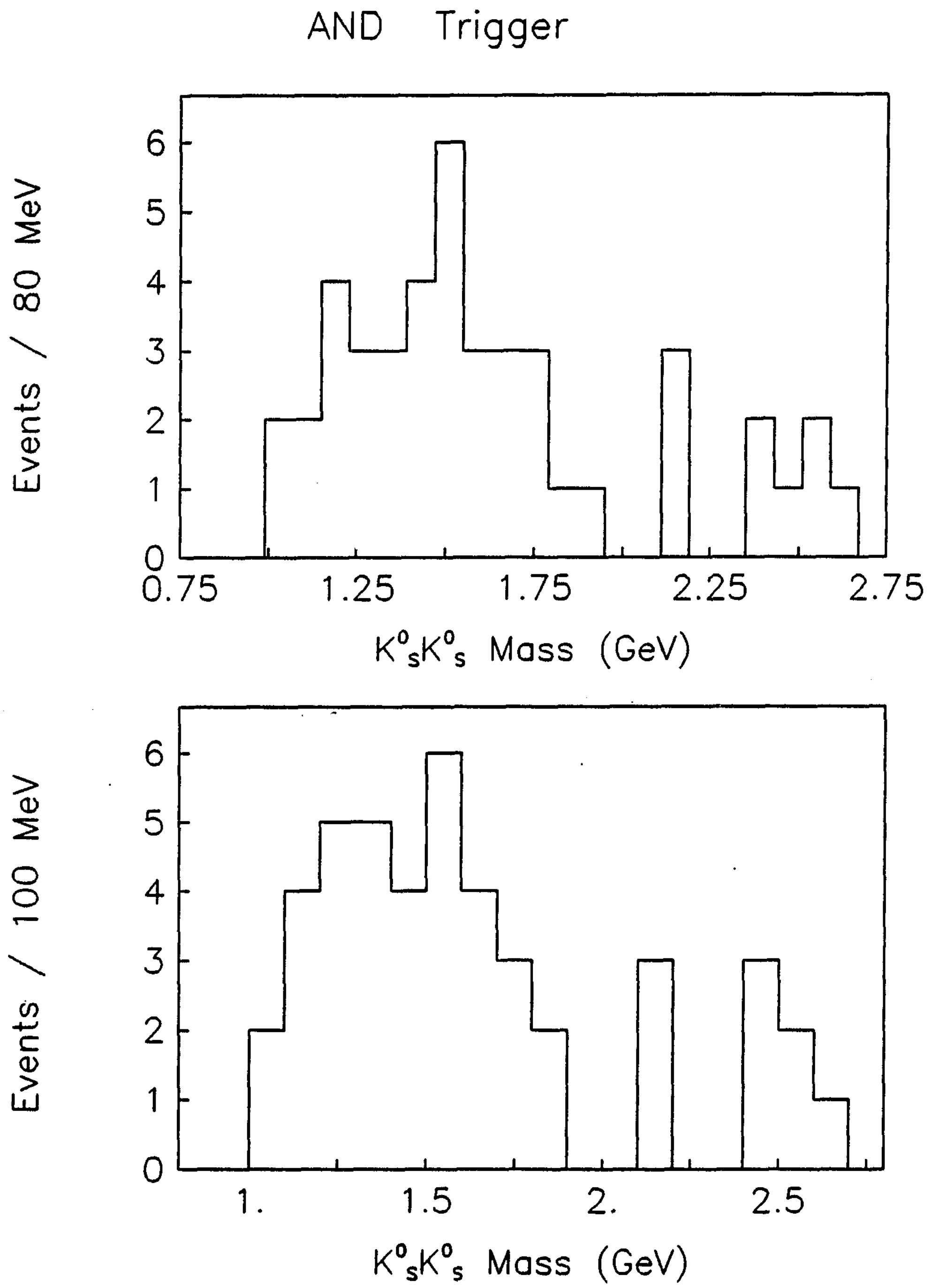

Figure 4.13 $K^0_sK^0_s$ central system mass distributions with 80 MeV bins (top) and 100 MeV bins (bottom) for the AND trigger data

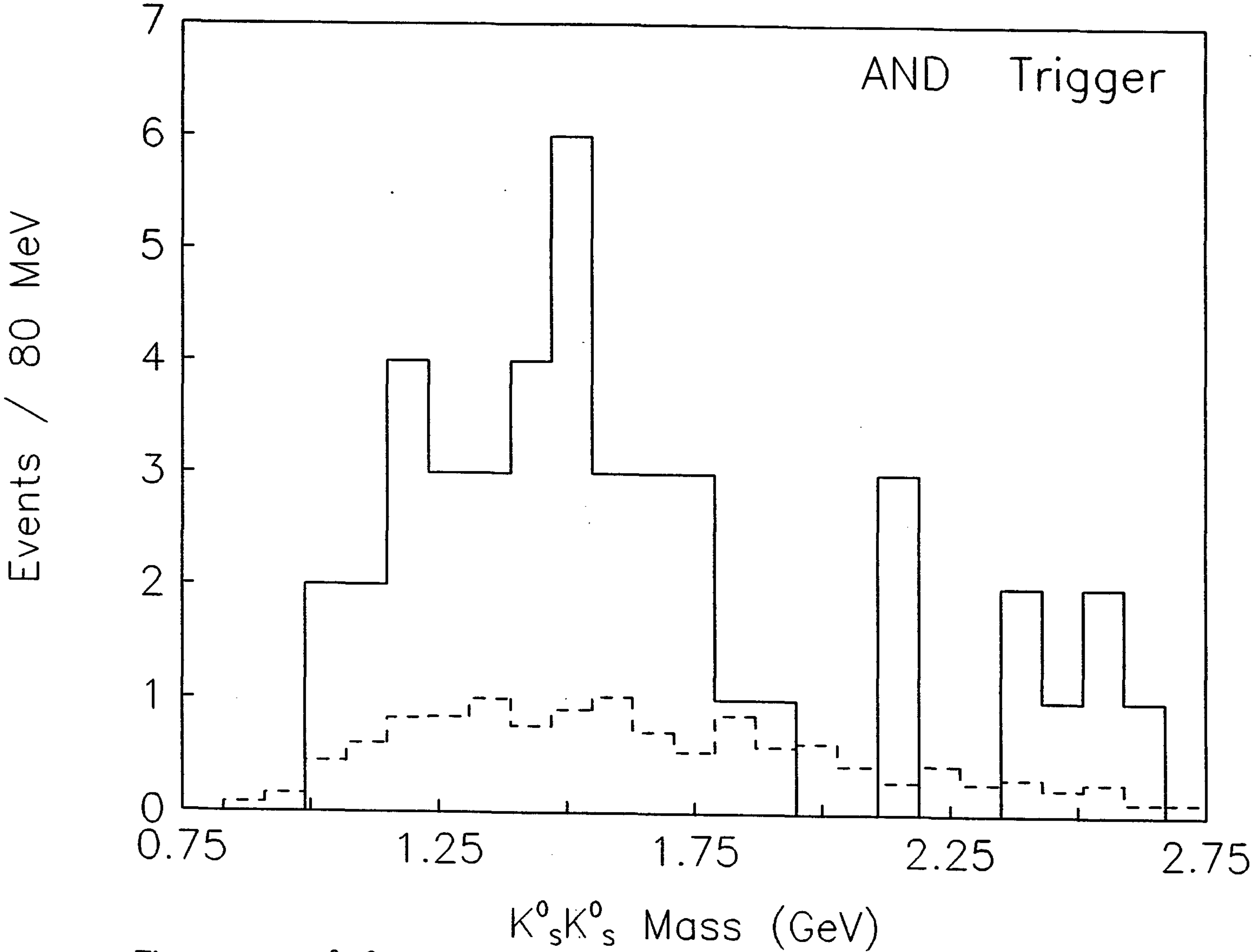

Figure 4.14 $K^0_s K^0_s$ central system mass (solid line) with the background superimposed (dashed line)

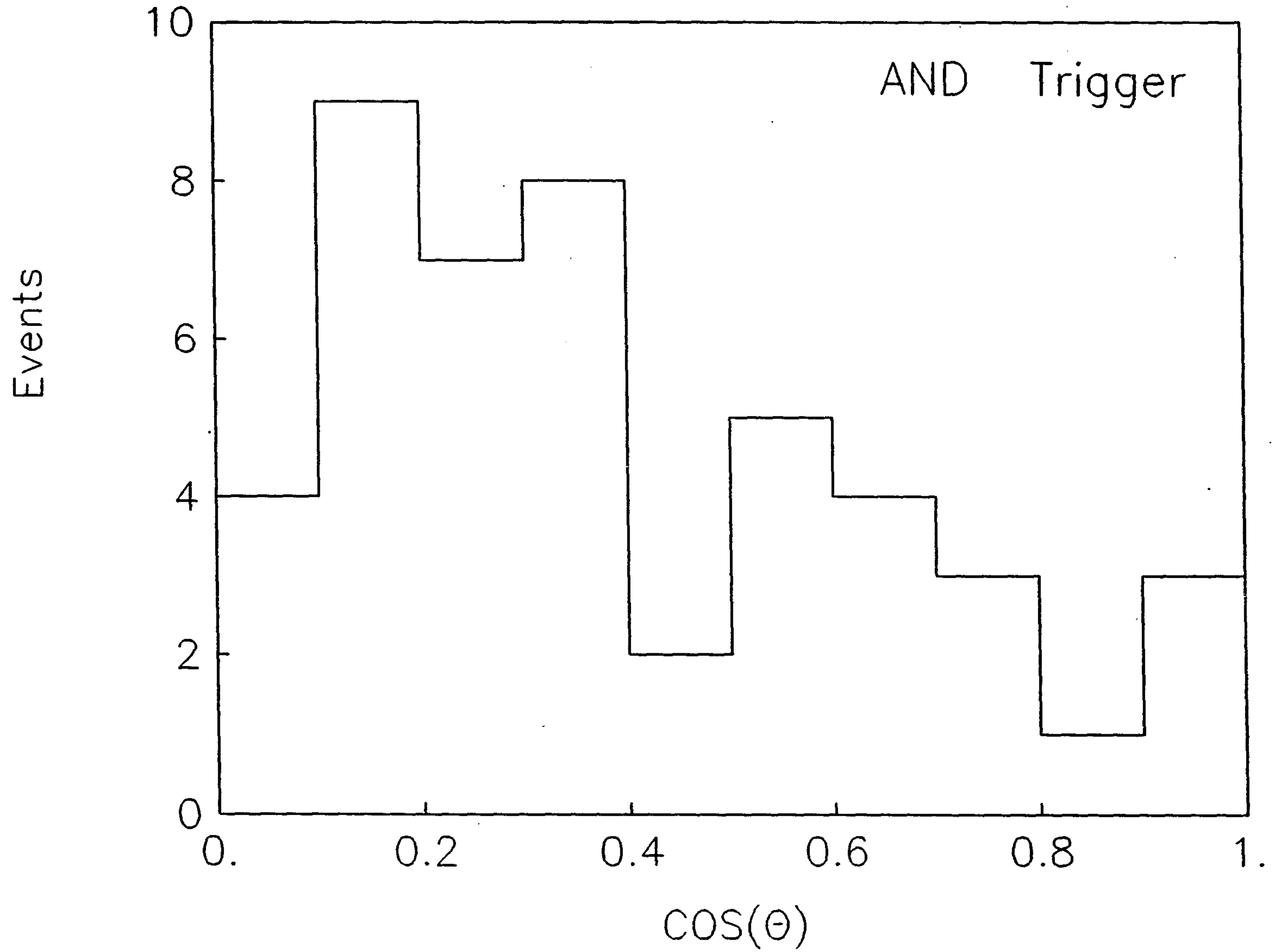

Figure 4.15 $cos(\theta)$ distribution of the angle between the K_s^0 particle and one of the Pomerons in the Pomeron-Pomeron rest frame

4.1.3 TOF trigger data

The treatment of the data was carried out using the same method as in the OR and AND trigger data. The equivalent Figures to 4.2-4.8 are shown in Figures 4.16-4.22. A probability cut of 0.02 was used for this trigger also. The distributions in the decay angle cosine theta and the phi angle are similar to those in Figures 3.3 and 3.4 for the TOF trigger.

It is evident from Figures 4.18 and 4.19, that the TOF trigger data also contain a second K_s^0 particle. The gaussian fits yield a central value of 478 ± 25 MeV with a width of 91 ± 24 MeV for the unfitted variables and a central value of 499 ± 6 MeV with a width of 31 ± 5.1 MeV for the fitted variables.

The number of events in the $K_s^0 K_s^0$ sample is 30 events. The distribution of the invariant mass of the $K_s^0 K_s^0$ central system is shown in Figure 4.20 for 80 MeV and 100 MeV bin sizes. The two histograms show a strong peak at about 1200 MeV. This is similar to the OR trigger data in Figure 4.6. As mentioned in Section 4.1.1, the peak at 1200 is not near any well known meson mass resonances with even spin and positive parity. From Figure 4.18 the background is estimated to be 30%. With the shape of the background in the $K_s^0 K_s^0$ mass distribution of Figure 4.21 it is evident that the enhancement is not due to background in the data sample.

4.1.4 Combination of the three data sets, OR, AND, and TOF

In order to improve the statistics available for studying the central system mass combinations, data from the three trigger samples were combined. Since the AND trigger data show a different distribution in the mass of the whole system, it was decided to look at the sum of all three distributions and also to combine the OR and TOF samples without the AND trigger data. Because of the requirement

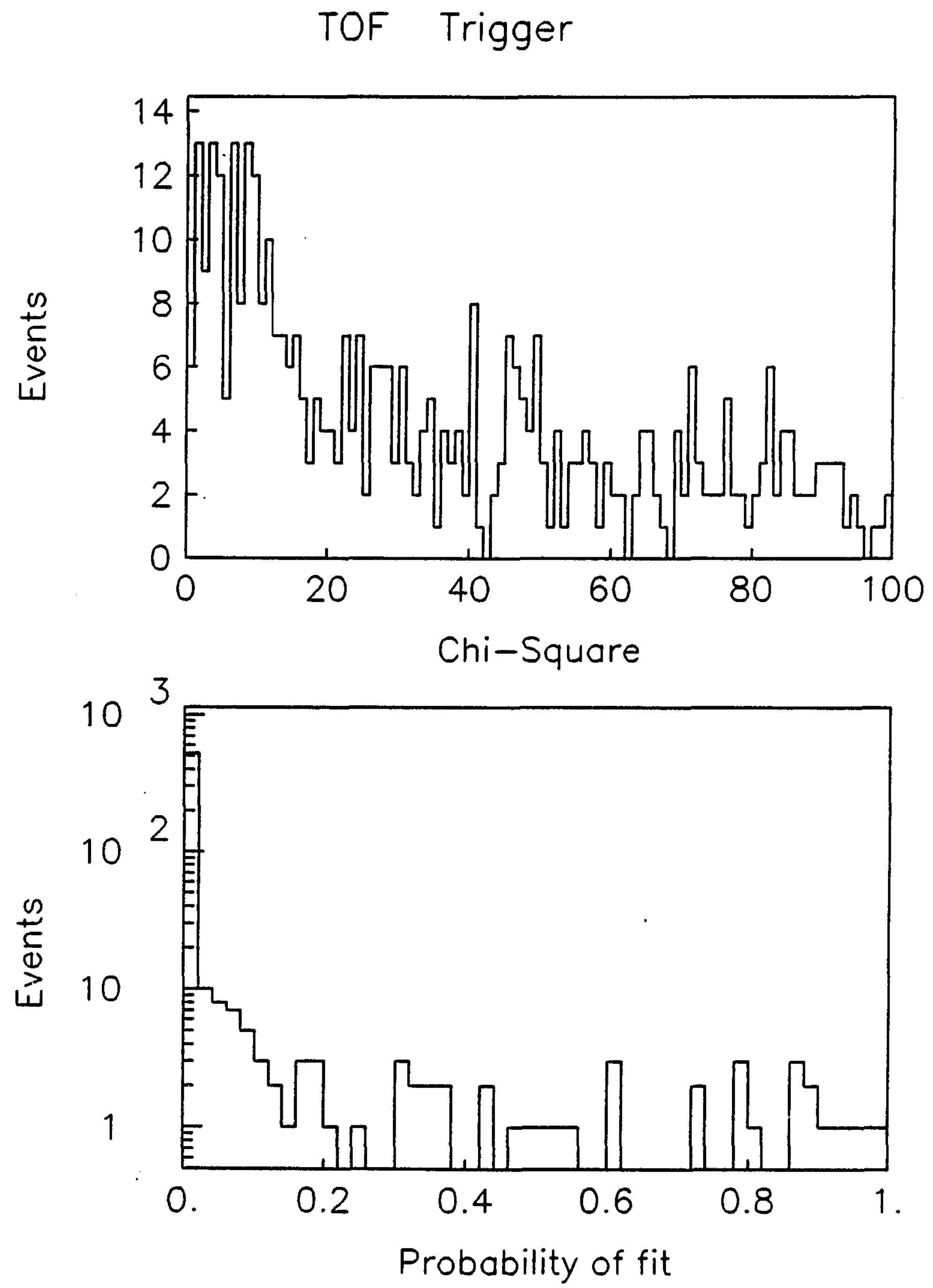

Figure 4.16 χ^2 (top) and probability of fit (bottom) distributions for the TOF data

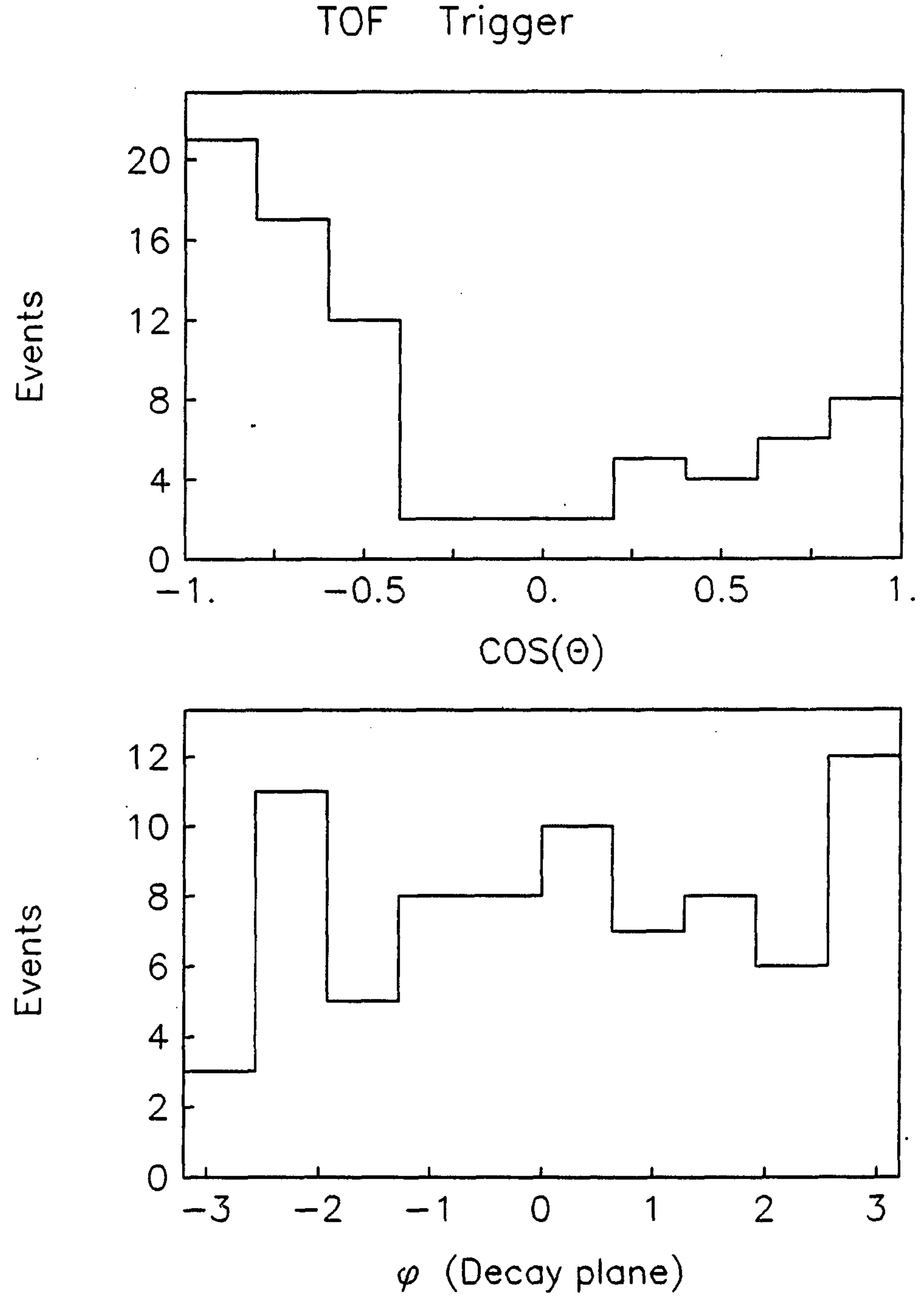

Figure 4.17 K_s^0 distribution of *cos*(θ) (top), and of the decay plane orientation angle, for the TOF trigger data

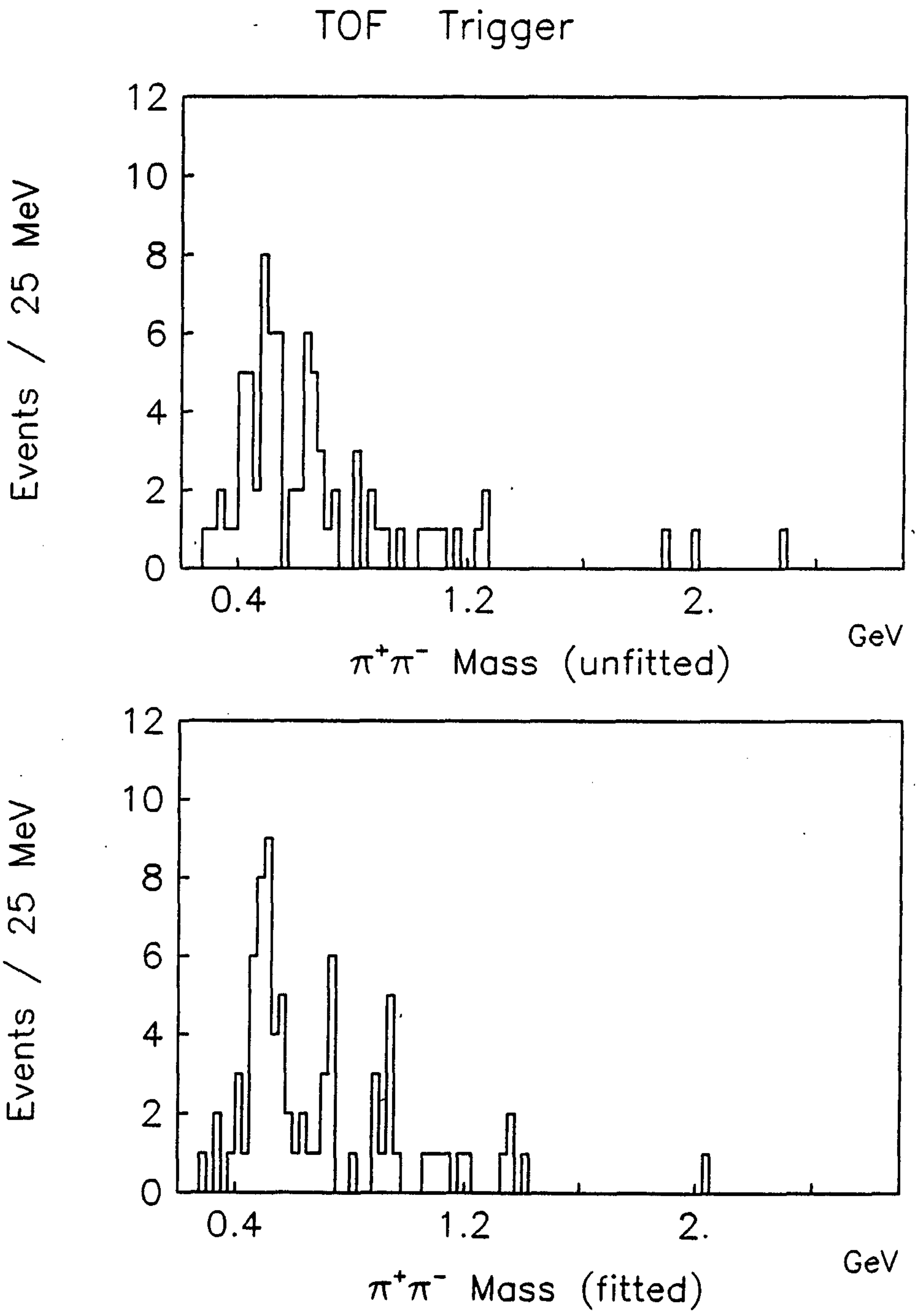

Figure 4.18 Invariant mass of the $\pi^+\pi^-$ pair not associated with the K_s^0 particle for the TOF trigger data; both the unfitted (top) and fitted (bottom) variables are shown

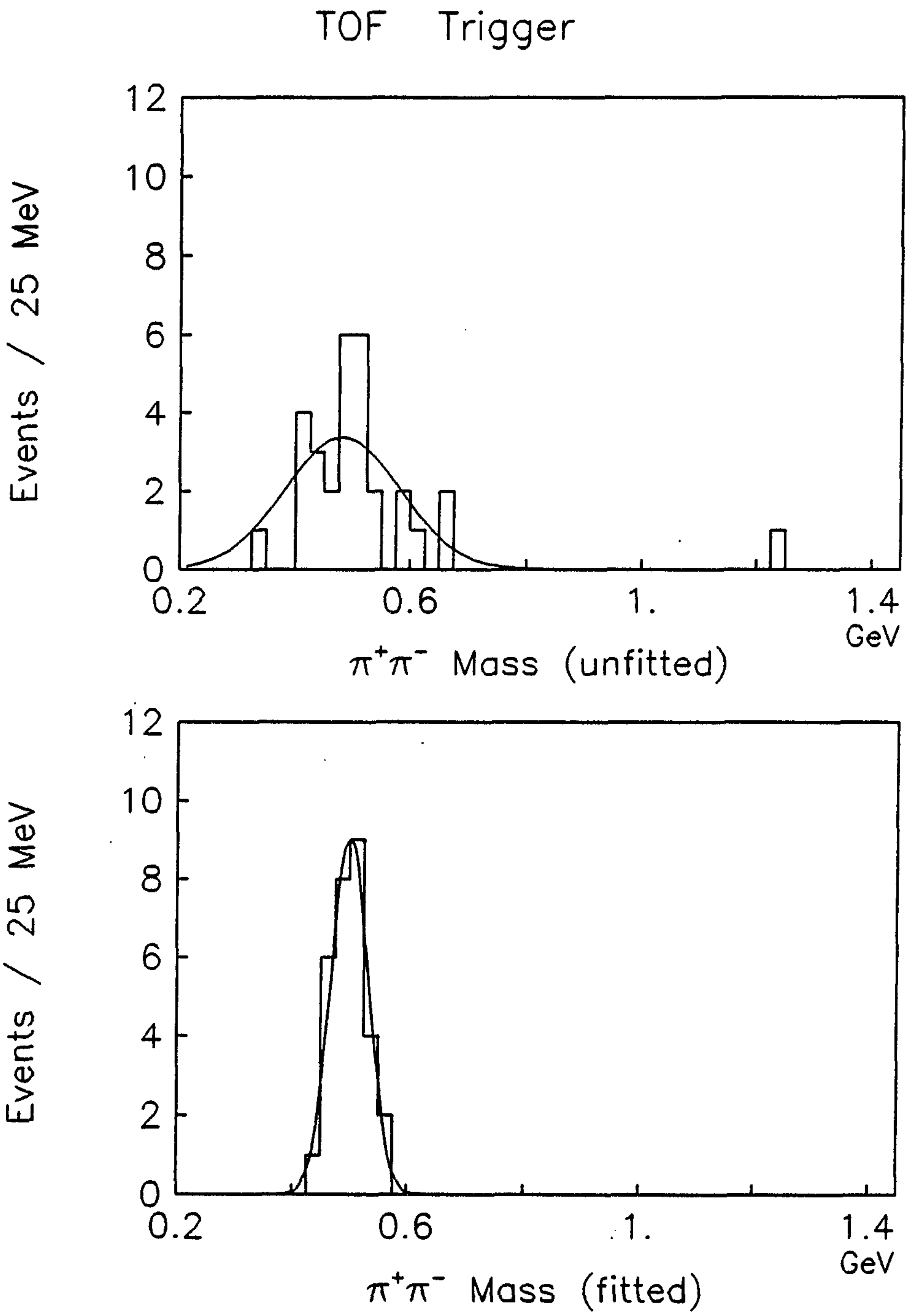

Figure 4.19 The $\pi^+\pi^-$ pair mass distribution of the TOF trigger data after the mass cut on the fitted variables for unfitted (top) and fitted (bottom) variables; a gaussian fit is shown superimposed for each

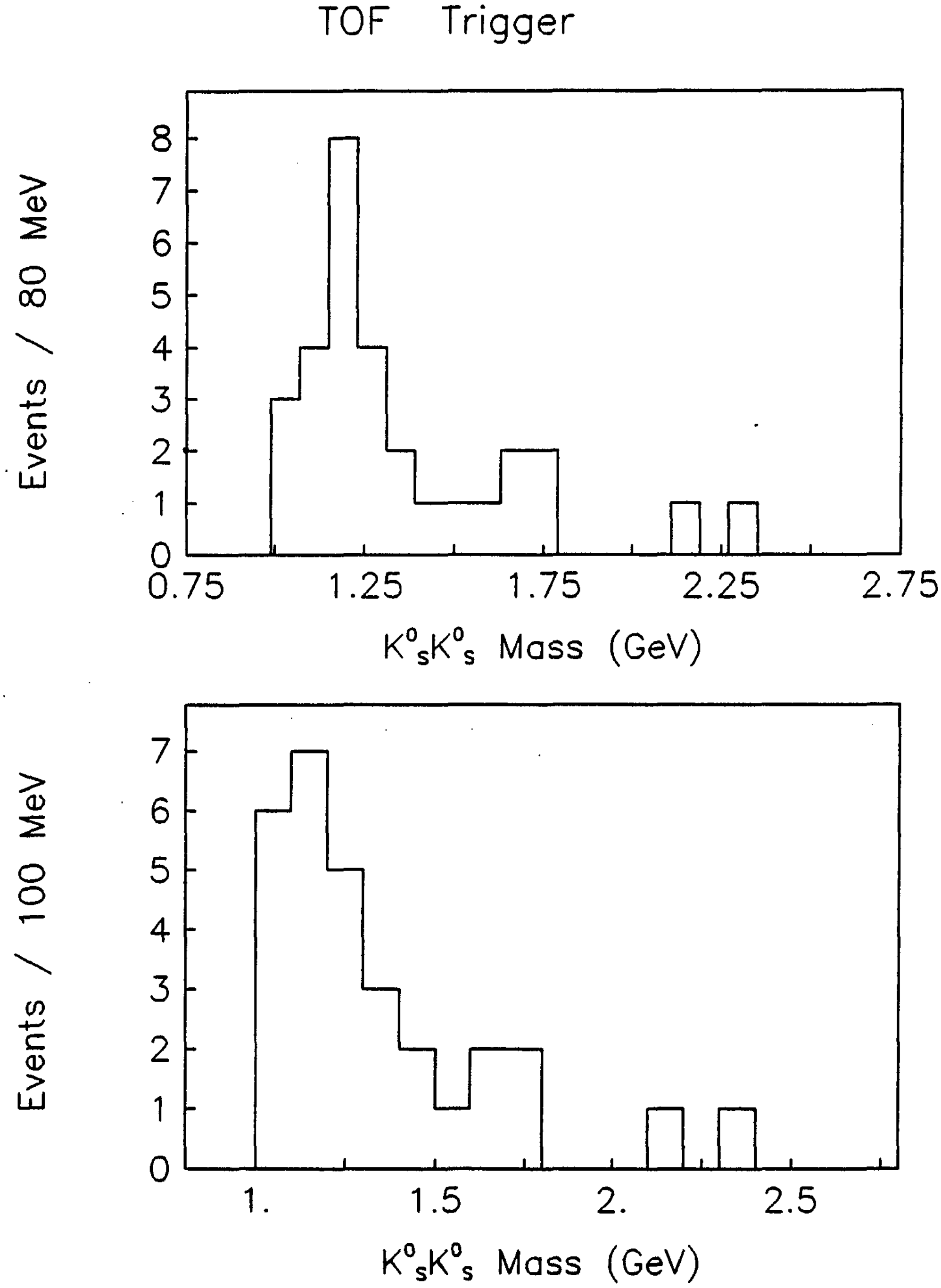

Figure 4.20 $K^0_sK^0_s$ central system mass distributions with 80 MeV bins (top) and 100 MeV bins (bottom) for the TOF trigger data

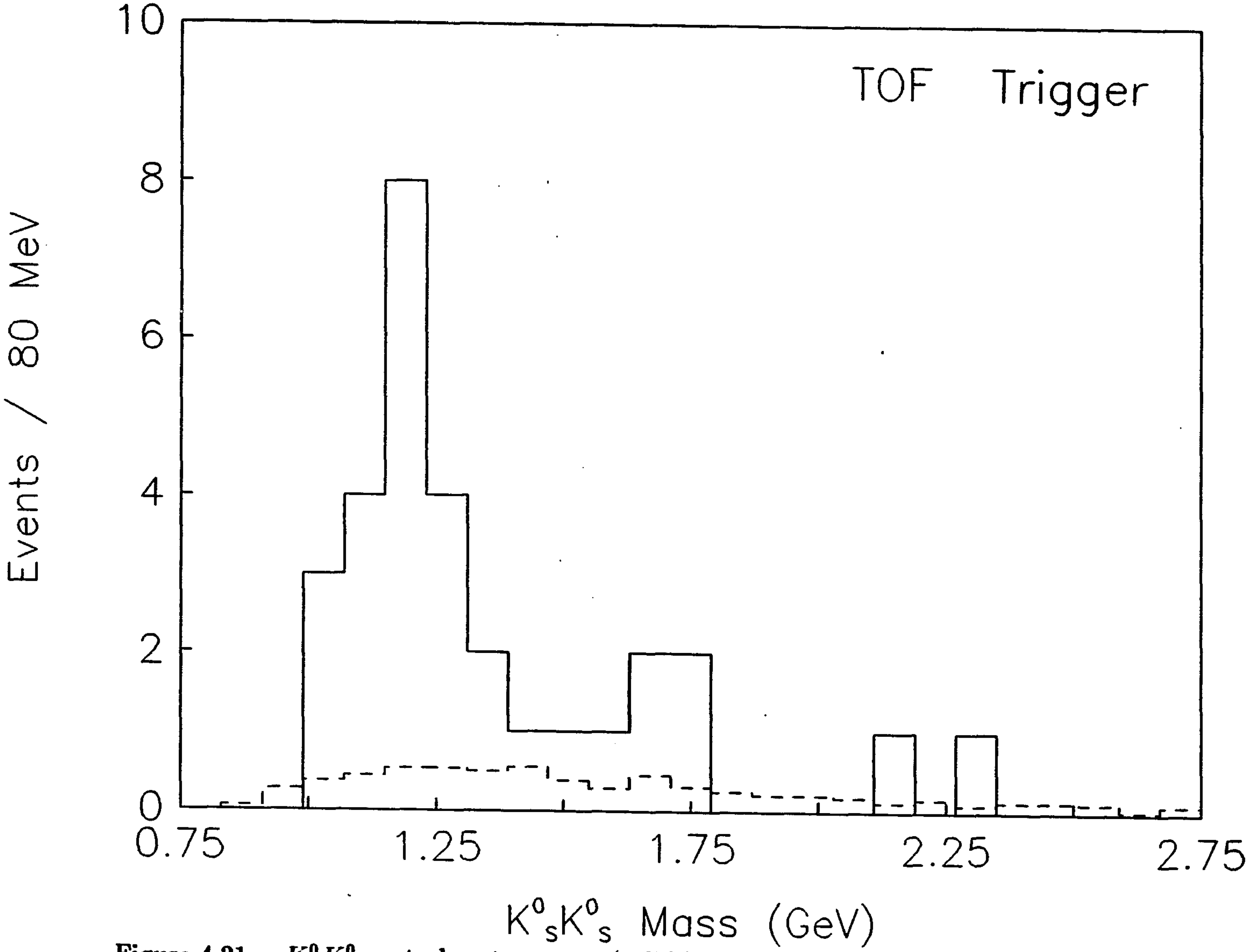

Figure 4.21 $K_s^0 K_s^0$ central system mass (solid line) with the background superimposed (dashed line)

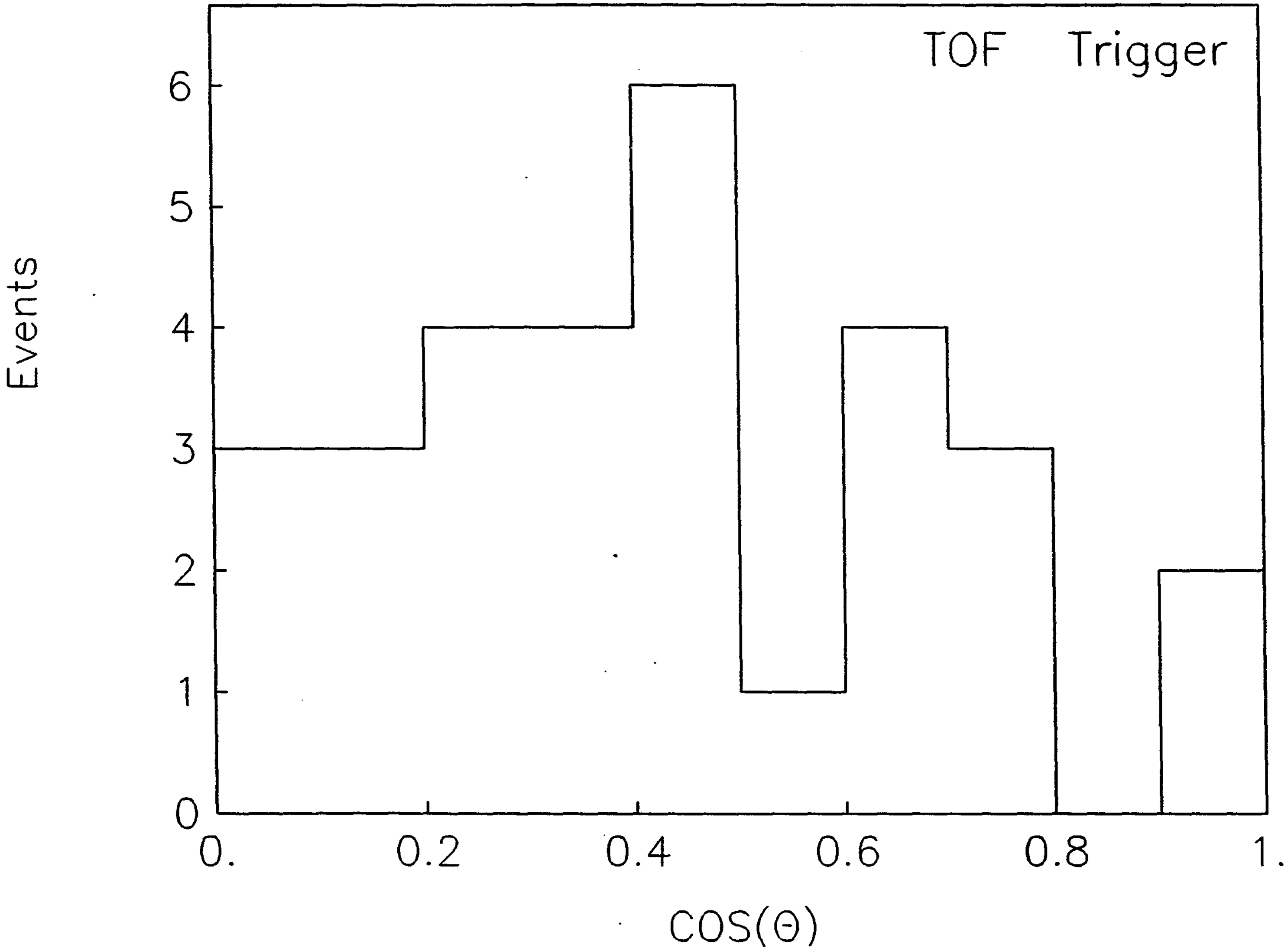

Figure 4.22 $cos(\theta)$ distribution of the angle between the K_s^0 particle and one of the Pomerons in the Pomeron-Pomeron rest frame

of charged particles on both sides of the detector in the central region, the AND trigger samples a different region of phase space from the OR and TOF triggers. Specifically, the AND data sample contains a bias towards higher mass events in the central system. This bias is due to the requirement in the trigger of one hit on the positive x side and also one on the negative x side of the detector. Since there is a center of mass motion in the negative x direction, the momentum of the particle at the positive side for each event will be biased to higher momenta on average than will the OR or TOF triggers which only require a hit on one side of the detector in the central region.

The mass distribution for the $K_s^0 K_s^0$ central system is shown in Figure 4.23 for the three data sets combined with the background superimposed. The peak at 1200 MeV remains. The cosine of theta distribution in the Pomeron-Pomeron rest frame of the angle between the K_s^0 particle and one of the Pomerons is shown in Figure 4.24 for the three data sets combined.

The mass distribution for the $K_s^0 K_s^0$ central system is shown in Figure 4.25 for the OR and TOF data sets combined with the background superimposed. The peak at 1200 MeV is enhanced. This gives more weight to the argument that there is probably some sort of resonant state in this mass region. The cosine theta distribution in the Pomeron-Pomeron rest frame of the angle between the K_s^0 particle and one of the Pomerons is shown in Figure 4.26 for the OR and TOF data sets combined. It appears that the central system decays largely via s-wave. In order to verify this statement, the data have to be corrected for geometric and trigger acceptances. As indicated earlier, this is discussed in Chapter 6.

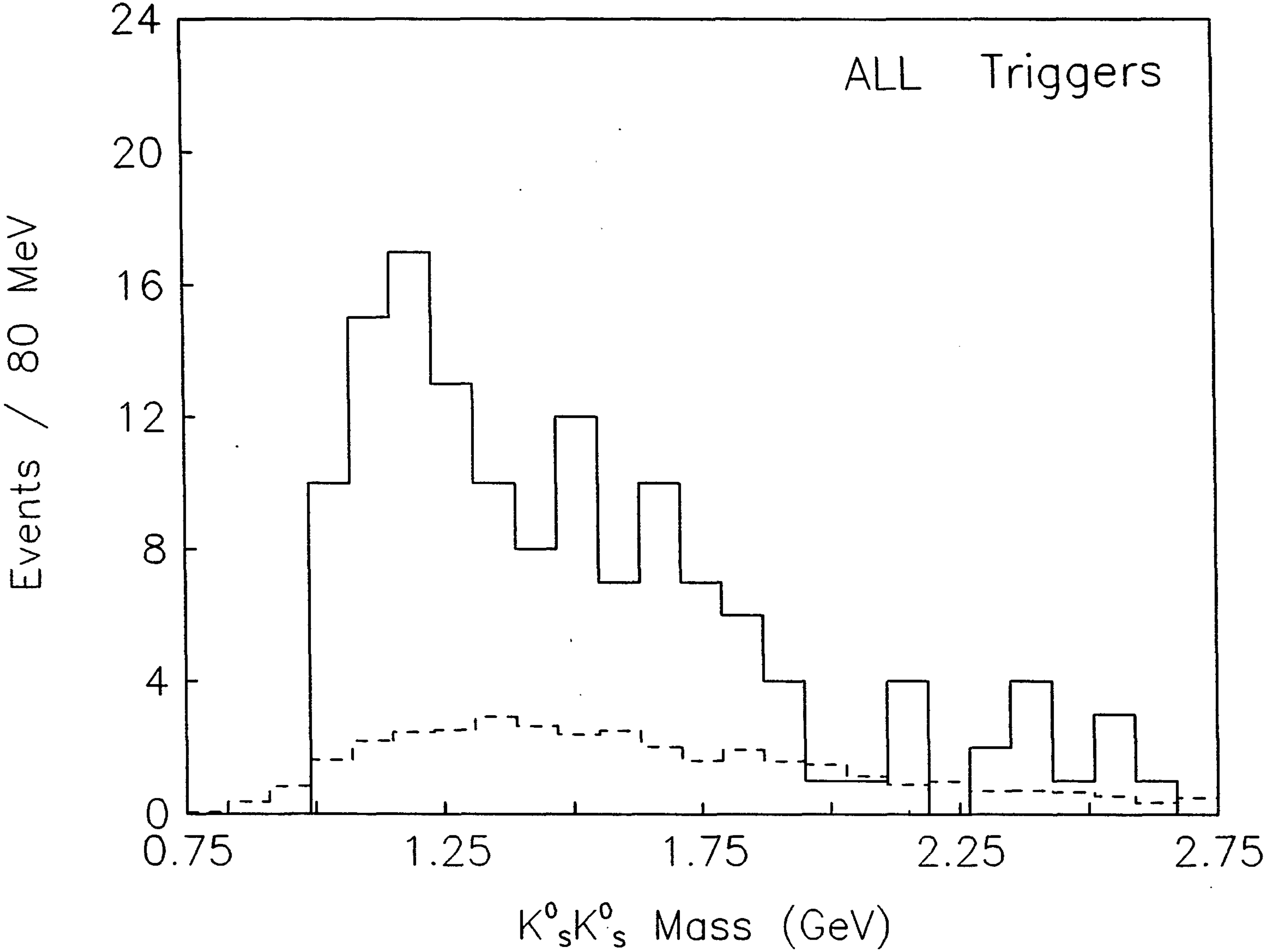

Figure 4.23 $K^0_s K^0_s$ mass distribution (solid line) for the three data sets combined with the background (dashed line) superimposed

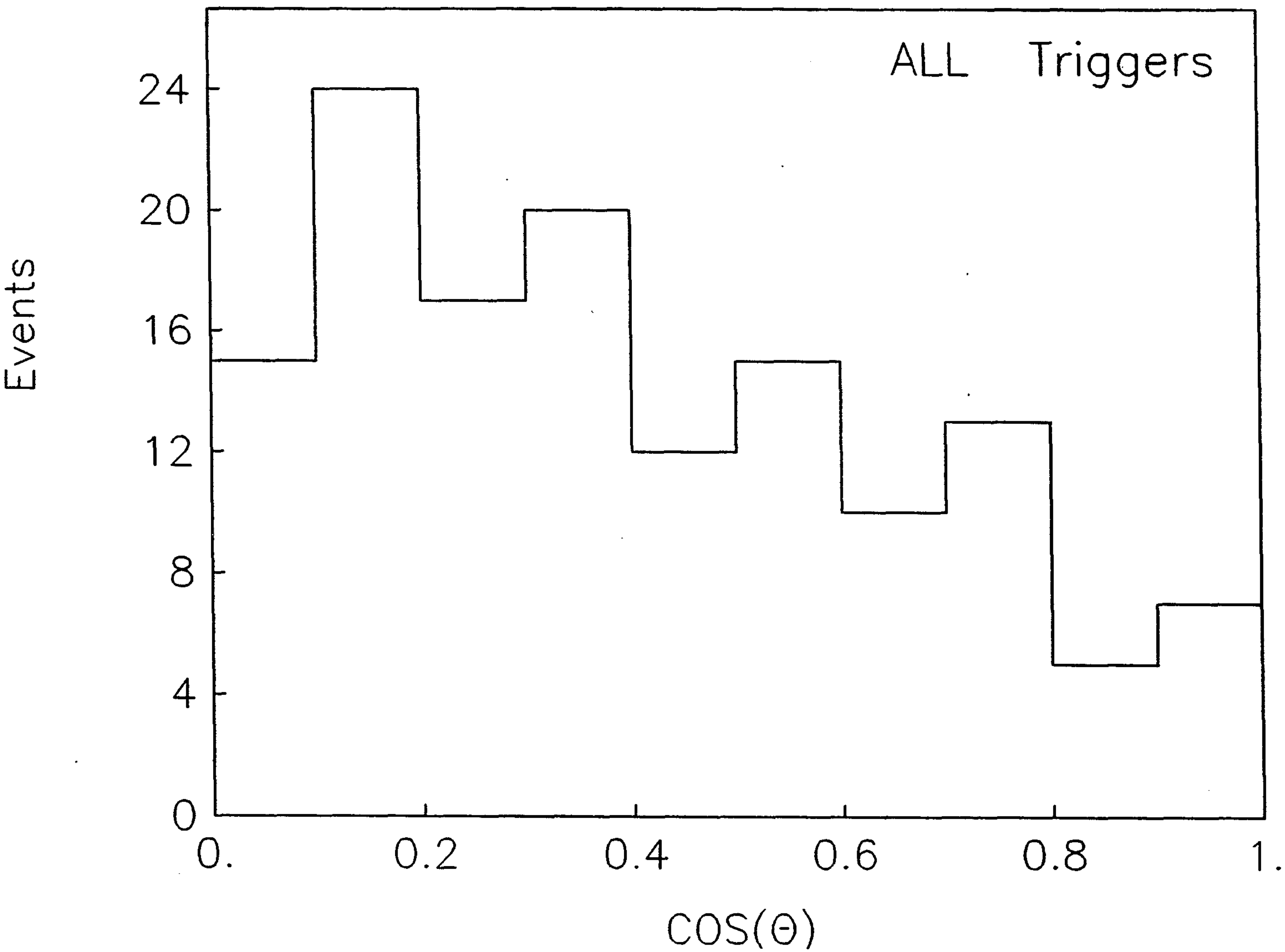

Figure 4.24 $cos(\theta)$ distribution of the angle between the K_s^0 particle and one of the Pomerons in the Pomeron-Pomeron rest frame for all triggers

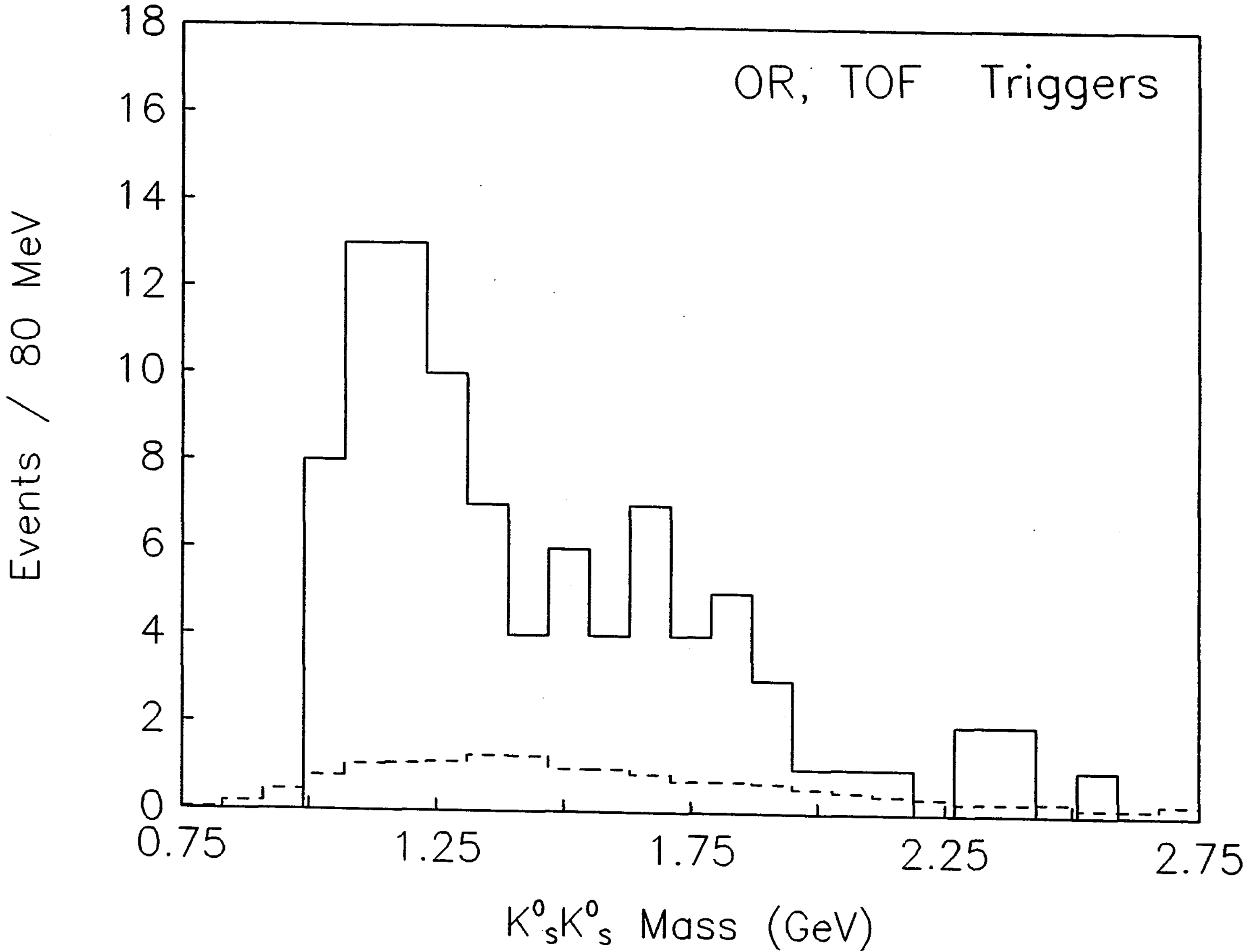

Figure 4.25 $K^0_s K^0_s$ mass distribution (solid line) for the OR, TOF data sets combined with the background (dashed line) superimposed

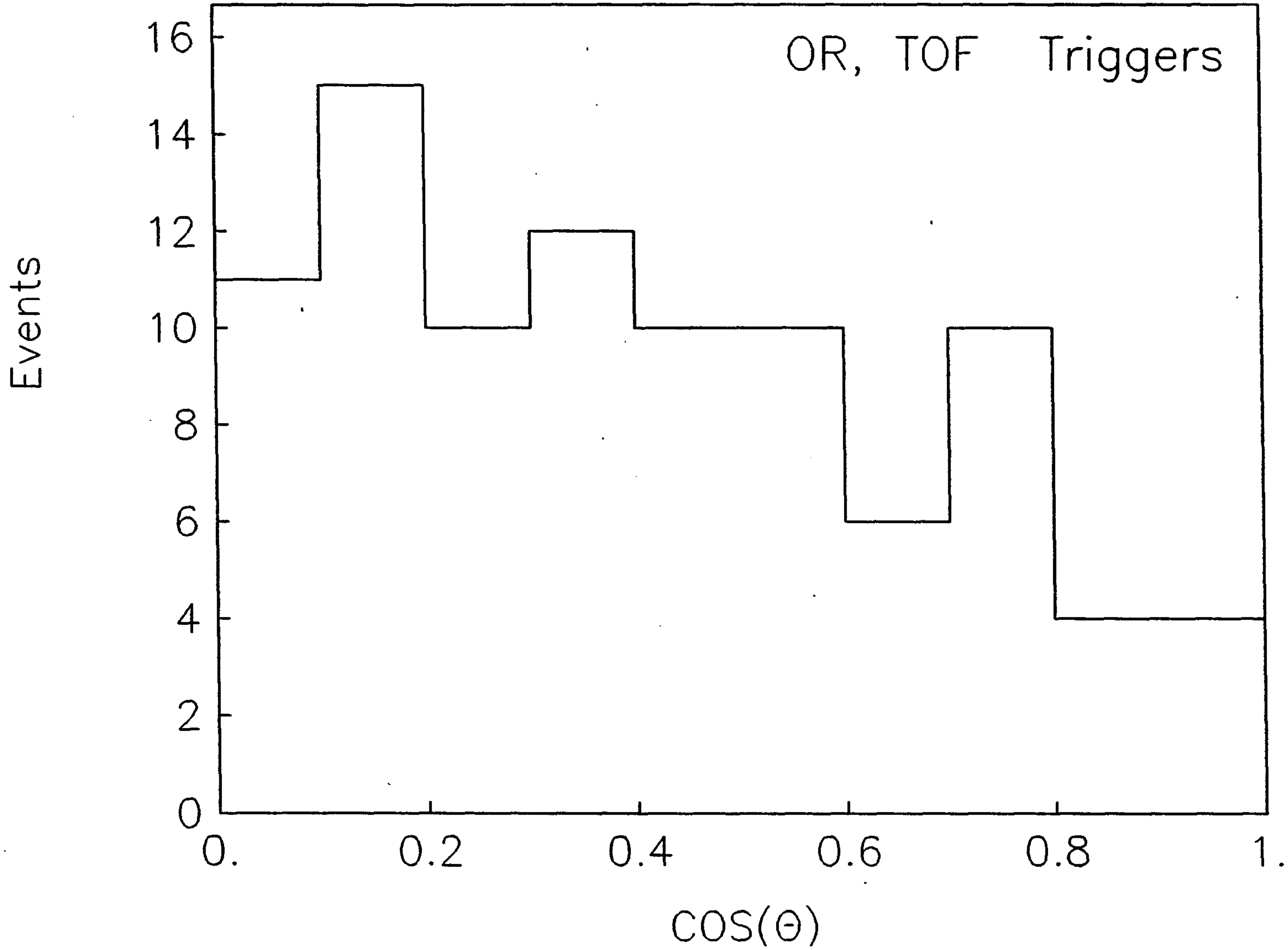

Figure 4.26 $cos(\theta)$ distribution of the angle between the K_s^0 particle and one of the Pomerons in the Pomeron-Pomeron rest frame

4.1.5 Search for physics biases in the data samples

Scatter-plots of the $\pi^+\pi^-$ mass versus the $K_s^0K_s^0$ mass in the central system are shown in Figure 4.27 for each of the three triggers. There seem to be no obvious correlations in the figures. The same scatter-plot with all three triggers on the same graph is shown in Figure 4.28 and again shows no obvious correlations or differences in the data apart from the enhancements already discussed in Section 4.1.4.

Scatter-plots of the $K_s^0K_s^0$ central system mass versus the probability of fit is shown for the three triggers in Figure 4.29 and show no obvious biases apart from slightly higher statistics in the low probability region which is to be expected from the way the probability of fit cuts were made in each of the data sets.

In Figure 4.30 a scatter plot of the mass of the $K_s^0K_s^0$ central system versus cosine theta in the Pomeron-Pomeron rest frame is shown. There appears to be a slight bias towards higher mass values for low cosine theta. This bias could be explained by the forward veto in the three triggers. Since the Pomeron momenta tend to favor the forward proton directions, larger central system momenta will be excluded by the veto in the forward direction. Acceptance corrections eliminate this effect in cosine theta as will be shown in Chapter 6. In Figure 4.31 a scatter plot of the $\pi^+\pi^-$ mass versus the cosine of theta in the Pomeron-Pomeron rest frame reveals no new information.

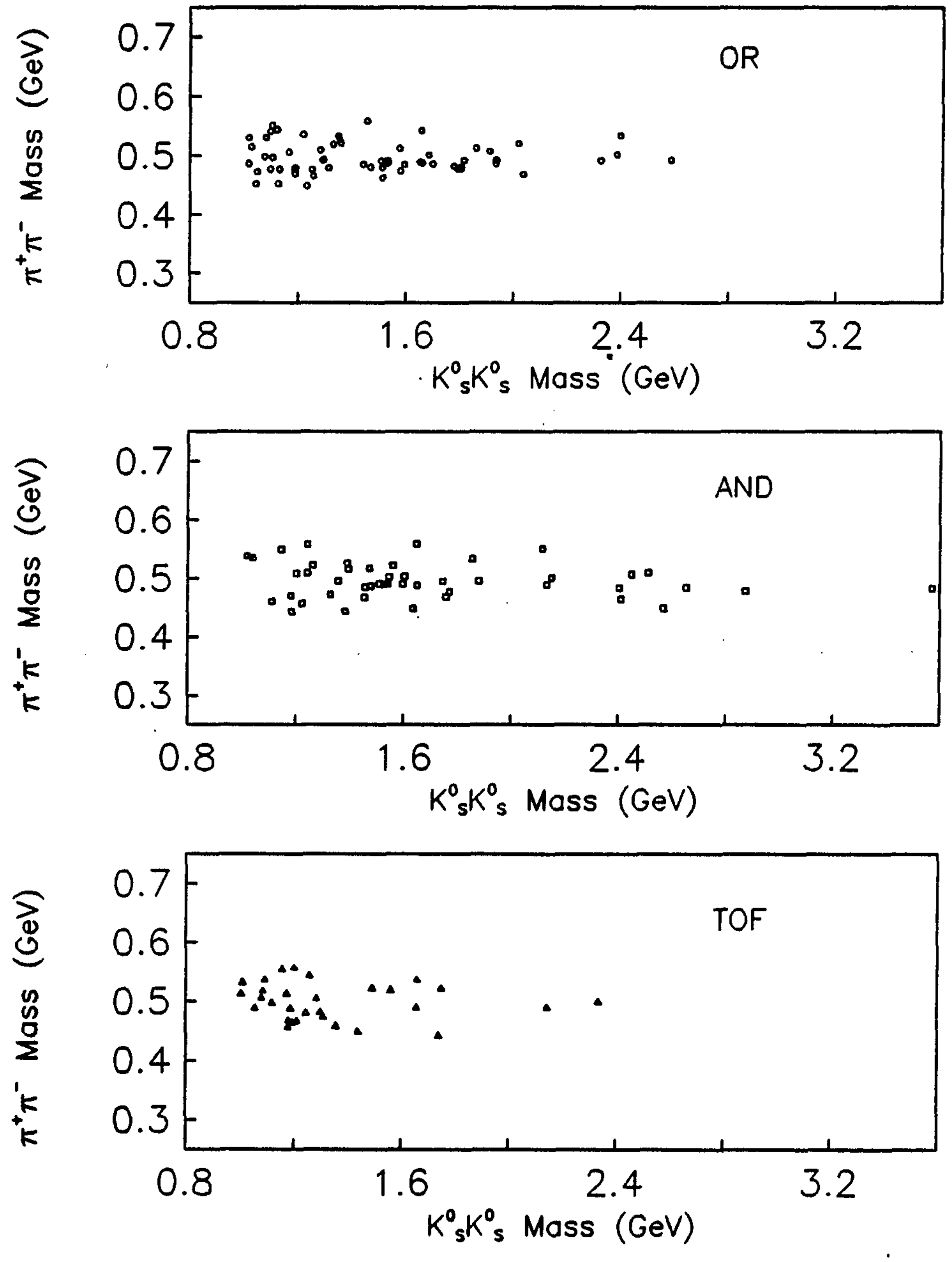

Figure 4.27 $\pi^+\pi^-$ mass versus $K^0_sK^0_s$ mass for each trigger

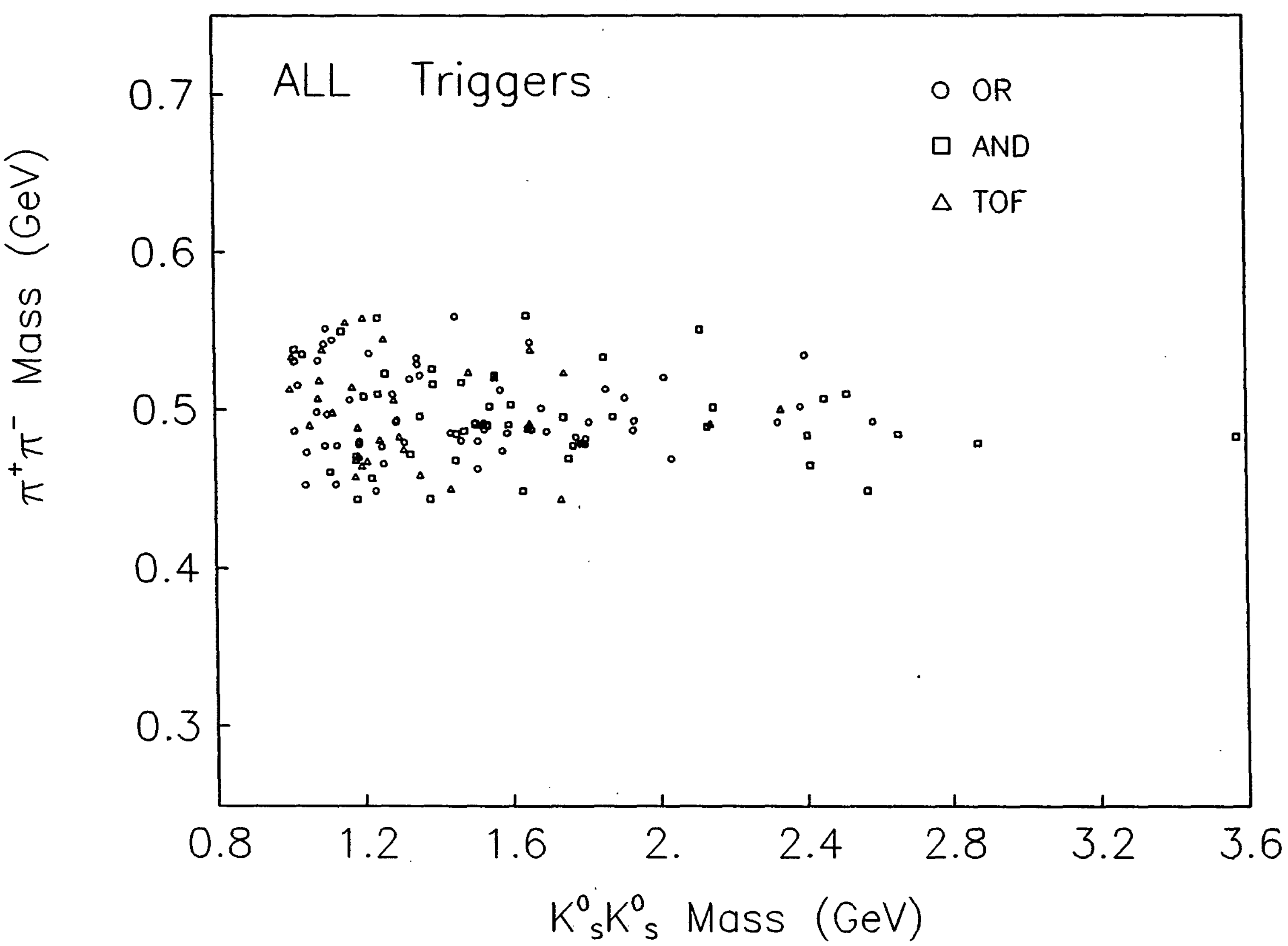

Figure 4.28 $\pi^+\pi^-$ mass versus $K^0_sK^0_s$ mass for all three triggers

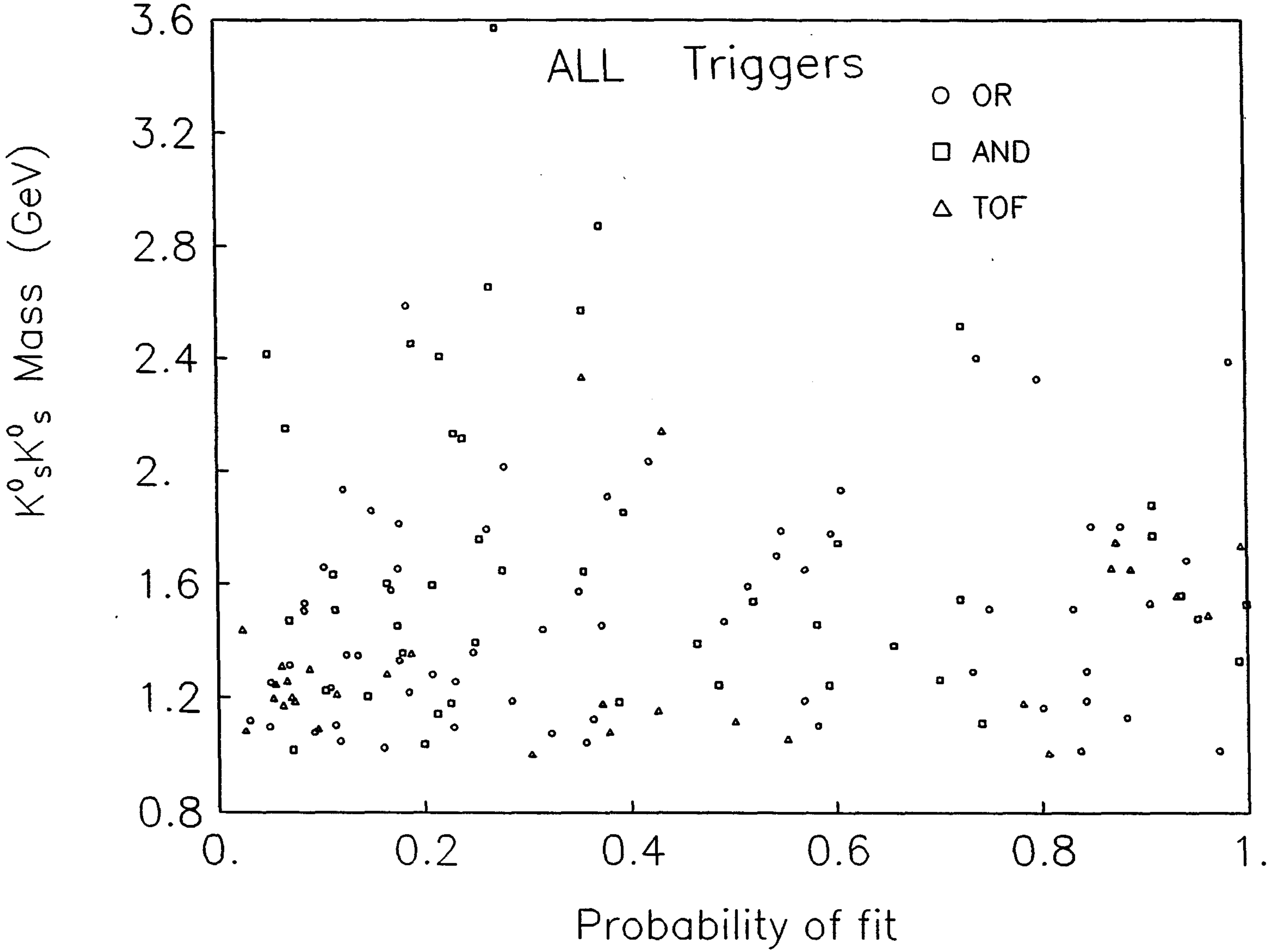

Figure 4.29 $K^0_s K^0_s$ **mass versus probability of fit for all three triggers**

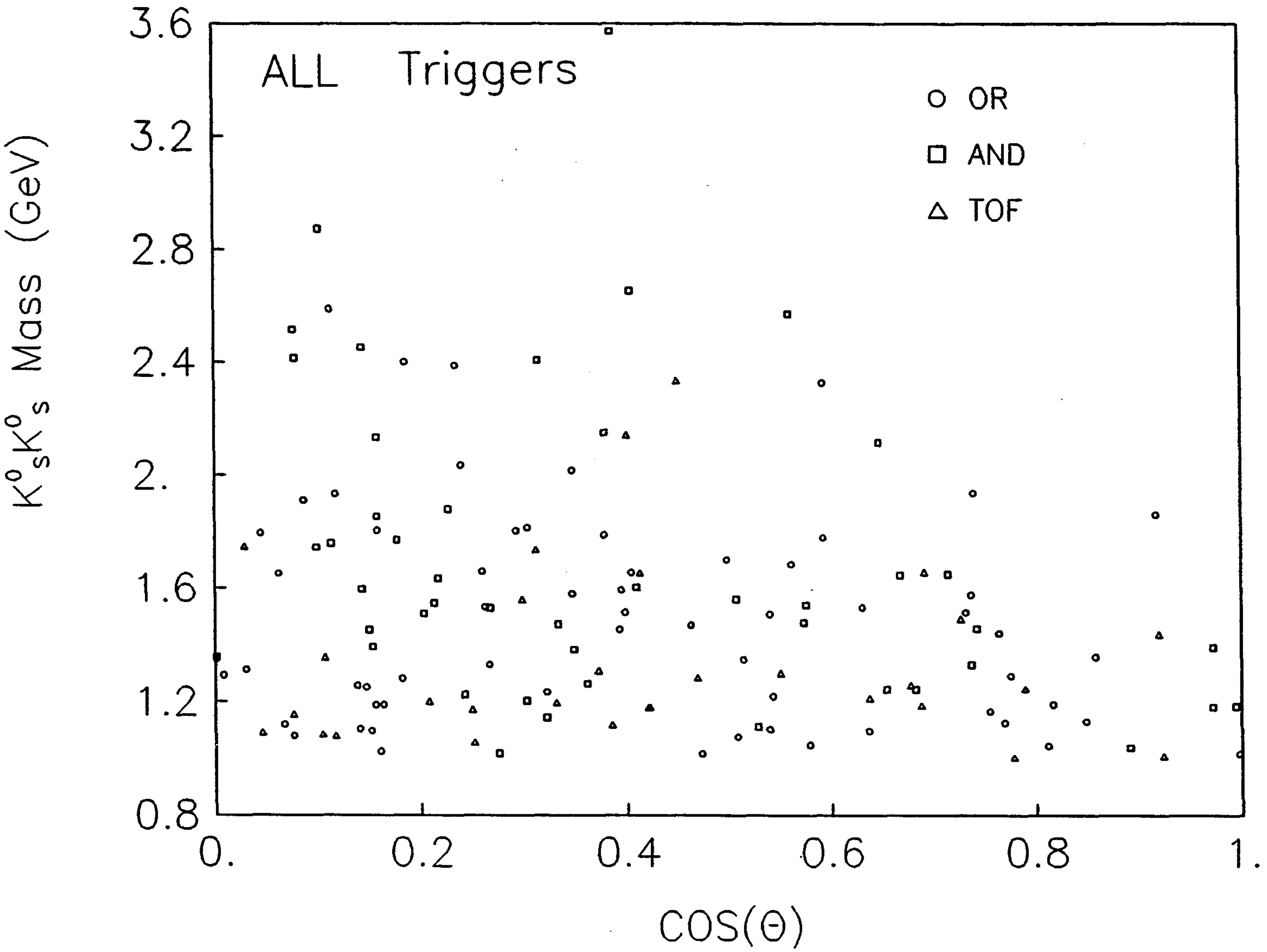

Figure 4.30 $K_s^0 K_s^0$ mass versus $cos(\theta)$ for the three triggers

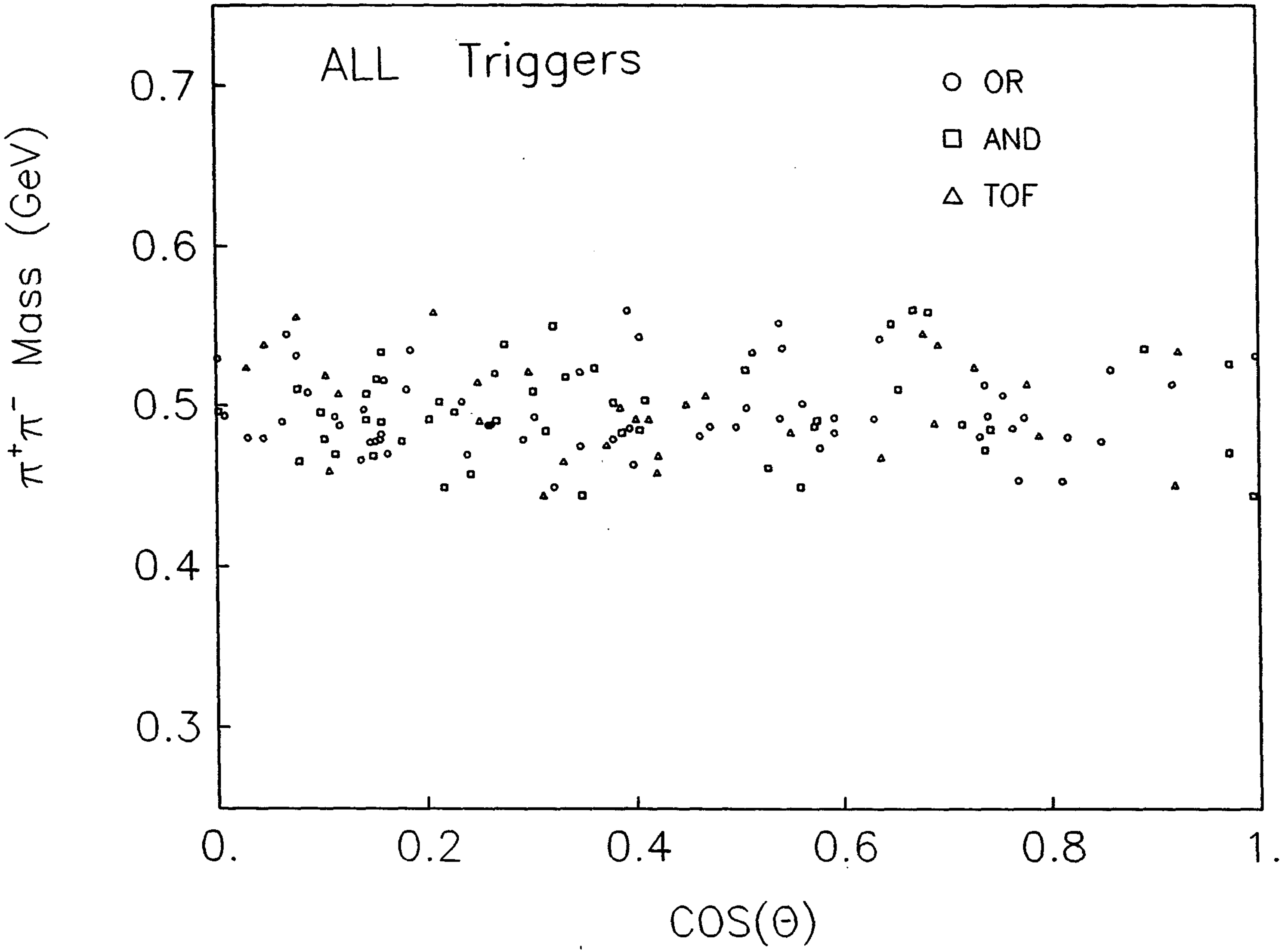

Figure 4.31 $\pi^+\pi^-$ mass versus $cos(\theta)$ for the three triggers

4.2 $K_s^0K^{\pm}\pi^{\mp}$ Central System

All of the 6-prong events containing at least one identified K_s^0 particle given from the V^0 program were further processed using the 4-C fit routine discussed in Section 3.5. The masses of the particles for the reaction 3.6 were assigned as discussed in Section 3.4 and are listed in Table 4.2. These masses were required to be consistent with any available time of flight information on the DST. The momenta and angles as described in Section 3.5 for each of the particles were input to the 4-C fit routine. The probability of fit distribution is shown in Figure 4.32 for the OR trigger data. The probability distributions for the AND and TOF data are similar. In each of the three data sets the probability of fit cut was set at 0.02. Although a higher cut could be justified, it was found from background studies based on TOF mass information that higher probability cuts only reduced backgrounds by about 3-5%.

Table 4.2 Summary of particles whose four momenta are input to the 4-C fit in the $K_s^0K^{\pm}\pi^{\mp}$ central system hypothesis

Particle(s)	Mass (MeV)	Description
p, p	938.2796	Two ingoing beam protons
$K^{\pm}$	493.646	One central kaon (charged opposite to $\pi^{\mp}$)
$\pi^{\mp}$	139.5685	One central pion (charged opposite to $K^{\pm}$)
K_s^0	497.72	One V^0 Central particle
p, p	938.2796	Two fast outgoing protons

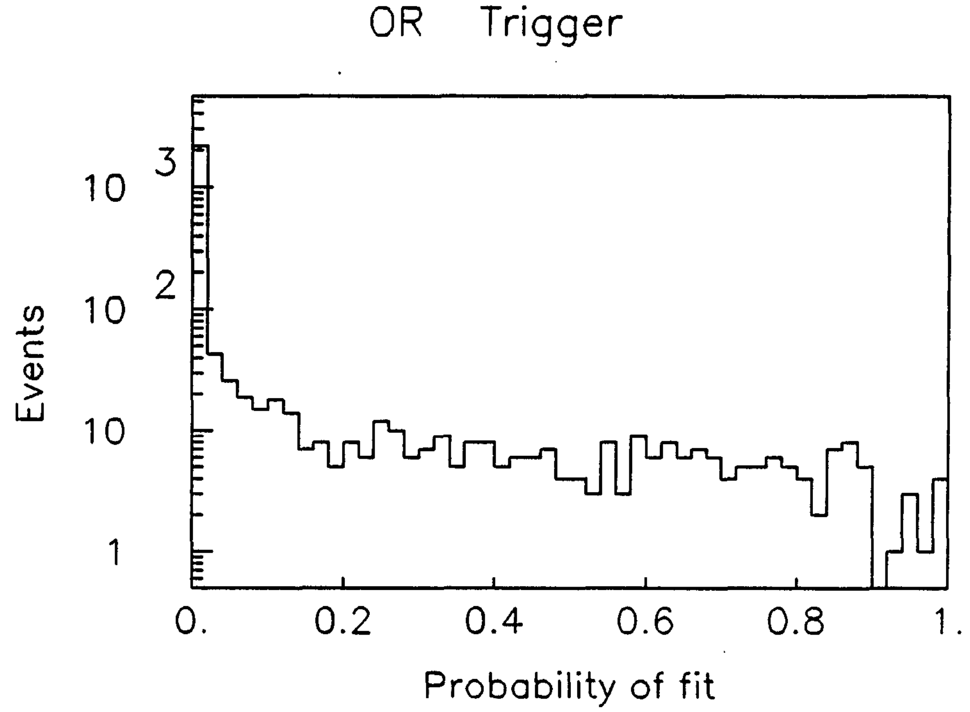

Figure 4.32 Probability of fit distribution for the OR trigger data

4.2.1 OR trigger data

A total of 1565 events were fitted and of these, 246 events were fitted successfully by the 4-C fit routine for at least one mass combination. Of the 246 events, 136 were fitted successfully with both charged $K^{\pm}\pi^{\mp}$ mass combinations. Figure 4.33(a) shows the $K^{\pm}\pi^{\mp}$ mass distribution with a broad peak at 825 MeV. This is two low to be a neutral K^* (mass 892 MeV) particle. Figure 4.33(b) shows the $K^0_s\pi^{\pm}$ mass distribution, and there is an enhancement at the charged K^* mass of 896 MeV. The $K^0_sK^{\pm}$ mass distribution is shown in Figure 4.33(c) and shows a peak at 1250 MeV.

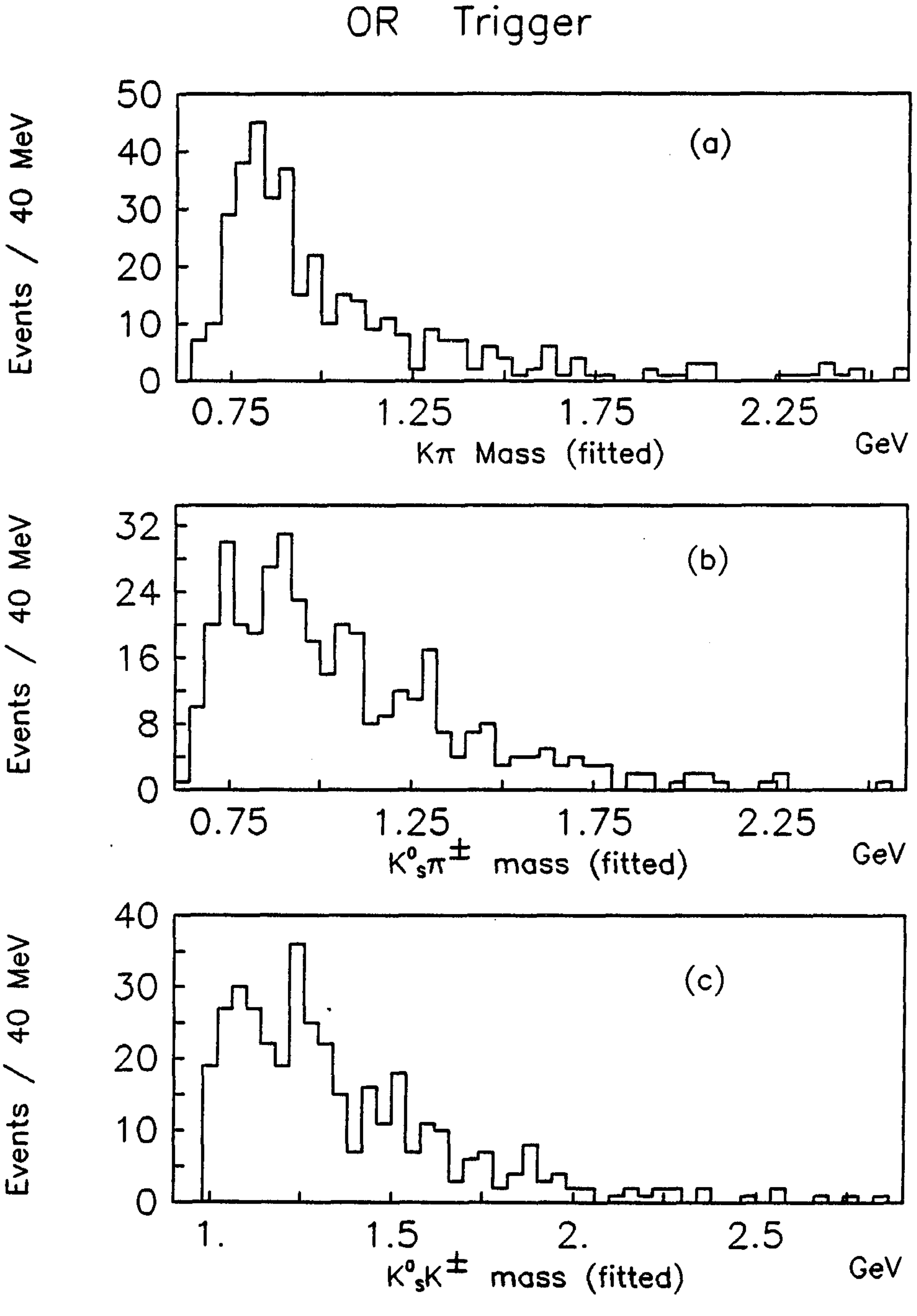

Figure 4.33 Invariant Mass distributions before excluding the $K_s^0 K_s^0$ events for the (a) $K^{\pm}\pi^{\mp}$, (b) $K_s^0\pi^{\pm}$, and (c) $K_s^0 K^{\pm}$ particle pairs

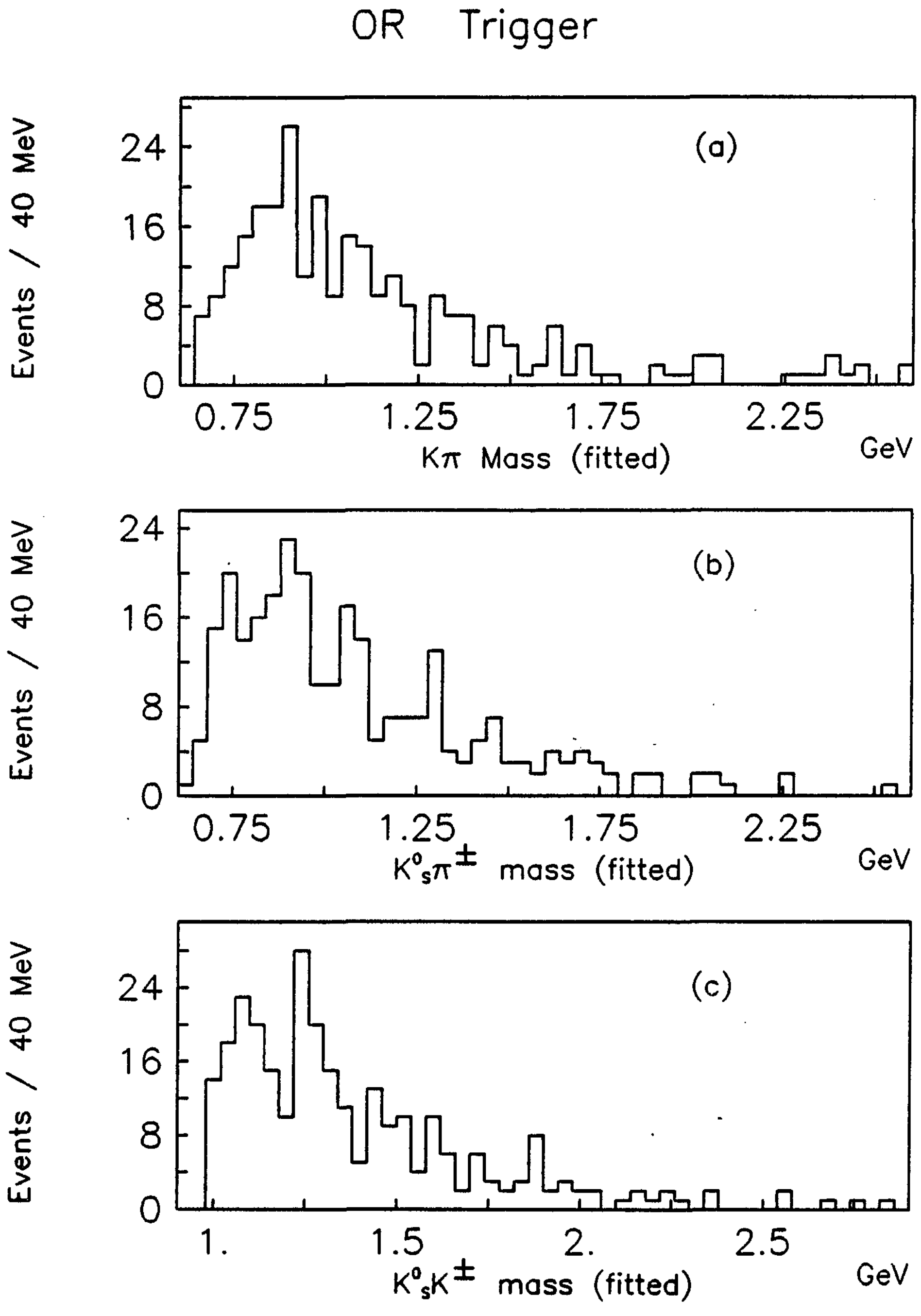

Figure 4.34 **Invariant Mass distributions after excluding the $K^0_sK^0_s$ events for the (a) $K^\pm\pi^\mp$, (b) $K^0_s\pi^\pm$, and (c) $K^0_sK^\pm$ particle pairs**

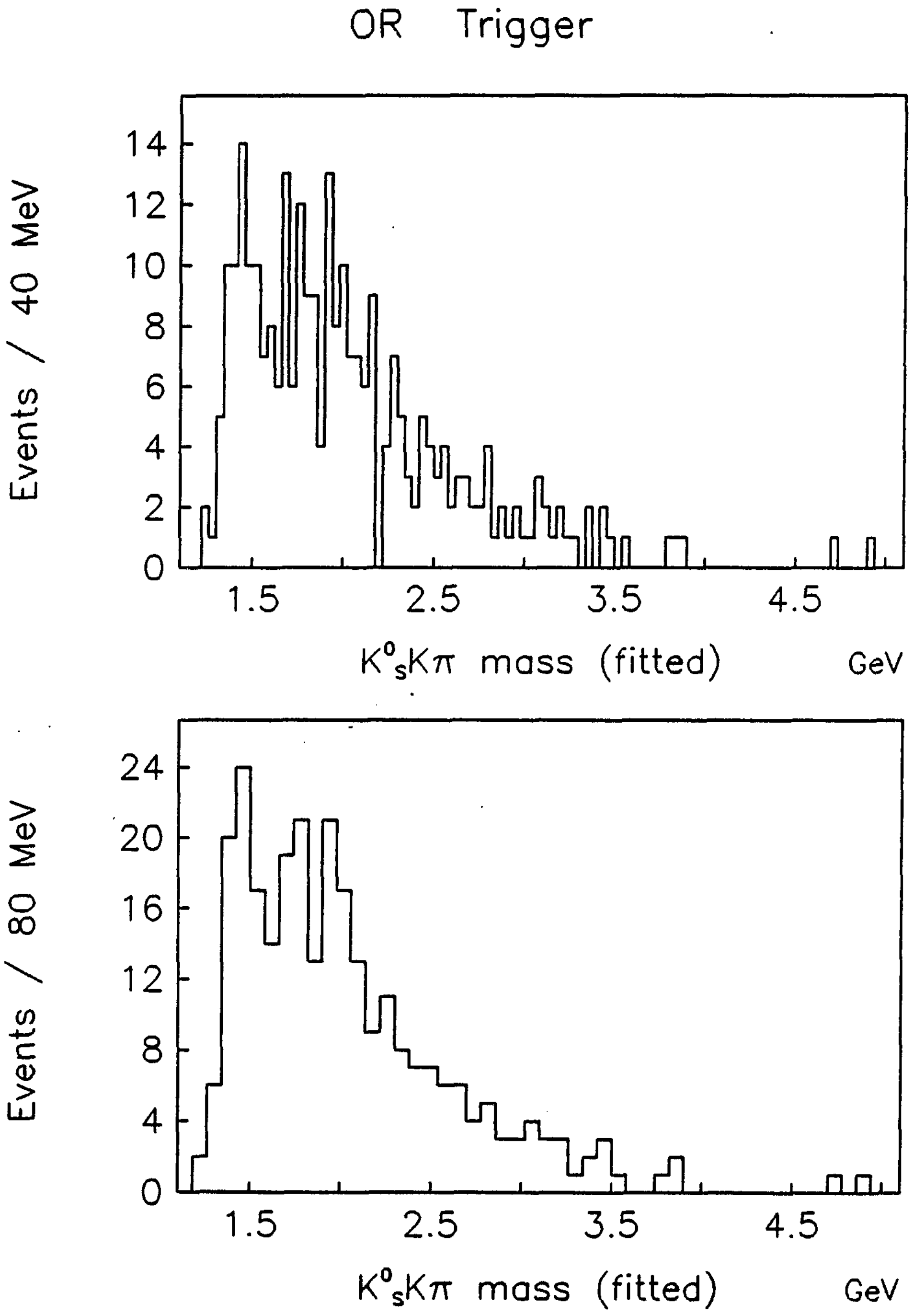

Figure 4.35 Invariant mass of the $K^0_s K^\pm \pi^\mp$ central system with 40 MeV bin sizes (top) and with 80 MeV bin sizes (bottom)

Further study of these events compared with the $K_s^0K_s^0$ central system events, shows that a large portion of the $K_s^0K_s^0$ events also pass the 4-C fit in this $K_s^0K^{\pm}\pi^{\mp}$ system. Therefore, these events were removed from the distributions and Figures 4.34(a-c) show the resulting mass distributions. In the $K^{\pm}\pi^{\mp}$ mass distribution, the peak at 825 MeV disappears, while most of the events that were at 875-900 MeV remain. The $K_s^0\pi^{\pm}$ mass distribution also retains the peak at the charged K^* mass while the 775 MeV mass peak becomes smaller. The $K_s^0K^{\pm}$ mass distribution shows the same shape as previously, with the 1250 MeV peak even more pronounced. Since it is possible to have a three body decay into $K_s^0K^{\pm}\pi^{\mp}$, this $K_s^0K^{\pm}\pi^{\mp}$ central system mass distribution is shown in Figure 4.35 for 40 MeV and 80 MeV bin sizes. There is the possibility of an enhancement at 1450 MeV, but it is not significant enough at this stage to claim a resonance state. The enhancement brings to mind $\gamma\gamma$ interactions in e^+e^- experiments [CELLO Collaboration 1989, Baglin et al. 1987, Mark II Collaboration 1986]. The $f_1(1420), J^{PC} = 1^{++}$, has been seen to decay to $K_s^0K^{\pm}\pi^{\mp}$ (i.e., K^*K) via $\gamma\gamma$ interactions. However, in this experiment, only even spin states may be produced for the entire central system (see Chapter 1). Thus, any resonant state at this mass would have to be a different particle. The possibility of the $\eta(1440)$ being produced exists, but it has been identified as a negative parity particle [Particle Data Group 1988] whereas DPE states must have positive parity.

In an attempt to estimate the background in these plots, the events containing TOF information for the charged kaon particles were studied. The event samples before and after the 4-C fit, but prior to the requirement of TOF mass consistency were analyzed. The ratio of identified K's to π's was calculated. The results show that prior to the 4-C fit, the K/π ratio is 85/787, or 0.11. After the 4-C fit and prior to the TOF consistency check, the K/π ratio is 15/80, or 0.19. Thus, the background after the fit decreases, but remains high (80%).

The consistency check for the K using the TOF data effectively removes the mass combinations with misidentified K's, but it does not necessarily show whether the other combination is correct. The removal of the $K_s^0 K_s^0$ events helps to reduce the background in this case. This additional cut of the $K_s^0 K_s^0$ events leaves a total of 186 events, with 95 of these events containing both mass combinations. Therefore, the background at this stage of the analysis is estimated to be 70% for the events and about 30% of the background is attributable to combinatorials.

In an attempt to enhance any possible K^* signals, a plot of the invariant $K^{\pm}\pi^{\mp}$ mass versus the $K_s^0\pi^{\pm}$ is shown in Figure 4.36. The bands are centered around the neutral K^* (892 MeV) and charged K^* (896 MeV) masses. The K^* has a width of 50 MeV and the study of the $K_s^0 K_s^0$ system in Section 4.1 gives a mass resolution of about 30 MeV. Therefore, the widths of the bands were taken to be 160 MeV. A considerable fraction of the events are within these bands (shown as solid circles in Figure 4.36) and these events are candidates for K^*K events. The invariant $K_s^0 K^{\pm}\pi^{\mp}$ mass distribution is shown for events that are inside the bands in Figure 4.37(a). The enhancement at 1450 MeV remains, and is more pronounced than in Figure 4.35. There is the possibility of some sort of threshold effect occuring rather than a genuine resonance. As a check on the 4-C fit probability, the events were subjected to a higher cut of 0.20 to see the effect on the distribution. This is shown in Figure 4.37(b). The peak at 1450 MeV becomes more significant, and therefore, it is possible that something is happening at this mass region. However, since the statistics are low and the background is known to be high, it is hard to draw a conclusion.

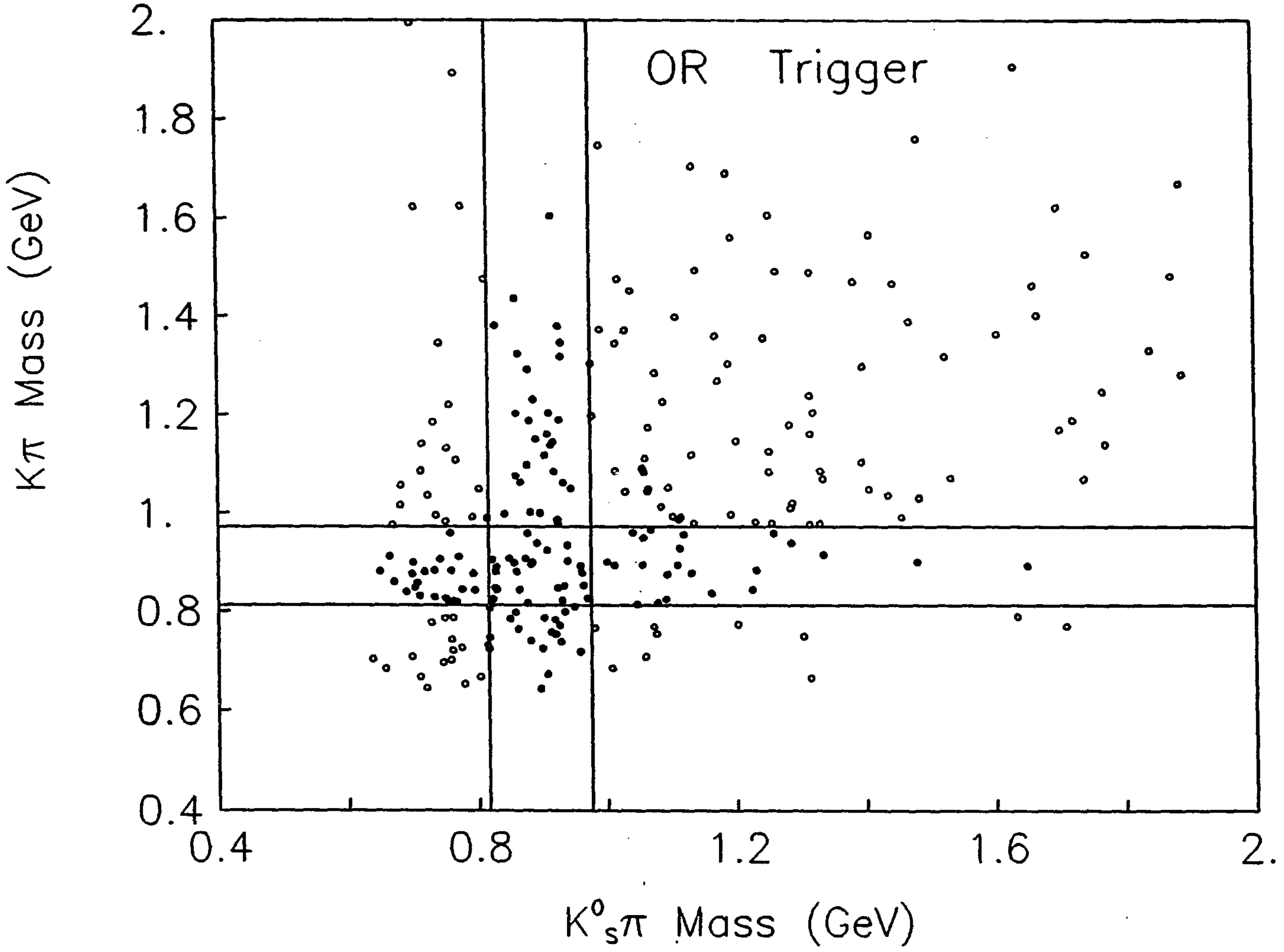

Figure 4.36 Invariant $K^{\pm}\pi^{\mp}$ mass versus $K^0_s\pi^{\pm}$ mass

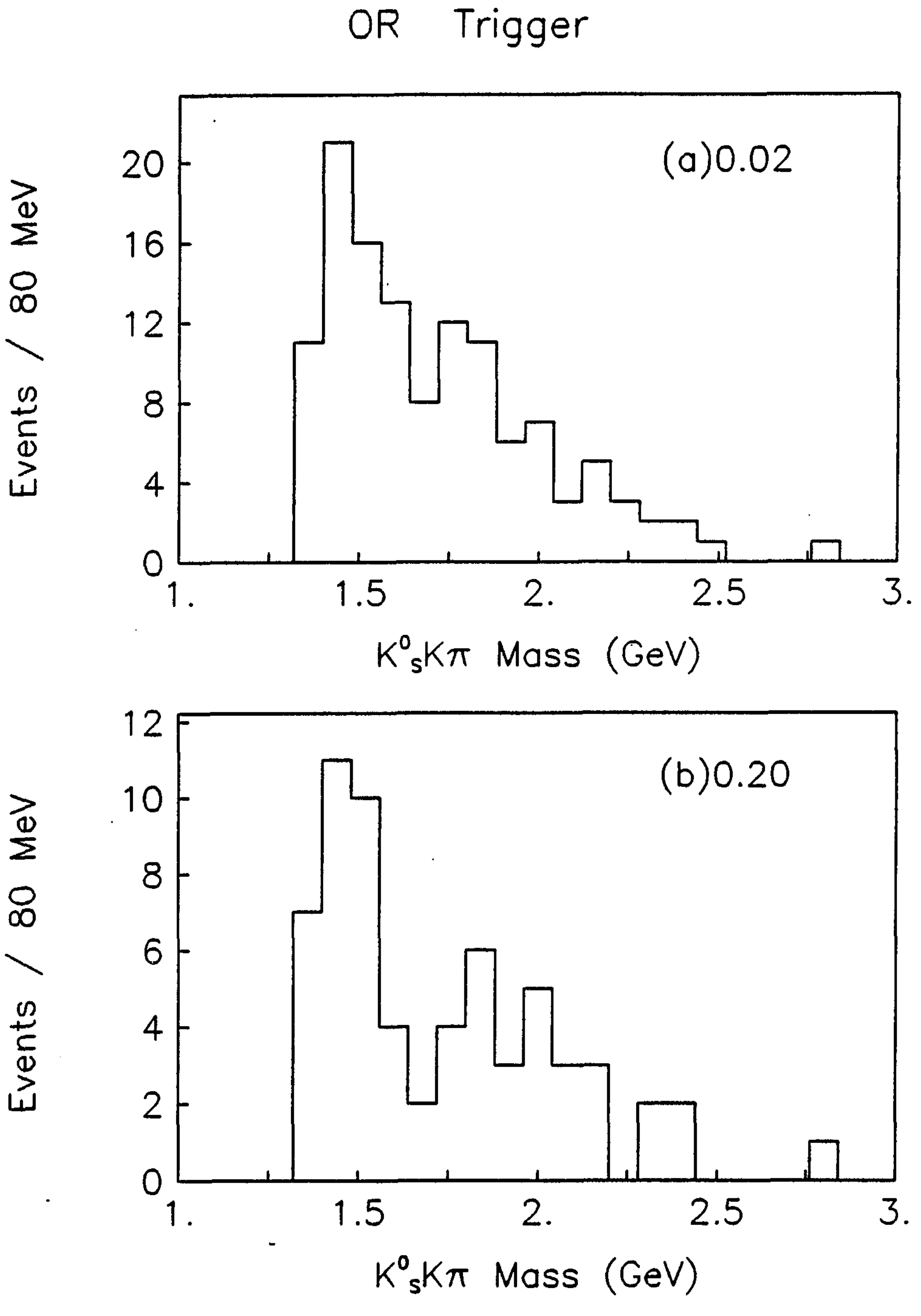

Figure 4.37 $K_s^0 K^\pm \pi^\mp$ mass distribution for events within the K^* mass range and satisfying probability of fit (a) greater than 0.02 and (b) greater than 0.20

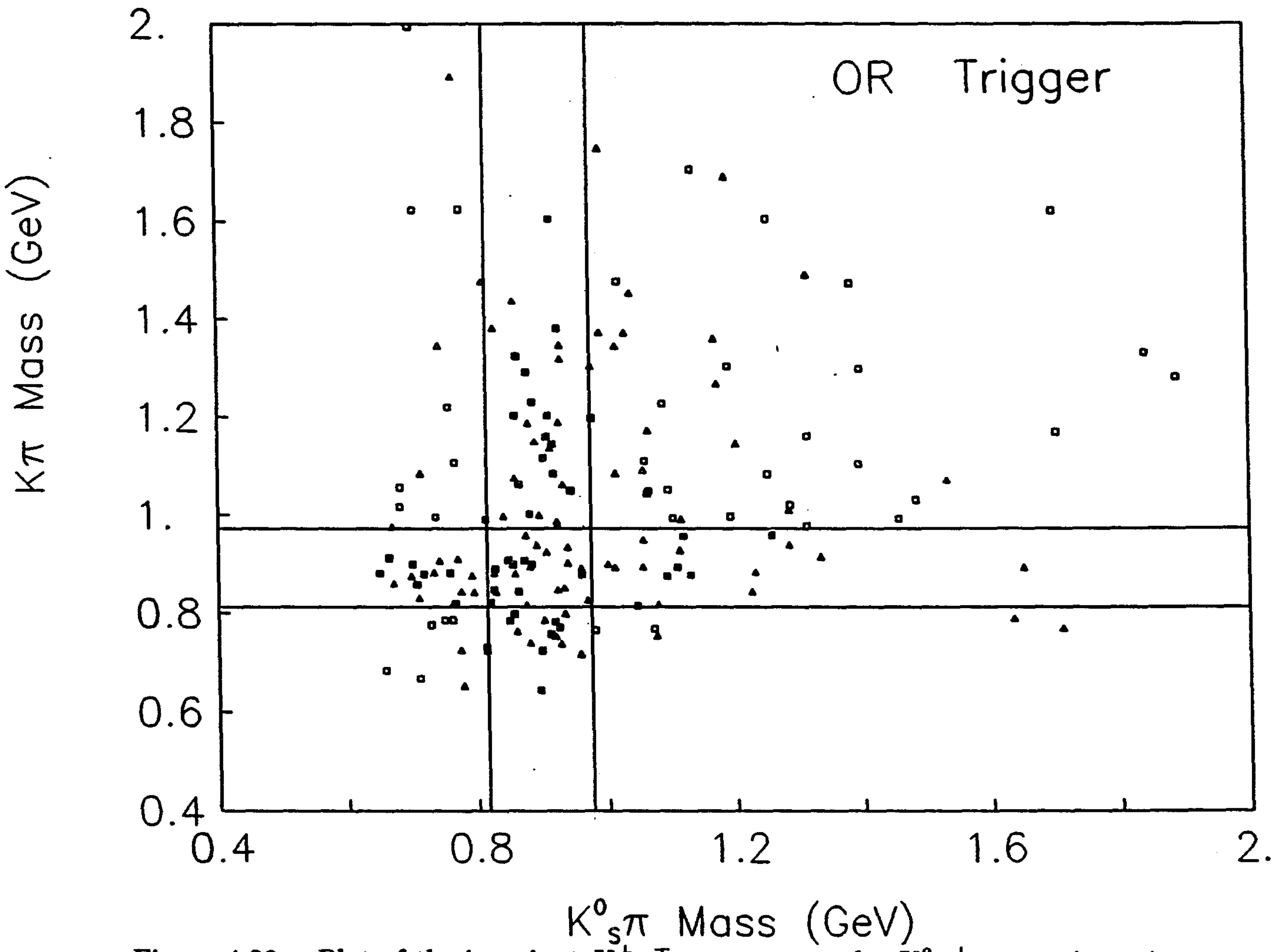

Figure 4.38 Plot of the invariant $K^{\pm}\pi^{\mp}$ mass versus the $K_s^0\pi^{\pm}$ mass after selecting only the best K^* mass combination; triangles represent events that previously had two combinatorial fits and squares represent events which were only fitted successfully for one mass combination

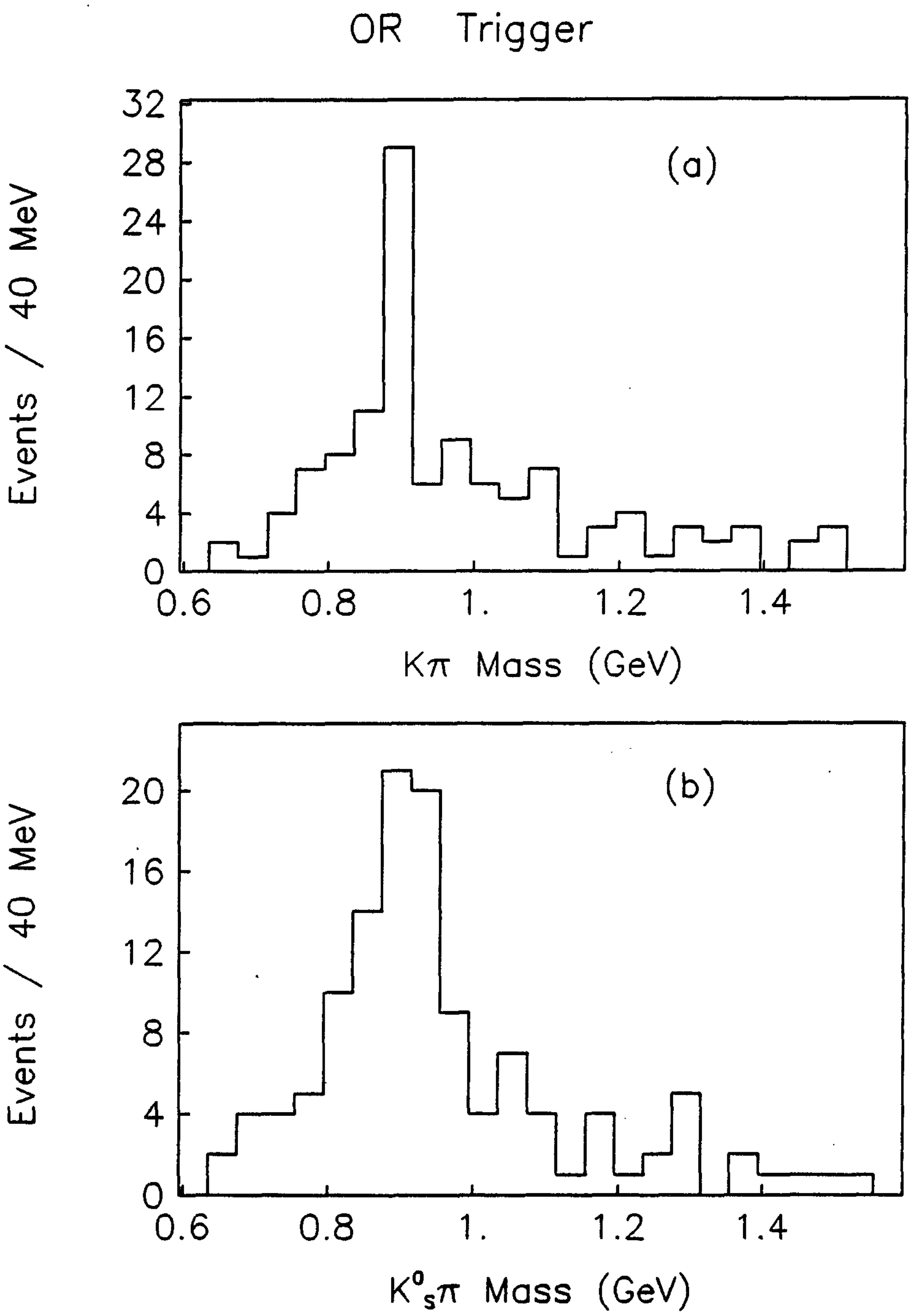

Figure 4.39 Projection of events in Figure 4.38 onto the $K^{\pm}\pi^{\mp}$ mass axis with (a) events in the $K_s^0\pi^{\pm}$ band excluded and (b) events in the $K^{\pm}\pi^{\mp}$ band excluded

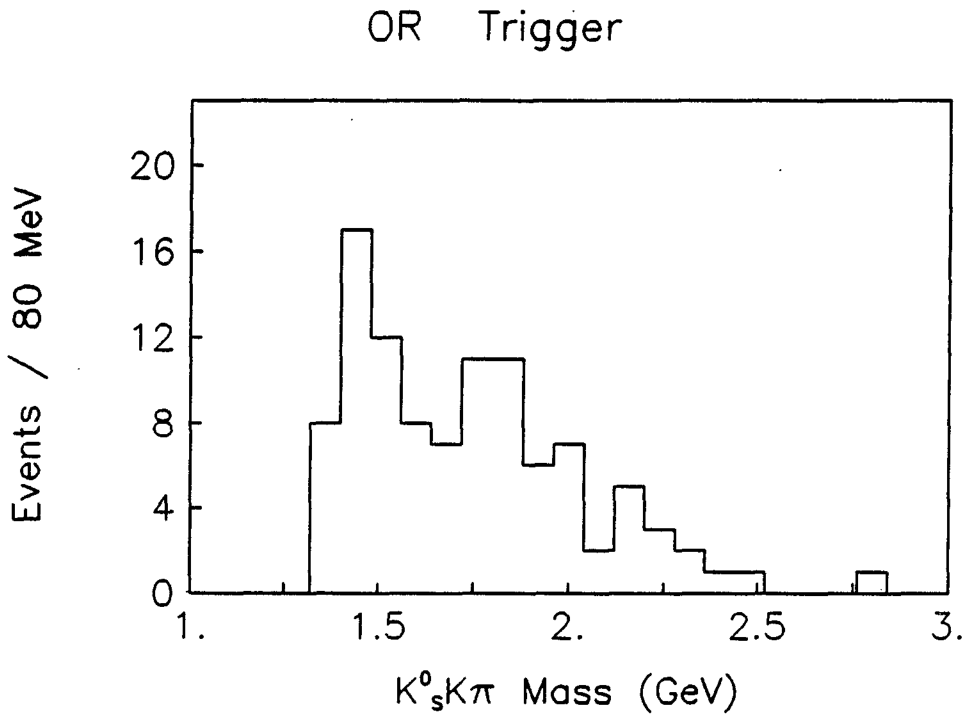

Figure 4.40 $K^0_s K^\pm \pi^\mp$ mass distribution using the best K^* mass combination

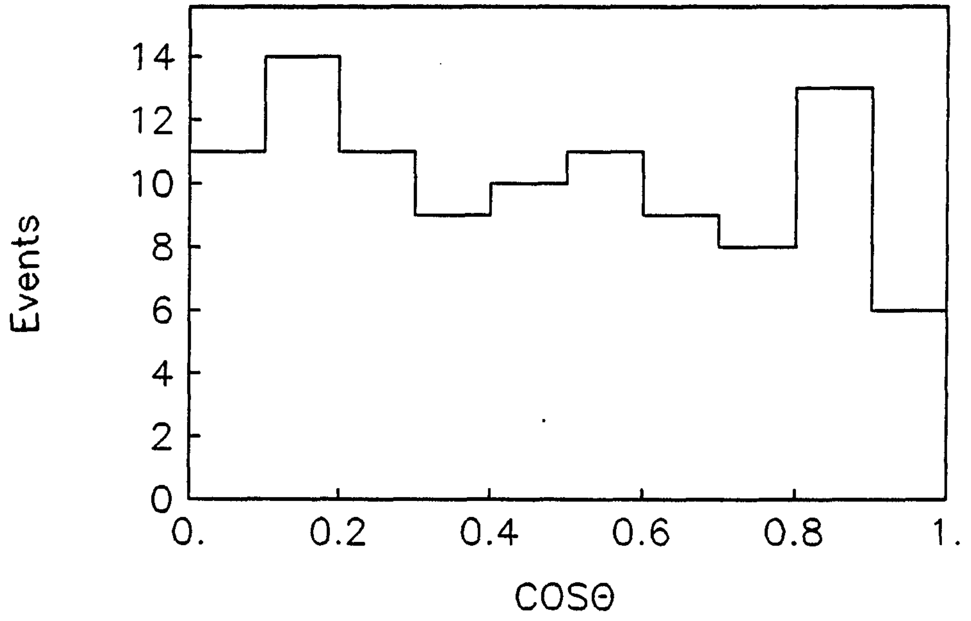

Figure 4.41 $cos(\theta)$ distribution of the angle between the best K^* mass combination and one of the Pomerons in the Pomeron-Pomeron rest frame

In an effort to reduce the combinatorial background further, only the best K^* candidate will be considered for events with two successful fits. Effectively, this is accomplished by calculating the invariant masses of the $K^{\pm}\pi^{\mp}$ and $K_s^0\pi^{\pm}$ combinations and selecting the combination which has a mass closest to the K^*. A scatter plot of the invariant $K^{\pm}\pi^{\mp}$ mass versus the $K_s^0\pi^{\pm}$ mass is shown in Figure 4.38 after making this selection. The triangles represent events with the best mass combination. A projection of these events onto the $K^{\pm}\pi^{\mp}$ axis with the exclusion of the events in the $K_s^0\pi^{\pm}$ band, is shown in Figure 4.39(a). The alternate projection of the events onto the $K_s^0\pi^{\pm}$ axis is shown in Figure 4.39(b) with events in the $K^{\pm}\pi^{\mp}$ band excluded. Both projections reveal an enhancement near the true K^* masses. However, one must keep in mind that the data have now been biased towards these masses by excluding the other combinatorial from the plots. The invariant $K_s^0K^{\pm}\pi^{\mp}$ distribution is shown in Figure 4.40. The distribution remains roughly the same. The $cos(\theta)$ distribution is shown in Figure 4.41 of the angle between the best K^* candidate and one of the Pomerons in the Pomeron-Pomeron rest frame. This distribution is relatively flat, showing no preferred spin direction.

4.2.2 AND trigger data

The method of treatment used in the AND trigger data is similar to that used in the OR trigger data. A total of 1236 events were fitted and of these, 177 events were fitted successfully by the 4-C fit routine for at least one mass combination. Of the 177 events, 69 were fitted successfully with both charged $K^{\pm}\pi^{\mp}$ mass combinations.

As in the OR data, some of these events were $K_s^0K_s^0$ events that also passed the 4-C fit in this $K_s^0K^{\pm}\pi^{\mp}$ system. Therefore, these events were removed from the sample. This additional cut of the $K_s^0K_s^0$ events leaves a total of 132 events with 50 of these events containing both mass combinations. Figure 4.42(a) shows the $K^{\pm}\pi^{\mp}$ mass distribution for the events after the removal of the $K_s^0K_s^0$ events. There is a very slight concentration of events near the K^* mass. Figure 4.42(b) shows the $K_s^0\pi^{\pm}$ mass distribution which also shows some evidence for a K^* signal. Figure 4.42(c) shows the $K_s^0K^{\pm}$ mass distribution and there is a broad enhancement at 1250 MeV. The $K_s^0K^{\pm}\pi^{\mp}$ mass distribution is shown in Figure 4.43 for 40 MeV and 80 MeV bin sizes. Unlike the OR trigger data, there is no enhancement at the 1450 MeV mass region.

The background in these plots has been estimated using the same method as in the OR trigger data. Prior to the 4-C fit, the K/π ratio is 90/874, or 0.10. After the 4-C fit and prior to the TOF consistency check, the K/π ratio is 17/91, or 0.19. Thus, the background after the fit decreases, but remains high (80%). The background after the TOF consistency check, and removal of the $K_s^0K_s^0$ events is estimated to be 70% with about 30% attributable to combinatorial background.

The equivalent plot to Figure 4.36 is shown in Figure 4.44 for the AND trigger data. The square symbols represent events that were only fitted successfully for one mass combination. The triangles represent the best mass combination consistent with a K^* for events that were fitted for both mass combinations, and the circles represent the worst mass combination. Unlike the OR trigger data there does not appear to be a significant concentration of events within these bands. A projection of these events onto the $K^{\pm}\pi^{\mp}$ axis with the exclusion of the $K_s^0\pi^{\pm}$ band, is shown in Figure 4.45(a). The alternate projection of the events onto the $K_s^0\pi^{\pm}$ axis is shown in Figure 4.45(b) with the $K^{\pm}\pi^{\mp}$ band excluded. Both projections show slight enhancements near the K^* mass, but the background is high. The

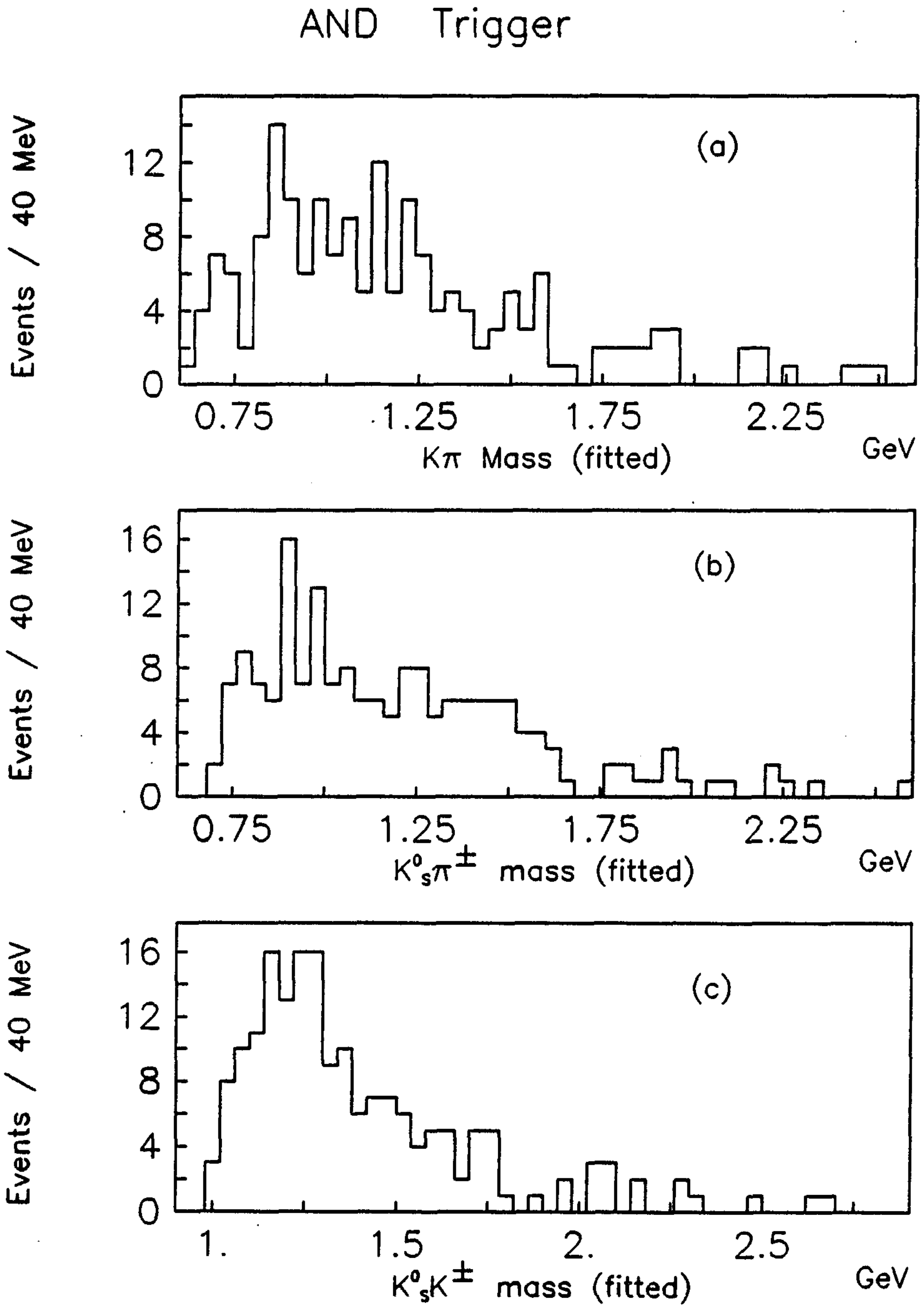

Figure 4.42 Invariant Mass distributions after excluding the $K_s^0 K_s^0$ events for the (a) $K^{\pm}\pi^{\mp}$, (b) $K_s^0\pi^{\pm}$, and (c) $K_s^0 K^{\pm}$ particle pairs

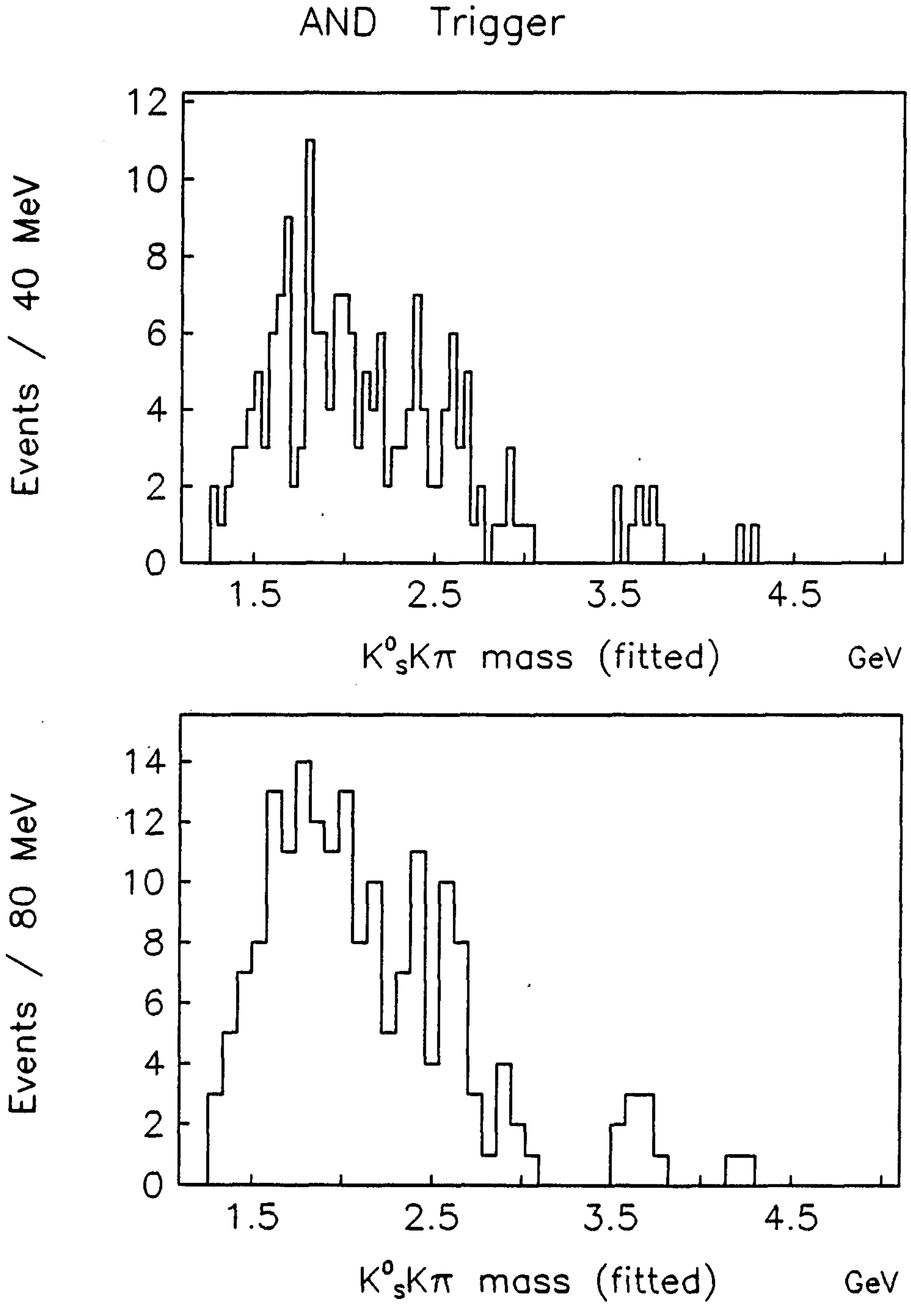

Figure 4.43 Invariant mass of the $K^0_s K^{\pm} \pi^{\mp}$ central system with 40 MeV bin sizes (top) and with 80 MeV bin sizes (bottom)

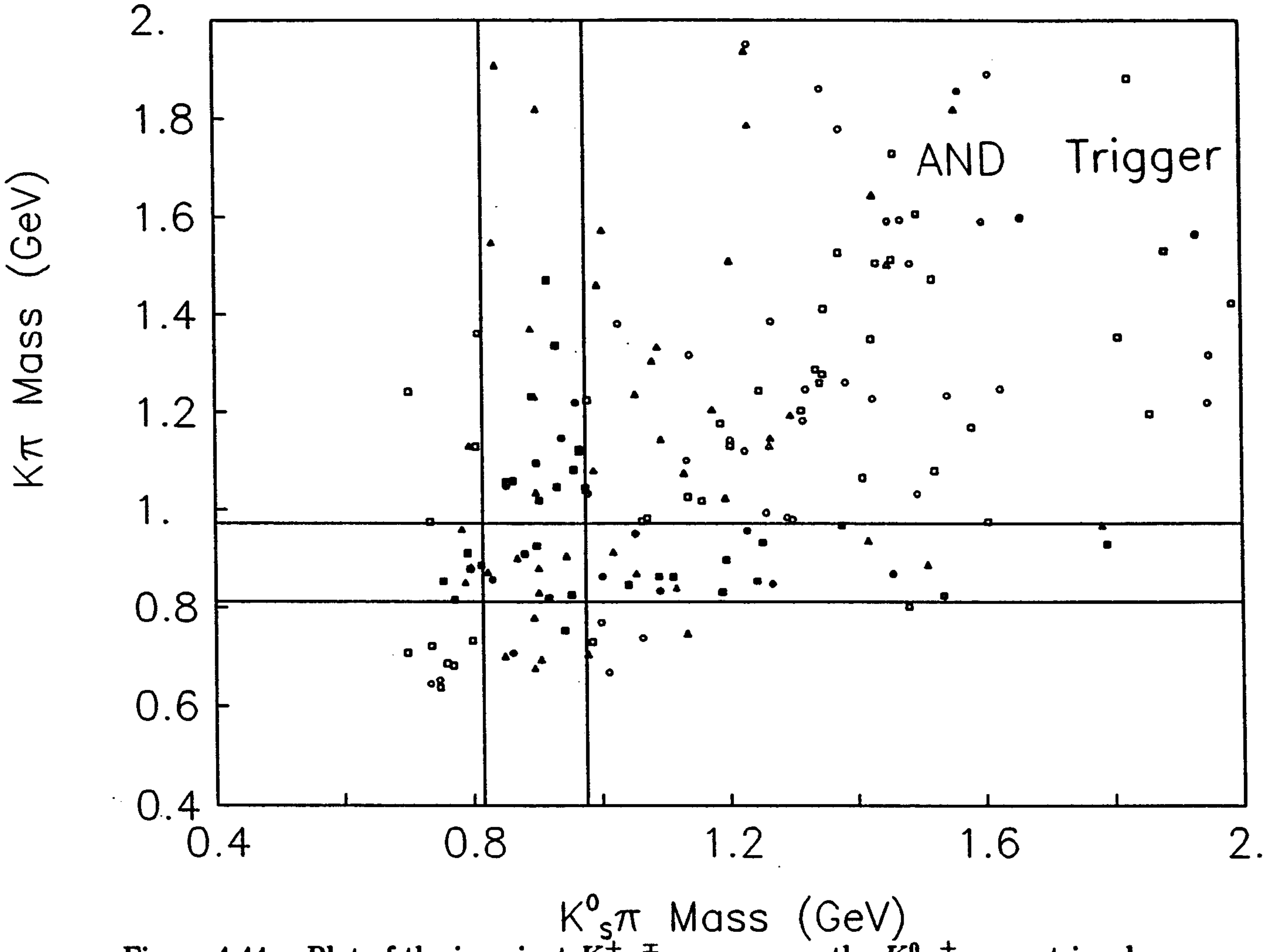

Figure 4.44 Plot of the invariant $K^{\pm}\pi^{\mp}$ mass versus the $K_s^0\pi^{\pm}$ mass; triangles represent the best K^* mass combination and circles the worst for events that had two combinatorial fits, and squares represent events which were fitted successfully for only one mass combination

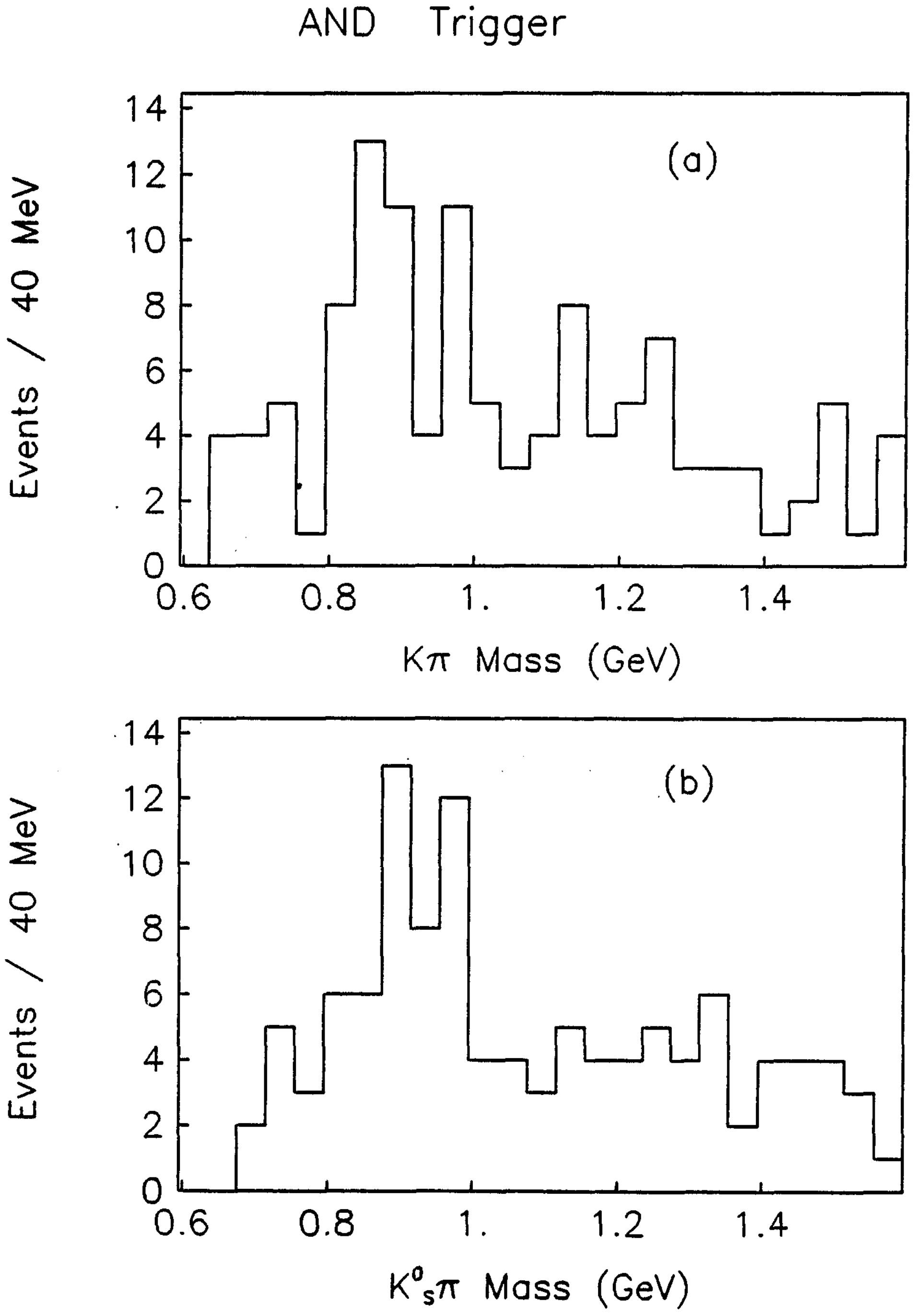

Figure 4.45 Projection of events in Figure 4.44 onto the $K^{\pm}\pi^{\mp}$ mass axis with (a) events in the $K_s^0\pi^{\pm}$ band excluded and (b) events in the $K^{\pm}\pi^{\mp}$ band excluded

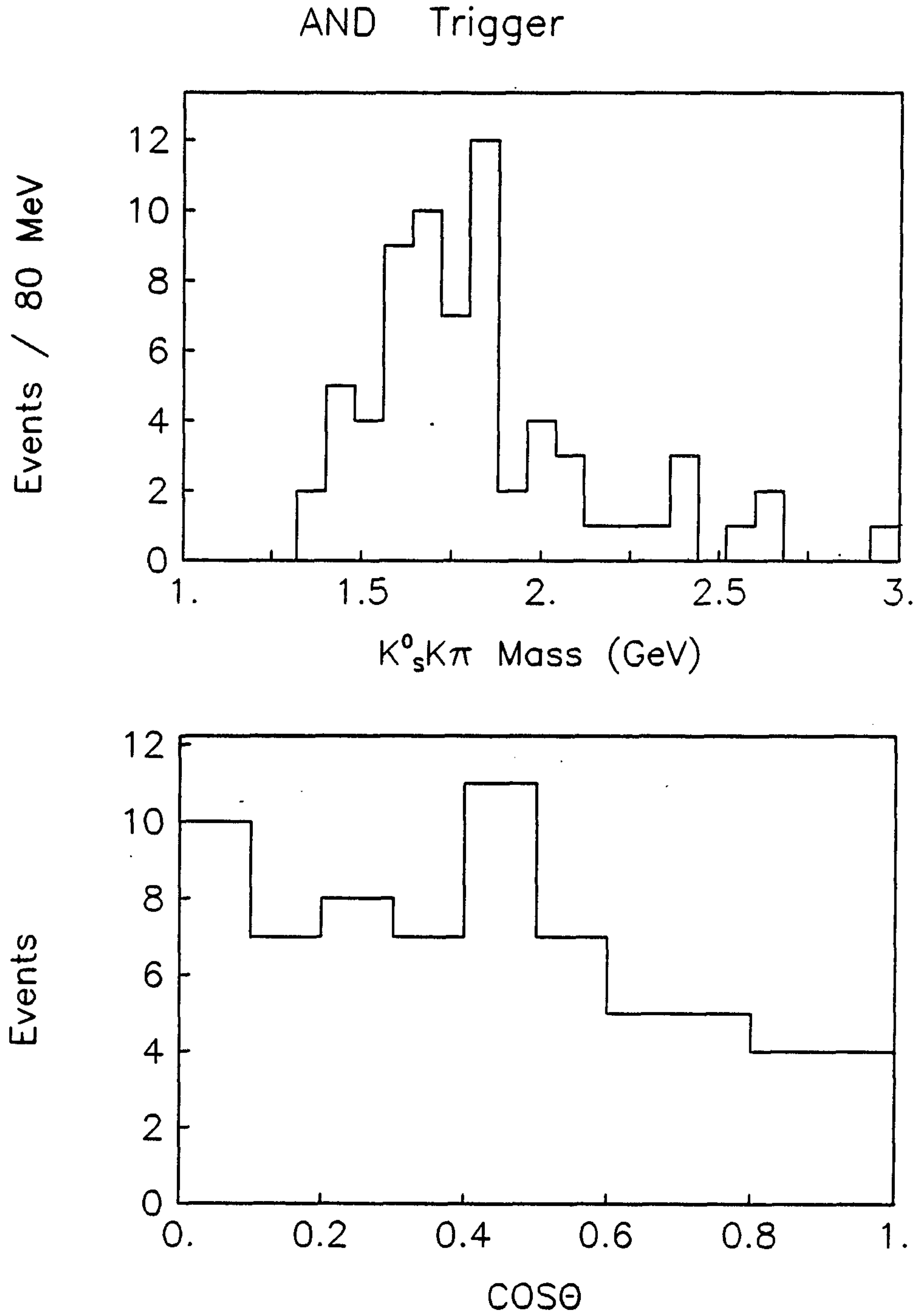

Figure 4.46 Invariant $K^0_sK^{\pm}\pi^{\mp}$ mass distribution for events within the K^* mass range (top) and $cos(\theta)$ distribution of the angle between the K^* and one of the Pomerons (bottom)

equivalent distributions to Figures 4.40 and 4.41 are shown in Figure 4.46. No significant structure is seen.

4.2.3 TOF trigger data

A total of 111 events were fitted successfully by the 4-C fit routine for at least one mass combination. Of the 111 events, 54 were fitted successfully with both charged $K^{\pm}\pi^{\mp}$ mass combinations. As in the OR and AND data, some of these events were $K_s^0 K_s^0$ events that also passed the 4-C fit in this $K_s^0 K^{\pm}\pi^{\mp}$ system. Therefore, these events were removed from the sample. Figures 4.47(a-c) and 4.48(a-c) show the invariant mass distributions for the three possible mass combinations both before and after removing the $K_s^0 K_s^0$ events. The low mass enhancements in the $K^{\pm}\pi^{\mp}$ and $K_s^0\pi^{\pm}$ distributions of Figure 4.47 disappear after removal and there are enhancements near the K^* masses in Figure 4.48. However, the statistics are low. The $K_s^0 K^{\pm}\pi^{\mp}$ mass distributions are shown in Figure 4.49 for 40 MeV and 80 MeV bin sizes. Aside from lower statistics, they are similar to the OR data.

The background in these plots has been estimated using the same method as in the OR and AND trigger. Prior to the 4-C fit, the K/π ratio is 158/490, or 0.32. After the 4-C fit and prior to the TOF consistency check, the K/π ratio is 26/34, or 0.77. The background after the TOF consistency check, and removal of the $K_s^0 K_s^0$ events is estimated to be 40% with about 30% attributable to combinatorial background. Thus, the background is significantly lower for the TOF data. This is expected because the TOF trigger was designed to enhance kaons and protons produced in the central region. A plot equivalent to Figure 4.44, of the $K^{\pm}\pi^{\mp}$ mass versus the $K_s^0\pi^{\pm}$ mass, is shown in Figure 4.50. There is a concentration of

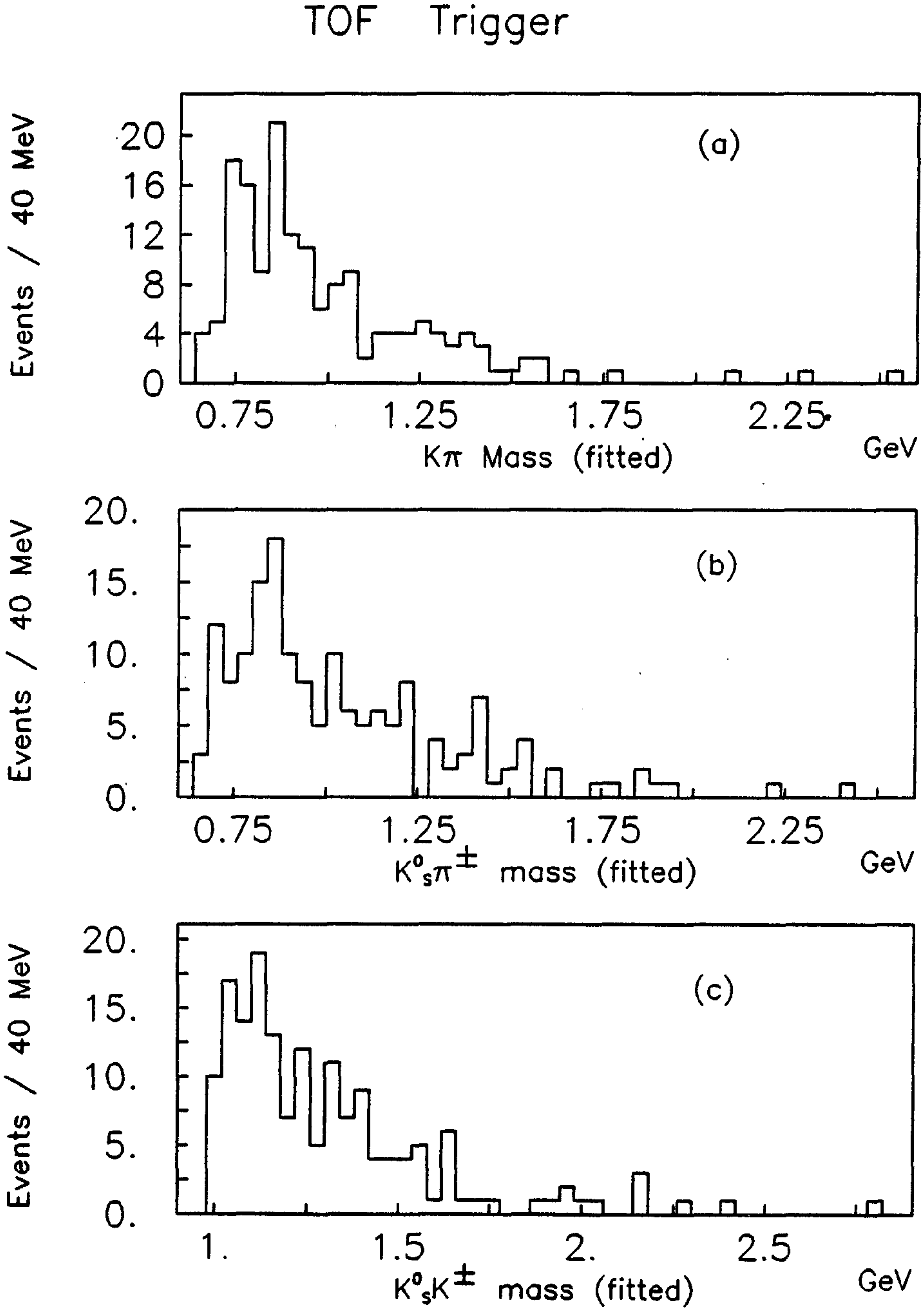

Figure 4.47 Invariant Mass distributions before excluding the $K_s^0 K_s^0$ events for the (a) $K^{\pm}\pi^{\mp}$, (b) $K_s^0\pi^{\pm}$, and (c) $K_s^0 K^{\pm}$ particle pairs

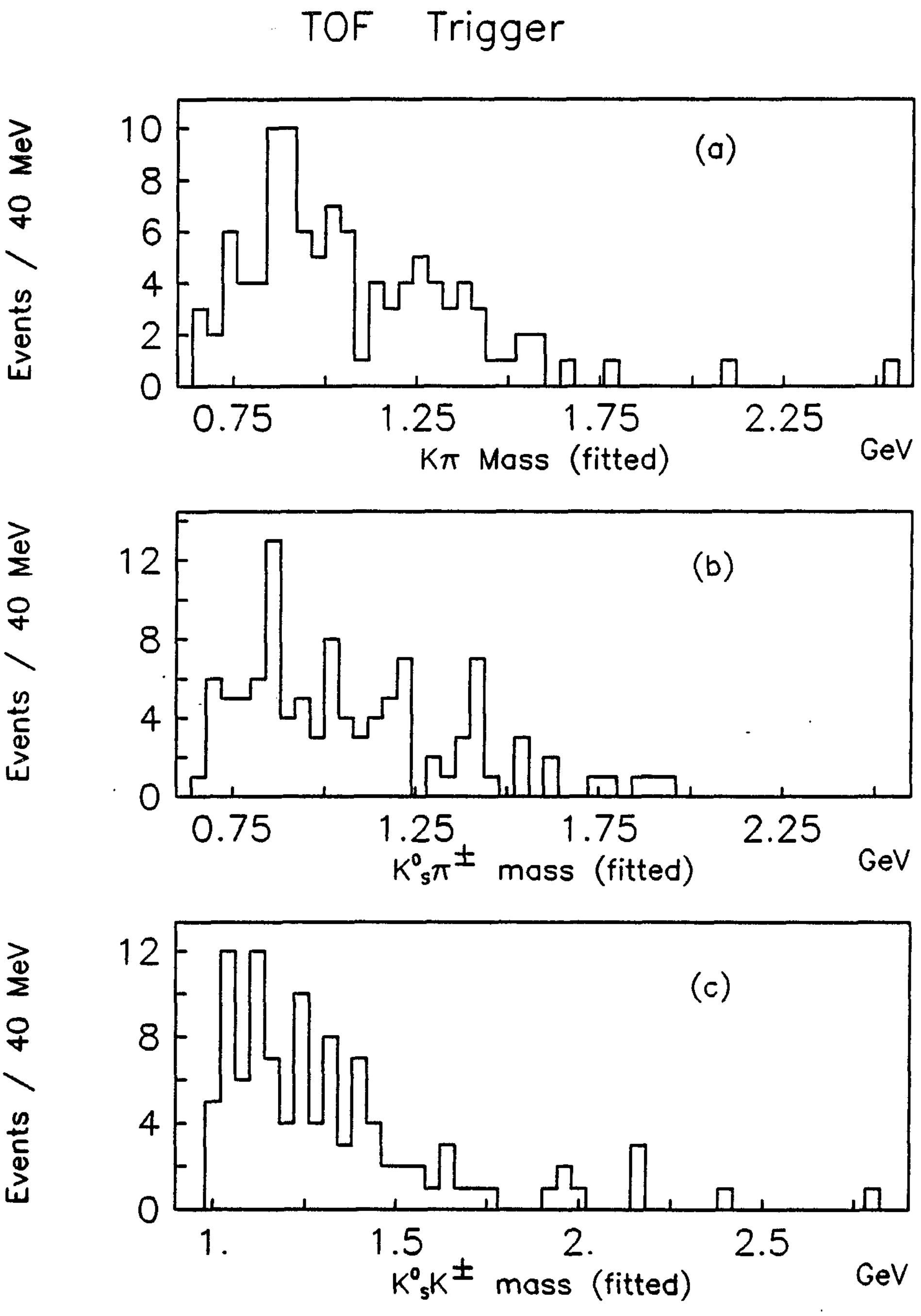

Figure 4.48 Invariant Mass distributions after excluding the $K_s^0 K_s^0$ events for the (a) $K^{\pm}\pi^{\mp}$, (b) $K_s^0\pi^{\pm}$, and (c) $K_s^0 K^{\pm}$ particle pairs

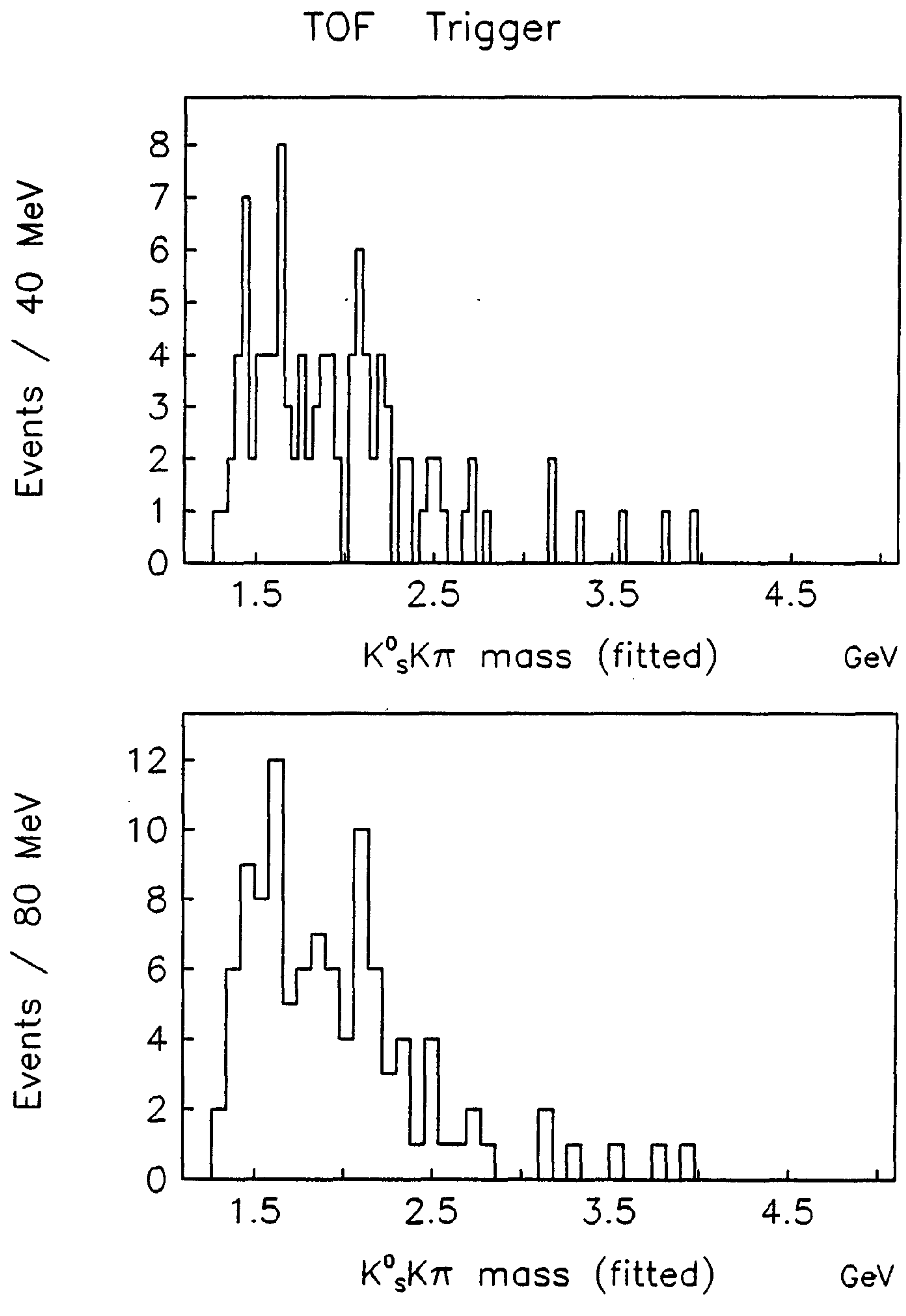

Figure 4.49 Invariant mass of the $K^0_s K^{\pm}\pi^{\mp}$ central system with 40 MeV bin sizes (top) and with 80 MeV bin sizes (bottom)

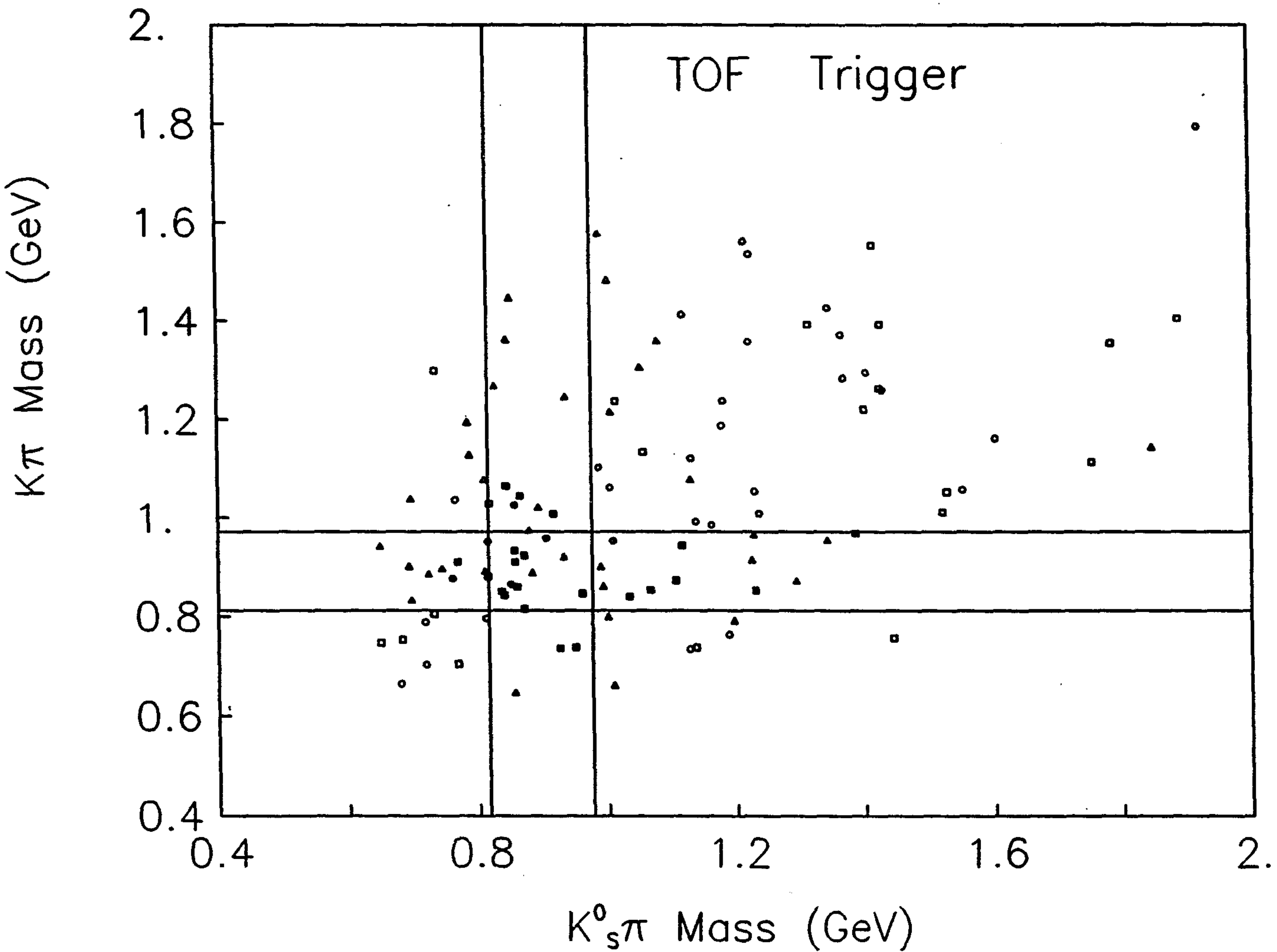

Figure 4.50 Plot of the invariant $K^{\pm}\pi^{\mp}$ mass versus the $K_s^0\pi^{\pm}$ mass; triangles represent the best K^* mass combination and circles the worst for events that had two combinatorial fits, and squares represent events which were fitted successfully for only one mass combination

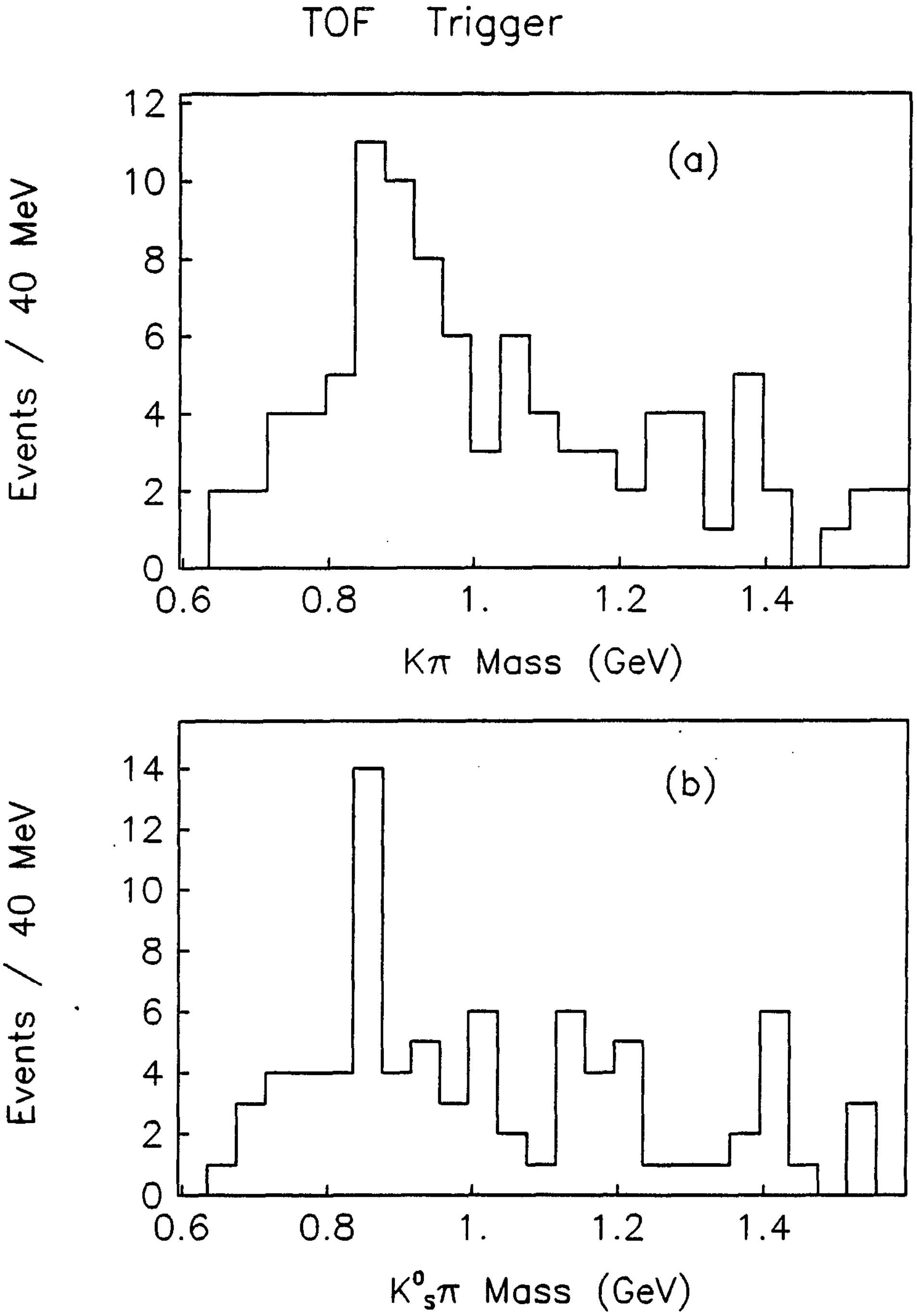

Figure 4.51 **Projection of events in Figure 4.50 onto the $K^{\pm}\pi^{\mp}$ mass axis with (a) events in the $K^0_s\pi^{\pm}$ band excluded and (b) events in the $K^{\pm}\pi^{\mp}$ band excluded**

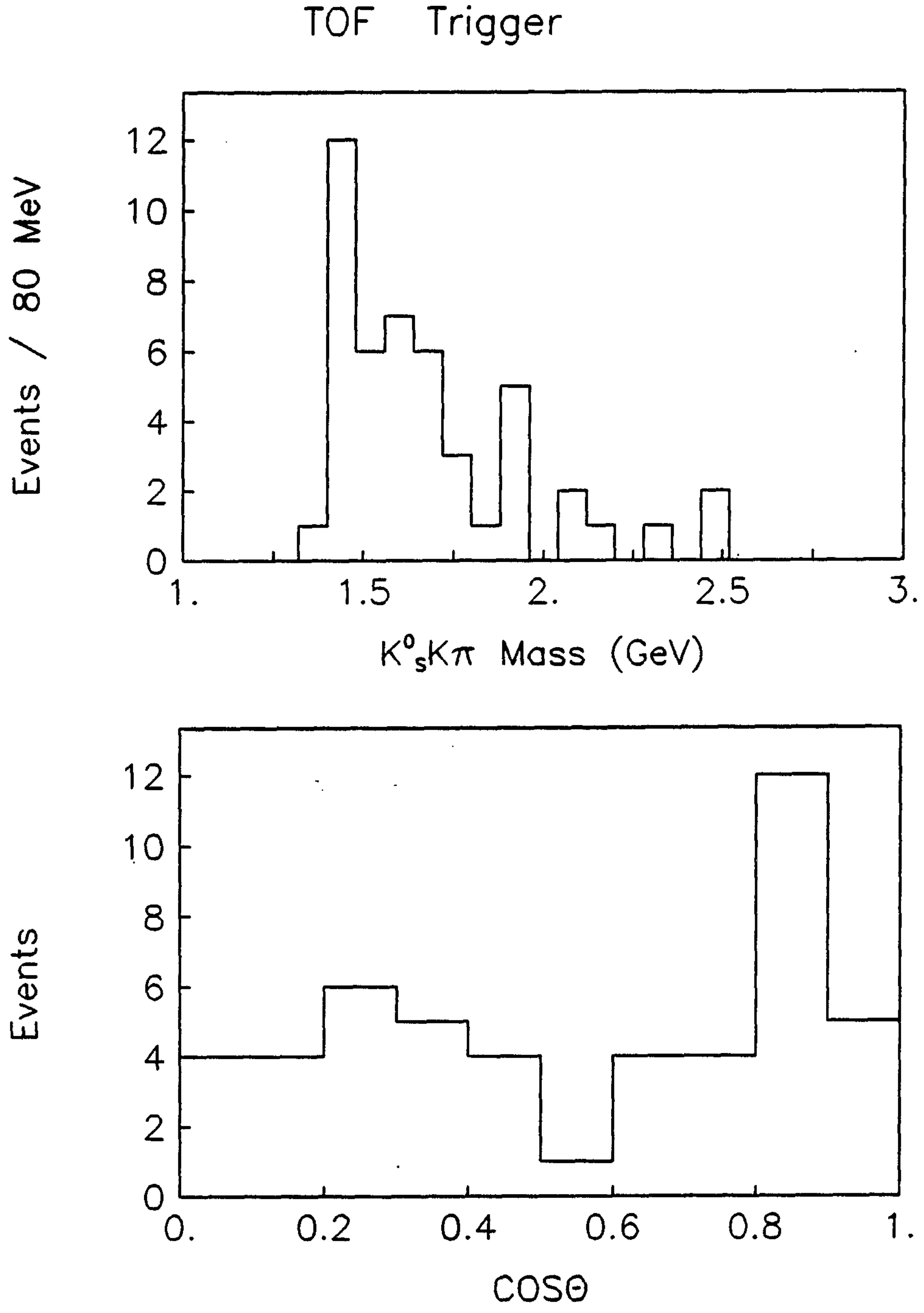

Figure 4.52 $K^0_s K^{\pm}\pi^{\mp}$ mass for events within the K^* mass range (top), and $cos(\theta)$ distribution of the angle between the K^* and one of the Pomerons (bottom)

events in the K^* bands. A projection of these events onto the $K^{\pm}\pi^{\mp}$ axis with the exclusion of the $K^0_s\pi^{\pm}$ band, is shown in Figure 4.51(a). The alternate projection of the events onto the $K^0_s\pi^{\pm}$ axis is shown in Figure 4.51(b) with the $K^{\pm}\pi^{\mp}$ band excluded. Both projections show enhancements near the K^* mass, but the $K^0_s\pi^{\pm}$ projection shows all the events in one bin slightly below the K^* mass at about 860 Mev. The equivalent distributions to the Figures 4.40 and 4.41 are shown in Figure 4.52. The mass distribution is similar to the OR data except the low mass enhancement is only one bin wide. It is consistent with a kinematic threshold effect.

4.3 Summary of the $\mathbf{K^0_sK^0_s}$ and $\mathbf{K^0_sK^{\pm}\pi^{\mp}}$ Systems

In the $K^0_sK^0_s$ system, all three data sets feature a good sample of $K^0_sK^0_s$ events. The OR and TOF trigger data indicate an enhancement near 1200 MeV in the $K^0_sK^0_s$ mass distribution. The AND trigger data do not exhibit this enhancement, but it could be due to trigger acceptance problems in this mass region. The cosine theta distributions, where theta is the angle between a K^0_s particle and one of the Pomerons, indicate a predominantly s-wave spin state for the three data sets with a falloff in statistics at large values of cosine theta. As mentioned in Section 4.1.5, this reduction of statistics is likely due to acceptance of the trigger. Estimates of the DPE cross sections for this $K^0_sK^0_s$ system will be made upon calculation of geometrical and trigger acceptance in Chapter 6.

In the $K^0_sK^{\pm}\pi^{\mp}$ system, the data seem to indicate poor rejection of events not consistent with the $K^0_sK^{\pm}\pi^{\mp}$ mass hypothesis. This makes subsequent analysis subject to justifiable criticism, however, the K^* studies indicate some evidence for the $K^0_sK^{\pm}\pi^{\mp}$ events being produced via KK^* . Complete understanding of this

system appears unlikely due to low statistics and high background in the data samples. Thus, only rough estimates of the cross sections appear feasible upon calculation of detector acceptance. This will be considered in Chapter 6.

5 EXCLUSIVE INTERACTIONS INVOLVING AT LEAST ONE $\Lambda^0/\bar{\Lambda}^0$ PARTICLE

5.1 $\Lambda^0\bar{\Lambda}^0$ Central System

All of the 6-prong events containing at least one identified Λ^0 or $\bar{\Lambda}^0$ particle given from the V^0 program were further processed using the 4-C fit routine discussed in Section 3.5. Only the best $\Lambda^0/\bar{\Lambda}^0$ fit was used from the V^0 program (i.e., lowest χ^2 value) in the event processing. The masses of the particles for the reaction 3.7 were assigned as discussed in Section 3.4 and are listed in Table 5.1 for the case of a Λ^0 or a $\bar{\Lambda}^0$ shown in parenthesis. Due to low statistics the two cases were combined in the analysis. These masses (for the charged particles) were required to be consistent with any available time of flight information on the DST for each event. The momenta and angles as described in Section 3.5 for each of the

Table 5.1 Summary of particles whose four momenta are input to the 4-C fit in the $\Lambda^0\bar{\Lambda}^0$ central system hypothesis

Particle(s)	Mass (MeV)	Description
p, p	938.2796	Two ingoing beam protons
$\pi^-(\pi^+)$	139.5685	one central pion
$p(\bar{p})$	938.2796	one central proton
Λ^0 ($\bar{\Lambda}^0$)	1115.63	One V^0 Central particle
p, p	938.2796	Two fast outgoing protons

particles were input to the 4-C fit routine. The probability of fit distributions for each of the three data sets are shown in Figure 5.1. A probability cut of .02 was used in subsequent analysis of the data.

5.1.1 OR trigger data

In the OR trigger data, a total of 1116 events were fitted, and of these, 134 events passed the criterion for the probability of fit. Figure 5.2(a) shows the distribution in $cos(\theta)$ of the angle between the $\Lambda^0/\bar{\Lambda}^0$ and its positive decay particle. This distribution is strikingly different from those in Figure 3.12. The events at ± 1 were screened out of the event sample since they were contaminated by γ conversions into e^+e^- pairs and therefore, these events did not conserve momentum. Figure 5.2(b) shows the decay plane orientation angle ϕ of the $\Lambda^0/\bar{\Lambda}^0$ particle. Aside from the lower statistics, this distribution is similar to Figure 3.11 for the OR trigger data.

In order to estimate the background in these plots, the events containing TOF information for at least one charged track were studied. The event samples before and after the 4-C fit, but prior to the requirement of TOF mass consistency were analyzed. The ratio of TOF identified p's to π's was calculated for the central system particles assigned proton masses. The results show that prior to the 4-C fit the p/π ratio is 40/823 or 0.049. After the 4-C fit and prior to the TOF consistency check, the p/π ratio is 6/80 or 0.075. Thus, the background for this data is extremely high ($\approx 93\%$).

The invariant mass of the $p^{\pm}\pi^{\mp}$ pairs not associated with the $\Lambda^0/\bar{\Lambda}^0$ particle is shown in Figure 5.3 for 25 MeV and 40 MeV bin sizes. There appears to be no evidence for a second $\Lambda^0/\bar{\Lambda}^0$ particle (mass 1115 MeV). There is an enhancement

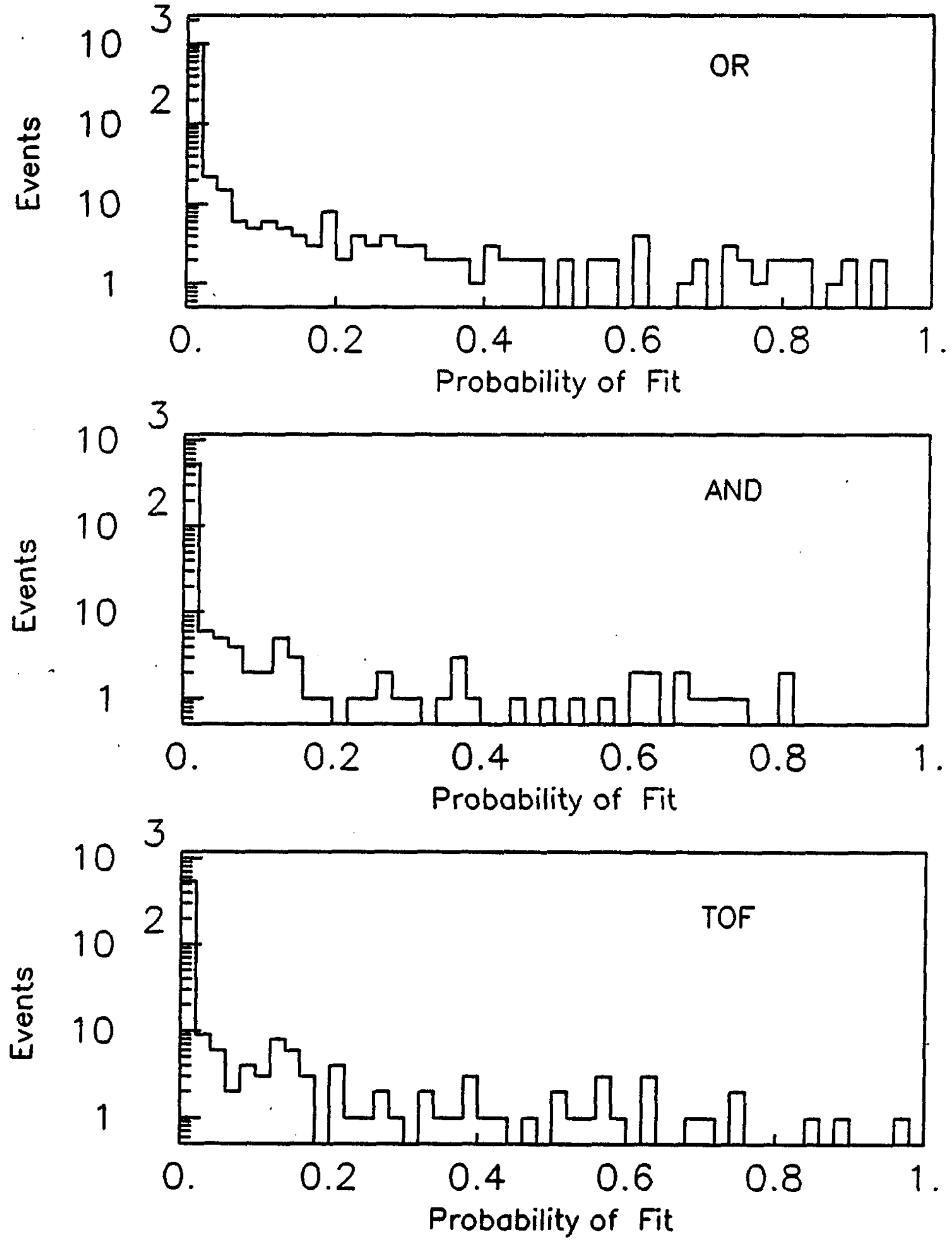

Figure 5.1 Probability of fit distribution for the OR (top), AND (middle), and TOF (bottom) trigger data

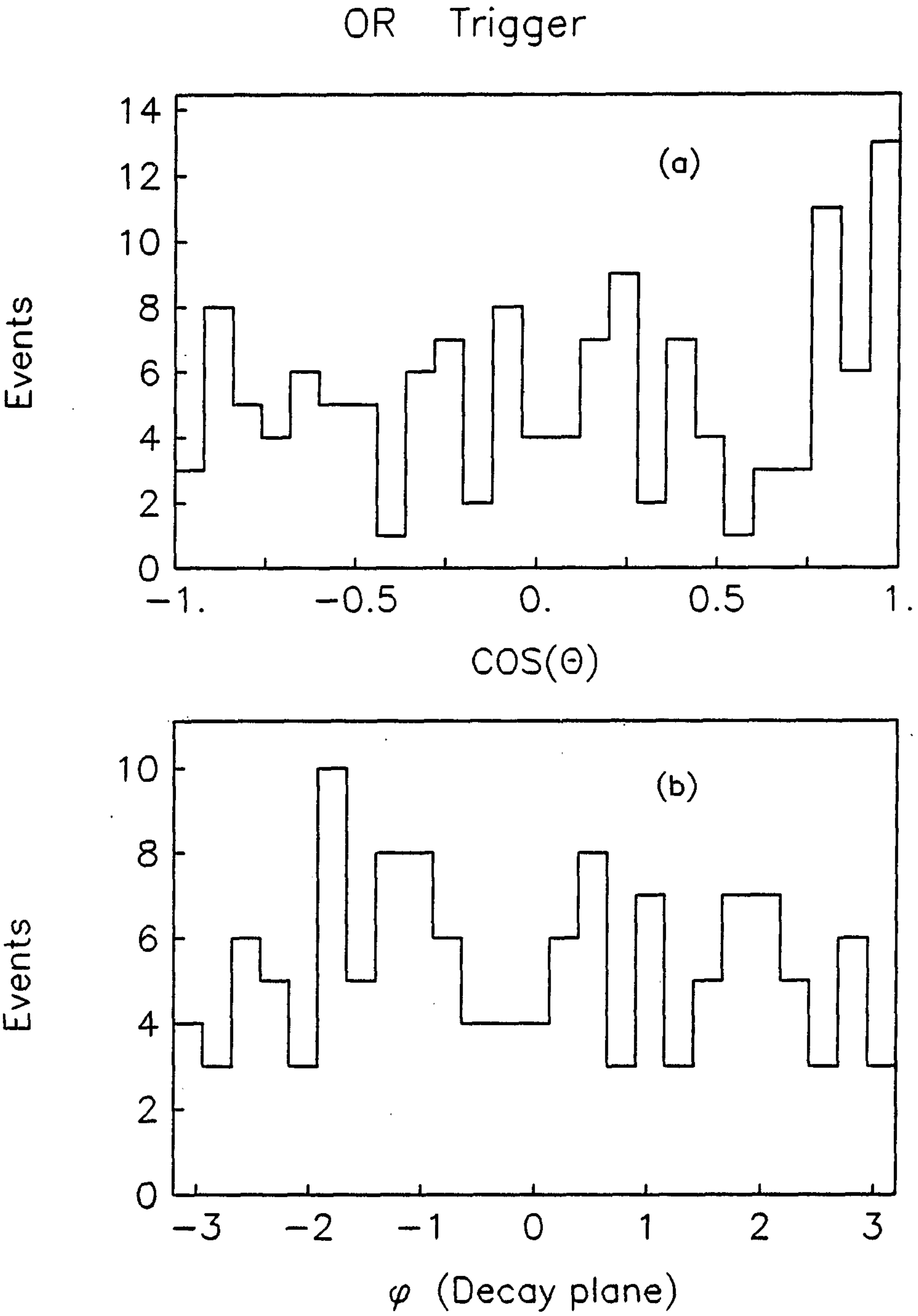

Figure 5.2 Distribution in (a) $cos(\theta)$ for the $\Lambda^0/\bar{\Lambda}^0$ particle and (b) ϕ decay plane orientation angle of the $\Lambda^0/\bar{\Lambda}^0$ particle

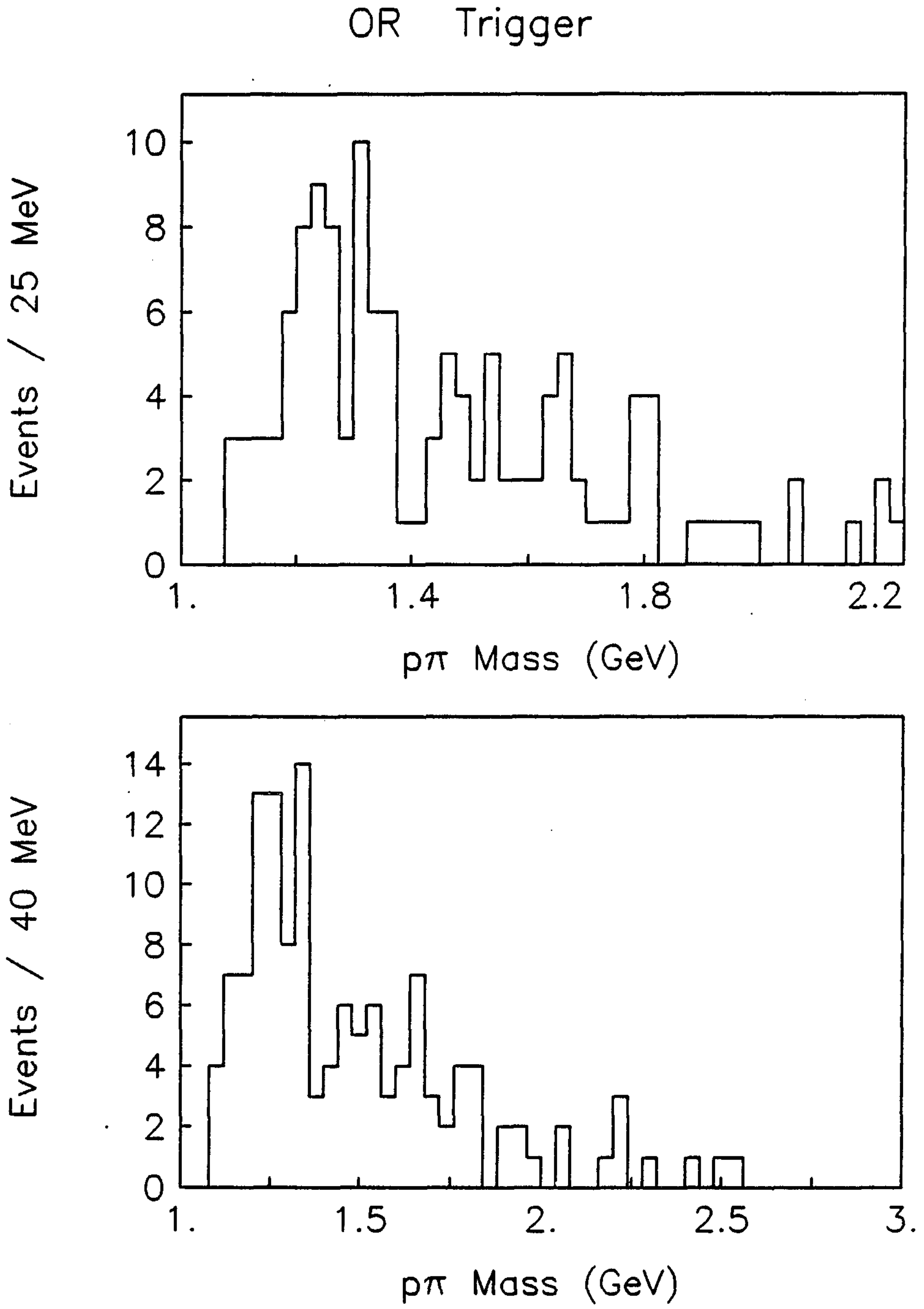

Figure 5.3 Invariant mass of the $p^{\pm}\pi^{\mp}$ pairs for 25 MeV bins (top) and 40 MeV bins (bottom)

near 1250 MeV, but it is too high to be a $\Lambda^0/\bar{\Lambda}^0$ particle. It is likely that these events are from some other momentum conserving interaction.

The absence of a $\Lambda^0/\bar{\Lambda}^0$ signal is not surprising in this trigger, since two charged p 's (one proton and one anti-proton) are required to be produced in the central system per event. The proton production is known to be low compared to pions for this trigger. In addition, there is a problem of inefficiency in the V^0 reconstruction for decays within one centimeter of the vertex. Also, the long decay length ($c\tau$ = 7.89 cm) will cause more $\Lambda^0\bar{\Lambda}^0$ events to be missed by the reconstruction code (i.e., the vertex will not be defined as well).

5.1.2 AND trigger data

In the AND trigger data, a total of 587 events were fitted and of these, 53 events passed the criterion for the probability of fit. Figure 5.4(a) shows the $cos(\theta)$ distribution for the $\Lambda^0/\bar{\Lambda}^0$ particle and its positive decay particle. As in the OR trigger, the $cos(\theta)$ distribution no longer exhibits the spikes at ±1. Figure 5.4(b) shows the ϕ decay plane orientation angle for the $\Lambda^0/\bar{\Lambda}^0$ particle. Aside from the lower statistics, this distribution is similar to Figure 3.11 for the AND trigger.

As in the OR trigger, the background has been estimated using the available TOF information. Prior to the 4-C fit the p/π ratio is 65/886 or 0.07. After the 4-C fit and prior to the TOF consistency check, the p/π ratio is 7/68 or 0.10. Thus, the background for this data is very high ($\approx$ 91%).

The invariant mass of the $p^{\pm}\pi^{\mp}$ pairs not associated with the $\Lambda^0/\bar{\Lambda}^0$ particle is shown in Figure 5.5 for 25 MeV and 40 MeV bin sizes. As in the OR trigger, there is little evidence for a second $\Lambda^0/\bar{\Lambda}^0$ particle produced. There is an enhancement at 1250 MeV which is too high to be a $\Lambda^0/\bar{\Lambda}^0$.

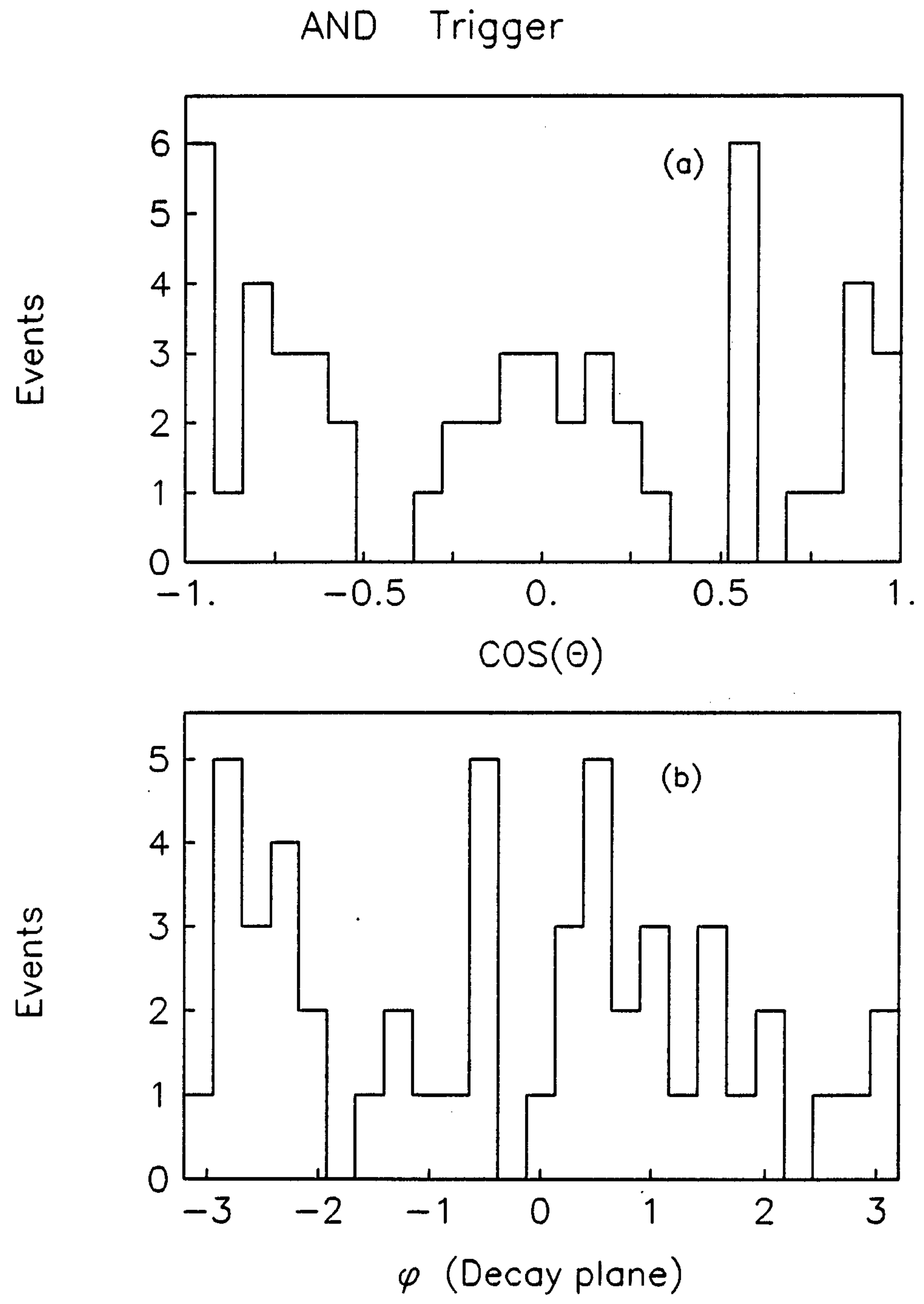

Figure 5.4 Distribution in (a) *cos*(θ) for the $\Lambda^0/\bar{\Lambda}^0$ particle and (b) ϕ decay plane orientation angle of the $\Lambda^0/\bar{\Lambda}^0$ particle

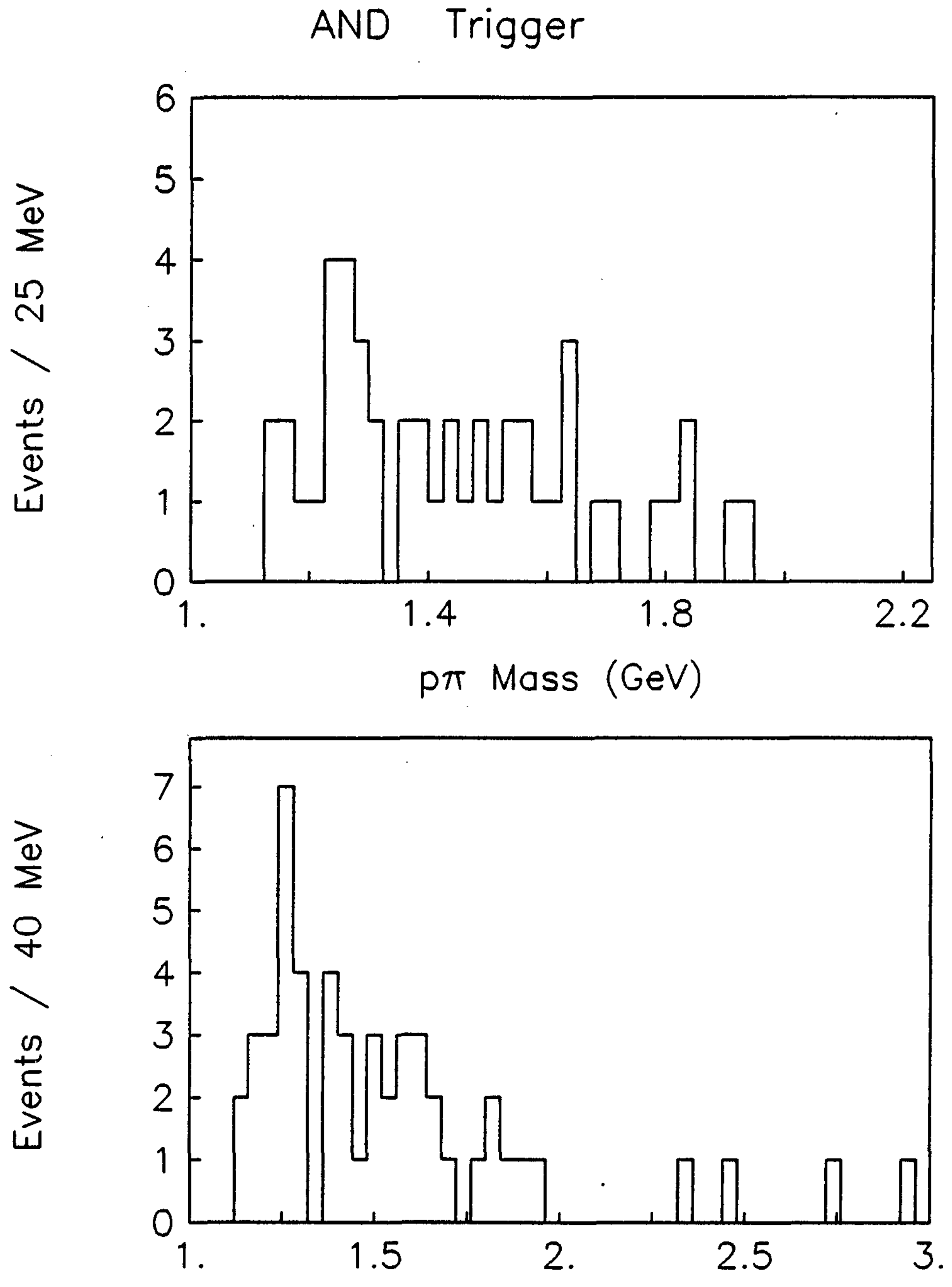

Figure 5.5 Invariant mass of the $p^{\pm}\pi^{\mp}$ pairs for 25 MeV bins (top) and 40 MeV bins (bottom)

5.1.3 TOF trigger data

In the TOF trigger data, a total of 618 events were fitted, and of these, 76 events passed the criterion for the probability of fit. Figure 5.6(a) shows the distribution in $cos(\theta)$ of the angle between the $\Lambda^0/\bar{\Lambda}^0$ and its positive decay particle. As in the OR and AND triggers, the spikes at ±1 are missing from the distribution. Figure 5.6(b) shows the ϕ decay plane orientation angle of the $\Lambda^0/\bar{\Lambda}^0$ particle. Aside from the lower statistics, this distribution is similar to Figure 3.11 for the TOF trigger data.

As in the OR and AND triggers, the background has been estimated using the available TOF information. Prior to the 4-C fit the p/π ratio is 282/627 or 0.45. After the 4-C fit and prior to the TOF consistency check, the p/π ratio is 38/46 or 0.83. Thus, the background for this data is much lower than the OR and AND triggers ($\approx$ 55%).

The invariant mass of the $p^{\pm}\pi^{\mp}$ pairs not associated with the $\Lambda^0/\bar{\Lambda}^0$ particle is shown in Figure 5.7 for 25 MeV and 40 MeV bin sizes. There appears to be some evidence for a second $\Lambda^0/\bar{\Lambda}^0$ particle (mass 1115 MeV). There are thirteen events near 1115 MeV. In order to separate out a $\Lambda^0\bar{\Lambda}^0$ signal, a cut was made on the $p^{\pm}\pi^{\mp}$ mass in the range of ±80 MeV around the $\Lambda^0/\bar{\Lambda}^0$ mass. The resulting $\Lambda^0\bar{\Lambda}^0$ invariant mass distribution is shown in Figure 5.8 for 40 MeV and 80 MeV bin sizes. There is a concentration of events at 2.5 GeV, but the statistics are very low.

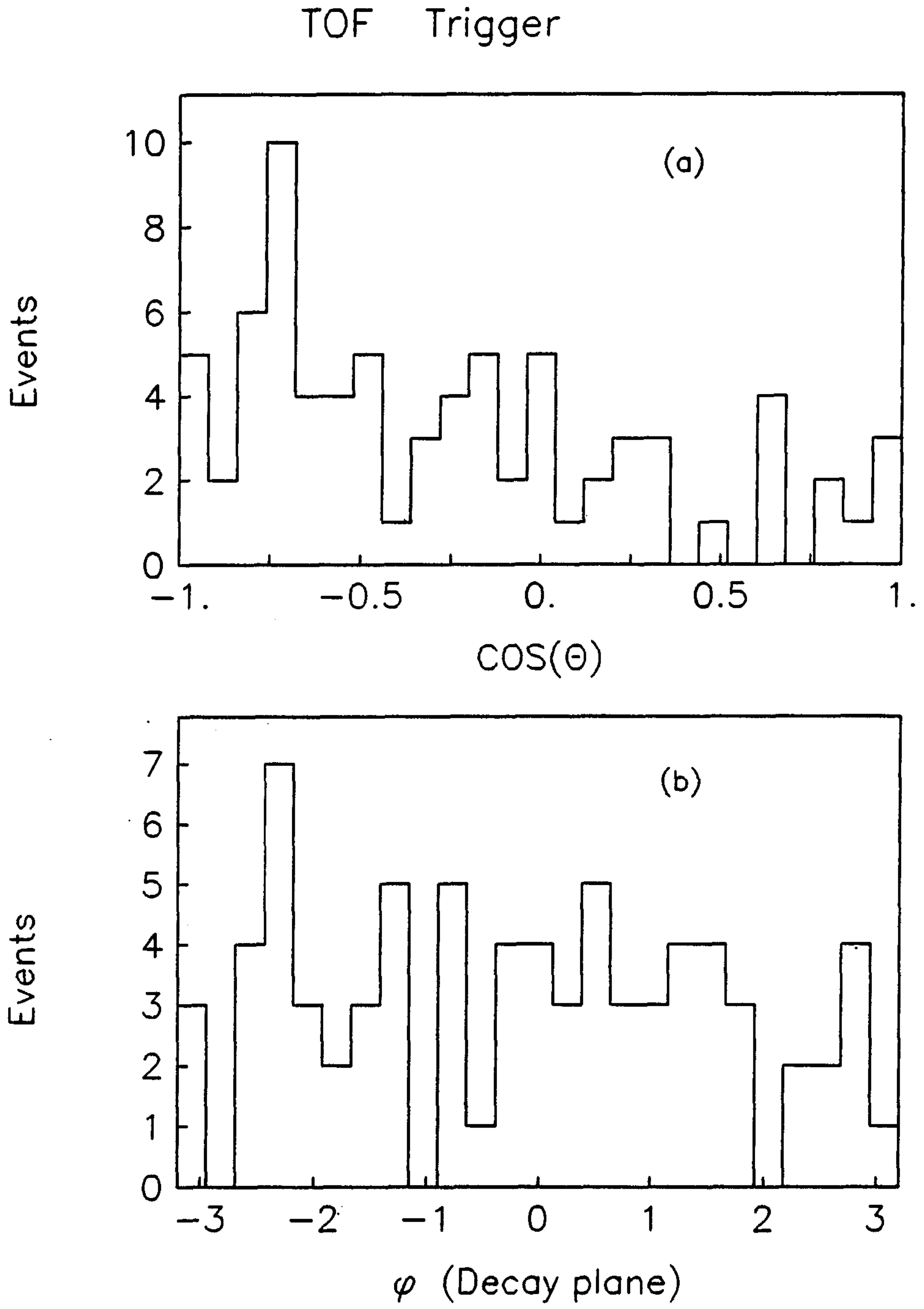

Figure 5.6 Distribution in (a) $cos(\theta)$ for the $\Lambda^0/\bar{\Lambda}^0$ particle and (b) ϕ decay plane orientation angle of the $\Lambda^0/\bar{\Lambda}^0$ particle

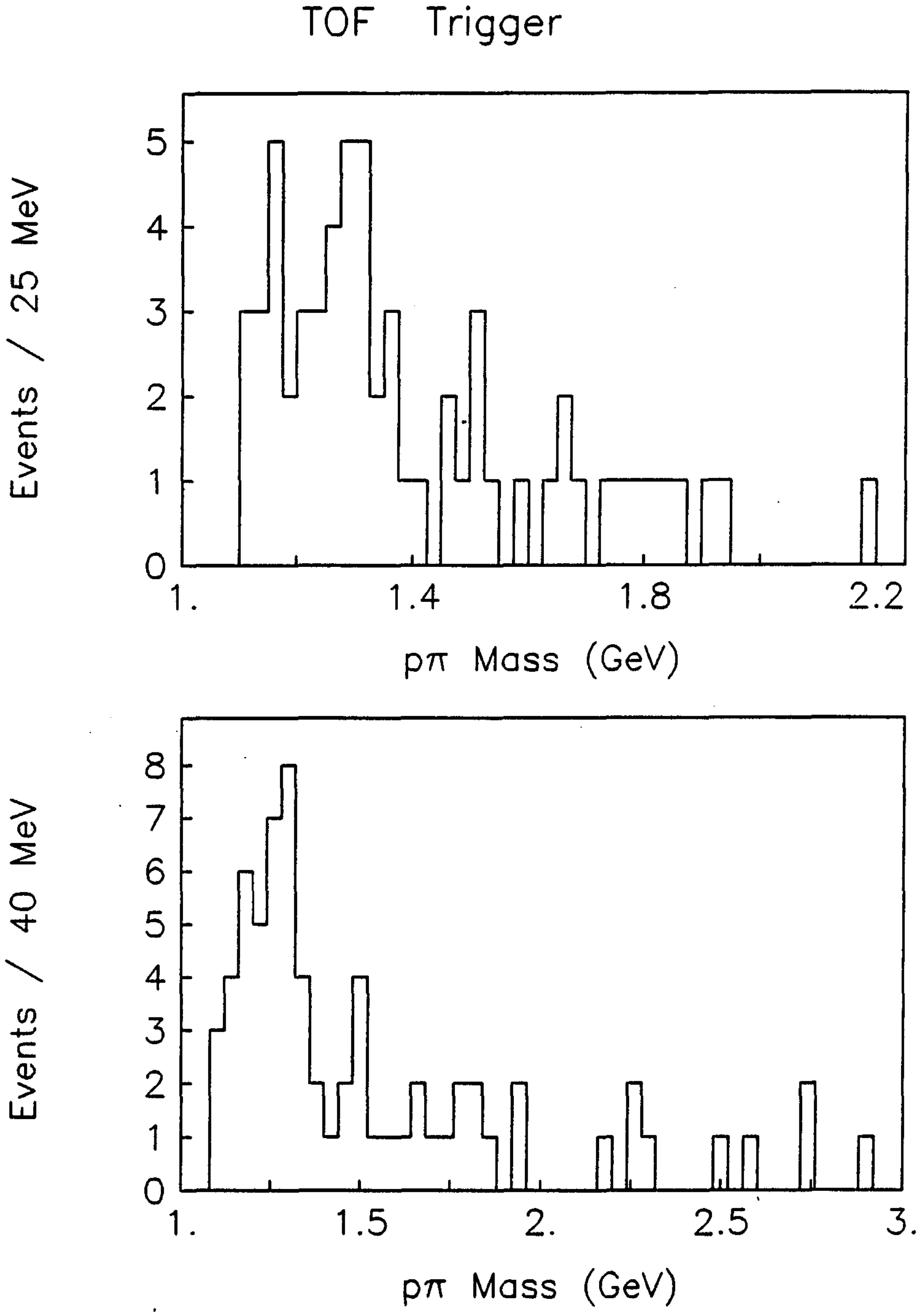

Figure 5.7 **Invariant mass of the $p^{\pm}\pi^{\mp}$ pairs for 25 MeV bins (top) and 40 MeV bins (bottom)**

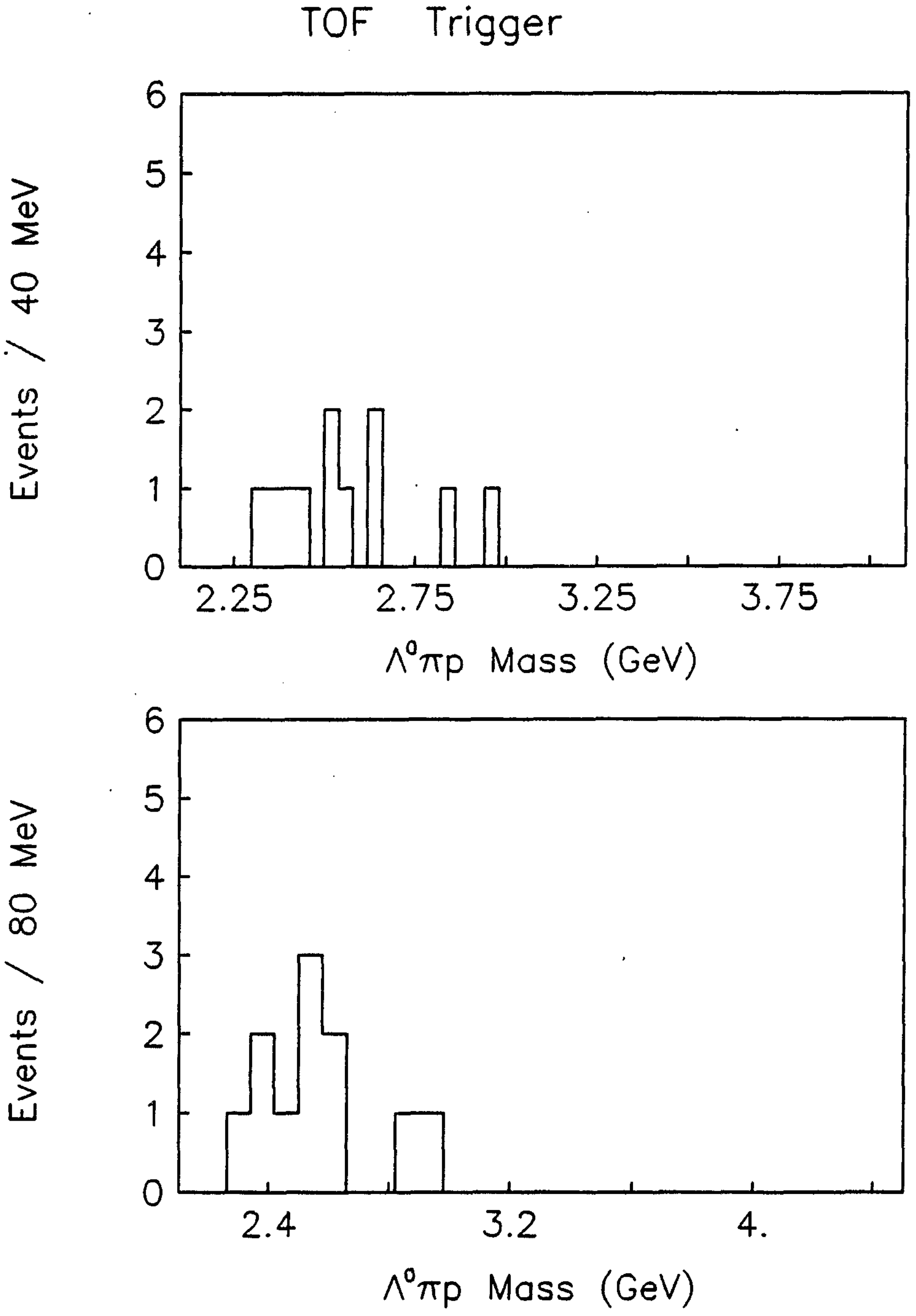

Figure 5.8 $\Lambda^0\bar{\Lambda}^0$ invariant mass for 40 MeV bins (top) and 80 MeV bins (bottom)

5.2 $\Lambda^0\bar{\Lambda}^{0*}$ ($\Lambda^{0*}\bar{\Lambda}^0$) Central System

All of the 6-prong events containing at least one identified Λ^0 or $\bar{\Lambda}^0$ particle given from the V^0 program were further processed using the 4-C fit routine discussed in Section 3.5. Only the best $\Lambda^0/\bar{\Lambda}^0$ fit was used from the V^0 program (i.e., lowest χ^2 value) in the event processing. The masses of the particles for the reaction 3.8 were assigned as discussed in Section 3.4 and are listed in Table 5.2 for the case of a Λ^0 or a $\bar{\Lambda}^0$ shown in parentheses. Due to low statistics, the two cases were combined in the analysis. These masses (for the charged particles) were required to be consistent with any available time of flight information on the DST for each event. The momenta and angles as described in Section 3.5 for each of the particles were input to the 4-C fit routine. The probability of fit distributions are shown for each of the three triggers in Figure 5.9. A probability cut of .02 was used in subsequent data analysis.

Table 5.2 Summary of particles whose four momenta are input to the 4-C fit in the $\Lambda^0\bar{\Lambda}^{0*}$ ($\Lambda^{0*}\bar{\Lambda}^0$) central system hypothesis

Particle(s)	Mass (MeV)	Description
p,p	938.2796	Two ingoing beam protons
$K^-(K^+)$	139.5685	one central pion
$p(\bar{p})$	938.2796	one central proton
Λ^0 ($\bar{\Lambda}^0$)	1115.63	One V^0 Central particle
p,p	938.2796	Two fast outgoing protons

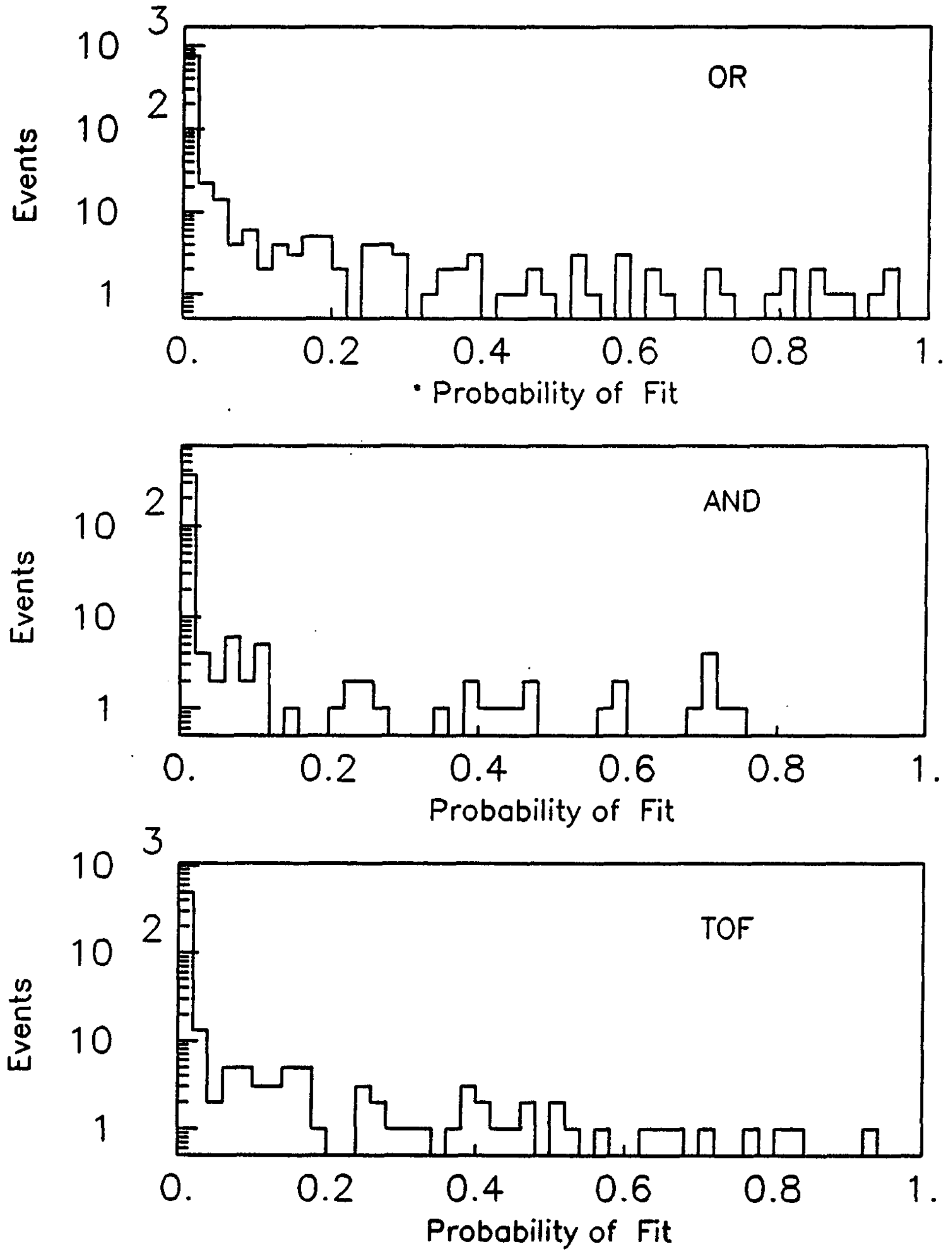

Figure 5.9 Probability of fit distribution for the OR (top), AND (middle), and TOF (bottom) trigger data

5.2.1 OR trigger data

A total of 859 events were fitted, and of these, 109 events passed the criterion for the probability of fit. The distribution in $cos(\theta)$ of the angle between the $\Lambda^0/\bar{\Lambda}^0$ and its positive decay particle is similar to the distribution for Section 5.1.1.

In order to estimate the background in these plots, the events containing TOF information for at least one charged track were studied. The event samples before and after the 4-C fit, but prior to the requirement of TOF mass consistency were analyzed. The ratio of the number of TOF identified p's and K's to the number of π's was calculated for the central system particles assigned proton and kaon masses. The results show that prior to the 4-C fit the $(p+K)/\pi$ ratio is 80/1423 or 0.056. After the 4-C fit and prior to the TOF consistency check, the $(p+K)/\pi$ ratio is 14/151 or 0.093. Thus, the background for this data is high, ($\approx 92\%$) as in the $\Lambda^0\bar{\Lambda}^0$ system hypothesis.

The invariant mass of the $p^{\pm}K^{\mp}$ pairs not associated with the $\Lambda^0/\bar{\Lambda}^0$ particle is shown in Figure 5.10 for 25 MeV and 40 MeV bin sizes. There appears to be slight evidence for a second Λ^* particle (mass 1520 MeV). There is an enhancement near 1500 MeV, but it is very broad and the statistics are low. This makes the identification of the enhancement at 1520 MeV as a bonafide Λ^* resonance subject to criticism. Although it is possible that this would be more easily identified in the data than a second $\Lambda^0/\bar{\Lambda}^0$ because there is no V^0 inefficiency to consider for each event. The Λ^* would decay at the primary vertex reducing the inefficiency problem to one V^0 and giving a more clearly defined primary vertex.

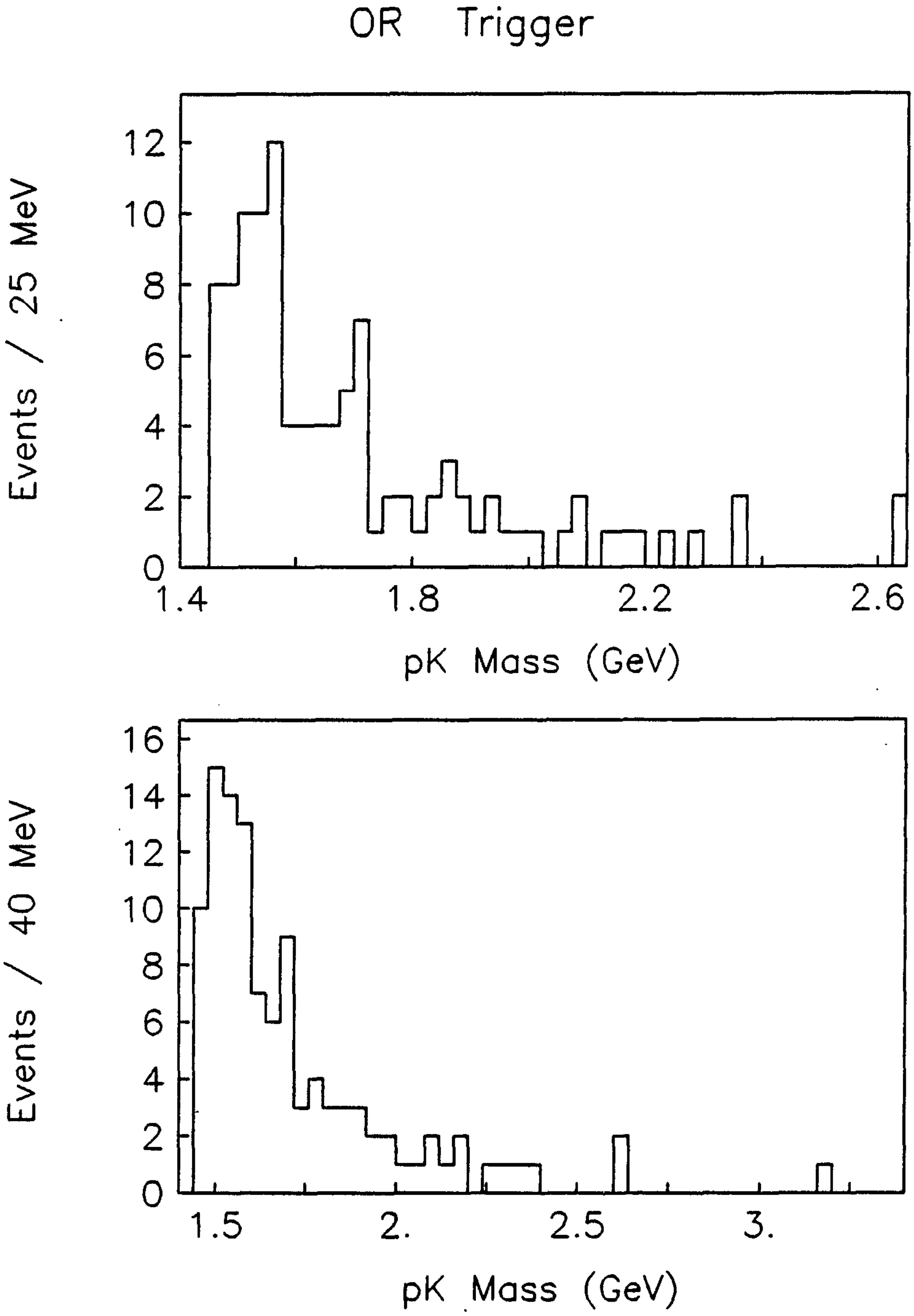

Figure 5.10 $p^{\pm}K^{\mp}$ invariant mass for 25 MeV bins (top) and 40 MeV bins (bottom)

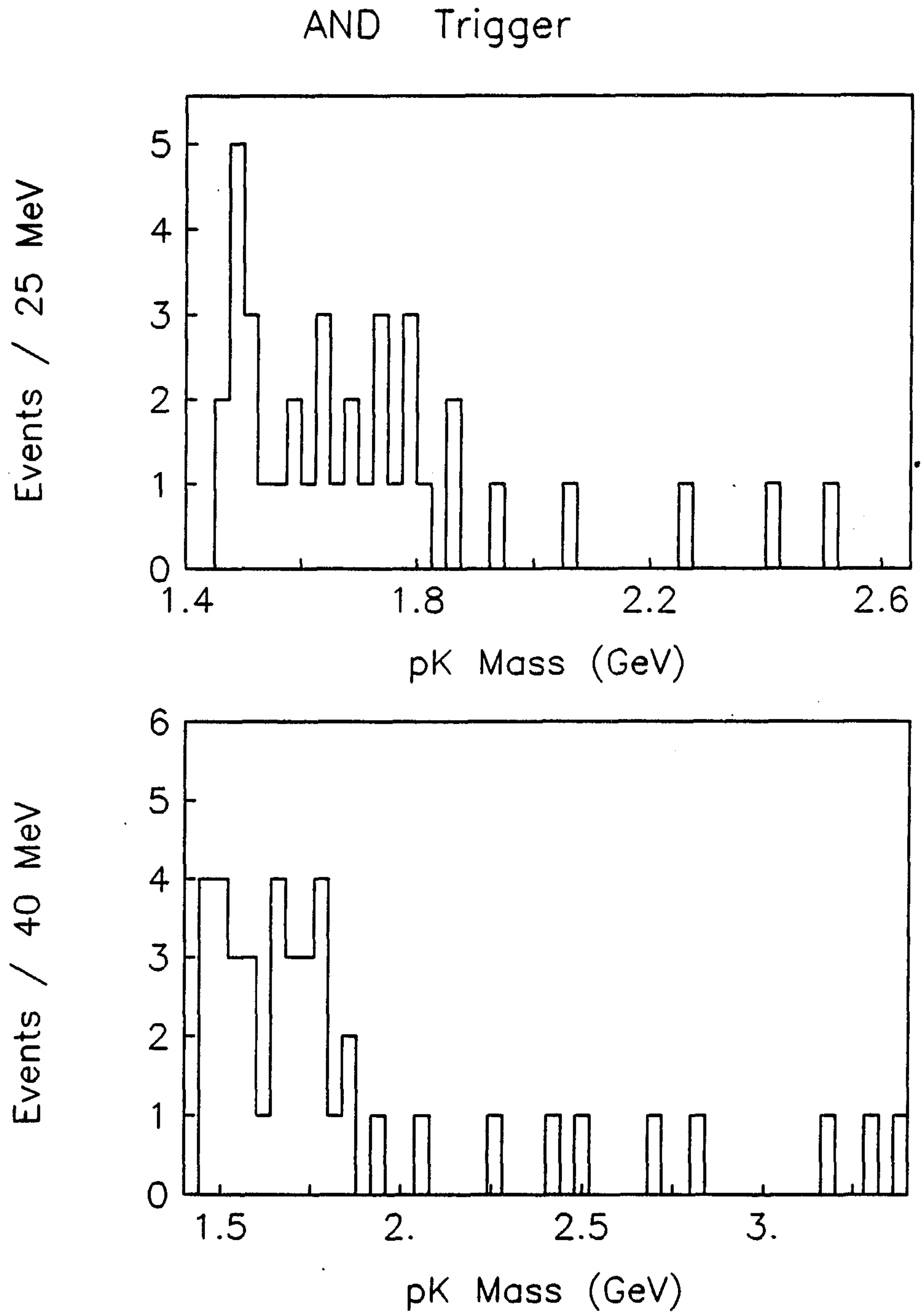

Figure 5.11 $p^{\pm}K^{\mp}$ invariant mass for 25 MeV bins (top) and 40 MeV bins (bottom)

5.2.2 AND trigger data

In the AND trigger data, a total of 404 events were fitted and of these, 42 events passed the criterion for the probability of fit. The distributions in $cos(\theta)$ and ϕ of the $\Lambda^0/\bar{\Lambda}^0$ are similar to those in Section 5.1.2.

As in the OR trigger, the background has been estimated using the available TOF information. Prior to the 4-C fit the $(p+K)/\pi$ ratio is 112/1354 or 0.083. After the 4-C fit and prior to the TOF consistency check, the $(p+K)/\pi$ ratio is 12/98 or 0.12. Thus, the background for this data is very high ($\approx 89\%$).

The invariant mass of the $p^{\pm}K^{\mp}$ pairs not associated with the $\Lambda^0/\bar{\Lambda}^0$ particle is shown in Figure 5.11 for 25 MeV and 40 MeV bin sizes. As in the OR trigger, there is slight evidence for a Λ^* (1520) particle produced. There is an enhancement at 1520 MeV which could be a Λ^* particle, but the statistics are low.

5.2.3 TOF trigger data

In the TOF trigger data, a total of 564 events were fitted, and of these, 72 events passed the criterion for the probability of fit. The distribution in $cos(\theta)$ of the angle between the $\Lambda^0/\bar{\Lambda}^0$ and its positive decay particle is similar to the distribution for Section 5.1.3.

As in the OR and AND triggers, the background has been estimated using the available TOF information. Prior to the 4-C fit the $(p+K)/\pi$ ratio is 389/792 or 0.49. After the 4-C fit and prior to the TOF consistency check, the $(p+K)/\pi$ ratio is 50/83 or 0.60. Thus, the background for this data is much lower than the OR and AND data, ($\approx 62\%$) as in the $\Lambda^0\bar{\Lambda}^0$ system hypothesis.

The invariant mass of the $p^{\pm}K^{\mp}$ pairs not associated with the $\Lambda^0/\bar{\Lambda}^0$ particle

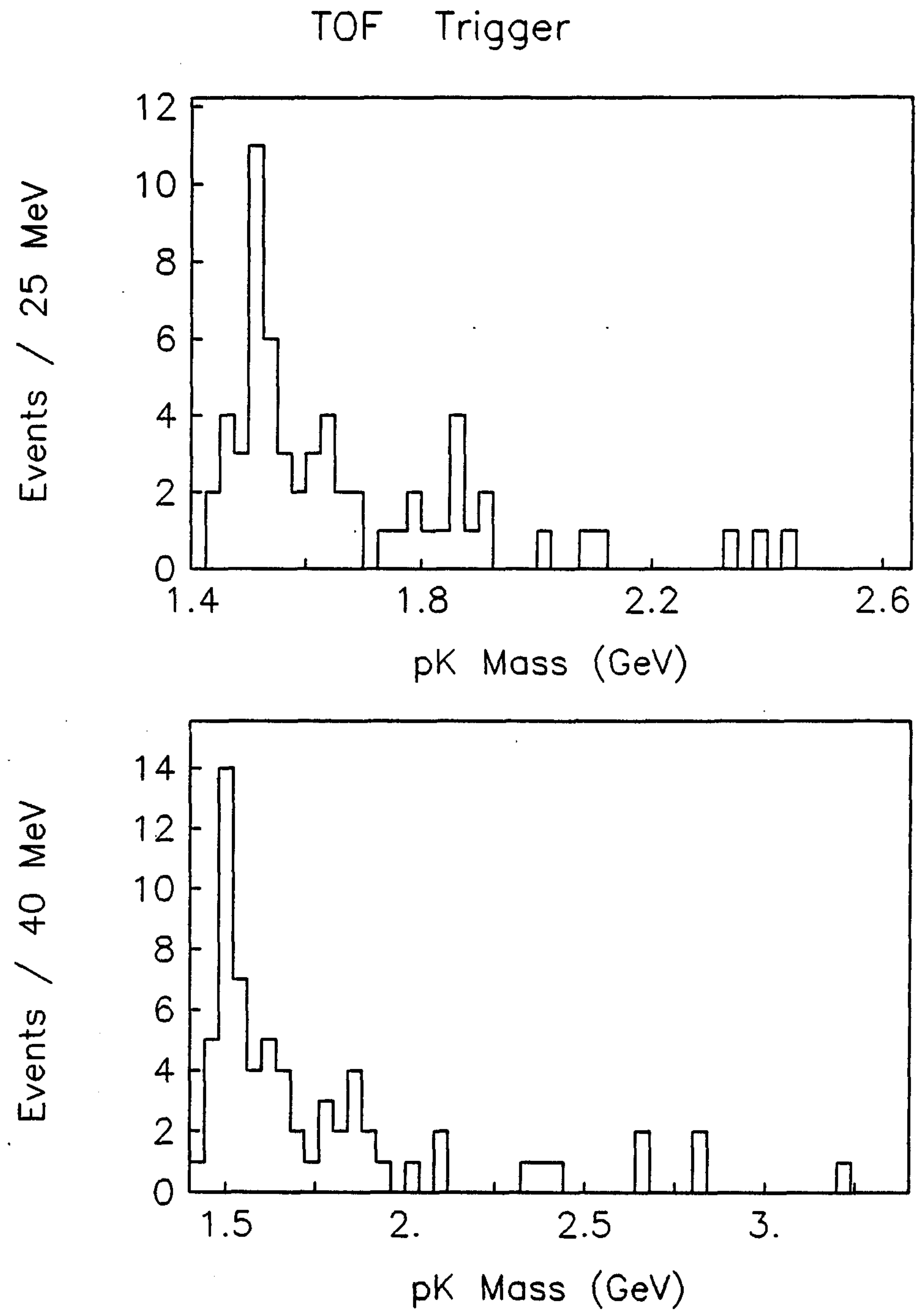

Figure 5.12 $p^{\pm}K^{\mp}$ **invariant mass for 25 MeV bins (top) and 40 MeV bins (bottom)**

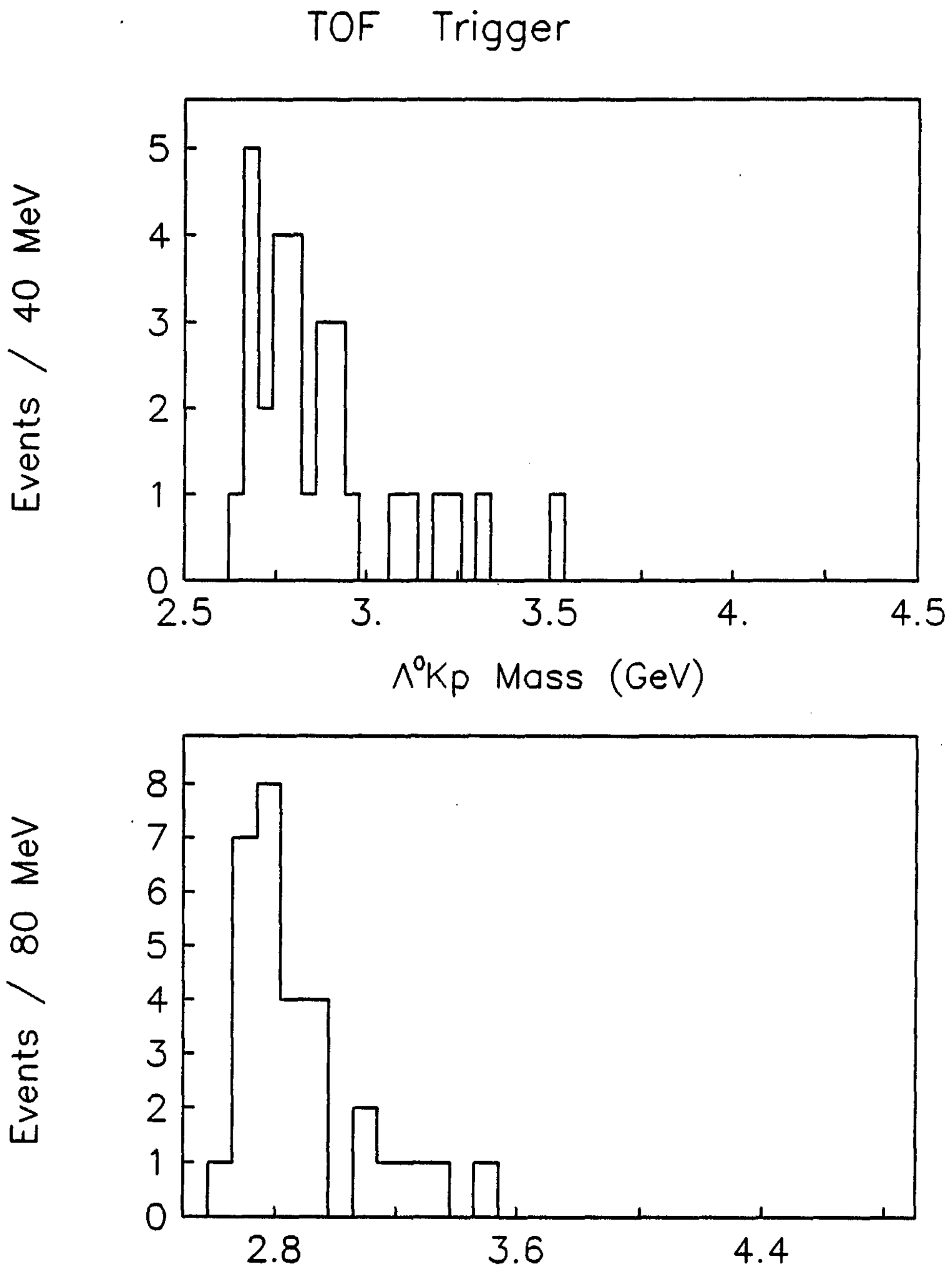

Figure 5.13 Invariant $\Lambda^0\bar{\Lambda}^{0*}$ mass distribution

is shown in Figure 5.12 for 25 MeV and 40 MeV bin sizes. There appears to be evidence for a second Λ^* particle (mass 1520 MeV). There is a significant enhancement near 1500 MeV. This enhancement is probably a Λ^* (1520) resonance. Figure 5.13 shows the distribution of the $\Lambda^0\bar{\Lambda}^{0*}$ central system mass containing only events within a band of ±80 MeV around the Λ^* mass of 1520 MeV for the $p^{\pm}K^{\mp}$ mass of Figure 5.12. Most of the events are concentrated near the threshold at about 2700 MeV. There are no known neutral resonances at 2700 MeV with even spin and positive parity.

5.3 Summary of the $\Lambda^0\bar{\Lambda}^0$ and $\Lambda^0\bar{\Lambda}^{0*}$ Systems

In the $\Lambda^0\bar{\Lambda}^0$ system, the OR and AND triggers do not exhibit any clear $\Lambda^0/\bar{\Lambda}^0$ signals in the $p^{\pm}\pi^{\mp}$ mass distributions. The absence of a signal in these two triggers is not surprising due to high background, low statistics, the long $\Lambda^0/\bar{\Lambda}^0$ decay length, and presence of central protons required of the decay products. The TOF trigger data are somewhat more promising since the background was found to be only 55% and this trigger enhances kaon and proton production. It is evident that there is a small $\Lambda^0/\bar{\Lambda}^0$ signal in the $p^{\pm}\pi^{\mp}$ mass distributions.

In the $\Lambda^0\bar{\Lambda}^{0*}$ system, the OR and AND triggers exhibit small enhancements at the Λ^* mass, but the high background and low statistics in these two samples makes signal extraction unlikely. The TOF trigger data exhibit a clear, sharp signal at the Λ^* mass of 1520 MeV and this is evidence for $\Lambda^0\bar{\Lambda}^{0*}$ being produced. The mass of the $\Lambda^0\bar{\Lambda}^{0*}$ system yields a significant concentration of events near 2700 MeV which could be evidence of a new resonant state.

Since the TOF trigger data show signals in both the $\Lambda^0\bar{\Lambda}^0$ and $\Lambda^0\bar{\Lambda}^{0*}$ central systems, calculations of cross sections are feasible.

6 ACCEPTANCES AND CROSS SECTIONS

6.1 Efficiencies and Systematic Effects

The V^0 program contains inefficiencies in the track finding algorithms. One can estimate the efficiencies for finding a V^0 and use this in the final acceptances. A direct estimate of the event fraction lost due to the decay length of the K_s^0 or $\Lambda^0/\bar{\Lambda}^0$ can be made from the decay length distributions of the particles in their respective rest frames. This is accomplished by transforming the measured decay length in the lab frame into the rest frame of the V^0 particle using the measured lab momentum and the V^0 mass. The desired expression is

$$x_r = ct_r = \frac{mc}{p} d_l \tag{6.1}$$

Where x_r is the transformed decay length lifetime in centimeters, t_r is the lifetime in the V^0 rest frame in seconds, m is the V^0 mass, d_l is the measured decay length, c is the speed of light, and p is the measured momentum of the V^0 particle.

Figure 6.1 shows the transformed decay length distribution of the K_s^0 particles after transforming into the K_s^0 rest frame for each event containing at least one K_s^0 particle for each of the three data sets. All three triggers show the same distribution shape. A fit to the data has been performed using an exponential decay distribution of the form

$$N(x) = N_0 e^{-x_r/\lambda} \tag{6.2}$$

where $x_r = ct_r$ is the lifetime (t_r) multiplied by the speed of light (c) for a particular K_s^0 particle, λ is the time at which a fraction e^{-1} of the particles decay, N_0 is the amplitude, and N is the observed number of K_s^0 decays at a particular distance x. These curves indicate a loss of events at shorter decay lengths. A subtraction of

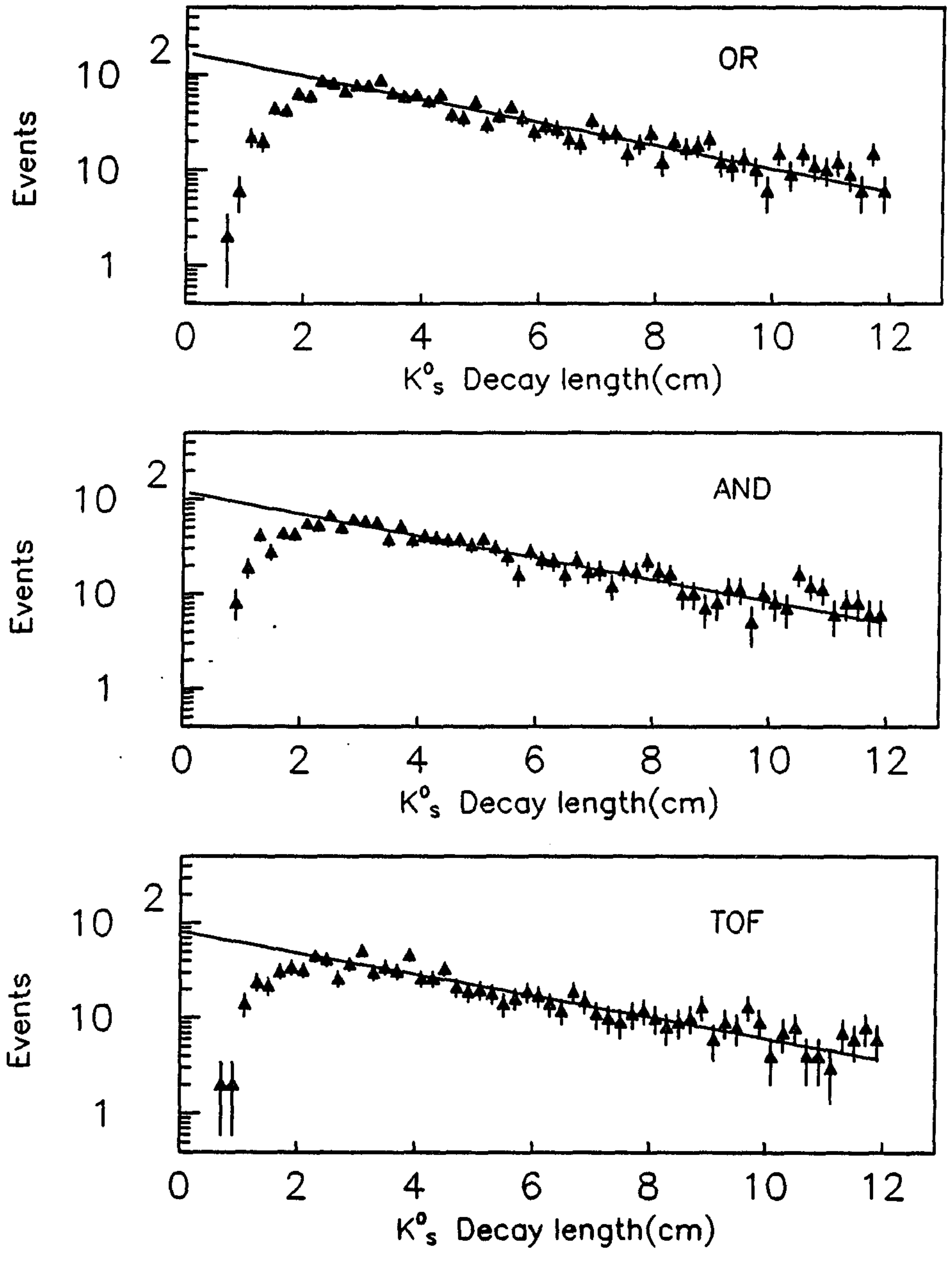

Figure 6.1 Transformed decay length of the K_s^0 particles for the OR (top), AND (center), and TOF (bottom) triggers

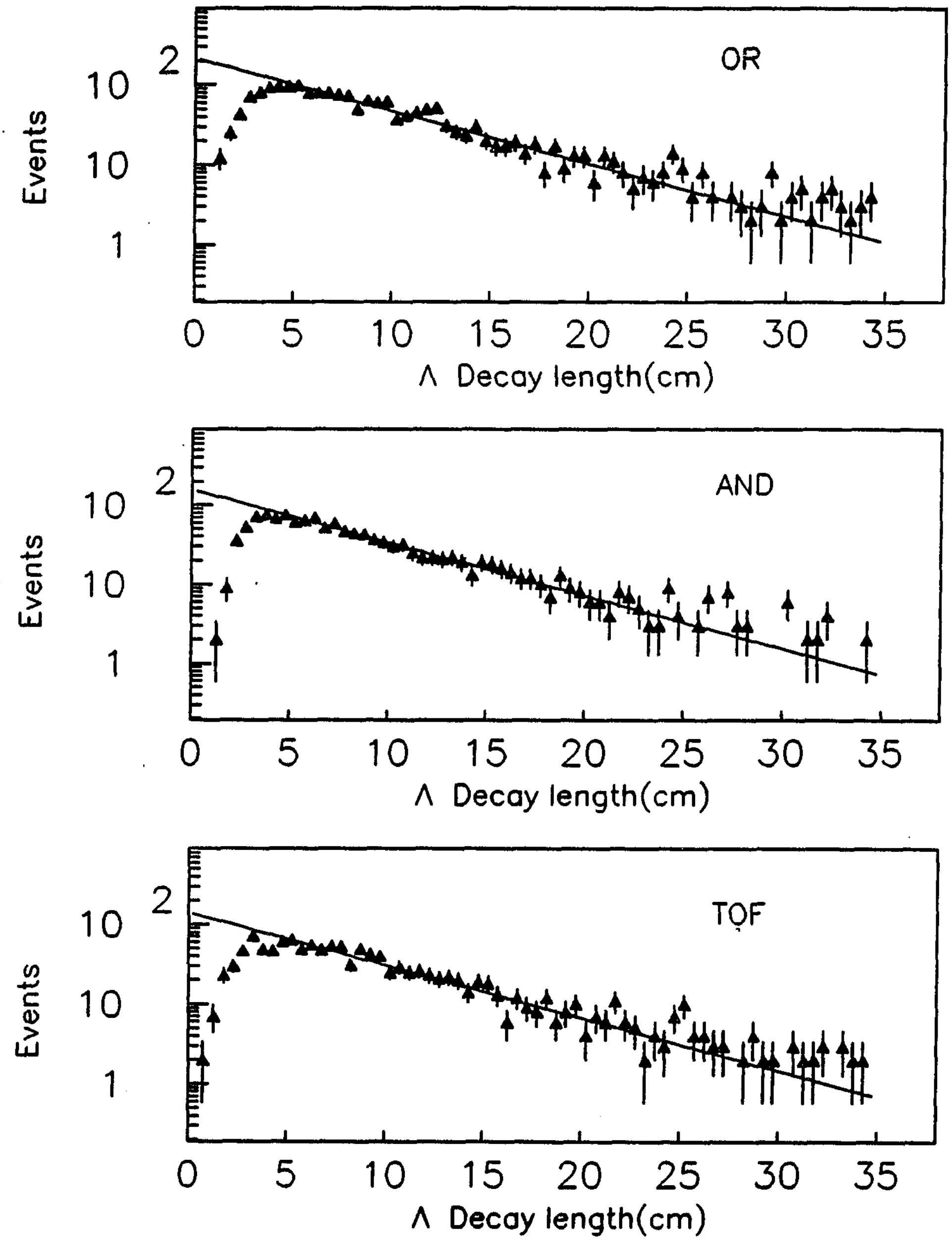

Figure 6.2 Transformed decay length of the $\Lambda^0/\bar{\Lambda}^0$ particles for the OR (top), AND (center), and TOF (bottom) triggers

the events from the curve yields an efficiency of .66 for the K_s^0 found by the V^0 program. For the second K_s^0 in reaction 3.5, the efficiency will be 1-.66, yielding .34 for the second K_s^0 particle. The remaining inefficiency comes from the V^0 track finding algorithm's ability to recognize a V^0 decay that is in the higher decay length region and to define the primary and secondary vertices properly. This overall efficiency is estimated to be 0.5 [Raschnabel 1981].

Figure 6.2 shows the transformed decay length of the $\Lambda^0/\bar{\Lambda}^0$ particles for each of the three data sets. A fit to the data using equation 6.2 yields the curves superimposed over the data. A subtraction from the fit of the events gives .68 for the $\Lambda^0/\bar{\Lambda}^0$ found by the V^0 program. The second $\Lambda^0/\bar{\Lambda}^0$ in reaction 3.7 will have an efficiency of .32. The remaining inefficiencies for the $\Lambda^0/\bar{\Lambda}^0$ come from the V^0 track finding algorithms. This efficiency is estimated to be about the same as in the K_s^0 case, i.e., 0.5. In addition, there is an ambiguity in some of the V^0 fits between a Λ and a $\bar{\Lambda}$ particle. This efficiency due to the $\Lambda^0/\bar{\Lambda}^0$ ambiguity is estimated at 0.8.

The systematic effects have been estimated to be 1.5 for this experiment [Breakstone et al. 1989]. These are due to uncertainties in overall acceptance and luminosity calibrations. There is a further systematic effect due to the V^0 track finding efficiencies computed from the lifetime distributions. Table 6.1 shows the fitted values of λ for the K_s^0 and $\Lambda^0/\bar{\Lambda}^0$ particles for each trigger. It is clear that there are event losses in the distributions since the decay lengths are slightly different from the known decay lengths. The known decay length is $c\tau = 2.7$ cm for the K_s^0 and $c\tau = 7.9$ cm for the $\Lambda^0/\bar{\Lambda}^0$. In the K_s^0 case there are losses at shorter lifetimes. These losses are probably due to secondary vertices not being seen since they are too close to the primary vertex. In the $\Lambda^0/\bar{\Lambda}^0$ case there are event losses

Table 6.1 fitted decay length lifetimes for the K_s^0 and $\Lambda^0/\bar{\Lambda}^0$ particles for each trigger

Particle	OR	AND	TOF
K_s^0	$3.6 \pm .2$ cm	$3.7 \pm .2$ cm	$3.8 \pm .1$ cm
$\Lambda^0/\bar{\Lambda}^0$	$6.6 \pm .2$ cm	$6.5 \pm .2$ cm	$6.6 \pm .2$ cm

at larger lifetimes. These losses are probably due to particles escaping the detector and not being seen by the reconstruction code. These losses must be considered as a systematic effect in the calculation of efficiencies. This effect is estimated to be about 1.15. This will give an overall total systematic uncertainty in the cross sections of 1.7.

6.2 Acceptance Calculations

The SFM detector acceptances for the $K_s^0K_s^0$, $K_s^0K^{\pm}\pi^{\mp}$, $\Lambda^0\bar{\Lambda}^0$, and $\Lambda^0\bar{\Lambda}^{0*}$ central systems have been calculated. This was necessary to obtain absolute cross sections for these interactions. The acceptances were computed using a two step Monte-Carlo technique. This technique is similar to the one that has been used in Breakstone et al. [1989].

In the first step, single particles were generated for all momenta and angles that could envelop the trigger chambers. The particle trajectories were tracked through the magnetic field, the detector chambers, and the TOF stands [Messerli]. Energy losses, scattering, and particle decays were taken into account. The measured TOF masses for K's and p's were also included when applicable. "Trigger-tables" were constructed from this tracking information for quantized regions of the polar angle θ, azimuth ϕ, and momentum p of a particle. This was done for all possible particle trajectories which satisfied the trigger requirement.

In the second step, events were generated for the central systems $\pi^+\pi^-\pi^+\pi^-$ and $p\bar{p}\pi^+\pi^-$ using a double peripheral model [James 1967]. Production of the fast outgoing protons was performed using a matrix element squared of the form $e^{-6t_1}e^{-6t_2}$, where t_1, t_2 are the momentum transfers for each of the protons. For the reaction 3.5, an isotropic decay was used. For the reactions 3.6-3.8, a damped decay distribution was used in the transverse momenta, p_T, where p_T is defined with respect to the Pomeron direction in the system X. The matrix element squared

$$\prod_{i=1}^{n} e^{-A(E_T)_i}, \quad (E_T)_i = \sqrt{(p_T)_i^2 + m_i^2} \tag{6.3}$$

was used with $A \approx 2$ giving a good fit to the data, m_i stands for the i^{th} particle mass, and n is four. An estimate of systematic errors resulting from model dependences was obtained from comparison to acceptances resulting from isotropic decay in the central system. The differences in acceptance were found to be small so that the p_T-damped model is acceptable for these reactions since the statistics in the real data are too low to do extensive studies of the angular distributions. The acceptance for each of the triggers was obtained by examining each track in the event against "trigger-tables" to determine if the trigger requirements were satisfied. To obtain an acceptance, the SFM and trigger acceptances were combined for the complete event. The overall efficiencies discussed in Section 6.1 were included in the final acceptances.

For the $K_s^0 K_s^0$ central system, the acceptances have been calculated from the $\pi^+\pi^-\pi^+\pi^-$ Monte-Carlo events with an additional cut around each $\pi^+\pi^-$ pair

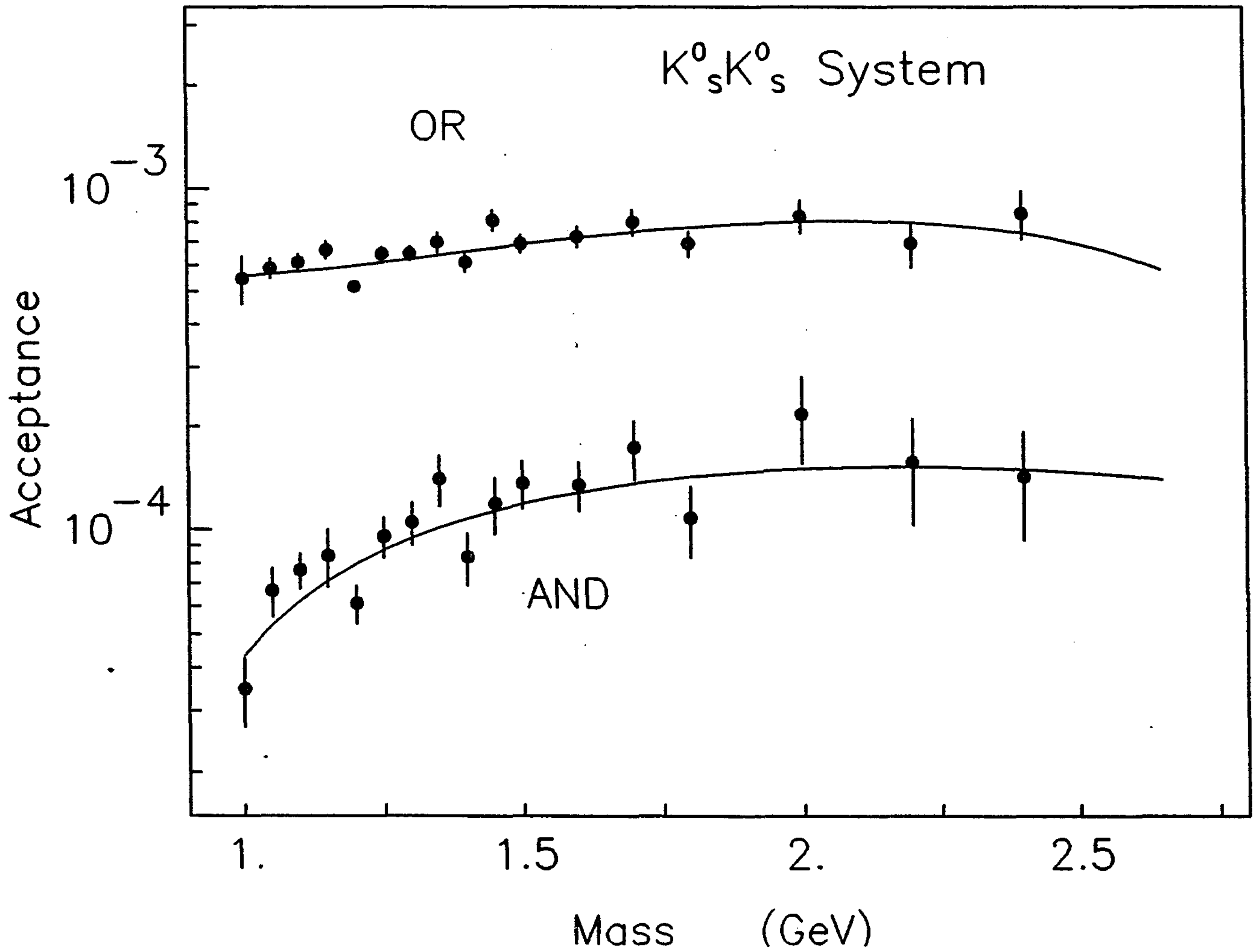

Figure 6.3 Acceptance values and errors for the OR and AND triggers in the $K^0_sK^0_s$ system. The curves shown superimposed represent third degree polynomial fits to the data

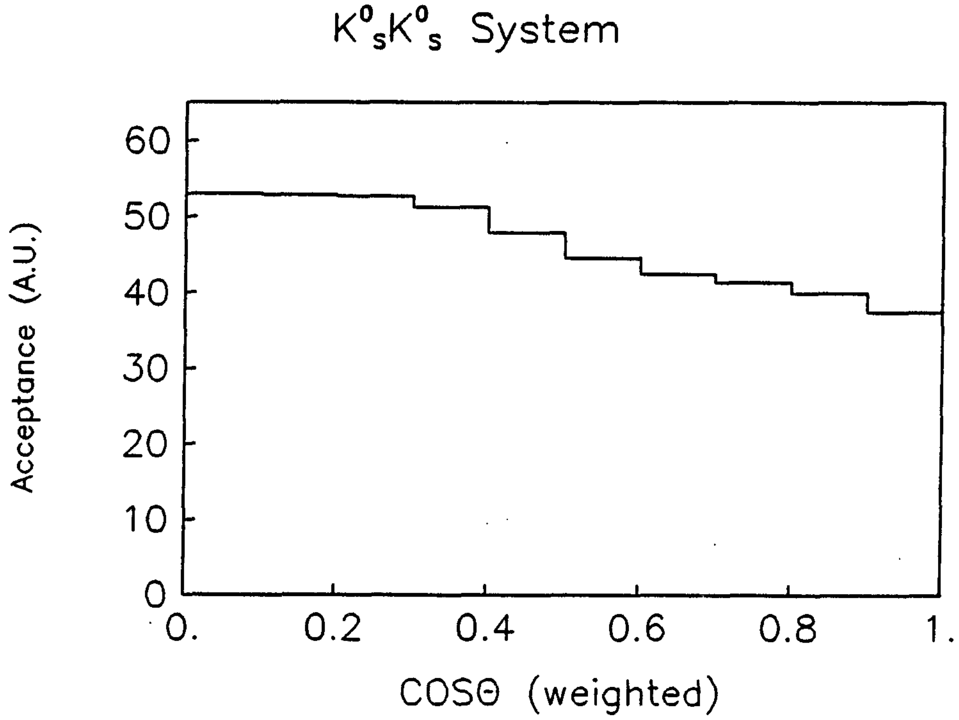

Figure 6.4 Acceptance $cos(\theta)$ distribution of the angle between the K_s^0 and the Pomeron in the Pomeron-Pomeron rest frame for a central system mass of 1200 MeV (Arbitrary Units, A.U.)

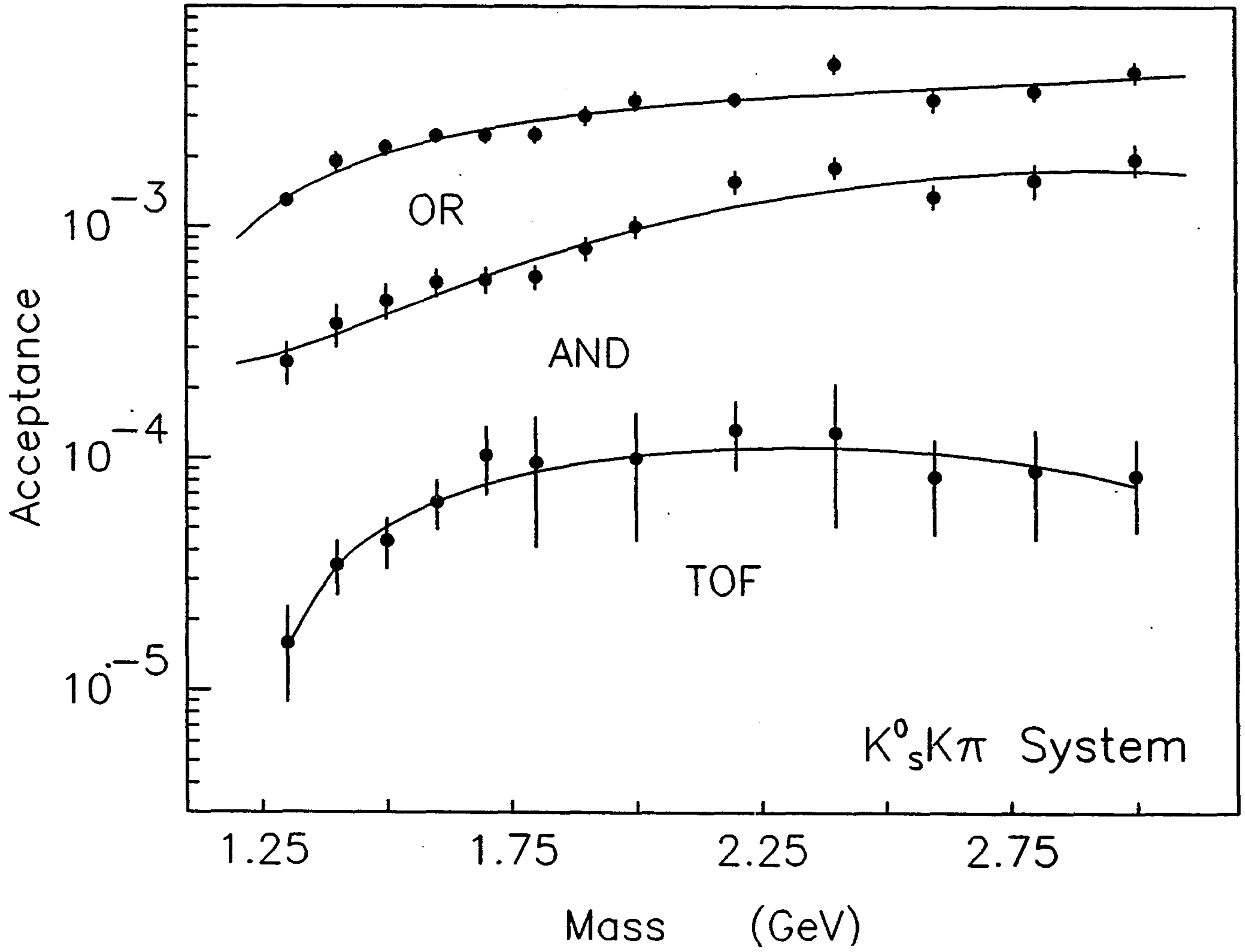

Figure 6.5 Acceptance values and errors for the OR, AND and TOF triggers in the $K^0_s K^{\pm}\pi^{\mp}$ system. The curves shown superimposed represent third degree polynomial fits to the data

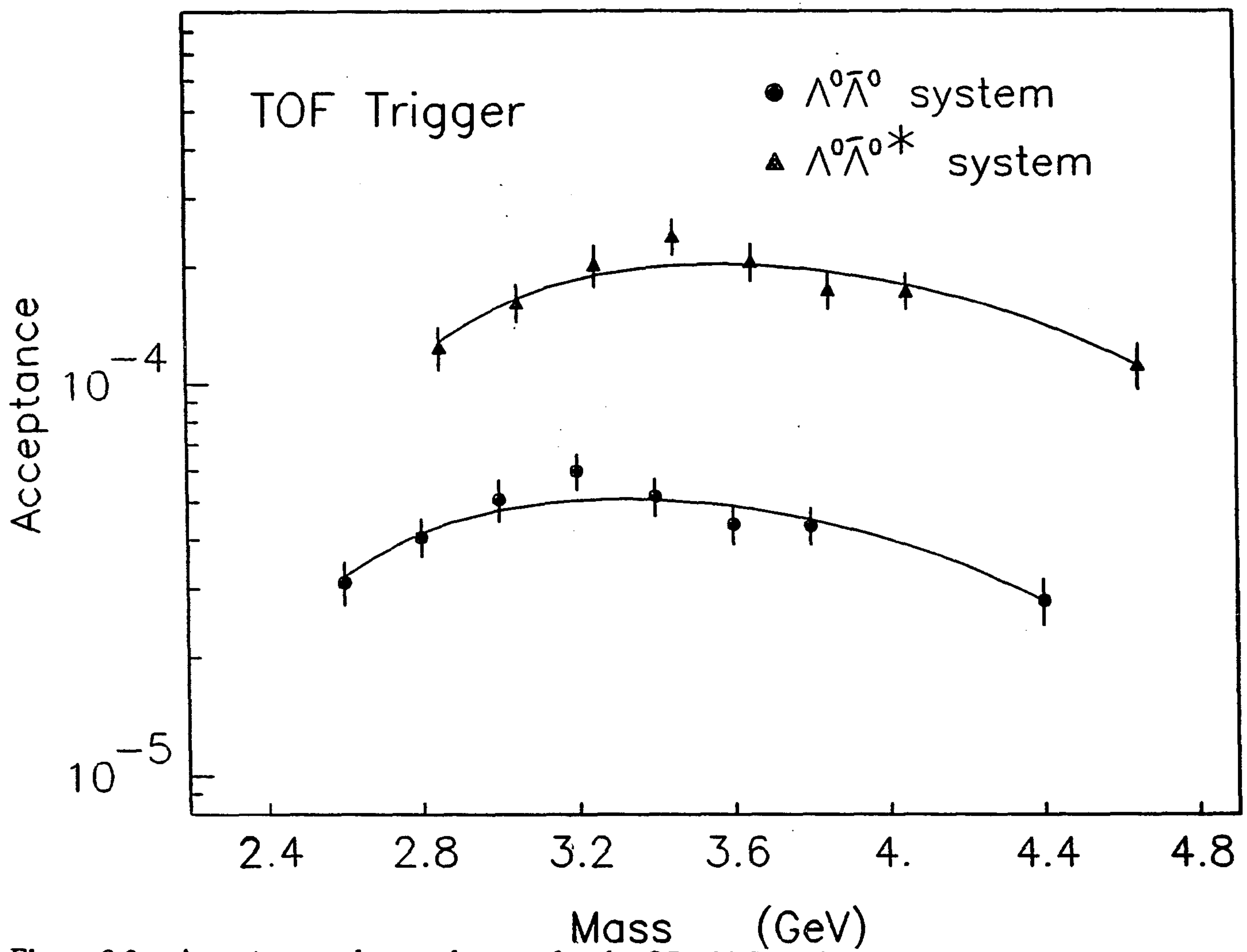

Figure 6.6 Acceptance values and errors for the OR, AND and TOF triggers in the $\Lambda^0\bar{\Lambda}^0$ and $\Lambda^0\bar{\Lambda}^{0*}$ systems. The curves shown superimposed represent third degree polynomial fits to the data

mass of 497 ± 50 MeV. The acceptance values and errors are shown in Figure 6.3 for the OR and AND triggers. The actual acceptances are approximated by polynomial fits of the form

$$A = p_1 + p_2 m + p_3 m^2 + p_4 m^3 \tag{6.4}$$

where m is the central system mass, p_i are the fit coefficients, and A is the acceptance. These fits are shown by the curves in Figure 6.3. In this $K_s^0 K_s^0$ system, the TOF acceptance is very similar to the OR acceptance since four π's are produced. Thus, the OR acceptance was used for the TOF data also. The $cos(\theta)$ of the angle between a K_s^0 and one of the Pomerons in the Pomeron-Pomeron rest frame is shown in Figure 6.4 for the OR trigger at a central system mass of 1200 MeV. Notice that the same falloff in the data for large values of $cos(\theta)$ is seen as in Chapter 4 for this $K_s^0 K_s^0$ system.

The acceptances for the $K_s^0 K^\pm \pi^\mp$ system were calculated starting with the $\pi^+\pi^-\pi^+\pi^-$ events. A cut on one $\pi^+\pi^-$ pair mass of ±50 MeV was made around the K_s^0 mass. One charged π from the other pair was converted to a K particle by changing the π mass in the central system rest frame to a K mass and Lorentz transforming the momentum and energy of this particle back into the laboratory frame. The events were then subjected to the analysis of SFM and trigger requirements and complete acceptances calculated using the p_T-damped decay method. For the $K_s^0 K^\pm \pi^\mp$ system the TOF trigger acceptance was calculated also. The shape of the acceptances of the OR and TOF triggers were similar, but not identical in this system. The computed acceptances are shown in Figure 6.5 for the OR, AND, and TOF triggers.

The calculation of acceptances in the $\Lambda^0 \bar{\Lambda}^0$ system was attempted using the $p\bar{p}\pi^+\pi^-$ Monte-Carlo events. A cut on each $p\pi^-$ pair was made around the $\Lambda^0/\bar{\Lambda}^0$

mass of ±100 MeV. The acceptance was found to have very large errors, as the Monte-Carlo statistics were too low to give reliable values. Thus, it was decided to compute the acceptances using all of the $p\bar{p}\pi^+\pi^-$ Monte-Carlo events. This has been done and the acceptance is shown in Figure 6.6.

In the $\Lambda^0\bar{\Lambda}^{0*}$ system a technique similar to the $K^0_s K^\pm\pi^\mp$ acceptance procedure yielded very large errors. Therefore, the $p\bar{p}\pi^+\pi^-$ data were used assuming the same overall factor behavior as between the $K^0_s K^0_s$ and the $K^0_s K^\pm\pi^\mp$ systems. This gives the curve shown in Figure 6.6. The phase space difference was accounted for by shifting the $\Lambda^0\bar{\Lambda}^0$ curve to account for the difference in mass threshold.

6.3 Cross Sections

Table 6.2 shows the estimated total cross sections for reactions 3.5-3.8. The OR trigger data were used in the calculation of the total cross sections for the reactions involving K^0_s particles (since this trigger has the best acceptance). These were computed using the sum of the acceptance corrected central system mass distributions of figures 6.8 and 6.10 for the OR trigger. The errors are simply the sum of the statistical errors of each bin in the observed number of events for each interaction. The background estimate used for the $K^0_s K^0_s$ system was the same as the estimate in Section 4.1 of 30%. In the $K^0_s K^\pm\pi^\mp$ system the background estimate is reduced considerably by using Figure 4.39. From these distributions one obtains 48%. This is consistent with the higher background before the mass cut so that the KK^* system is the major contributor to the total cross section in this analysis.

The TOF trigger data were used in the total cross section for the reactions involving $\Lambda^0/\bar{\Lambda}^0$ particles (since only this trigger contained a signal). In addition

Table 6.2 Total cross sections for reactions 3.5-3.8; the quoted errors do not include an overall systematic error of 1.7 which results from an uncertainty in acceptance and luminosity calibrations

Reaction	Raw Events	Background	Real Events	Cross Section (μb)
$pp \rightarrow pp(K_s^0 K_s^0)$	62	30%	43	$1.3 \pm .64$
$pp \rightarrow pp(K_s^0 K^{\pm} \pi^{\mp})$	94	48%	49	$.44 \pm .14$
$pp \rightarrow pp(\Lambda^0 \bar{\Lambda}^0)$	13	54%	7	$.20 \pm .14$
$pp \rightarrow pp(\Lambda^0 \bar{\Lambda}^{0*})$	30	50%	15	$.13 \pm .06$

there is an overall systematic uncertainty of 1.7 as discussed in Section 6.2. Figures 5.8 and 5.13 were used in the $\Lambda^0\bar{\Lambda}^0$ and $\Lambda^0\bar{\Lambda}^{0*}$ systems to estimate the background percentages and the results were similar to the TOF information estimates from Chapter 5.

6.3.1 $K_s^0 K_s^0$ system

The *cos*(θ) distributions, where θ is the angle between a K_s^0 particle and one of the Pomerons in the Pomeron-Pomeron rest frame, is shown in Figure 6.7 for each of the three triggers. These distributions have been corrected for acceptance of the detector and the falloff at large *cos*(θ) values is no longer observed. Therefore, since these distributions are now flat, it is likely that the $K_s^0 K_s^0$ events are predominantly s-wave, i.e., they have no preferred spin direction.

The cross sections as a function of the $K_s^0 K_s^0$ invariant mass are shown for each of the three triggers in Figure 6.8 for 100 MeV bin sizes. The errors are statistical errors for the observed number of events in each bin. The distributions are similar to the raw event mass distributions in Chapter 4.

The cross sections for the OR and TOF data added and for the OR, AND, and TOF data added are shown in Figure 6.9. Both distributions feature an enhancement at 1.1-1.2 GeV. It is possible that the effect could be due to two resonances, the $f_0(975)$ and the $f_0(1240)$. The $f_0(975)$ is at threshold for $K_s^0K_s^0$ production and the $f_0(1240)$ has been seen to decay to $K_s^0K_s^0$ [Etkin et al. 1982]. Since the statistics in these data are low, these two resonances could account for the distributions.

6.3.2 $K_s^0K^\pm\pi^\mp$ *system*

The cross sections as a function of the $K_s^0K^\pm\pi^\mp$ invariant mass for events consistent with containing a K^* particle, are shown in Figure 6.10 for each of the three data sets. The OR data show a clear enhancement at 1400-1500 MeV. The AND and TOF data contain lower statistics, and show enhancements at this mass range also. The cross sections for the OR and TOF data added and for the OR, AND, and TOF data added are shown in Figure 6.11. Both feature the enhancement at 1400 MeV. A possible resonance at this mass is the $f_0(1400)$ which decays to $K\bar{K}$, but it is not clear why it is not visible in the $K_s^0K_s^0$ system. This could be due to the threshold enhancement at the lower mass of $\approx$ 1200 MeV dominating in that case.

6.3.3 $\Lambda^0\bar{\Lambda}^0$ *and* $\Lambda^0\bar{\Lambda}^{0*}$ *systems*

Figure 6.12 shows the cross sections as a function of mass for the $\Lambda^0\bar{\Lambda}^0$ and the $\Lambda^0\bar{\Lambda}^{0*}$ central systems. The lack of event statistics has caused large error bars, so that it is difficult to make conclusions. There is a low mass enhancement at threshold as discussed in Chapter 5 for both reactions.

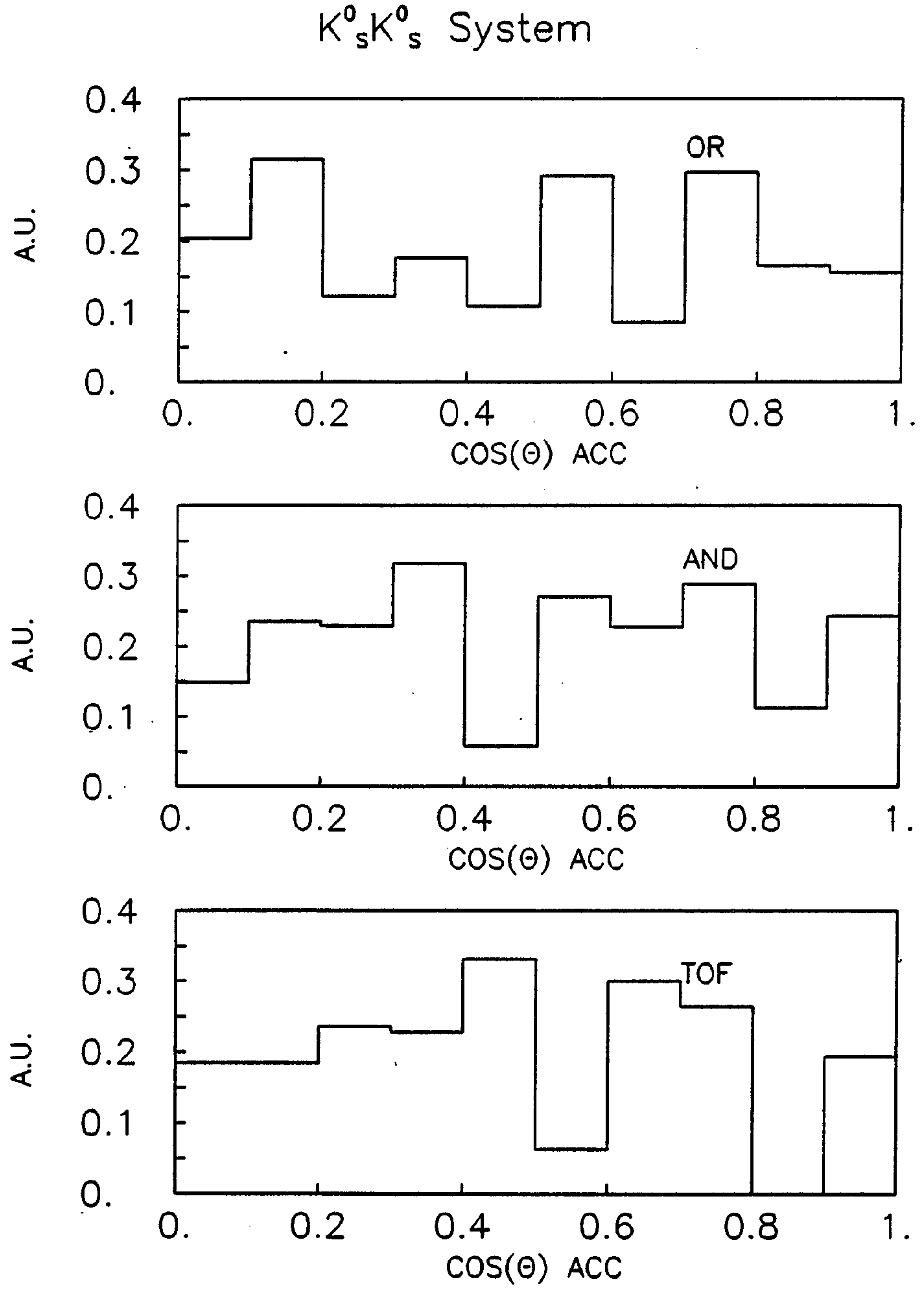

Figure 6.7 Corrected *cos*(θ) distributions of the K_s^0 , Pomeron angle for the $K_s^0 K_s^0$ system

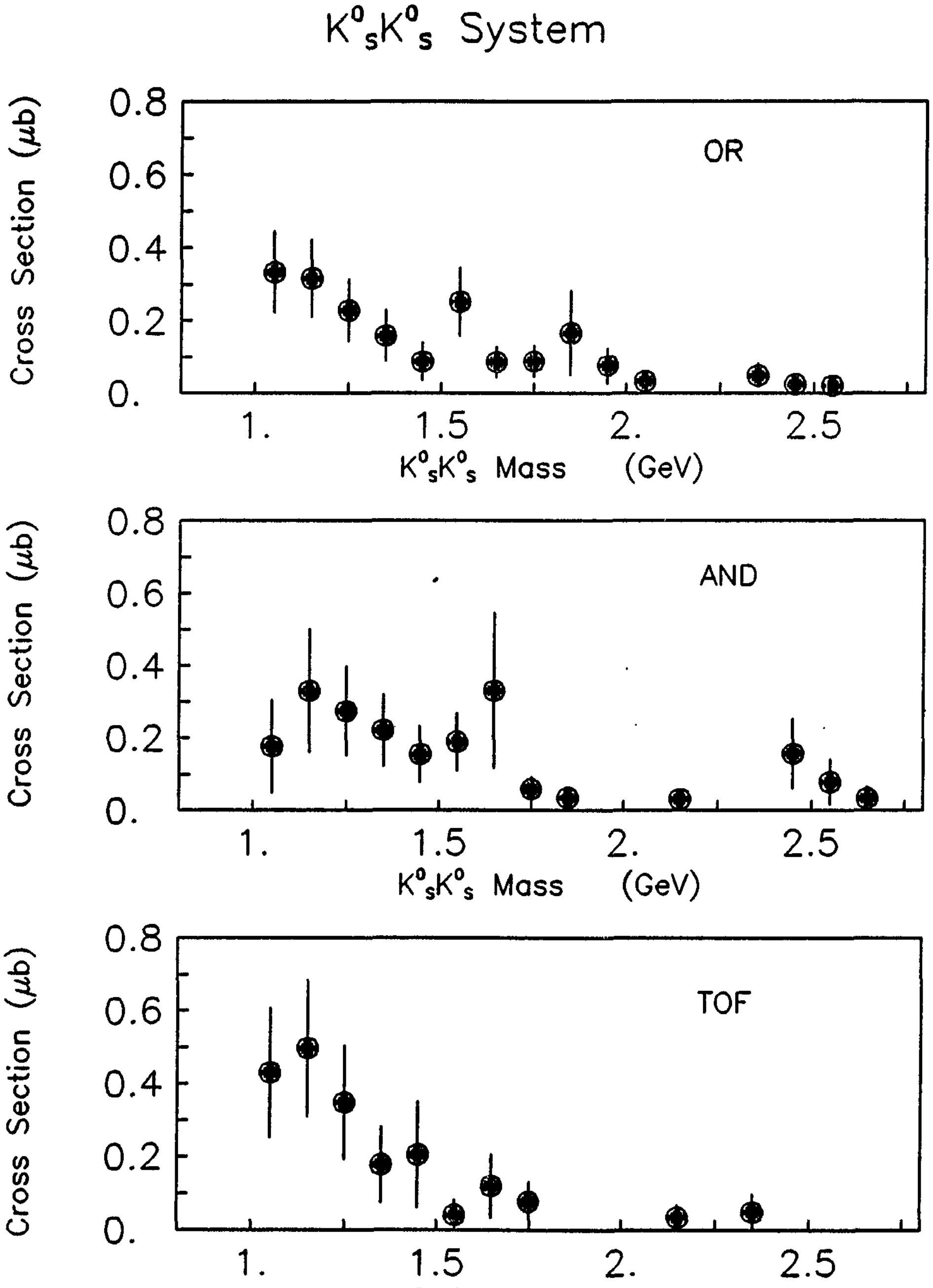

Figure 6.8 Cross sections in μb / 100 MeV as a function of the $K^0_sK^0_s$ mass for the OR (top), AND (center), and TOF (bottom) triggers

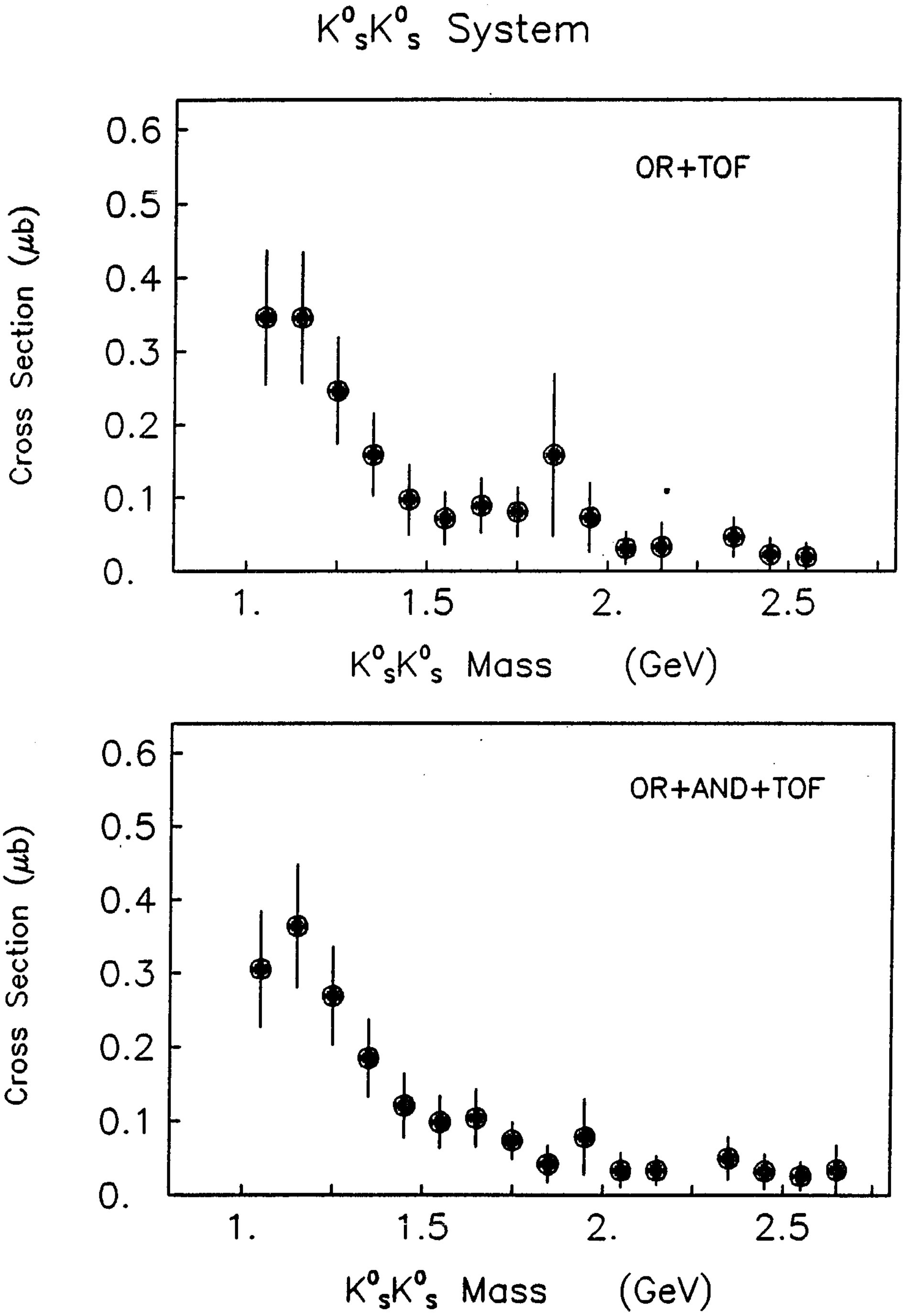

Figure 6.9 Cross sections in μb / 100 MeV as a function of the $K^0_s K^0_s$ mass for the OR and TOF data sets added (top) and the OR, AND, and TOF data sets added (bottom)

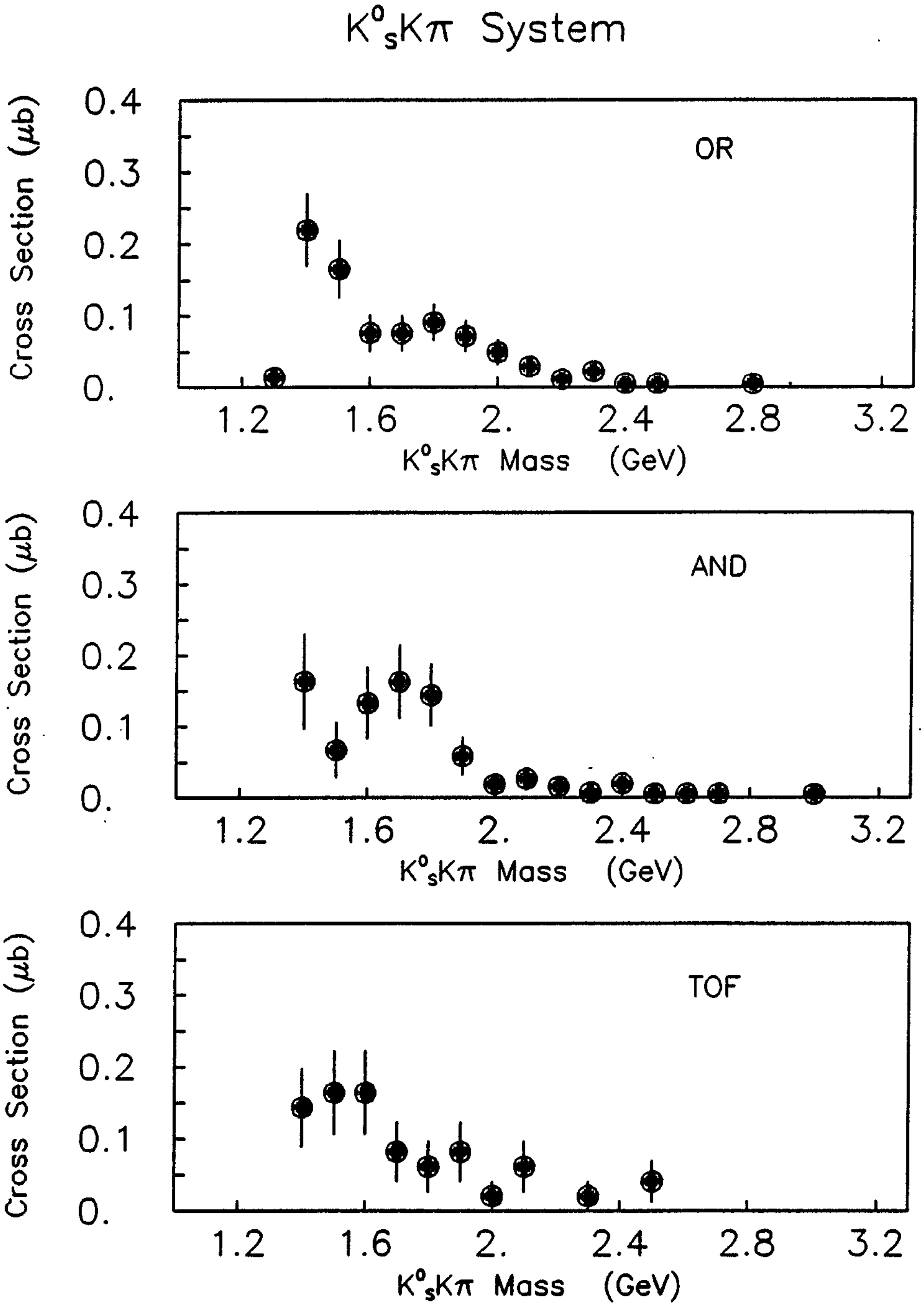

Figure 6.10 Cross sections in μb / 100 MeV as a function of the $K^0_s K^{\pm}\pi^{\mp}$ mass for the OR (top), AND (center), and TOF (bottom) triggers

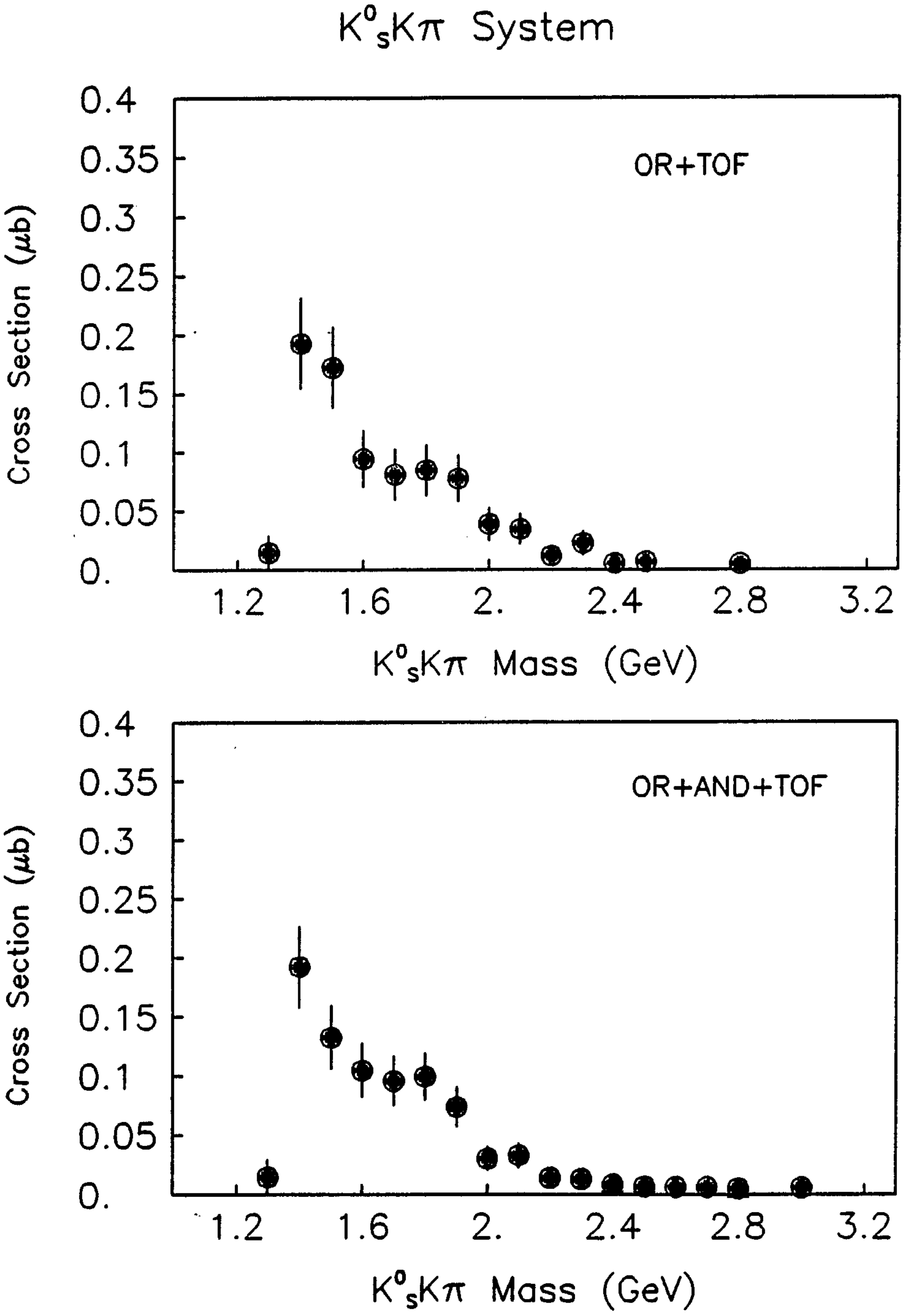

Figure 6.11 Cross sections in μb / 100 MeV as a function of the $K_s^0 K^\pm \pi^\mp$ mass for the OR and TOF data sets added (top) and the OR, AND, and TOF data sets added (bottom)

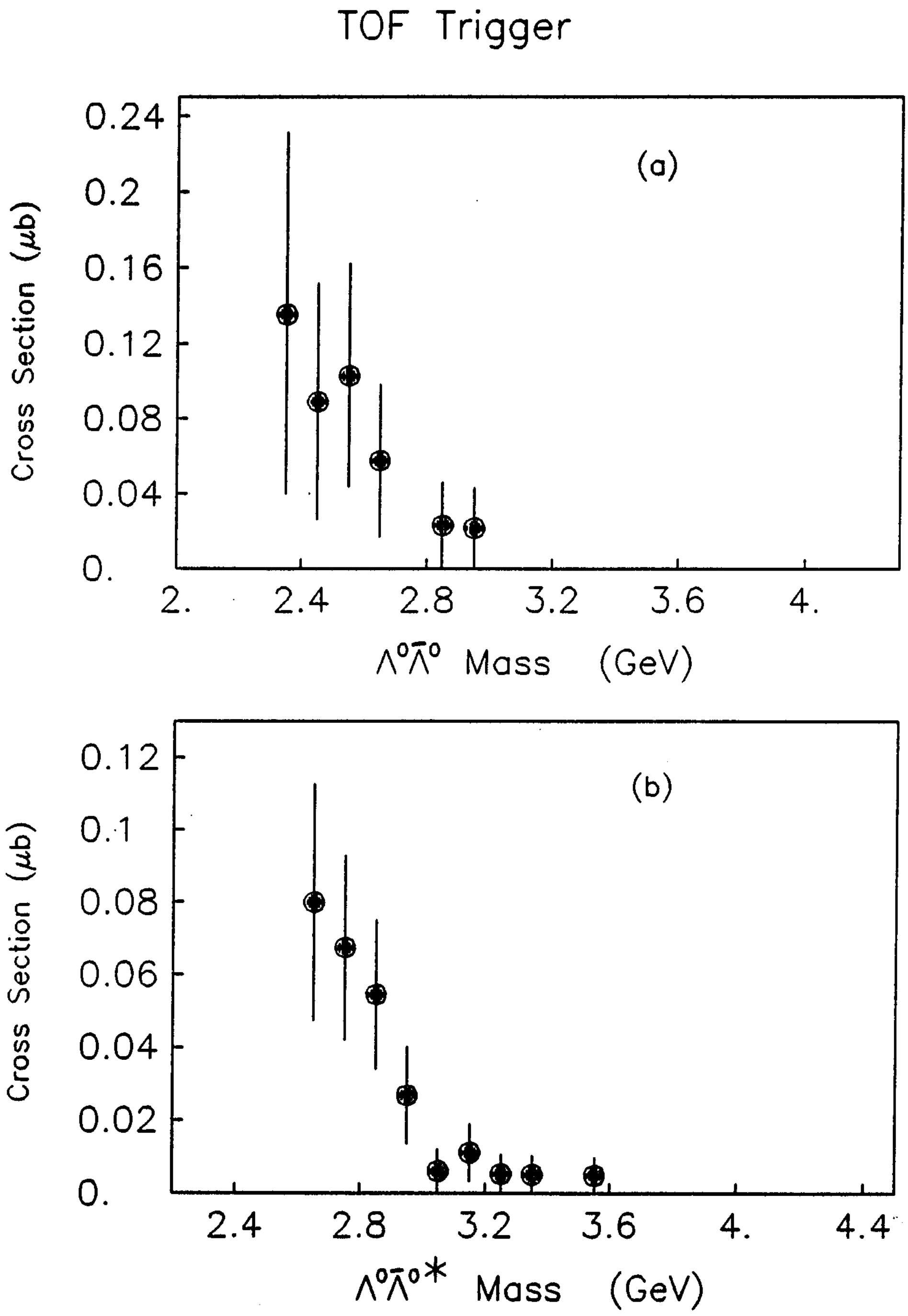

Figure 6.12 Cross sections in μb / 100 MeV as a function of the $\Lambda^0\bar{\Lambda}^0$ mass (top) and the $\Lambda^0\bar{\Lambda}^{0*}$ mass (bottom)

7 SUMMARY AND CONCLUSIONS

The isolation and analysis of the $K_s^0 K_s^0$ system has yielded a total cross section estimate of $1.3 \pm 0.6\,\mu b$. Since the K^0 particle is 50% K_s^0 and 50% K_l^0 (likewise for the $\bar{K}^0$), one can estimate the $K^0\bar{K}^0$ cross section to be $5.2 \pm 2.4\,\mu b$. This is consistent with the K^+K^- cross section estimate of $6.5 \pm 1.7\,\mu b$ for this experiment [Breakstone et al. 1989]. The low mass enhancement near 1200 MeV is also seen in the K^+K^- mass distributions and could be due to a resonant state. The resonance is likely to have the quantum numbers of $J^{PC} = 0^{++}$. A phase amplitude analysis in πp reactions has yielded a similar resonance termed the $f_0(1240)$ [Particle Data Group 1988]. $\gamma\gamma$ interactions have yielded strikingly different distributions in this $K_s^0 K_s^0$ system [CELLO Collaboration 1988]. However, the $f(1525)$ production seen in $\gamma\gamma$ interactions cannot be ruled out of the mass distributions for DPE in this experiment.

The $K_s^0 K^\pm \pi^\mp$ system analysis has proved interesting, but not as reliable due to the larger backgrounds involved. It has nevertheless yielded an estimate of the KK^* cross section of $.44 \pm .14\,\mu b$. There is the possible identification of the 1400 MeV enhancement as the $f_0(1400)$ particle, but low statistics and K^* ambiguities render a detailed study of the $cos(\theta)$ distributions inconclusive. In $\gamma\gamma$ interactions, the $K_s^0 K^\pm \pi^\mp$ system has produced a resonance at the same mass with spin one, i.e., the $f_1(1420)$ particle [CELLO Collaboration 1989].

The $\Lambda^0\bar{\Lambda}^0$ results have been much harder to obtain, showing a signal in only the TOF trigger data. The statistics are very low, and the TOF trigger acceptance is poor. An estimate of the total cross section of $.20 \pm .14\,\mu b$ has been obtained. The $\Lambda^0\bar{\Lambda}^{0*}$ system has been more encouraging with a clear enhancement seen at the $\Lambda(1520)$ resonance. A cross section estimate of $.13 \pm .06\,\mu b$ has been obtained for this system. These cross sections are a factor of ≈ 2 smaller than the total $p\bar{p}$ and $p\bar{p}\pi^+\pi^-$ cross sections for this experiment [Breakstone et al. 1989]. The existence of a possible $\Lambda^0\bar{\Lambda}^0$ signal, though small, is significant, since it has not been seen in other interactions such as πp or $\gamma\gamma$. However, the J/Ψ has been seen to decay to $\Lambda^0\bar{\Lambda}^0$ [Particle Data Group 1988].

The analysis presented here on neutral strange particle production in exclusive reactions has been interesting. These data represent the only known experimental information for exclusive neutral strange particle reactions in the DPE mechanism. In order to study these systems further, more information is needed on DPE reactions (i.e., $pp \rightarrow ppX$), which may only be obtained by taking more data with higher statistics. With the dismantling of the ISR in 1984, this will prove difficult to do. Experiments utilizing fixed targets have isolated some fraction of DPE events [Armstrong et al. 1989], but the obtainable rapidity gap is not of the same quality as at the ISR.

8 REFERENCES

U. Amaldi, M. Jacob, and G. Matthiae, Ann. Rev. Nucl. Sci. 26, 385 (1976).

T. Armstrong et al., "Study of the $\pi^+\pi^+\pi^-\pi^-$ System Centrally Produced By Incident π^+ and p Beams at 85 GeV/c", preprint CERN/EP 89-24, January 1989.

J. J. Aubert and C. Broll, Nucl. Instr. Methods 120, 137 (1974).

J. E. Augustin et al., Z. Phys. C36, 369 (1987).

Baglin et al., Phys. Lett. B187, 191 (1987).

W. Bell et al., Nucl. Instr. Methods 156, 111 (1978).

W. Bell et al., Nucl. Instr. Methods 124, 437 (1975).

B. Berg, A. Billoire, and C. Vohwinkel, Phys. Rev. Lett. 57, 400 (1986).

B. Berg, A. Billoire, and C. Rebbi, Ann. Phys. 142, 185 (1982).

R. Bouclier et al., Nucl. Instr. Methods 125, 19 (1975).

R. Bouclier et al., Nucl. Instr. Methods 115, 235 (1974).

A. Brandt et al., Nucl. Instr. Methods 126, 519 (1975).

A. Breakstone et al., Z. Phys. C42, 387 (1989).

A. Breakstone et al., Z. Phys. C31, 185 (1986).

P. Bryant, "Beam Crossing Angles at the SFM", SFM Internal Note, 13/8/73.

CELLO Collaboration, Z. Phys. C42, 367 (1989).

CELLO Collaboration, "The $K^0_s K^0_s$ Final State in $\gamma\gamma$ interactions", DESY 88-193, December 1988.

G. Chew, S. Frautschi, and S. Mandelstam, Phys. Rev. 126, 1202 (1962).

T. A. DeGrand, Phys. Rev. D36, 176 (1987).

D. Drijard et al., Nucl. Phys. B143, 61 (1978).

D. Drijard, "Momentum Analysis by Using a Quintic Spline Model for the Track", SFM Internal Note (1976).

A. Etkin et al., Phys. Rev. D25, 2446 (1982).

C. Fischer et al., IEEE Trans. on Nucl. Sci. NS-26, 3155 (1979).

Ph. de Forcrand et al., Z. Phys. C31, 87 (1986).

A. G. Frodesen, O. Skjeggestad, and H. Tofte, Probability and Statistics in Particle Physics (Universitetsforlaget, Bergen, 1979).

M. Heiden, "A Measurement of Direct Electron Production in Proton-Proton Collisions at the CERN ISR", CERN EP Internal Report 82-05, November 1982.

K. N. Henrichsen et al., in Proc. IXth Intern. Conf. on High Energy Accel., 390 (1974).

K. Huang, Quarks, Leptons, and Gauge Fields (World Scientific, Singapore, 1982).

K. Hubner, "ISR Performance for Pedestrians", CERN 77-15 (1977).

L. D. Isenhower, Ph.D. thesis, Iowa State University, 1986 (unpublished).

K. Ishikawa, G. Schierholz, and M. Teper, Phys. Lett. B110, 399 (1982).

R. L. Jaffe, K. Johnson, and Z. Ryzak, Ann. Phys. 168, 344 (1986).

F. James: FOWL, CERN Program Library (1967).

A. B. Kaidalow and K. A. Ter-Martirosyan, Nucl. Phys. B75, 471 (1974).

H. Kamenzki and B. Berg, Phys. Rev. D33, 596 (1986).

E. Keil, "Intersecting Storage Rings", CERN 72-14, July 1972.

F. E. Low, Phys. Rev. D12, 163 (1975).

Mark II Collaboration, Presented by G. Gidal: Proc. 23^{rd} Int. Conf. on High Energy Physics (Session 19), Berkeley, 1986.

R. Messerli: SFMGENER, CERN (unpublished).

E. G. Michaelis, "Notes on Particles Accelerators", CERN Summer Student Programme Lectures, 1981.

A. Minten, Internal Note CERN/SFMD 72-4 (1972).

S. Nussinov, Phys. Rev. Lett. 34, 1286 (1975).

L. B. Okun and I. Ia. Pomeranchuk, Soviet Phys. JETP 3, 307 (1956).

Particle Data Group, "Review of Particle Properties", Phys. Lett. B204, (1988).

D. H. Perkins, Introduction to High Energy Physics (Addison-Wesley, Reading, Massachusetts, 1982).

I. Ia. Pomeranchuk, Soviet Phys. JETP 7, 499 (1958).

I. Ia. Pomeranchuk, Soviet Phys. JETP 3, 306 (1956).

J. Pumplin and E. Lehman, Z. Phys. C9, 25 (1981).

C. Quigg, Gauge Theories of the Strong, Weak, and Electromagnetic Interactions (The Benjamin/Cummings Publishing Company Inc., Menlo Park, CA., 1983).

K. Rauschnabel, "V^0 Reconstruction in the Split Field Magnet Spectrometer", CERN EP Internal Report 81-1, April 1981.

D. Robson, Nucl. Phys. B130, 328 (1977).

D. P. Roy and G. G. Roberts, Nucl. Phys. B82, 422 (1974).

G. Schierholz, "The Glueball Mass Spectrum in SU(3) Lattice Gauge Theory", DESY 88-184, December 1988a.

G. Schierholz, "Status of Lattice Glueball Mass Calculations", DESY 88-172, November 1988b.

G. Schierholz, "Glueball Masses in SU(3) Lattice Gauge Theory", DESY 87-157 December 1987.

B. F. L. Ward, Phys. Rev. D33, 1900 (1986).

H. Wind, Nucl. Instr. Methods 153, 195 (1978).

H. Wind, Nucl. Instr. Methods 115, 431 (1974).

9 ACKNOWLEDGMENTS

I first want to thank God for giving us such a fascinating world of physics to study. I would like to thank my wife, Leann, for her support during my work here at Iowa State. She has helped me considerably with her encouragement and kind criticism in helping to proof read my thesis. I would also like to thank my mother and stepfather, Marge and Gene Sease, for their continued encouragement and support. I would like to thank my father Ronald Skeens. Thanks also go to my wife's parents, Bud and Norma Hohensee. Thanks also to my four brothers, especially Tim, for their encouragement. I particularly would like to thank my son Carl John for inspiration.

I would like to thank Dr. Alexander Firestone for his many helpful suggestions and kind criticisms on my dissertation work. Thanks to Dr. Don Isenhower and Dr. H. Bert Crawley for helping me get started on my thesis topic. Their earlier work proved invaluable in the initial debugging and running of the analysis programs. A special thanks goes to Dr. Walter Thomas Meyer for graciously filling in for Dr. Crawley for my final oral examination. His kind suggestions and advice were greatly appreciated. A special thanks also to Dr. Eli I. Rosenberg for filling in for Dr. Firestone for my final oral exam and also giving me the encouragement I needed to finish this work. Thanks to the other members of my committee, Dr. Bing-Lin Young, Dr. Fred Wohn, and Dr. Gary Lieberman.

I would especially like to thank Dr. Jerry Lamsa, who helped me greatly in calculations of the acceptances used in this thesis. I would also like to thank the people who have contributed to the many parts of this experiment to make it work. In addition, I would like to thank some of the people who have helped me at various stages of my work, Dr. Mark Gorbics, Dr. David Slaven, and Ms. Linda Shuck.

This work was performed at Ames Laboratory under contract No. W-7405-eng-82 with the U. S. Department of Energy. The United States government has assigned the DOE Report number IS-T 1420 to this thesis.